EXPERIMENTAL AND QUANTITATIVE ANALYSIS OF MULTIPHASE CATALYTIC REACTIONS UNDER MICROFLUIDIC FLOW CONDITIONS AND GEOMETRIES

by

Mustafa Karakaya

B.S, Chemical Engineering, Boğaziçi University, 2003

M.S, Chemical Engineering, Boğaziçi University, 2006

Submitted to the Institute for Graduate Studies in
Science and Engineering in partial fulfillment of
the requirements for the degree of
Doctor of Philosophy

Graduate Program in Chemical Engineering

Boğaziçi University

2012

EXPERIMENTAL AND QUANTITATIVE ANALYSIS OF MULTIPHASE CATALYTIC REACTIONS UNDER MICROFLUIDIC FLOW CONDITIONS AND GEOMETRIES

APPROVED BY:

Assoc. Prof. Ahmet Kerim Avcı .....
(Thesis Supervisor)

Prof. Ayşe Nilgün Akın .....

Prof. Ahmet Erhan Aksoylu .....

Assist. Prof. Seda Keskin Avcı .....

Prof. Zeynep İlsen Önsan .....

DATE OF APPROVAL: 7.6.2012

dedicated to the loving memories of

Coco, Katja and Cilki

ACKNOWLEDGEMENTS

I would like to express my gratitude to my supervisor, Assoc. Prof. Ahmet Kerim Avcı, whose expertise, understanding and patience added greatly to my graduate experience. I would like to thank him for the assistance and "occupational therapy" he provided at all levels in the course of the research. He became more of a friend or a mentor, than a professor. Not even these few paragraphs would have come to life had I not the luck to work with him.

I owe a great lot to Prof. Ahmet Erhan Aksoylu and Prof. Zeynep İlsen Önsan for their academic and personal guidance, and of course, for their patience.

The departmental and Kare Blok support staff have always treated me kindly and assisted me with everything I asked for. Mr. Yakup Bal, Ms. Belgin Balkan, Mr. Nurettin Bektaş, Mr. Bilgi Dedeoğlu, Ms. Melike Gürbüz, Ms. Esma Toprak, Ms. Başak Ünen and all other friends, I will be missing you dearly.

Two other people I have already sorely missed are Ms. Ceylan Çölmekçi and Ms. Dicle Hasdemir. May you live your lives to the fullest, and accomplish every dream of yours!

I would like to express my gratitude to Ms. Bilge Gedik Uluocak for her assistance in electron microscopy analyses, and to Mr. Erkan Karabekmez for his assistance in X-ray diffraction analyses conducted at Boğaziçi University Advanced Technologies R&D Center.

I recognize that this research would not have been possible without the financial support provided by TÜBİTAK (Türkiye Bilimsel ve Teknolojik Araştırma Kurumu) through project **MAG-108M509**, by Boğaziçi University Research Fund through projects **BAP-06A503** and **BAP-09HA507D**, by the **TÜBA-GEBİP** (Türkiye Bilimler Akademisi Üstün Başarılı Genç Bilim İnsanlarını Ödüllendirme Programı) pro-

gram, and by Boğaziçi University Foundation through the **Fahir İlkel Ph.D. grant**.

A very personal note: It would have been much harder to get through with this work had I not found you Burcu, the Moon of My Life. Thank you for being there whenever I need you.

I am incapable of giving coherent, clear, or effective expressions to my feelings about my family. All I can say is that I am greatly indebted to these patient people for the support they provided me through my entire life.

To Coco, Katja, Tilki and all my other cronies: Rest in peace; may the eternal and celestial serenity find you...

ABSTRACT

EXPERIMENTAL AND QUANTITATIVE ANALYSIS OF MULTIPHASE CATALYTIC REACTIONS UNDER MICROFLUIDIC FLOW CONDITIONS AND GEOMETRIES

Catalytic synthesis gas and hydrogen production in coupled and decoupled compact reaction/heat exchange systems are investigated by computational and experimental techniques. Computer-based modeling and simulation studies carried out in the first phase of the research demonstrate the effects of the structural parameters of microchannel reactors on combustion-assisted conversion of C_1 and C_2 hydrocarbons and alcohols, and light petroleum distillates to synthesis gas/hydrogen. Outcomes of these studies set the basis for the design and construction of wall-coated catalyst integrated microchannel reactors that are used in the second part of the research involving experimental studies in which microfluidic methane-to-synthesis gas conversions via steam reforming and autothermal reforming mechanisms over Ni, Rh, Ru and Pt-based catalysts are investigated. For each catalyst, impacts of parameters such as temperature, residence time, feed compositions on methane conversion and product distribution/synthesis gas production rates are studied. The wall-coated microchannel reactor performance is also compared with that of a conventional packed-bed reactor configuration under identical conditions. The outcomes clearly show that (i) robust control of heat transfer is possible in compact reaction systems, (ii) synthesis gas production is possible with energy requirements lower than the amounts used in industrial applications, and (iii) methane conversions and synthesis gas production rates are notably higher than those obtained from a packed-bed reactor operated under identical conditions.

ÖZET

ÇOK FAZLI KATALİTİK REAKSİYONLARIN MİKROAKIŞ KOŞUL VE GEOMETRİLERİNDE DENEYSEL VE HESAPLAMALI YÖNTEMLERLE İNCELENMESİ

Katalitik sentez gazı ve hidrojen üretimi birleşik ve ayrışık kompakt reaksiyon/ısı değişim sistemlerinde hesaplamalı ve deneysel yöntemlerle incelenmiştir. Araştırmanın ilk bölümünde yürütülen hesaplamalı çalışmalar, tek ve çift karbonlu hidrokarbon ve alkollerin ve hafif petrol distilatlarının ısı değişimi destekli olarak sentez gazı/hidrojene dönüşümlerinde mikrokanal reaktör yapısının etkilerini ortaya koymaktadır. Elde edilen sonuçlar ışığında tasarlanan ve imal edilen, katalizörün kaplı bir tabaka halinde bulunduğu mikrokanal reaktörler araştırmanın ikinci bölümündeki deneysel çalışmalarda kullanılmıştır. Bu çalışmalar kapsamında metanın sentez gazına mikroakış koşullarında oksijensiz ve oksijen destekli metan buhar reformlama reaksiyonları ile dönüşümü Ni, Rh, Ru ve Pt bazlı katalizörler üzerinde incelenmiş, her katalizör için sıcaklık, alıkonma süresi, besleme karışımı değerleri gibi değişkenlerin metan dönüşümü ve ürün dağılımı/sentez gazı üretim hızları üzerindeki etkileri araştırılmıştır. Ayrıca, mikrokanal reaktör düzeni, klasik sabit yatak reaktör düzeni ile denk koşullarda karşılaştırılmıştır. Sonuçlar, (i) kompakt reaksiyon sistemlerinde ısı transferi kontrolünün son derece gelişmiş olduğunu, (ii) bu birimlerdeki sentez gazı üretiminin, endüstride uygulanan koşullara kıyasla, daha düşük enerji girdileri ile gerçekleşebileceğini ve (iii) denk koşullarda çalışan sabit yataklı reaktörlere göre mikrokanal birimlerde çok daha yüksek metan dönüşümü ve sentez gazı üretim hızları elde edilebileceğini somut olarak ortaya koymaktadır.

TABLE OF CONTENTS

LIST OF FIGURES

LIST OF TABLES

LIST OF SYMBOLS

A_{cj}	Cross-sectional area of cascade reactor j (m^2)
$A_{k_s,j}$	Pre-exponential factor for rate of reaction k_v in channel j
A_{sj}	Active surface area of catalytic washcoat in channel j (m^{-1})
c_{lj}	Molar concentration of species l in channel j ($\mathrm{mol\,m}^{-2}$, $\mathrm{mol\,m}^{-3}$)
$c_{p_{fj}}$	Heat capacity of fluid in channel j ($\mathrm{J\,kg}^{-1}\,\mathrm{K}^{-1}$)
$c_{p_{ij}}$	Heat capacity of species i in channel or cascade j ($\mathrm{J\,kg}^{-1}\,\mathrm{K}^{-1}$)
$c_{p_{sj}}$	Heat capacity of catalytic washcoat in channel j ($\mathrm{J\,kg}^{-1}\,\mathrm{K}^{-1}$)
c_{p_w}	Heat capacity of solid wall (fin) ($\mathrm{J\,kg}^{-1}\,\mathrm{K}^{-1}$)
C_{2j}	Inertial resistance coefficient of the washcoat in channel j (m^{-1})
C_{Fj}	Forchheimer coefficient of the washcoat in channel j
d_H	Hydraulic diameter of the microchannel (m)
d_{pj}	Particle diameter of catalyst in channel j (m)
$d_{\mathrm{pore},j}$	Average pore diameter of the catalyst in channel j (m)
D	Diameter of the housing (m)
$D_{il,j}$	Binary diffusion coefficients in channel j ($\mathrm{m}^2\,\mathrm{s}^{-1}$)
$D_{i,mj}$	Diffusivity of species i in the mixture in channel j ($\mathrm{m}^2\,\mathrm{s}^{-1}$)
$D_{\mathrm{eff},i,mj}$	Effective diffusivity of species i in the mixture in channel j ($\mathrm{m}^2\,\mathrm{s}^{-1}$)
$D_{K,ij}$	Knudsen diffusion coefficient for species i in channel j ($\mathrm{m}^2\,\mathrm{s}^{-1}$)
Da_j	Darcy number($=\alpha_j/\delta_{sj}$) for the washcoat in channel j
E_{k_s}	Activation energy of k_sth surface reaction ($\mathrm{kJ\,mol}^{-1}$)
E_{k_v}	Activation energy of k_vth volumetric reaction ($\mathrm{kJ\,mol}^{-1}$)
f	Fluid
F_{ij}	Molar flow rate of species i in channel or cascade j ($\mathrm{mol\,s}^{-1}$)
$\vec{\mathbf{F}}_j$	Momentum source/sink term in channel j ($\mathrm{kg\,m}^{-2}\,\mathrm{s}^{-2}$)
$\vec{g}$	Gravitational acceleration ($\mathrm{m\,s}^{-2}$)
h_{ij}	Sensible enthalpy of species i in channel j ($\mathrm{J\,kg}^{-1}$)

H_j	Height of microchannel j (m)
i	Species index
$\mathbf{I}$	Identity matrix, unit tensor
in	Channel or reactor inlet
j	Reaction channel index
$\vec{J}_{ij}$	Diffusive mass flux of species i in channel j ($\mathrm{kg\,m^{-2}\,s^{-1}}$)
k_{fj}	Thermal conductivity of the fluid in channel j ($\mathrm{W\,m^{-1}\,K^{-1}}$)
$k_{\mathrm{eff},j}$	Effective thermal conductivity of the fluid in channel j ($\mathrm{W\,m^{-1}\,K^{-1}}$)
k^s_{eff}	Effective thermal conductivity of the washcoat ($\mathrm{W\,m^{-1}\,K^{-1}}$)
k_{ij}	Thermal conductivity of species i in channel j ($\mathrm{W\,m^{-1}\,K^{-1}}$)
$k_g^{\mathrm{OX,\ SR}}$	Mass transfer coefficients at the gas-Pt and gas-Rh catalyst interfaces ($\mathrm{m\,s^{-1}}$)
$k^{\mathrm{ads}}_{k_s,j}$	Rate constant for the k_sth adsorption reaction in channel j
k_s	Index for the surface reactions
$k^{\mathrm{s}}_{k_s,j}$	Rate constant for the k_sth surface reaction in channel j
$k^{\mathrm{v}}_{k_v,j}$	Rate constant for the k_vth volumetric reaction in channel j
k_v	Index for the volumetric reactions
k_{sj}	Thermal conductivity of the washcoat in channel j ($\mathrm{W\,m^{-1}\,K^{-1}}$)
k_w	Thermal conductivity of solid wall (fin) ($\mathrm{W\,m^{-1}\,K^{-1}}$)
K_i	Adsorption constant for the species i
$K_{p,k_v}, K_{\mathrm{eq}}^{\mathrm{I,II,III}}$	Equilibrium constants
l	Species index
L_j	Length of microchannel j (m)
L_s	Characteristic dimension of the catalyst washcoat (m)
m	Site species index
$\dot{m}_j$	Mass flow rate in channel j ($\mathrm{kg\,s^{-1}}$)
M_{ij}	Molecular weight of species i in channel j ($\mathrm{kg\,mol^{-1}}$)
M_j	Mean molecular weight of the gas mixture in channel j ($\mathrm{kg\,mol^{-1}}$)
$\vec{\mathbf{n}}$	Normal unit vector

N_g	Number of gas-phase species
N_s	Number of surface-adsorbed species
N_{srxn}	Number of surface reactions
N_{vrxn}	Number of volumetric reactions
Nu	Nusselt number
out	Channel or reactor outlet
p_i	Partial pressure of species i (bar, kPa)
p_j	Pressure field in channel or cascade j (bar, Pa)
r	Radial coordinate (m)
R	Universal gas constant ($\mathrm{J\,mol^{-1}\,K^{-1}}$)
$\mathcal{R}^{\text{s}}_{k_s,j}$	Rate of k_sth surface reaction ($\mathrm{mol\,m^{-2}\,s^{-1}}$)
$\mathcal{R}^{\text{v}}_{k_v,j}$	Rate of k_vth volumetric reaction ($\mathrm{mol\,m^{-3}\,s^{-1}}$)
$\Re^s_{ij}$	Source of species i in channel j due to surface reaction ($\mathrm{mol\,m^{-2}\,s^{-1}}$)
$\Re^v_{ij}$	Source of species i in channel j due to volumetric reaction ($\mathrm{mol\,m^{-3}\,s^{-1}}$)
$S_{\text{BET},j}$	BET surface area of catalytic washcoat in channel j ($\mathrm{m^2\,g^{-1}}$)
S_{hj}	Heat source due to chemical reaction in channel j ($\mathrm{W\,m^{-3}}$)
$S^0_{k_s,j}$	Initial sticking coefficient for rate of reaction k_s in channel j
S_{CO}	Carbon monoxide percent selectivity
Sh	Sherwood number
SL	Side length of a microchannel (m, μm)
t	Time (s)
T_j	Temperature in channel or cascade j (°C, K)
T_w	Wall (fin) temperature (°C)
U^{in}_j	Normal inflow velocity to channel j (m)
$\vec{\mathbf{v}}_j$	Velocity field in channel j ($\mathrm{m\,s^{-1}}$)
V_{sj}	Volume of catalyst in channel j ($\mathrm{m^{-3}}$)
w_{sj}	Mass of catalyst in channel or cascade j (g)
W_j	Width of microchannel j (m)
WT	Wall (fin) thickness (m, μm)
x_{ij}	Mole fraction of species i in channel j

x, y, z	Cartesian coordinates (m)
Y_{ij}	Mass fraction of species i in channel j
α_g	Heat transfer coefficient at the gas-solid interface ($\mathrm{W\,m^{-2}\,K^{-1}}$)
α_j	Permeability of the catalytic washcoat in channel j ($\mathrm{m^2}$)
β^0	Parameter in Ergun equation
β_{k_s}	Temperature dependence coefficient of reaction k_s
Γ_j	Surface site density of catalytic washcoat in channel j ($\mathrm{mol\,m^{-2}}$)
$\vert_{\Gamma_{\mathrm{gas}}}$, $\vert_{\Gamma_{\mathrm{solid}}}$	Gas/solid side of the gas-solid interface
δ_{sj}	Thickness of catalytic washcoat in channel j (m, μm)
ΔH^0_{298}	Standard enthalpy of reaction ($\mathrm{kJ\,mol^{-1}}$)
ΔH_i	Adsorption enthalpy of species i ($\mathrm{kJ\,mol^{-1}}$)
ΔH_{k_s}	Enthalpy of k_sth surface reaction ($\mathrm{kJ\,mol^{-1}}$)
ΔH_{k_v}	Enthalpy of k_vth volumetric reaction ($\mathrm{kJ\,mol^{-1}}$)
ΔS_i	Adsorption entropy of species i ($\mathrm{kJ\,mol^{-1}}$)
$\epsilon_{\mathrm{cat},j}$	Porosity of catalyst in channel or cascade j
ϵ_{m,k_s}	Coverage parameter for site species m in reaction k_s
η_{m,k_s}	Coverage parameter for site species m in reaction k_s
θ_{mj}	Surface coverage of species m in channel j
μ_{ij}	Viscosity of species i in channel j ($\mathrm{kg\,m^{-1}\,s^{-1}}$)
μ_j	Viscosity of the gas mixture in channel j ($\mathrm{kg\,m^{-1}\,s^{-1}}$)
$\mu_{\mathrm{eff},j}$	Effective viscosity of the gas mixture in the washcoat in channel j ($\mathrm{kg\,m^{-1}\,s^{-1}}$)
μ_{m,k_s}	Coverage parameter for site species m in reaction k_s
$\nu'_{i,k_s,j}$	Stoichiometric coefficient of reactant i in the k_sth surface reaction
$\nu''_{i,k_s,j}$	Stoichiometric coefficient of product i in the k_sth surface reaction
ρ_{fj}	Fluid density in channel j ($\mathrm{kg\,m^{-3}}$)
ρ_{sj}	Solid density of catalyst in channel or cascade j ($\mathrm{kg\,m^{-3}}$)

ρ_w	Solid wall (fin) density ($\mathrm{kg\,m^{-3}}$)
τ	Residence time of the reactants in the microchannels (ms)
$\tau_{\mathrm{cat},j}$	Tortuosity of catalytic washcoat in channel j
$\bar{\bar{\tau}}_j$	Stress tensor in channel j due to flow ($\mathrm{kg\,m^{-2}\,s^{-2}}$)
χ_i	Percent conversion of species i
Ψ	Test parameter for existence of transport limitations
ϖ_i	Collision diameter of species i
Ω_i	Collision integral of species i

LIST OF ACRONYMS/ABBREVIATIONS

2D	Two Dimensional
3D	Three Dimensional
APU	Auxiliary Power Unit
AS	Axisymmetric
ASF	Anderson-Schulz-Flory
ATR	Autothermal Reforming
BET	Brunauer-Emmett-Teller
BSE	Backscattering Electron
CFD	Computational Fluid Dynamics
COMB	Combustion
CPO	Catalytic Partial Oxidation
DME	Dimethyl Ether
ED	Ethane Dehydrogenation
EDX	Energy Dispersive X-Ray Analysis
EXO	Exothermic
ENDO	Endothermic
FEM	Finite Element Method
FT	Fischer-Tropsch
FTS	Fischer-Tropsch Synthesis
FVM	Finite Volume method
GC	Gas Chromatograph
GHSV	Gas Hourly Space Velocity
HEX	Heat Exchanger
HPLC	High-Pressure Liquid Chromatography
HTFT	High-Temperature Fischer-Tropsch
HTS	High-Temperature Shift
IPOX	Indirect Partial Oxidation
LHHW	Langmuir-Hinshelwood-Hougen-Watson

LHV	Lower Heating Value
LIGA	Lithographie, Galvanoformung, Abformung
LNG	Liquefied Natural Gas
LPG	Liquefied Petroleum Gas
LTFT	Low-Temperature Fischer-Tropsch
LTS	Low-Temperature Shift
MAB	Multiple Adiabatic Beds
MC	Microchannel
MF	Micro-Baffled
O_2:C	Oxygen-to-Carbon Ratio
ODE	Ordinary Differential Equation
OX	Oxidation
PB	Packed Bed
PCHE	Printed Circuit Heat Exchanger
PDE	Partial Differential Equation
PEMFC	Proton Exchange Membrane Fuel Cell
POX	Partial Oxidation
PROX	Preferential Oxidation
S:C	Steam-to-Carbon Ratio
SEM	Scanning Electron Microscopy
SR	Steam Reforming
SRM	Steam Reforming of Methane
ST	Straight-Through
TCD	Thermal Conductivity Detector
TOF	Turnover Frequency
TOX	Total Oxidation
WGS	Water-Gas Shift
WHSV	Weight Hourly Space Velocity
XRD	X-Ray Diffraction

1. INTRODUCTION

In today's world, great emphasis is placed on the value of sustainable development in its environmental, social and economic dimensions. The inevitable change in industrial production methods brings about challenges that are about meeting the increasing demand for energy and products without sacrificing the principles of sustainability. For the chemical industries, these challenges manifest themselves mainly as the depletion of nonrenewable resources, rising oil prices, and environmental problems. In search of viable solutions, the chemical engineering community has coined the term *process intensification* [1] to describe the strategy that aims to deliver significant improvements in manufacturing and processing. Smaller equipment sizes, increased output and economic value per unit of raw material, reduced capital costs, and minimal environmental impact are examples of these improvements.

Interpretation of process intensification leads to various approaches that refer to all scales existing in chemical processes, from molecular to meso- and macroscale [2]. One of these is the association of process intensification with a reduction either in size of individual process equipment or number of unit operations designed to achieve a given production objective in unit time. Stankiewicz and Moulijn [3] extend the scope of the term process intensification by considering size reduction merely as a result of such holistic improvements as increase in production capacity within a given volume, decrease in energy consumption per ton of product, and marked cut in waste and by-product formation. Process intensification, in an up-to-date sense, comprises novel equipment, processing techniques and process development methods that, compared with conventional ones, offer substantial improvements in chemical manufacturing and processing [4].

Process intensification can be achieved through development of process-intensifying equipment, such as heat- and mass-transfer devices and chemical reactors that enhance mixing and reduce transport lengths, to name but a few. Apart from novel equipment design, implementation of methods such as hybrid separations, integration

of reaction and heat transfer, and of new process control algorithms can also lead to process intensification [3].

Miniaturization, down to the submillimeter scale, of confinements and/or repeated units within a process equipment is one of the crucial strategies toward process intensification. Such microstructured equipment has internal characteristic dimensions like channel diameter or gap height within the micrometer range [5]. Compared with conventional equipment comprised of macrosized elements, the common feature of microstructured devices is their distinctly better-defined operating condition range, higher flexibility and availability for internal and external numbering-up to increase the throughput [6].

Chemical manufacturing systems that can be used in small scale and in distributed production are seen to have significant advantages such as reduced capital cost, smaller plant footprints and potentially easier transportation [4]. These advantages can also be particularly valuable when considering the exploitation of remote resources such as offshore reserves of natural gas.

The high surface-to-volume ratio of microchannel reactors is their principal feature that is often exploited so as to overcome heat and mass transfer limitations frequently encountered in traditional reactors. The specific surface in microchannel reactors vary in the range $10000 - 50000\ \mathrm{m^2\,m^{-3}}$ whereas it seldom exceeds $1000\ \mathrm{m^2\,m^{-3}}$ in conventional laboratory and production vessels [7]. In such microfluidic geometries, owing to the several orders-of-magnitude increase both in the heat-exchange surface per unit volume and the heat transfer coefficient, very high overall heat transfer rates can be realized, which is particularly important for efficient removal of heat generated during highly exothermic reactions and suppression of hot spots [8].

Coupling exothermic and endothermic reactions in various configurations within a microchannel reactor stack is a very efficient way of improved heat utilization [9–22]. One of the most frequently encountered applications is coupling of combustion and steam reforming/decomposition reactions in microchannels for syngas and hydrogen

production. The reactions are allowed to take place in alternating combustion and reforming/decomposition channels (and/or plates) either in co-current or counter-current mode; thus, the heat produced by the exothermic reaction can be quickly utilized by the endothermic reaction.

Taking advantage of improved heat and mass transfer in microdevices allows for higher production yields and efficiencies. One current drawback in attempting to implement widespread use of microchannel reactors in chemical processing is the fabrication cost arising from their delicate structures. Process efficiency may drop as a result of catalyst deactivation in a single microchannel stack, for instance [23]. In such a case, the microchannel module has to be replaced altogether, which will be wastefully costly.

Apart from complete miniaturization of the process equipment, highly intensified, highly integrated processes can be devised by promoting intensification in heat transfer while decoupling it from the reaction zones, as demonstrated by Seris and coworkers [24, 25] via a pilot plant for the production of syngas by methane steam reforming. The fine passages employed during the fabrication of the Printed Circuit Heat Exchanger (PCHE) [26–28] have characteristic dimensions of around 1 mm, ideally suited to miniaturization. The reaction compartments, on the other hand, are of packed-bed or monolithic types on the conventional design basis. In case when a packed bed is used, smaller particles might be preferred in order to increase catalyst effectiveness so as to assist process intensification, but pressure drop should still be acceptable. One other advantage of using PCHEs and adiabatic beds is that flow patterns can be configured to produce flat temperature profiles, thereby avoiding hot spots. The *multiple adiabatic bed* arrangement also allows periodic injection of fresh reactants, hence the exothermicity of the reactions is kept within the safety margins [24].

The objective of the presented research is the experimental and quantitative investigation of multiphase catalytic reactions in microchannel reactors in the context of production of H_2 for fuel cells and syngas for feedstock. The proposed reactor designs are explored to meet specific physical criteria using detailed mathematical models and

enhanced simulation tools via a parametric approach, and are then implemented into experimental rigs for testing purposes.

Chapter 2 is comprised of an up-to-date literature review of the scope for process intensification, achieved by miniaturization of process equipment, in particular of heat exchange equipment and chemical reactors, and by possible cascading of these devices at the micro or macro level according to novel process design guidelines. In line with the goals of this research, well-established conventional fuel processing technologies for hydrogen-rich syngas production are also introduced in Chapter 2. The specific processes modeled (e.g. combustion-assisted reforming of heptane or octane, steam/autothermal reforming of methane) are described in detail in Chapter 3 together with the mathematical models and numerical solution techniques employed. The techniques, procedures and equipments used in the experiments are thoroughly described in Chapter 4. Results of the research and the highlights are presented and discussed in Chapter 5. Finally, Chapter 6 involves major conclusions and recommendations for future work.

2. LITERATURE SURVEY

Rendering a reduction in the dimensions of a channel through which a given amount of fluid is forced to flow provides a larger transfer area per unit volume. Heat and mass transport rates are hence drastically enhanced that have direct influence on exchange phenomena. Further, carrying out certain chemical reactions in microchannels is shown to warrant high yields [29, 30]. Still, in many cases, these benefits offered by microchannel reactors and heat exchangers can be augmented by novel integration of heat exchanger and reactor compartments. However, the increase in effectiveness and productivity comes with a number of usually irreversible penalties due to the difficulties associated with working at the microscale: fouling in channels, deactivation of coated catalyst, increased pressure drop, complex design of distribution manifolds and flow instabilities induced by structured geometries. One of the aims of extensive research being done in the field of microfluidics is to establish, in well-defined terms, the thermal and hydraulic properties of single- and multiphase fluid flow in microstructured devices. While doing so, ways are also sought of numbering up and integrating these in the most efficient configuration. In due course, the basic issues that need to be addressed are cost-effective manufacturing processes, assurance of reliable operation and determination of thermal and hydraulic performance characteristics [31]. In accordance with the requirements stated above, major works in the available literature are surveyed as they fall into three specific but related parts: microchannel heat exchangers, microchannel reactors and integrated reaction/heat exchange systems. The first part involves a descriptive review of the properties such as the dimensions and the flow regime that characterize microchannel heat exchangers and the essential manufacturing techniques used. A compilation of correlations for the heat transfer coefficient in the laminar flow regime is also made. However, care must be taken while doing so, because the correlations are only valid under the assumption of continuum flow (the "no slip" condition), which might, in certain cases, be inapplicable due to very small channel diameters. After a brief comparison with conventional heat exchange equipment on the basis of scaling effects and performance criteria, computer-based studies on modeling, simulation and design of microchannel heat exchangers are reviewed. The

latter is particularly important for the optimization of the distribution manifold design and flow configuration. Computational fluid dynamics (CFD) investigation of the heat exchange systems not only give accurate results but it also allows for testing many different geometries with lesser effort.

The review of works on microchannel reaction systems is made with consideration of two very important processes:

- Processing of hydrocarbons and alcohols into *synthesis gas* (mixture of hydrogen and carbon monoxide), which is an intermediate product that is used as feedstock in commodity chemicals production processes (e.g. Fischer-Tropsch, methanol and dimethyl ether syntheses), and that is further purified for use in fuel cells which require CO-free hydrogen.
- *Fischer-Tropsch synthesis*, also known as carbon monoxide hydrogenation, for production of a wide range of hydrocarbons, including paraffins, olefins and oxygenates.

Experimental studies on each reaction system are evaluated, involving enough detail as to the catalyst type, microchannel dimensions and reaction conditions. Major modeling and simulation works that make use of different computational tools are also included in the survey. The ongoing transition to microchannel reaction systems takes its roots from well-known and widely-applied integrated reactor/heat exchanger systems. Coupling highly exothermic and endothermic reactions in various configurations and geometries provides efficient heat utilization, even at the macroscale. This part of the literature survey is concerned with studies that aim at devising and experimentally testing different ways of coupling reaction(s) and heat transfer, either in micro or macro geometries. These include parallel microchannel reactors as well as plate-type and annular reactors. However, the drawbacks of such novel arrangements might be that efficient and uniform heat transfer be unachievable due to insufficient transfer rates and reactions exhibiting different dynamics. Even worse is that in case of catalyst deactivation or channel fouling, the microchannel module becomes totally useless since the damage is irreversible. The decoupling of reaction and heat transfer, on the

other hand, might be the solution to overcome these difficulties. Cascade arrangement of microchannel heat exchangers and microchannel or conventional adiabatic fixed-bed reactors where intermediate heat transfer takes place between reactor effluent streams seems to be a promising route to achieving process intensification and a compromise between ease of operation, equipment size and cost.

2.1. Microchannel Heat Exchangers

2.1.1. General Characteristics

With hydraulic diameter being the characteristic dimension, channels are classified such that those with diameter in the range from 1 μm to 100 μm are referred to as microchannels; as mesochannels when the diameter is between 100 μm and 1 mm, as compact passages when it is between 1 mm and 6 mm, and as conventional passages for diameters greater than 6 mm [32]. For practical purposes, however, all channels with characteristic dimensions in the submillimeter range are called microchannels.

Lower bounds on the microchannel dimensions exist due to rarefaction effects that become evident in extremely narrow flow passages. This effect is characterized by the Knudsen number, Kn, for gas flows:

$$\mathrm{Kn} = \lambda / d_H \tag{2.1}$$

where λ is the mean free path of the gas molecules and d_H is the microchannel hydraulic diameter. Table 2.1 gives the values of mean free paths for different gases [31]. For Kn numbers greater than 10^{-3} the continuum assumption of no slip at the wall does not hold. With $\lambda \approx 50$ μm for gases at standard temperature and pressure and $\mathrm{Kn} \approx 10^{-3}$, the lower limit for microchannel diameter is approximately 50 μm. Noncontinuum effects might occur for a characteristic channel dimension that is less than this critical value. For liquids it can be assumed that the critical value of d_H is ten times smaller than that for gases [33].

Table 2.1. Mean free paths for different gases.

Gas	λ, μ**m**
Air	0.068
Helium	0.194
Hydrogen	0.125
Nitrogen	0.066

Heat transfer on small scales can be characterized by several scaling effects on moving from macrosized to microsized devices. These are [33]

- low Reynolds number flow
- axial heat conduction in the fluid
- conjugate heat transfer between fluids and solid surfaces
- variable fluid property effects due to temperature and composition

An order-of-magnitude analysis for the Reynolds number in microflows shows that it is around 1, that is, the flow is dominantly laminar, therefore, $1/\mathrm{Re}^2$ is not small. Also assuming that the flow is not fully developed, especially at the channel inlet, the full set of Navier-Stokes equations taking into account axial heat conduction and viscous dissipation have to be considered. This is the main reason why computational fluid dynamics (CFD) calculations are needed in the first place when modeling microsystems.

The critical Reynolds numbers for transition from laminar to turbulent regime in internal flows are in the order of 10^3 when Re is defined with a mean velocity and a characteristic wall-to-wall distance. Even though there is some controversy whether the critical Reynolds numbers for microdevices are smaller than those for macrogeometries, $\mathrm{O}(\mathrm{Re}_c) = 10^3$ is generally accepted [33, 34]. Moreover, axial heat conduction in a fluid cannot be neglected unless the Peclet number is high. It has to be accounted for in the energy balance since in microgeometries $\mathrm{Pe} = \mathrm{RePr}$ is often small. Heat conduction in the walls of a microdevice can also be important, because the wall thickness is usually

much greater than the characteristic channel diameter. In this case, strong conjugate heat transfer effects (heat conduction in the wall combined with convection into the fluid) are observed [35, 36]. Due to significant axial variations in both the fluid and the solid, constant-property approximations are not suitable for microflows. Methods that account for the temperature-dependent fluid properties (e.g. density, viscosity) assume large Reynolds numbers. Therefore, in going from macro- to microscales, the correlations have to be readjusted for the laminar flow regime.

The material of fabrication of microchannel heat exchangers depends on the know-how and technology available to the manufacturer as well as on the targeted application [37]. Stainless steel, aluminum alloys, copper, silver and titanium are frequently used [38]. Material choice is very important during the design process as it might have great impact on heat transfer efficiency. Considering counter-current flow arrangement in a microchannel array, while high conductivity materials such as copper (having a thermal conductivity of $\sim 380\,\mathrm{W\,m^{-1}\,K^{-1}}$) and those with very low conductivity (in the $1 - 15\,\mathrm{W\,m^{-1}\,K^{-1}}$ range) turn out to give low heat transfer efficiency, materials of medium conductivity give the best results, reaching efficiencies up to 85% [38]. Ceramic and its composites have also proven to be desirable for micro heat exchanger fabrication owing to their relatively low costs and high resistance to corrosion [37, 39, 40].

2.1.2. Fabrication Techniques

Existing microfabrication technologies developed for microfluidic applications cover a broad range of machining principles, from traditional milling to modern laser beaming, as depicted taxonomically in Figure 2.1. The aim here is to briefly summarize the state-of-the-art techniques used for fabrication and interconnection of microplates.

Silicon- and metal-based bulk and surface micromachining techniques are commonly employed in the mass fabrication of microstructured components. In bulk micromachining, layers of the starting substrate (silicon or metal) are selectively removed once and for all. In contrast, surface micromachining creates the final form on or above the starting substrate through a series of deposition, patterning and etching

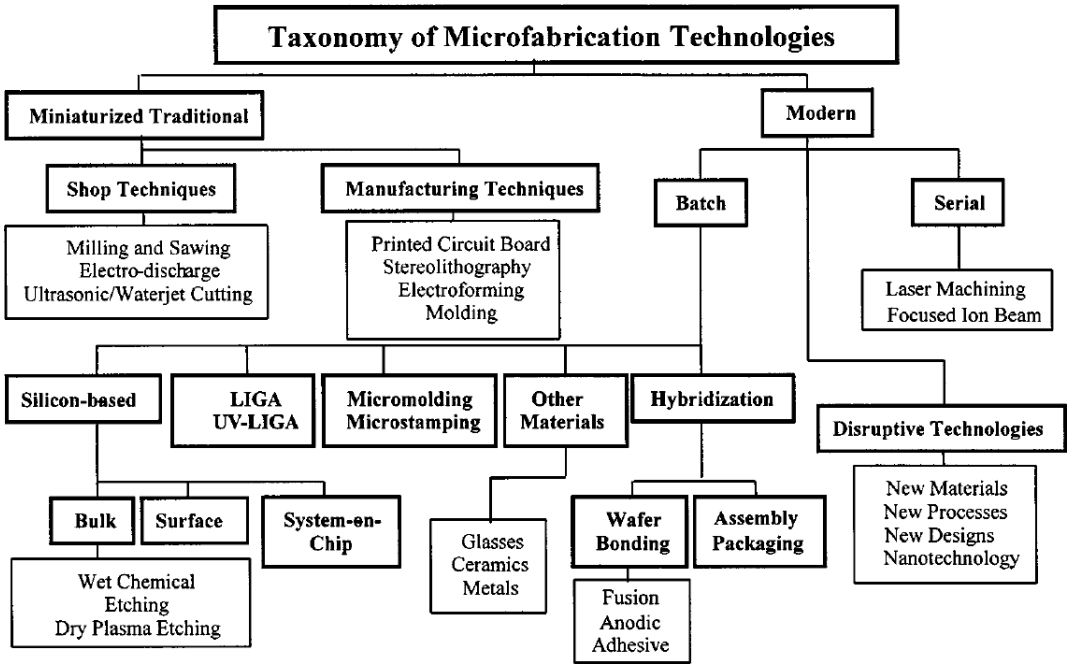

Figure 2.1. Taxonomic chart of microfabrication technologies [31].

(a)

(b)

Figure 2.2. (a) Isotropic and (b) anisotropic etches.

steps. Since the original substrate remains stress-free at the end of the bulk machining technique, the final structure has tremendous strength [31].

Etching process constitutes the major part of the bulk micromachining technique. It is used to chemically remove layers from the surface of a wafer during manufacturing. The two fundamental types of etching are wet chemical etching and dry (plasma-phase) etching, and both have isotropic and anisotropic variants [41]. Figure 2.2 illustrates the difference between isotropic and anisotropic etches. The dark region is the masking layer resistant to the chemical, and the gray region is the layer to be removed (etched). Figure 2.2a shows the isotropic etch that produces round sidewalls, and Figure 2.2b shows the anisotropic etch that produces vertical sidewalls. Modern processes greatly prefer anisotropic etches, because they produce sharp, well-controlled features.

Wet chemical etching process uses liquid-phase etchants such as potassium hydroxide for silicon and buffered hydrofluoric acid and nitric acid for stainless steel. Since wet etchants are usually isotropic and give typical etch rates in the range of 1 μm/min, they are seldom used in microfabrication [31].

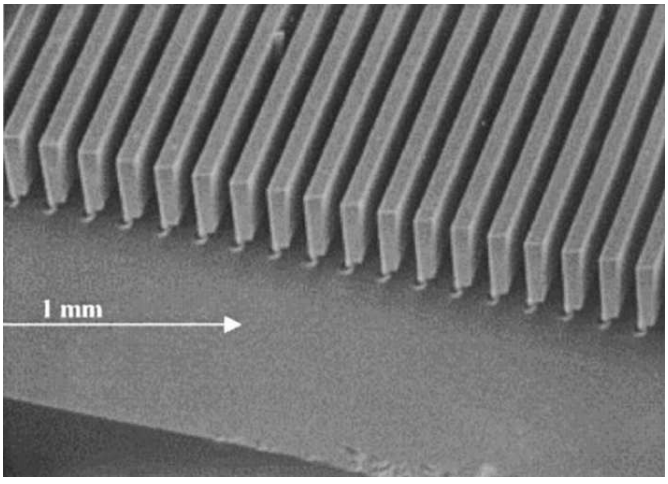

Figure 2.3. Microchannel array formed by dry ion etching [41].

Emergence of dry etching technology, on the other hand, has enabled the creation of perfectly anisotropic profiles with very large aspect ratios at etch rates as high as 20 μm/min. Figure 2.3 shows a set of microchannels with 42 μm trenches that are etched to greater than 100 μm [31]. In wet chemical etching the wafer is immersed in a bath

of etchant, whereas in dry etching, the reaction chamber is fitted with an inductively coupled energy source to create the plasma that produces energetic ions that bombard the surface of the wafer. Because the etching is performed by ions, which approach the wafer approximately from one direction, this process is highly anisotropic.

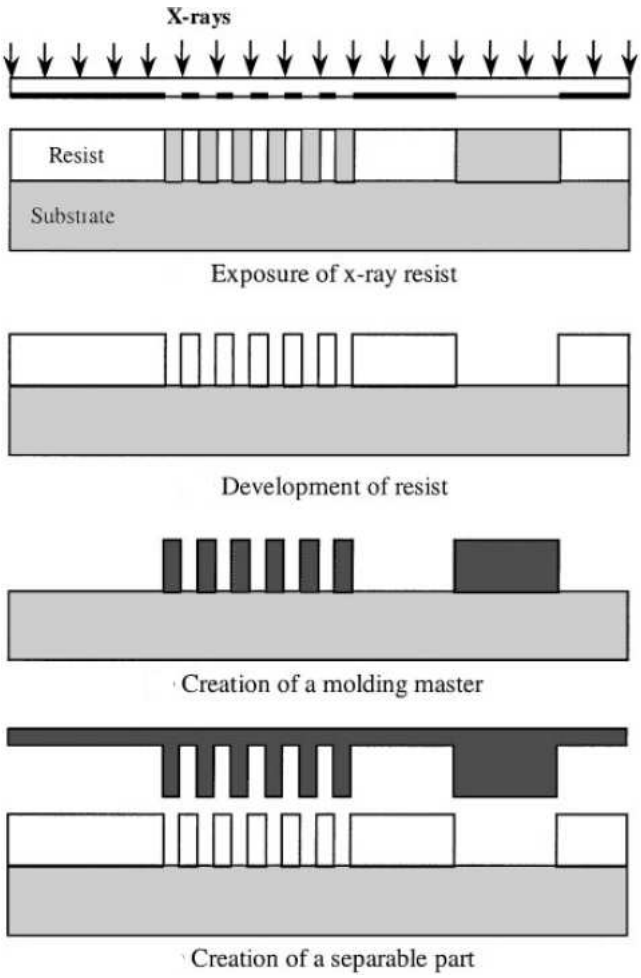

Figure 2.4. The LIGA process [31].

LIGA (German acronym for **Li**thographie, **G**alvanoformung, **A**bformung) is based on a sequence of process steps combining lithography, electroforming and molding. The first step of the LIGA process involves generation of a microstructure by means of a lithographic process in a thick resistant layer. This can be achieved by utilizing a laser, a high-energy electron or ion beam as well as standard ultraviolet or X-ray lithography with synchrotron radiation [38]. Ultraprecise microstructures with large aspect ratios can be produced using X-rays. In the second step, a complementary metal structure is generated from the resistant layer by means of electroforming. This metal structure is

used, in the third step, as a mold insert allowing the molding process to be replicated for mass fabrication. The LIGA process, shown schematically in Figure 2.4, is very convenient and feasible when working with ceramic, stainless steel or metal alloys. Fabrication of microstructures using the LIGA process is characterized by high precision, high surface quality and large aspect ratios. For inexpensive mass production, molding processes in its framework are gaining importance [38].

Advanced precision engineering techniques that make use of mechanical principles include cutting with diamond tools, milling, turning and drilling. Parallel grooves of usually rectangular shape are made by ground-in precision diamonds or ceramic inserts as cutting tools [38]. Figure 2.5 shows the cross section of a stack of microstructured plates of a cross-flow heat exchanger obtained by surface cutting with diamond.

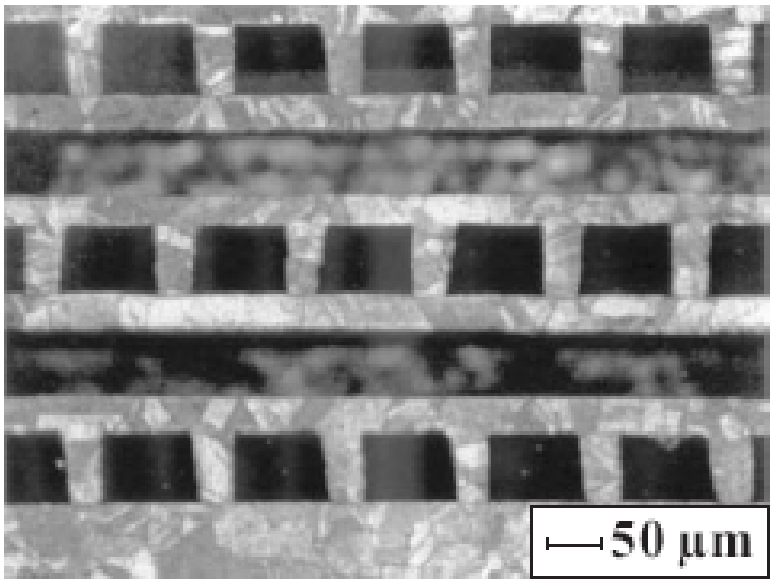

Figure 2.5. Cut view of a stack of microstructured plates of a cross-flow heat exchanger [38].

Owing to the fact that stainless steel is a preferred material for thermal and chemical applications, mechanical techniques such as milling, turning and drilling are often used for the fabrication of larger fluidic channels in the range of several hundred micrometers. SEM image of stainless steel channels micromachined using mechanical techniques is shown in Figure 2.6. Precise manufacture of housing and distribution manifolds is also possible using these techniques [38].

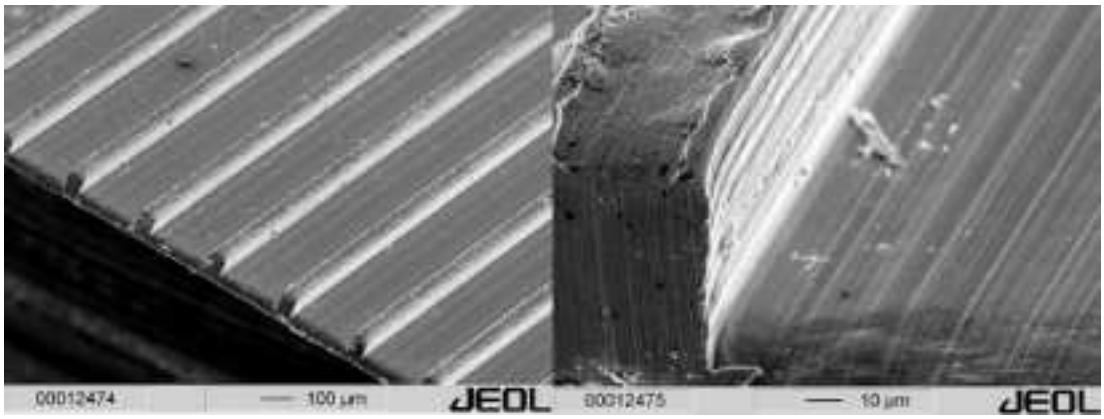

Figure 2.6. SEM of linear microchannels in stainless steel, generated by mechanical micromachining. The channels are about 200 μm wide and 70 μm deep. Right: SEM detail of the photo left [40].

The second stage in the microfabrication process is assembling, directly followed by the third stage, the bonding process. The main point is the adjustment and alignment accuracy of the parts. Depending on the surface roughness and the bonding technology applied, alignment errors may be severe as to reach the characteristic dimensions of the microstructure itself. Alignment techniques can be simple mechanical methods like the use of alignment pins or optical methods like assembling under microscope [40].

Sealing of microstructured plates on top of one another using graphite foils is a standard method. Leak tightness is difficult to achieve, however, due to surface roughness. Most other methods that involve alteration of the materials are irreversible. They can be differentiated into those needing additional material for interconnection such as brazing, soldering and intermetallic bonding, and those in which no other material is introduced, like diffusion bonding and laser welding. Using different materials for joining plates, however, introduces flaws into the complete structure and reduces its resistance to stress, especially under very high pressure [40].

The industrially attractive technique of diffusion bonding is a process by which two nominally flat interfaces can be joined at elevated temperatures higher than 2/3 of the melting point of the parent material using an applied pressure for a time ranging

from a few minutes to a few hours. The furnace where bonding takes place is either evacuated or filled with an inert gas at preset pressure [40]. If diffusion bonding proceeds to completion without flaws, very stable and irremovable interconnection between the plates is achieved. Care must be taken when applying this technique for bonding alloy materials because the process may lead to local composition changes [42]. In Figure 2.7 a cross-flow micro heat exhanger stack is shown prior to and after diffusion bonding.

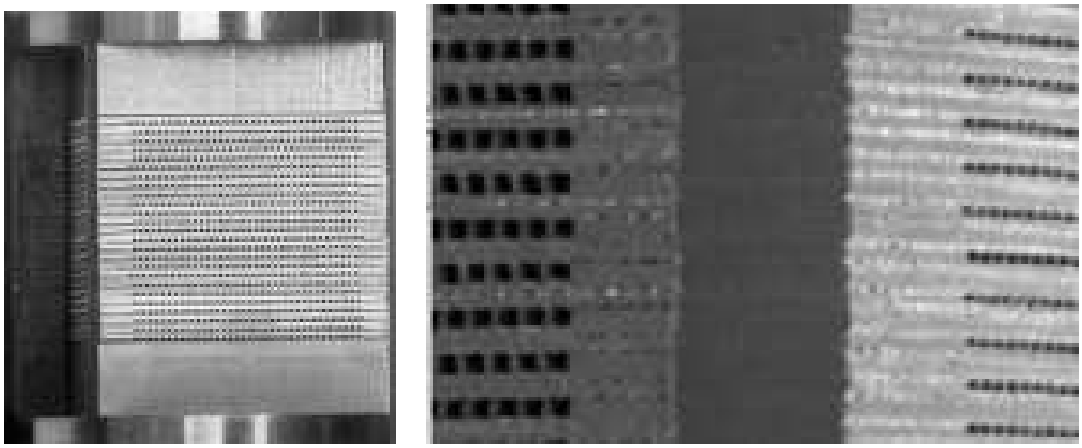

(a) (b)

Figure 2.7. (a) Stacked metal foils (b) microstructured plates after diffusion bonding [40].

Laser welding is a technique used to join multiple metal pieces through the use of a laser. The laser beam provides a concentrated heat source, allowing for narrow, deep welds and high welding rates. While not suited for bonding plates made of stainless steel and at high design pressures, laser microwelding is still of interest if diffusion bonding cannot be applied. This is the case for such materials as aluminum alloys, tantalum and alloyed steel. Nevertheless, laser welding of materials with tendency for oxidation and pore and crack formation is a challenge in microsystem technology [40].

The printed circuit heat exchanger (PCHE), manufactured in the UK by Heatric Ltd., is formed by the diffusion bonding of a stack of stainless steel plates with chemically milled fluid passages of diameters of ca. 700 μm. Diffusion bonding technique gives base-material strength and capacity to handle very high pressures, in addition

to resistance against corrosion. A typical cross section of a plate stack and photomicrograph of channel cross section are shown in Figure 2.8 [43]. Microchannel PCHEs are high-integrity heat exchangers that can withstand up to 600 bar of design pressure and 800°C of design temperature. The close temperature approaches that can be achieved with PCHEs offer considerable cost savings. By arranging microchannels in true counter-current flow configuration, high thermal effectiveness (99%) is possible with PCHEs [44].

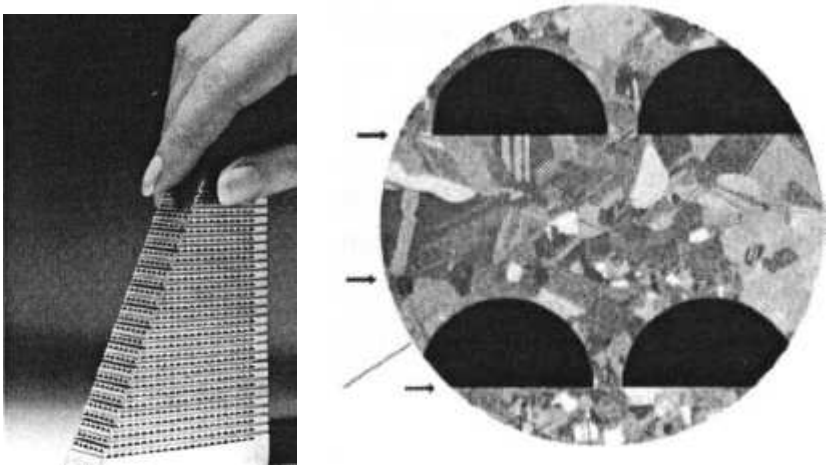

(a) (b)

Figure 2.8. (a) Cross section of PCHE stack (b) photomicrograph of channel cross section [43].

2.1.3. Heat Transfer Coefficients

Accurate prediction of convective heat transfer coefficients in microchannels are of vital importance for modeling and simulation purposes. Since the flow at the microscale is laminar, a number of investigations have been carried out in which experimental results have been compared with numerical results from conventional correlations originally worked out for macrosized channel flow. However, wide discrepancies between different sets of publications are seen [45–47]. Measured heat transfer coefficients have either well exceeded or falled far below those predicted for flow in conventional channels. Possible explanations to account for the deviation from classical theory includes surface roughness at the microscale [48] and aspect ratio effects [45].

Lee and coworkers [49] have compiled commonly used heat transfer correlations for laminar flow in channels that are widely employed in the literature for comparison against experimental results for microchannels. These are shown in Table 2.2; the correlations therein are categorized according to the state of development of the flow and thermal fields. Based on comparison with these conventional correlations, various conclusions have been drawn regarding their applicability to microchannel heat transfer. Table 2.3 summarizes the conditions considered in these microchannel studies, the conventional correlations against which results were compared, conclusions that were drawn regarding their applicability, and any new correlations that were proposed.

More recent studies have confirmed that the behavior of microchannels is quite similar to that of the conventional channels. Over a hydraulic diameter range of $244 - 974$ μm, conventional correlations offer reliable predictions for laminar flow in rectangular microchannels [49]. Another study that involved also the frictional pressure drop measurements for Reynolds numbers between 8 and 20 in $15 - 150$ μm diameter tubes showed no significant deviation from macroscale flow theory [50].

2.1.4. Comparison with Conventional Equipments

Due to enhanced heat transfer coefficients and increased surface area per unit volume, micro heat exchangers can be 85% smaller and lighter than an equivalent shell-and-tube exchanger [51]. Typical overall heat transfer coefficients of micro heat exchangers range from $2600\,\mathrm{W\,m^{-2}\,K^{-1}}$ for gas/liquid flow to $26000\,\mathrm{W\,m^{-2}\,K^{-1}}$ for liquid/liquid flow. Heat transfer coefficients in conventional heat exchangers, such as the plate-type exchanger which exhibits very good transfer characteristics, range from 200 to $2500\,\mathrm{W\,m^{-2}\,K^{-1}}$ for gas/liquid and liquid/liquid flow, respectively [52].

The application of microstructured devices in gas-phase processes can be demonstrated by means of a radical gas-phase reaction that is run at temperatures of about 500°C. Axiva, a former associate of Aventis Research & Technologies GmbH & Co. and currently owned by Siemens, compared the performance of a conventional preheater to that of a micro heat exchanger in a pilot plant unit for gas flow rates of about $1\,\mathrm{m^3\,h^{-1}}$.

Table 2.2. Conventional relations from the literature for the prediction of heat transfer in circular and rectangular ducts [49].

Conditions		**Range of validity**	**Correlation**
Geometry	**Flow regime**		
Rectangular	Fully developed	$\mathrm{Re} < 2200$	$\mathrm{Nu}_{fd} = 8.235\left(1 - 1.183/\alpha + 3.767/\alpha^2 - 5.814/\alpha^3 - 2/\alpha^5\right)$ (2.2)
Circular	Simultaneously developing	$\mathrm{Re} < 2200$	$\mathrm{Nu}_{fd} = 1.86\left(\mathrm{RePr}D/L\right)^{1/3}\left(\frac{\mu_f}{\mu_w}\right)^{0.14}$ (2.3)
Circular	Simultaneously developing (constant wall temperature)	$0.7 < \mathrm{Pr} < 7$ or $\mathrm{RePr}D/L < 33$ for $\mathrm{Pr} > 7$	$\mathrm{Nu}_{fd} = 3.657 + \frac{0.0677(\mathrm{RePr}D/L)^{1.33}}{1+0.1\mathrm{Pr}(\mathrm{Re}D/L)^{0.3}}$ (2.4)
Circular	Simultaneously developing (constant wall heat flux)	$0.7 < \mathrm{Pr} < 7$ or $\mathrm{RePr}D/L < 33$ for $\mathrm{Pr} > 7$	$\mathrm{Nu}_{fd} = 4.364 + \frac{0.086(\mathrm{RePr}D/L)^{1.33}}{1+0.1\mathrm{Pr}(\mathrm{Re}D/L)^{0.83}}$ (2.5)
Circular	Thermally developing laminar (constant wall temperature)	$\mathrm{Re} < 2200$	$\mathrm{Nu}_{fd} = 3.66 + \frac{0.19(\mathrm{RePr}D/L)^{0.8}}{1+0.117(\mathrm{RePr}D/L)^{0.467}}$ (2.6)
Circular	Simultaneously developing (constant wall heat flux)	$0.7 < \mathrm{Pr} < 7$ or $\mathrm{RePr}D/L < 33$ for $\mathrm{Pr} > 7$	$\mathrm{Nu} = \begin{cases} 1.953\left(\mathrm{RePr}D/L\right)^{1/3} & (\mathrm{RePr}D/L) \geq 33.3 \\ 4.364 + 0.0722\left(\mathrm{RePr}D/L\right) & (\mathrm{RePr}D/L) < 33.3 \end{cases}$ (2.7)

Table 2.3. Conclusions in the literature regarding the validity of conventional correlations [49].

Parameters	**Conclusions on the validity of conventional theory**	**Correlations used in the work**	**Proposed new correlation**
$w = 89-92$ μm $h = 493-572$ μm $L = 28$ mm $Re = 400-2200$	Measured Nu higher than prediction by conventional correlation	Equation 2.3 with Re $<$ 2200	$\mathrm{Nu} = 0.00222\mathrm{Re}^{1.09}\mathrm{Pr}^{0.4}$ (2.8)
$D = 3-81.2$ μm $L = 24-52$ mm $Re = 20-2000$	Measured Nu exhibit Re-dependence	—	$\mathrm{Nu} = 0.000972\mathrm{Re}^{1.17}\mathrm{Pr}^{1/3}$ (2.9)
$w = 100-300$ μm $h = 200-400$ μm $L = 50$ mm $Re = 50-2200$	Measured Nu lower than prediction by correlation	Equation 2.3	$\mathrm{Nu} = 0.1165\,(D/w_c)^{0.81} \times (h/w)^{-0.79} \times \mathrm{Re}^{0.62}\mathrm{Pr}^{0.33}$ (2.10)
$w = 270$ μm $h = 1000$ μm $L = 20.5$ mm $Re = 120-1300$	Measured Nu higher than prediction by correlation	Equation 2.9	—
$D = 172-520$ μm $L = 26.7$ mm $Re = 100-2200$	Measured Nu higher than prediction by correlation	Equation 2.6	—

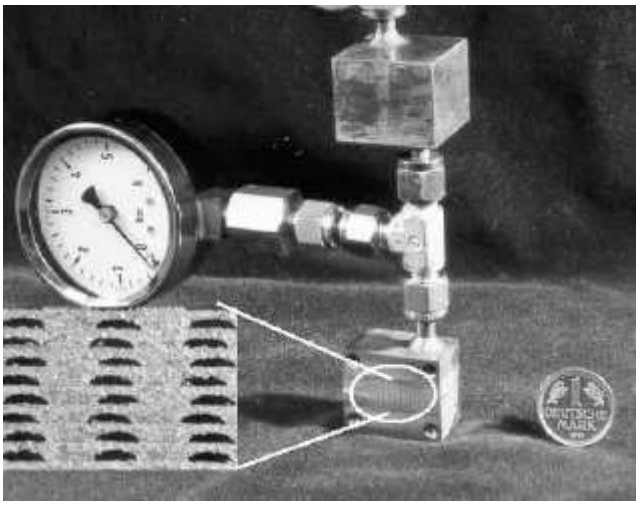

Figure 2.9. Electrically heated microstructured heat exchangers [53].

The reaction mixture consisting of the reactants and a radical precursor is heated up to the desired reaction temperature. During heating, radicals are formed and undesired by-products are generated. Therefore, fast heating is the key to low by-product formation. In the conventional process, preheating takes as long as the reaction itself ($\approx$ 1 s). Furthermore, a temperature overshoot is observed. In the pilot plant trials at Axiva, two electrically heated microstructured heat exchangers (Figure 2.9) were used in series for heating the gas stream. The preheating took about 5 ms, which was 15 times faster than the conventional equipment. Also, the desired temperature level was reached immediately without the occurrence of an overshoot (Figure 2.10). The micro heat exchanger acts like a temperature switch–very fast and accurate. Conversion in the reaction zone could be enhanced by 25% for the investigated reaction and space-time yield was nearly doubled [53].

2.1.5. Modeling, Simulation and Design

Numerous works are available in the literature that involve numerical modeling, simulation and design of various types of microchannel heat exchangers for different applications ranging from electronic package cooling to microchemical processing. Upon advance of commercial CFD package softwares, complexity of published works is ever increasing. Yet, when the proposed design poses massive CFD calculations, certain

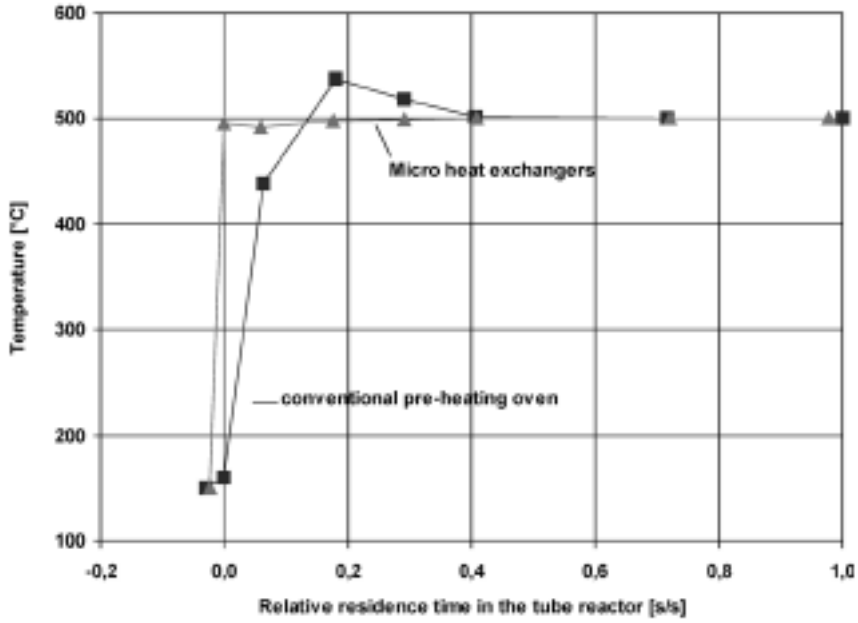

Figure 2.10. Performance comparion of preheating with conventional and microstructured heat exchangers [53].

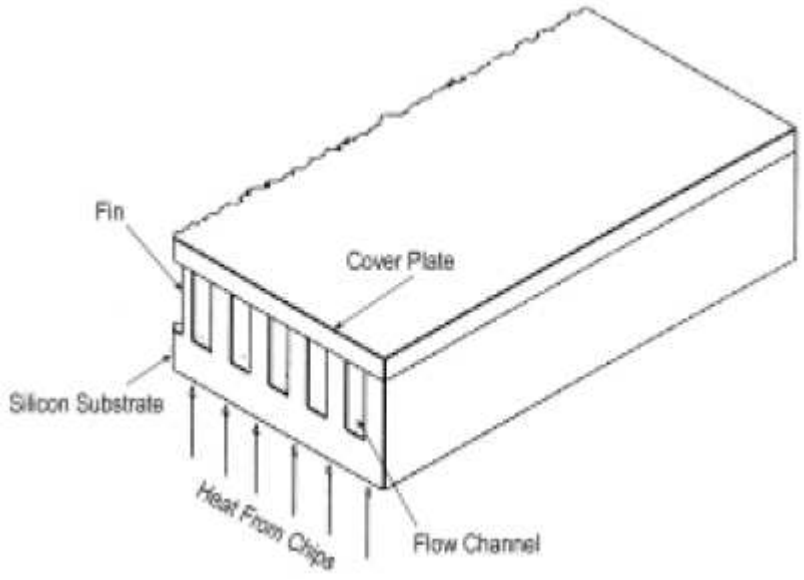

Figure 2.11. General structure of a microchannel heat sink.

plausible simplifications can be made that lead to solution using widely known and applied numerical techniques such as the finite element and finite volume methods. The study of Quadir and coworkers [54] is an example of non-CFD solution in which they have developed a Galerkin finite element formulation to study the performance of a microchannel heat exchanger used in electronic circuits (Figure 2.11). The method has been validated successfully against available results of uniform heat flux distribution for the same channel geometry and fluid flow conditions. The proposed methodology has an additional advantage of considering the non-uniform heat flux distribution as well. It is also useful for studying the effect of parameters such as the channel height and width, and fin thicknesses on the performance of the microchannel heat exchanger.

Performance of micro heat exchangers can be optimized with respect to certain design parameters like channel height, width and the aspect ratio. The study performed by Lee and coworkers [55] employs a hybrid artificial neural network-genetic algorithm method for predicting the effectiveness of a cross-flow micro heat exchanger whose performance has been determined using the finite element method for a limited number of parameters. In order to achieve maximum effectiveness, they propose a new set of design parameters.

The ultimate goal of process intensification is, of course, industrial production, which requires increasing the throughput. It can be done by numbering-up of microdevices once their working principles have well been understood. During this process of scaling-up, one is to come across many challenges such as fluid maldistribution into the microchannels, intolerable pressure drops and discrepancies between theory and experiment. Multi-scale optimization methods are an effective link that connects the microscopic world to the macroscopic world. Optimization can be done according to technical, thermodynamic and economic criteria. Constructal approach is an emerging tool that appropriately addresses the questions of developing a multi-scale engineering science. It hints to the idea that the scale parameters may be optimization variables themselves. This approach is exemplified in the studies of Fan and Luo [51] and Luo and coworkers [56] using the design optimization of a cross-flow exchanger with the constraint of pressure drop.

The most important design considerations for a micro heat exchanger are the shape and size of the flow passages, even distribution of working fluids into these passages and accuracy in the connection of microplates for prevention of mixing of different fluids. The first two of these issues can be resolved by resorting to CFD simulation of the flows. For determining the flow and thermal field inside microchannels, Navier-Stokes equations shown below for laminar flow have to be solved numerically using CFD.

Continuity:

$$\frac{\partial}{\partial x_i}\left(\rho u_i\right) = 0 \tag{2.11}$$

Momentum:

$$\rho u_j \frac{\partial u_i}{\partial x_j} = -\frac{p}{x_i} + \rho g_i + \frac{\partial \tau_{ij}}{\partial x_j} \tag{2.12}$$

where

$$\tau_{ij} = \mu\left(\frac{\partial u_i}{\partial x_j}\right) + \left(\beta - \frac{2}{3}\mu\right)\frac{\partial u_k}{\partial x_k}\delta_{ij}$$

Energy:

$$\rho u_j \frac{\partial h}{\partial x_i} = u_i \frac{\partial p}{\partial x_i} + \phi + \frac{\partial}{\partial x_i}\left(k\frac{\partial T}{\partial x_i}\right) \tag{2.13}$$

where

$$\phi = \tau_{ij}\frac{\partial u_i}{\partial x_j}$$

CFD analysis combined with analytical approaches is often employed in simulation and design of micro heat exchangers since it gives reliable results over a wide range of geometries and operating conditions. Foli and coworkers [57] have investigated the optimal dimensions of parallel rectangular microchannels of width between 100 and 1000 μm in order to maximize the transfer between two gas streams flowing through alternate channels in counter-current arrangement (Figure 2.12). Their approach also involved the usage of multi-objective genetic algorithms in combination with CFD simulation so that pressure drop would be at a minimum while the heat load would be maximized.

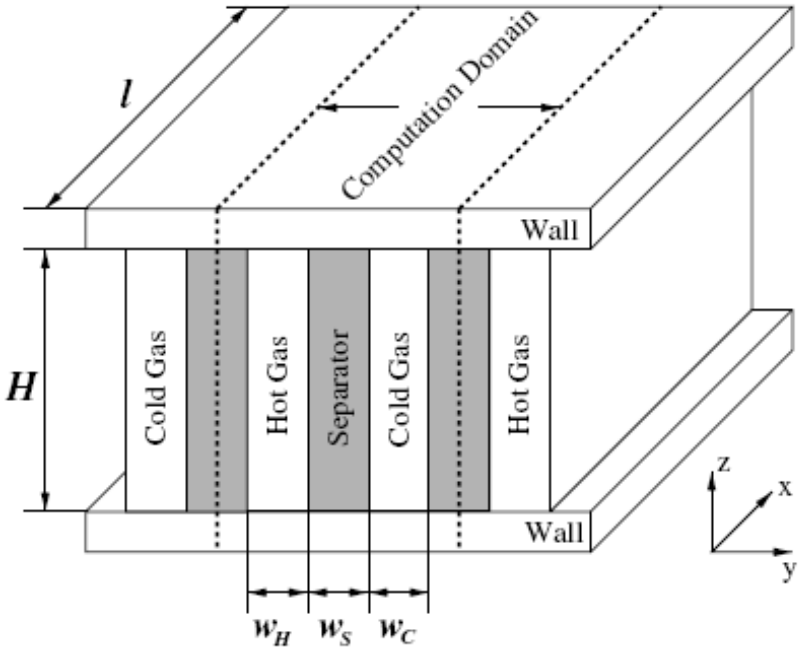

Figure 2.12. Counter-current heat transfer in alternating rectangular microchannels [57].

Maldistribution of the fluids into the channels is expected to reduce the heat exchanger effectiveness, therefore, good design of distribution manifolds is necessary. A CFD-based optimization method was proposed by Tonomura and coworkers [58] for the design of plate-fin microdevices. They investigated the influence of channel length and manifold shape and size on uniform flow distribution. According to the parametric study, flow distribution was seen to be more uniform in longer microchannels that had a greater outlet manifold area.

Temperature dependence of fluid properties such as density and viscosity has to be taken into account when downscaling flows in ducts to microscales. The multi-objective optimization study carried out by Husain and Kim [59] involves solving the set of three-dimensional Navier-Stokes equations for determining the design parameters that minimize the thermal resistance of a silicon-based microchannel heat sink and the pumping power. Thermal conductivity and viscosity of liquid water have been assumed to be varying with temperature. The schematic of the heat sink is shown in Figure 2.13. The design variables were chosen to be $\theta\,(= W_c/H_c)$ and $\phi\,(= W_w/H_c)$. Depth of the microchannels $H_c = 400$ μm was kept constant for all trials in order to assess the effect of the channel and fin widths on the objectives. The two objectives are competing in nature as the decrease in pumping power leads to an increase in thermal resistance. Due to this fact, only Pareto optimal solutions could be obtained.

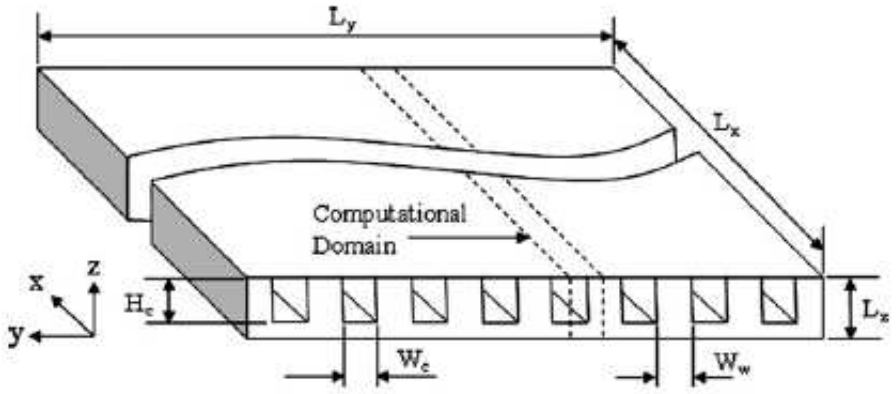

Figure 2.13. Microchannel heat sink with water flowing as the cooling fluid.

2.2. Production of H_2-Rich Syngas for Fuel Cells

2.2.1. On-Board Fuel Conversion Processes

Conversion of liquid or gaseous fuels into hydrogen for fuel cells, commonly referred to as *fuel processing*, most often involves either hydrocarbons, like methane, propane or alcohols, e.g. methanol and ethanol. The conversion of fuels to hydrogen, or hydrogen–rich product streams may be carried out by two basically different types of processes. One is endothermic *steam reforming* (**SR**) in which the hydrocarbon

or alcohol is reacted catalytically with steam. The heat required is supplied either by combustion of part of the feed, by burning combustible off-gases or by a combination of both. The other type of process is exothermic *partial oxidation* (**POX**), where the feed reacts directly with air at a balanced oxygen–to–fuel ratio. In either of the processes, thermal integration is the key to achieve high overall efficiencies [60–62].

Steam reforming of either natural gas (Equation 2.14) or liquid hydrocarbons like heptane (Equation 2.15) on Ni-based catalysts is the well-known route to hydrogen:

$$\mathrm{CH_4 + H_2O \rightleftharpoons CO + 3H_2} \qquad \Delta H^0_{298} = 206.2\,\mathrm{kJ\,mol^{-1}} \tag{2.14}$$

$$\mathrm{C_7H_{16} + 7H_2O \rightleftharpoons 7CO + 15H_2} \qquad \Delta H^0_{298} = 1175.2\,\mathrm{kJ\,mol^{-1}} \tag{2.15}$$

For small–scale applications, steam reforming of methanol (Equation 2.16) may be an attractive alternative [63]:

$$\mathrm{CH_3OH + H_2O \rightleftharpoons CO_2 + 3H_2} \qquad \Delta H^0_{298} = 49.6\,\mathrm{kJ\,mol^{-1}} \tag{2.16}$$

The *water–gas shift* (**WGS**) reaction (Equation 2.17), takes place independently and increases the hydrogen produced while lowering the undesired carbon monoxide:

$$\mathrm{CO + H_2O \rightleftharpoons CO_2 + H_2} \qquad \Delta H^0_{298} = -41.2\,\mathrm{kJ\,mol^{-1}} \tag{2.17}$$

Direct partial oxidation, or *catalytic partial oxidation* (**CPO**), represented by

Equation 2.18, is another route to hydrogen:

$$CH_4 + \tfrac{1}{2}O_2 \rightarrow CO + 2H_2 \qquad \Delta H^0_{298} = -35.7\,\mathrm{kJ\,mol^{-1}} \tag{2.18}$$

It has been shown that at temperatures as high as 1100°C and under extremely short residence times as low as $10^{-4} - 10^{-2}$ s, methane may be partially oxidized, forming H_2 and CO as the main products [64]. CPO is kinetically controlled due to the short contact times and to the oxidation reactions being much faster than the steam reforming and shift reactions. The process characteristics, temperature and concentration profiles, and eventually the entire product distribution are determined by heat and mass transfer resistances which dominate over kinetics [62, 65, 66].

Another promising method of hydrogen production is *Indirect Partial Oxidation* (**IPOX**), which is the combination of total oxidation of the fuel (Equation 2.19), SR and WGS [67, 68]. Oxidation can be catalytic (flameless) or non–catalytic, but the stoichiometry for the conversion is the same either way:

$$CH_4 + 2O_2 \rightarrow CO_2 + 2H_2O \qquad \Delta H^0_{298} = -802.3\,\mathrm{kJ\,mol^{-1}} \tag{2.19}$$

The heat required to initiate and sustain SR can be supplied by the exothermic oxidation. The water produced by oxidation is not sufficient to drive SR and WGS, so further water injection is needed. Also, in order to minimize coke formation during SR [69] and for temperature control [70], extra water is required. When water is fed together with the fuel and air, the process is also called *autothermal reforming* (**ATR**) [60]. Thermal integration due to the combination of exothermic and endothermic reactions, high space velocity and preset $H_2 : CO$ ratio regulated by the inlet fuel-to-oxygen and oxygen-to-water ratios are the main features of ATR [62, 71].

Compared to catalytic partial oxidation and autothermal reforming, steam reforming yields the highest hydrogen concentration in the product. For mobile applications, however, the CPO and ATR processes are more attractive because their

response to changes in demand is more robust and the hardware can be more compact [60]. Further, the advantages offered by the CPO process may be offset by the competing total oxidation reactions which significantly enhance process exothermicity [63]. Similar carbon monoxide and hydrogen selectivities as for CPO can also be obtained by ATR [62, 67, 68, 72].

2.2.2. Fuels and CO Removal Techniques

2.2.2.1. Fuels. The choice of the fuel for conversion to hydrogen varies with the application. In mobile applications it may be a liquid fuel such as methanol or gasoline. In stationary systems natural gas or propane (LPG) can be the fuel. Ethanol or biomass–derived materials can also be used depending on the availability and extent of renewability. During reforming of diesel, coke deposition on the catalyst is likely to occur, so it is not suitable for on–board conversion [62, 73].

Table 2.4 shows the temperature ranges in which steam reforming of different fuels takes place. Low-temperature reforming of methanol (Equation 2.16), in addition to its being in liquid form at ambient temperatures, is an attractive feature. Commercially available methanol possesses essentially no sulphur, as it can be removed at an early stage of manufacture [74].

Table 2.4. Reactor temperature ranges for steam reforming of different fuels [74].

Fuel	**Temperature range (K)**
Methane	$1000 - 1100$
Methanol	$500 - 560$
Ethanol	$\sim 800 - 1000$
Multi-carbon hydrocarbons	$1000 - 1150$

Approximate carbon monoxide concentrations in reformate streams obtained by SR of different fuels are presented in Table 2.5. Methanol reforming does not generate significant amounts of carbon monoxide, as opposed to the other fuels.

Table 2.5. Carbon monoxide contents after reforming of different fuels [74].

Fuel	**CO in product stream before WGS (mol%)**
Methane	11.2
Methanol	0.8
Ethanol	$10 - 14$
Multi-carbon hydrocarbons	20.0

The primary fuel for prototype fuel-cell-driven automobiles currently appears to be methanol. However, there are serious problems associated with practical usage of methanol for generating fuel-cell-grade hydrogen. Synthesis gas, produced by methane SR, is the feedstock for methanol production. Current methanol supply can only meet the requirements of a limited number of fuel-cell powered automobiles, if the latter becomes available for widespread use [62,75]. A reliable distribution network yet needs to be established. Methanol's toxicity, combined with its solubility in water is a serious environmental threat in case of a leakage and major spill [74].

Like methanol, gasoline offers advantages in terms of high energy density and easy fuel handling; but, unlike methanol, it has an existing refueling infrastructure. Furthermore, gasoline is directly obtained by refining crude oil, not requiring a synthesis step as does methanol. However, coke formation at the reforming conditions may occur due to the presence of aromatic hydrocarbons in the mixture [76]. Also, sulphur content above 30 ppm may cause catalyst deactivation [75,77]. Nevertheless, difficulties associated with its conversion can be overcome by novel technologies, so all major car manufacturers are developing prototypes resting on gasoline–based fuel cell systems [78].

Liquefied Petroleum Gas (LPG) is another fuel that can be stored in liquid form in pressurized vessels. LPG is a by-product in crude oil refining and is a mixture of propane and *n*–butane whose relative amounts depend on oil well location. Being a widely available and relatively cheap fuel with high energy density, LPG can be used as the primary fuel in small–scale stationary and mobile fuel cell applications [60].

Ethanol can be converted to hydrogen more easily than gasoline. It is termed a "renewable source" since it can be produced from sugar cane or corn via fermentation. Although complete gasification of the alcohol is necessary for SR [79], ethanol is potentially a primary fuel for on–board conversion. Literature on kinetics of ethanol steam reforming has been enhancing over the past decade [80–91]. Some groups have been carrying out thermodynamic analyses and testing catalysts [79, 92–94].

Natural gas, among many potential sources, is considered to be one of the ideal fuels for fuel-cell-grade hydrogen. Almost half the world's hydrogen feedstock is thought to be fixed in natural gas reserves [95]. Besides its abundance, natural gas has the lowest carbon dioxide emissions. It is mainly composed of $75 - 85$ per cent methane, the rest being ethane, propane and trace carbon dioxide [62, 96]. Thus the ratio of hydrogen atoms to carbon atoms is close to $4 : 1$, which makes natural gas cleaner than any other hydrocarbon. Apart from being environmentally benign, it is available through well-established distribution networks, either through pipelines in gaseous form or through shipping in the form of liquefied natural gas (LNG). Like gasoline and LPG, its composition varies from feedstock to feedstock.

Even though processing natural gas possesses many advantages, there are hindrances to its usage as a primary fuel for on–board conversion. It is a gas at ambient temperature and pressure, which requires bulky and costly pressurized cylinders for on-board storage. Also, methane molecule is very stable and considerable energy input is needed to initiate a reaction. Once it is triggered, higher temperatures are still required to sustain the reaction(s). The most common method, steam reforming of natural gas, which is endothermic, is well suited for steady-state operation and can deliver a relatively high concentration of hydrogen, but it suffers from a poor transient operation. Therefore, natural gas is not a suitable fuel for on-board conversion. Processing of natural gas for stationary (residential and commercial) applications and on–site hydrogen production, however, seems to be the promising solution. Commercialization of direct hydrogen storage technologies in the coming years is thought to pronounce the significance of on-site hydrogen production from natural gas [96].

2.2.2.2. CO Removal Techniques. Carbon monoxide content in a hydrogen–rich product stream from the reformer or IPOX reactor is usually $2-6$ mole per cent, which is 106 times higher than the tolerable limit below which a PEM fuel cell can safely operate. Therefore, before the stream is fed to the fuel cell, carbon monoxide must be removed catalytically. Majority of the CO can be removed by the WGS process (Equation 2.17). The shift reaction can be carried out at two different temperature ranges and is hence named accordingly: high–temperature shift (HTS) taking place in the range $623-673$ K, and low–temperature shift (LTS) in the range $453-523$ K. Iron supported on chromium oxides is used to catalyze the HTS, and the LTS is catalyzed by copper on zinc oxide support [62, 97]. Therefore, either or both of the HTS and LTS reactors can be placed downstream of the fuel processor to remove CO. However, neither configuration can achieve sufficient CO elimination, so additional removal techniques need to be applied.

Among several methods such as methanation of CO and the use of hydrogen diffusion membranes [62, 67], preferential oxidation of CO to CO_2 seems to be the optimal choice [62, 98, 99], since during methanation a significant amount of CO_2 may be converted along with CO, resulting in considerable hydrogen loss. Across Pd–based diffusion membranes, on the other hand, temperature and pressure differentials may be high and the overall efficiency may be significantly reduced. Simultaneously carrying out water–gas shift and preferential oxidation reactions by feeding oxygen into the shift reactor is also being investigated [100].

2.2.3. Fuel Processing Reactions of Methane

2.2.3.1. Total Oxidation. Catalytic combustion of hydrocarbons, because of its claims of near–zero pollutant emissions and a wide range of applications, is receiving increased attention as a candidate for replacing a number of gas-phase combustion processes in the future. It is already being employed in such applications as stationary gas turbine combustors [101], fuel cells [102], domestic and industrial process heaters [103]. Many important chemicals may also be produced by catalytic partial oxidation of fuel-rich hydrocarbon–air mixtures [104]. Homogeneous combustion of hydrocarbons requires

very high temperatures, leading to the formation of unwanted nitrogen oxides (NO_x).

Steam reforming of a hydrocarbon fuel is the well-known route to hydrogen for fuel cells. The heat input to the endothermic reaction can be supplied by means of an electric heater at the expense of a reduction in overall efficiency. Another and more feasible possibility is catalytically combusting part of the fuel to generate the necessary heat [67]:

$$CH_4 + 2O_2 \rightarrow CO_2 + 2H_2O \qquad \Delta H^0_{298} = -802.3\,\mathrm{kJ\,mol^{-1}} \tag{2.19}$$

Combination of total oxidation and steam reforming, also called indirect partial oxidation, is a thermally self-sustaining process. However, initiation of total oxidation of hydrocarbons cannot be achieved at ambient conditions since high temperatures are required. On the contrary, hydrogen and methanol are reported to have been oxidized at room temperaure over a precious metal catalyst such as platinum [105–107], and they can be used for triggering oxidation.

Unlike hydrogen and methanol, methane can be made to react at rigorous conditions since it is the most stable hydrocarbon. Precious metals that are relatively stable at high temperatures are used as the active phase of the oxidation catalysts. It is confirmed that platinum, palladium or a combination of both are suitable for combustion of hydrocarbons [104]. While the ignition (light-off) temperature of methane oxidation is the lowest on palladium-based catalysts [108–111], platinum-based [107,112,113] and rhodium–based [109] catalysts are also being utilized. Light-off temperature is usually defined as the temperature at which approximately 10 per cent of the hydrocarbon has been oxidized, and is an indication of the activity of the oxidation catalyst. On the basis of their activity, precious metals can be classified in the order Pd > Pt > Rh [108, 109].

The activity of oxidation catalysts is found to depend on metal particle size. Methane oxidation is a structure–sensitive reaction on supported Pd and Pt, with turnover frequencies (TOF) decreasing with increasing metal dispersion due to the

diminished influence of the support [114]. Oxidation kinetics of light hydrocarbons over $Pt/\gamma–Al_2O_3$ is influenced by platinum concentration and particle size [115]. Rate of oxidation is enhanced with an increase in Pt particle size, and with an increase in Pt concentration, TOF changed by one order of magnitude [116].

Understanding of catalyst ignition in all oxidation processes involving methane is important for process safety and start–up of partial and complete oxidation systems [117]. It is observed that an increase in methane inlet composition results in a decrease in light–off temperature of Pt–based catalysts [113]. However, the coupling of gas–phase and surface chemistry and transport phenomena hinders better understanding of mechanisms controlling ignition. Table 2.6 shows the light–off temperatures of methane oxidation over Pt/Al_2O_3 at different methane–to–oxygen ratios [107].

Table 2.6. Light-off temperatures of methane oxidation at different $CH_4 : O_2$ ratios [107].

$\mathbf{CH_4 : O_2}$	T_L **(K)**
0.27	724
0.9	641
2.53	623
5.04	589

There is a vast of amount of literature on kinetic studies conducted on hydrocarbon oxidation. Because of the absence of a universally accepted rate law and absence of agreement on the range of operating conditions, however, the subject receives considerable attention. Power-law rate expressions are usually valid in a narrow range of operating temperatures and hydrocarbon–to–oxygen ratios, but still some generalizations can be made. In general, the reaction orders with respect to the hydrocarbon are found to be positive, whereas oxygen is seen to have an effect as to decrease the rate of oxidation over Pt–based catalysts [61]. However, this negative dependency with respect to oxygen becomes less pronounced when the hydrocarbon-to-oxygen ratio is over-stoichiometric, and even positive orders may be observed [107]. A plausible explanation to this is that even though the heat of adsorption for oxygen is less, and

Table 2.7. Kinetic parameters for the oxidation of methane based on the power rate law expression [120].

Catalyst/ Support	**Fuel regime**	**Reaction order**		k ($\mathrm{mol\,h^{-1}\,kPa^{\alpha+\beta}}$)	**Activation energy** ($\mathrm{kJ\,mol^{-1}}$)	**Reference**
		CH_4 (α)	**O_2 (β)**			
Pt/ δ-Al_2O_3	CH_4-rich	0.95	−0.17	$1.20 \cdot 10^4 \mathrm{m_{cat}^{-2}}$	88.5	[107]
Pt-NiO/ δ-Al_2O_3	CH_4-rich	1.22	−0.38	$6.73 \cdot 10^{-3} \mathrm{g_{cat}^{-2}}$	80.9	[120]

hence it has a higher sticking probability, Pt surface becomes poisoned by excessive hydrocarbon molecules [118].

Use of bimetallic, bifunctional catalysts can be an innovative solution to the heat transfer problem arising in autothermal reforming of hydrocarbons. The heat released upon oxidation of the fuel can be transmitted with much higher efficiency to the reforming sites via oxides of the catalyst support, which act as micro–exchangers, in addition to transport via bulk fluid [61, 119]. In an experimental work conducted with bimetallic Pt–NiO/δ-Al_2O_3 catalyst [120], positive and negative dependencies of the oxidation rate on methane and oxygen concentrations, respectively, are seen to be in agreement with the generalizations made above, despite the non–monotonic behavior of oxygen. The use of a bimetallic catalyst is found to introduce a synergistic effect, which is attributed to the interaction of the two metal centers to form completely new active sites. The difference between the activation energy calculated for the bimetallic catalyst (80.88 $\mathrm{kJ\,mol^{-1}}$) and composition–weighted average of individual activation energies of the monometallic Pt and NiO catalysts (103.56 $\mathrm{kJ\,mol^{-1}}$) verifies the phenomenon. Kinetic parameters for two power–law rate expressions are presented in Table 2.7.

Kinetics of methane oxidation over Pt–based catalysts can also be expressed by theoretical Langmuir-Hinshelwood type expressions [107, 112]. Table 2.8 presents this type of kinetic expressions proposed for a series of Pt-based catalysts at different temperatures. The first term of the rate (Equation 2.21) accounts for the reaction between molecularly adsorbed methane and oxygen, while the second term describes the Eley-Rideal reaction between molecularly adsorbed methane and oxygen in the

Table 2.8. Kinetic parameters for the oxidation of methane based on Langmuir-Hinshelwood-Hougen-Watson (LHHW) type rate law expression.

Catalyst/ Support	**Temperature range (K)**	**Rate expression**	**Reference**
Pt/Al_2O_3 (porous)	< 813	$-r = \frac{k_1 p_{CH_4} p_{O_2}^{1/2}}{1 + K_1 p_{O_2}^{1/2}} + \frac{k_2 p_{CH_4} p_{O_2}}{1 + K_2 p_{O_2}}$ (2.20)	[112]
Pt/Al_2O_3 (porous)	> 813	$-r = \frac{k_1 p_{CH_4} p_{O_2}}{(1+K_1 p_{CH_4}+K_2 p_{O_2})^2} + \frac{k_2 p_{CH_4} p_{O_2}^{1/2}}{1+K_1 p_{CH_4}+K_2 p_{O_2}}$ (2.21)	[112]
Pt/Al_2O_3 (non-porous)	> 823	$-r = \frac{k_1 p_{CH_4} p_{O_2}}{(1 + K_1 p_{CH_4} + K_2 p_{O_2})^2}$ (2.22)	[112]
$Pt/\delta\text{-}Al_2O_3$	$663 - 723$	$-r = \frac{k_1 K_1 p_{CH_4} \sqrt{K_2 p_{O_2}}}{(1 + K_1 p_{CH_4} + \sqrt{K_2 p_{O_2}})^2}$ (2.23)	[107]

gas phase. The rate coefficients and adsorption constants are estimated at a fixed temperature of 830 K using a nonlinear regression method. The rate coefficients k_1 and k_2 in Equation 2.21 are considered to be dependent on temperature according to an Arrhenius-type equation [112].

2.2.3.2. Steam Reforming. Reforming means rearrangement of atoms. Catalytic steam reforming of hydrocarbons is the well-known route to hydrogen for fuel cells. Industrial-scale steam reforming is also the most economical way to produce hydrogen [95]. A good overview of the process is given in the literature [62, 72, 76, 121]. The process involves, in the presence of steam, catalytic conversion of hydrocarbons, usually natural gas, to a mixture of hydrogen, carbon monoxide, carbon dioxide and methane. The generic reactions for hydrocarbon steam reforming are

$$C_mH_n + mH_2O \rightleftharpoons mCO + (m + n/2)\,H_2 \qquad \Delta H^0_{298} > 0 \tag{2.24}$$

$$C_mH_n + (2m)\,H_2O \rightleftharpoons mCO_2 + (2m + n/2)\,H_2 \qquad \Delta H^0_{298} > 0 \tag{2.25}$$

The hydrocarbon is directly steam–reformed to carbon dioxide by the other primary reaction (Equation 2.25), which runs in parallel with reaction (Equation 2.24). Steam

reforming of methane (SRM) is specifically achieved through

$$CH_4 + H_2O \rightleftharpoons CO + 3H_2 \qquad \Delta H^0_{298} = 206.2\,\mathrm{kJ\,mol^{-1}} \tag{2.14}$$

$$CH_4 + 2H_2O \rightleftharpoons CO_2 + 4H_2 \qquad \Delta H^0_{298} = 165\,\mathrm{kJ\,mol^{-1}} \tag{2.26}$$

An important side reaction, the water–gas shift (WGS), takes place simultaneously with the SR reactions and favors the formation of carbon dioxide at lower temperatures. It is particularly crucial in fuel cell applications since part of the undesired carbon monoxide is converted to hydrogen:

$$CO + H_2O \rightleftharpoons CO_2 + H_2 \qquad \Delta H^0_{298} = -41.2\,\mathrm{kJ\,mol^{-1}} \tag{2.17}$$

Methanation reactions (the reverse of Equations 2.14 and 2.26) become significant at low temperatures:

$$CO + 3H_2 \rightleftharpoons CH_4 + H_2O \qquad \Delta H^0_{298} = -206.2\,\mathrm{kJ\,mol^{-1}} \tag{2.27}$$

$$CO_2 + 4H_2 \rightleftharpoons CH_4 + 2H_2O \qquad \Delta H^0_{298} = -165\,\mathrm{kJ\,mol^{-1}} \tag{2.28}$$

Steam reforming is thermodynamically favored at high temperatures, typically greater than 800°C, and at low pressures. However, in industrial practice, the reactions are carried out at pressures greater than 20 atm [95]. The overall process is highly endothermic, and considerable heat should be supplied from the surroundings. Primary reformers usually contain between 40 and 400 tubes, typically 6 to 12 meters long, 70 to 160 mm in diameter and 10 to 20 mm in wall thickness [76]. Reactor tubes usually contain cylindrical catalyst particles, nickel dispersed on alumina. Heat transfer from external burners to the catalyst bed is the most important operating factor with

respect to product distribution and optimal reactor performance [122].

Catalytic steam reforming in practice is almost invariably conducted on Ni-based catalysts as the metal is sufficiently active and can be obtained easily at a low price. However, as already mentioned, carbon formation over these catalysts is facilitated under steam reforming conditions. Coke deposition over Ni is usually overcome by keeping steam-to-carbon ratios above stoichiometric values; for methane, ratios between 2.5 and 3 are recommended [76].

Precious metals such as Rh and Ru are known to be more active and selective than Ni, and can safely operate without coke deposition [76,123] . The major hindrance to their commercial use is their high price. The activity of various catalysts for SRM is reported as follows [124]:

$$\mathrm{Ru, Rh} > \mathrm{Ir} > \mathrm{Pd, Ni, Pt} > \mathrm{Re} > \mathrm{Co}$$

Minimizing coke formation over nickel-based catalysts is also investigated. Doping of catalysts with small amounts of tin, antimony and silver results in significant reduction of coke formation rate in SRM [69]. Addition of SnO_2 and WO_3 as well as oxides of K, Na, Mg, Ca and Ba also helps in suppressing coking over nickel [125,126]. In search of more economically viable solutions, Ni catalysts doped with trace amounts of a noble metal (e.g. Ru [127], Rh [128], Pt [129]) were also studied. The effect of doping is such that methane adsorption is prevented, and hence its decomposition on the surface. Apart from doping, high activities in SRM are reported even at low steam–to–carbon ratios ($H_2O : CH_4 \sim 1$) when catalysts with low nickel content such as $Ni_{0.03}Mg_{0.97}O$ are used [130]. An extensive review of the methods to overcome the coke formation problem can be found in the work of Ma and coworkers [116].

The effect of catalyst support on SRM activity also deserves attention. It is revealed that activity of nickel supported on titania (TiO_2) is greater than nickel on

other catalyst supports [131]:

$$Ni/TiO_2 > Ni/C > Ni/SiO_2 > Ni/MgO$$

Similarly, nickel on alumina (Ni/Al_2O_3) is shown to be more active and stable than nickel on silica (Ni/SiO_2) [132].

A review and compilation of kinetics and mechanism of SRM can be found in the literature [76]. In general, the reaction rate expressions exhibit first order kinetics with respect to methane partial pressure. However, depending on the partial pressure of steam, the overall reaction orders attain negative or positive values; even zero-order reaction rates can be observed [133]. The results displayed by the comprehensive model proposed by Xu and Froment [134, 135] indeed contradicted their previously reported counterparts. The discrepancies, however, are attributed to the non-monotonic dependency of the reaction rate on partial pressure of steam [133].

Xu and Froment [134] investigated the intrinsic kinetics of SRM using a Ni/MgO-Al_2O_4 catalyst. To avoid reoxidation of the Ni catalyst by steam, the experiments were conducted with hydrogen in the feed. Langmuir-Hinshelwood type rate equations for SR toward CO and CO_2 (Equations 2.14 and 2.26), as well as for WGS (Equation 2.17), were constructed using the elementary–step kinetic model proposed, as presented in Table 2.9. The three rate equations are seen to be inversely proportional to the partial pressure of hydrogen, which will consequently give infinite reaction rates. Since the feed generally contains some hydrogen, simulation of a reactor will not suffer from this problem. Also, Xu and Froment [134] worked in a relatively lower temperature range; for obtaining the model they employed temperatures between 773 and 848 K and pressures between 3 and 15 bar. During the indirect partial oxidation process, however, high catalyst temperatures will occur due to the exothermic total oxidation reaction.

To simulate SRM at elevated tempeatures, the kinetic model proposed by Numaguchi and Kikuchi [136] can be used, for it was derived at higher catalyst temper-

Table 2.9. Rate equations for steam reforming of methane.

Reaction	**Rate expression**	**Reference**
(2.14)	$r = \frac{k_1/p_{H_2}^{2.5}\left(p_{CH_4}p_{H_2O} - p_{H_2}^3 p_{CO}/K_{eq}^{I}\right)}{DEN^2}$ (2.29)	[134]
(2.26)	$r = \frac{k_2/p_{H_2}^{3.5}\left(p_{CH_4}p_{H_2O}^2 - p_{H_2}^4 p_{CO_2}/K_{eq}^{II}\right)}{DEN^2}$ (2.30)	[134]
(2.17)	$r = \frac{k_3/p_{H_2}\left(p_{CO}p_{H_2O} - p^{H_2}p_{CO_2}/K_{eq}^{III}\right)}{DEN^2}$ (2.31)	[134]
(2.14)	$r = \frac{k_1\left(p_{CH_4} - p_{H_2}^3 p_{CO}/K_{eq}^{I}\right)}{p_{H_2}^{0.596}}$ (2.32)	[136]
(2.17)	$r = k_2\left(p_{CO} - p_{H_2}p_{CO_2}/K_{eq}^{III}\right)$ (2.33)	[136]

Table 2.10. SRM catalyst specifications.

	Xu and Froment [134]	**Numaguchi and Kikuchi [136]**
Catalyst	$Ni/MgO\text{-}Al_2O_4$	Ni/Al_2O_3
Metal Content (wt%)	15.2	8.7
Metal surface area ($m^2\,g^{-1}$)	4.1	3.6
Density ($kg\,m^{-3}$)	1870	1970

atures up to 1160 K and higher pressures up to 25 bar. Based on a rate–determining surface reaction, Langmuir-Hinshelwood type rate equations for SR towards CO were proposed, presented also in Table 2.9. Equation 2.26, which shows SRM toward CO_2 was not taken into account in the model of Numaguchi and Kikuchi. Properties of the catalysts used by Xu and Froment [134] and Numaguchi and Kikuchi [136] for performing SR experiments are shown in Table 2.10. The Ni-content of the Numaguchi-Kikuchi catalyst is lower than that of the catalyst used by Xu and Froment. The Ni-surface areas, however, are more or less identical and allow a reasonable comparison of both kinetic models.

The differences between the applied rate equations for steam reforming were examined by de Smet *et al.* [137] by calculating the corresponding reforming rates as a function of total operating pressure. The catalyst was at 800 K and the feed consisted of methane, oxygen, steam and some hydrogen whose composition was as

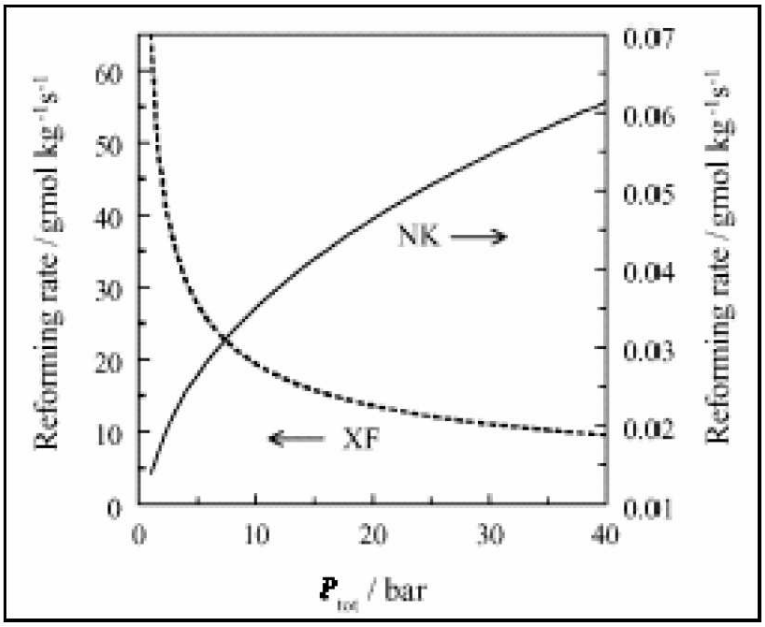

Figure 2.14. SRM rates calculated by XF and NK kinetic models versus total pressure [137].

follows: $CH_4 : O_2 : H_2O : H_2 = 33.3 : 16.7 : 49.9 : 0.1$. As indicated in Figure 2.14, the reforming rate decreases considerably at increasing total pressure in the case of the model of Xu and Froment, whereas the rate increases in the case of the rate equation proposed by Numaguchi and Kikuchi. The difference between the calculated reforming rates is attributed to the negative partial pressure reaction order with respect to hydrogen in the model of Xu and Froment. In the presence of significant amounts of hydrogen, the difference between the calculated rates is less pronounced. Different temperature and concentration profiles will thus be obtained when the proposed rate equations are applied at different operating pressures.

2.2.3.3. Autothermal Reforming and Catalytic Partial Oxidation. Steam reforming of hydrocarbons is the route to maximum hydrogen production, yet it suffers from the endothermicity of the reactions involved and the sluggish kinetics. Partial oxidation, on the other hand, is much faster, requires smaller amounts of catalyst and is energetically self-sustaining once started, all of which make it a candidate for supplying propulsion power in automobiles. Partial oxidation is known to occur via two pathways:

- Indirect partial oxidation (IPOX), or autothermal reforming (ATR), in which oxidation and steam reforming reactions are coupled since oxygen and steam are co-fed
- Direct partial oxidation in which the hydrocarbon is converted into syngas in a single-step process

Autothermal reforming is basically a combination of the oxidation and steam reforming reactions. What makes it distinct among the conversion routes is its autothermicity such that heat released by the oxidation of the fuel is harnessed by the endothermic steam reforming reactions. Thus, exogenous heat supply will not be necessary once the process is dynamically stable. This aspect of autothermal conversion is already realized in industrial practice in which non-catalytic (homogeneous) combustion is used to supply heat for catalytic methane steam reforming [138]. Problem of coke formation can partially be eliminated during homogeneous combustion by steam injection, but operation at elevated temperatures (> 2000 K) brings about more serious problems such as material degradation [139].

ATR of methane–model fuel for natural gas–is carried out over Ni-based catalysts at temperatures in excess of 900°C in order to affect the syngas feed ratio in favor of the Fischer-Tropsch ($2.00 < H_2 : CO < 2.15$) or methanol ($H_2 : CO \approx 3.0$) syntheses [140]. Problems associated with ATR over Ni include deactivation and loss of reforming activity of the catalysts by oxidation [141], hot spot formation upstream of the reactor due to very high oxidation rates [142], and carbon deposition on the catalysts [143]. Hot spots during ATR are reported to have been suppressed by utilizing Pt- [144] and Rh-based [145] catalysts. Moreover, along with Pt and Rh, other noble metals (Ru and Ir) exhibit prominently higher steam reforming activity [76], and are much less prone to carbon deposition [123]. Even though Ni-based catalysts are used in large-scale production of syngas, owing to their availability and low costs, sometimes use of noble metals may prove viable due to their superior activity, selectivity, and stability under harsh operating conditions [146]. Methane ATR performance increase via promotion of Ni catalysts by addition of trace amounts of a noble metal is also widely investigated in the literature [147–154].

In contrast with indirect partial oxidation, synthesis gas can be obtained from methane in a single-step process via direct partial oxidation:

$$\mathrm{CH_4} + \tfrac{1}{2}\mathrm{O_2} \rightarrow \mathrm{CO} + 2\mathrm{H_2} \qquad \Delta H^0_{298} = -35.7\,\mathrm{kJ\,mol^{-1}} \tag{2.18}$$

The advantage of the process is that synthesis gas in its ideal composition, i.e. $\mathrm{H_2} : \mathrm{CO} = 2 : 1$, is produced without the need for steam. However, for fuel cell applications post-processing of the effluent is necessary since carbon monoxide is a poison for PEM fuel cells.

Direct partial oxidation of methane to synthesis gas over Rh and Pt catalysts was investigated by Schmidt and coworkers [139, 155]. It was concluded that while Rh was selective to synthesis gas, Pt catalyzed olefin formation. Also, product composition was close to the equilibrium value at elevated temperatures usually exceeding 1000°C, at contact times on the order of milliseconds, at metal loadings greater than 10 per cent and at near-stoichiometric feed mixtures. Mass transfer resistances were also reported to affect product distribution. The possibility of direct partial oxidation of methane over $\mathrm{Ru/TiO_2}$ at lower temperatures has been reported as well [156]. Jin *et al.* [157] investigated the mechanism of catalytic partial oxidation of methane to synthesis gas over $\mathrm{Ni/Al_2O_3}$ catalyst. They observed that the partial oxidation reaction principally took place over a thin layer of the catalyst bed and that total oxygen and over 90 per cent of methane were converted in the main reaction zone. High methane conversion of 88.4 per cent and CO selectivity of about 96 per cent were obtained even on 1 mm of catalyst bed and at very high space velocities.

Compared with indirect partial oxidation, direct partial oxidation poses some operational challenges during on-board conversion. The process requires high temperatures, millisecond contact times and feed mixtures near the explosive limit, all of which are hindrances to practical applications involving frequent start-ups/shutdowns. However, direct partial oxidation coupled with water injection and low-temperature

water-gas shift was simulated and higher hydrogen yields compared with indirect partial oxidation were obtained [61, 158, 159]. Being dynamically responsive and more feasible a process, direct partial oxidation needs to be further considered for use in mobile applications.

2.2.4. Inhibition of Catalytic Activity

The three major routes for catalyst deactivation during fuel processing of hydrocarbons and alcohols are *poisoning*, *fouling* and *sintering*.

2.2.4.1. Poisoning. Interaction of a gas-phase species found in the feed or product streams and the active catalyst sites is the main reason for catalyst poisoning. Sulphur is well known for its poisoning activity, and heavy metals or their ions, and organic bases may also deactivate catalysts with high acidity. Trimm [67] reported that even a few parts-per-billion of H_2S is sufficient to cover majority of the active sites of a catalyst. The three types of catalyst poisons fall into the categories below: (i) Group 5A and 6A elements (5A: N, P, As, Sb, 6A: O, S, Se, Te), (ii) toxic heavy metals (e.g. Pb, Hg, Cd, Cu), and (iii) specific molecules that interact with catalyst surfaces (carbon monoxide poisoning of Pt-based catalysts within the PEM fuel cells) [160].

High-temperature oxidation is a way to regenerated catalysts poisoned by sulphur, because the sulphates that can react with supports such as alumina, break up to give SO_x, which can diffuse into the gas phase and be removed. Hydrodesulphurization is another technique to remove sulphur-containing compounds before they reach the reactor [160].

2.2.4.2. Fouling. Fouling is the deposition of a substance on the catalyst surface, and subsequent loss of activity due to physical blocking of the catalytic sites. Coke deposition during hydrocarbon processing is the well-known example of catalyst fouling [160]. Coke may be a combination of various kinds of carbonaceous deposits. Coking usually occurs under conditions employed for catalytic steam reforming. It is more

likely at high temperatures and at lower steam-to-carbon ratios. The typical coking reactions are as follows [67]:

$$\mathrm{CH_4} \rightleftharpoons \mathrm{C} + 2\mathrm{H_2} \qquad \Delta H^0_{298} = 74.9\,\mathrm{kJ\,mol^{-1}} \tag{2.34}$$

$$2\mathrm{CO} \rightleftharpoons \mathrm{C} + \mathrm{CO_2} \qquad \Delta H^0_{298} = -172.4\,\mathrm{kJ\,mol^{-1}} \tag{2.35}$$

$$\mathrm{CO} + \mathrm{H_2} \rightleftharpoons \mathrm{C} + \mathrm{H_2O} \qquad \Delta H^0_{298} = -135.6\,\mathrm{kJ\,mol^{-1}} \tag{2.36}$$

$$\mathrm{C}_n\mathrm{H}_{2n+2} \rightleftharpoons n\mathrm{C} + (n+1)\,\mathrm{H_2} \qquad \Delta H^0_{298} > 0 \tag{2.37}$$

Since the reactions are reversible, it is possible to minimize coke formation for example by increasing the amounts of carbon dioxide and water that will revert the directions of the Boudouard reaction (Equation 2.35) and the reaction given by Equation 2.36.

Three common types of carbon deposits have been identified in nickel-catalyzed steam reforming. These are (i) pyrolytic carbon, (ii) whisker-like carbon, and (iii) encapsulating carbon [161]. Pyrolytic carbon forms due to the thermal cracking reaction (Equation 2.37) of hydrocarbons at elevated temperatures (650 K) [161]. This type of carbon can also form at high residence times. Pyrolytic carbon works two ways to foul the process: by encapsulating the active Ni sites, and hence deactivating the catalyst, and by blocking the passages through which gas flows, and hence leading to excessive pressure drop and overall process inefficiency [76].

The formation of whisker carbon and encapsulating carbon can be explained by the coking mechanism over nickel [161]. The process is believed to initiate with the

dissociation of hydrocarbons into highly reactive monatomic carbon (C_α), which can easily be gasified to form carbon monoxide. However, if C_α is formed in excessive quantities or gasification is slow, then polymerization to C_β begins. It has been shown that C_β is much less reactive than C_α, so the gasification step is fairly slow [69]. As a result, C_β may either accumulate on the catalyst surface or dissolve in the nickel leading to encapsulated carbon or whisker carbon, respectively. Noble metal catalysts, on the other hand, do not dissolve carbon, i.e., do not favor the whisker formation mechanism, and therefore, possess greater resistance against coking [162].

2.2.4.3. Sintering. Catalysts that possess a high surface area are favorable in process engineering, but they are not favored by thermodynamics. Therefore, when the conditions are suitable (e.g. high temperatures and presence of a substance with high affinity for the catalytic material), the catalysts transform into agglomerates which have smaller surface areas. This is known as sintering, or thermal degradation [163]. Thermal rearrangement of most of the solids occurs usually at around $0.3 - 0.5$ times the melting point of the support material [164], which is sometimes accelerated under certain conditions. For example, hydrothermal conditions in steam reforming lead to sintering. Moist atmospheres are also known to facilitate sintering of oxide supports [67].

γ-Al_2O_3 is a commonly used catalyst support, but its high surface area (ca. $250\,m^2\,g^{-1}$) starts to decline at temperatures greater than 600°C. As the temperature increases, the γ phase transforms first into the δ phase, and then into the θ phase. Finally obtained at the excessive temperature of 1100°C is the highly stable phase α, which has a surface area as low as ca. $5\,m^2\,g^{-1}$ [165].

2.3. Fischer-Tropsch Synthesis

The conversion of synthesis gas (obtained from natural gas, light hydrocarbons, coal or biomass) to (heavy) hydrocarbons is currently one of the most promising topics in the energy sector due to economic utilization of remote natural gas or other fuels to

environmentally clean fuels, specialty chemicals and waxes. The conversion of syngas to aliphatic hydrocarbons over metal catalysts was discovered by Franz Fischer and Hans Tropsch at the Kaiser Wilhem Institute for Coal Research in Müllheim in 1923. They proved that CO hydrogenation over iron, cobalt or nickel catalysts at $180 - 250°C$ and atmospheric pressure results in a product mixture of linear hydrocarbons. The Fischer-Tropsch product spectrum consists of a complex multicomponent mixture of linear and branched hydrocarbons and oxygenated products. Main products are linear paraffins and α-olefins. The overall reactions of the Fischer-Tropsch (FT) synthesis are [166]

Main reactions:

Paraffins	$(2n+1)H_2 + nCO \rightarrow C_nH_{2n+2} + nH_2O$
Olefins	$2nH_2 + nCO \rightarrow C_nH_{2n} + nH_2O$
Water-gas shift	$CO + H_2O \rightleftharpoons CO_2 + H_2$

Side reactions:

Alcohols	$(2n)H_2 + nCO \rightarrow C_nH_{2n+2}O + (n-1)H_2O$
Boudouard reaction	$2CO \rightarrow C + CO_2$

Catalyst modifications:

Catalyst oxidation/reduction	$M_xO_y + yH_2 \rightleftharpoons yH_2O + xM$
	$M_xO_y + yCO \rightleftharpoons yCO_2 + xM$
Bulk carbide formation	$yC + xM \rightleftharpoons M_xC_y$

The reactions of the FT synthesis on iron catalysts can be simplified as a combination of the FT reaction and the water-gas shift (WGS) reaction:

$$\mathrm{CO} + (1 + m/2n)\mathrm{H_2} \rightarrow 1/n\mathrm{C}_n\mathrm{H}_m + \mathrm{H_2O} \quad \text{(FT)} \qquad -\Delta H_{\mathrm{FT}} = 165\,\mathrm{kJ\,mol^{-1}}$$

$$\mathrm{CO} + \mathrm{H_2O} \rightleftharpoons \mathrm{CO_2} + \mathrm{H_2} \qquad \text{(WGS)} \qquad -\Delta H_{\mathrm{WGS}} = 41.3\,\mathrm{kJ\,mol^{-1}}$$

where n is the average carbon number and m the average number of hydrogen atoms of the hydrocarbon products. Water is a primary product of the FT reaction, and CO_2 can be produced by the WGS reaction. The WGS activity can be high over potassium-promoted iron catalysts and is negligible over cobalt or ruthenium.

The compositions of the hydrocarbon products of Fischer-Tropsch synthesis show a distinctly regular pattern [167]. It was first noticed in 1946 by Herrington that the molar amount of individual carbon number fractions was to decline exponentially with carbon number, which was accepted to indicate similarity to polymerization kinetics [168, 169]. It is agreed that –CH_2– is acting as the monomer in FT synthesis and building blocks of hydrocarbons. It is then argued that there should be a way to indicate the growth probability of chains just as in ideal polymerization reactions [170].

In most of the studies in literature, it is concluded that the hydrocarbon product composition of the Fischer-Tropsch synthesis follows the Anderson-Schulz-Flory (ASF) distribution. This distribution is defined by a term called growth probability, α, which shows the probability of the addition of a carbon intermediate to a chain. Growth probability depends on reaction conditions and type of catalyst used [171,172]. ASF specifies growth probability as independent of the carbon number [173]. However, through experiment it was reported that there were significant deviations from ASF distribution, such as high methane yield, anomalies of ethane and ethene productions as a result of secondary reactions, and decrease in olefin-to-paraffin ratio. The deviations from ASF theory led researchers to seek new methods to predict the product distribution of FT synthesis [172].

FT synthesis involves the production of linear hydrocarbons, which directly affects the quality of the diesel and the gasoline produced [174]. The importance comes from the fact that the product aromaticity is low, and sulphur, nitrogen or heavy metal content is zero. The high cetane number of the middle distillate fraction obtained is the indicator of superior combustion properties and reduced emissions that result from burning the produced fuel [170, 175, 176]. The Fischer-Tropsch synthesis diesel has unique advantages when compared with other fuels; it has high energy density, i.e. the energy stored per volume is greater. Moreover, its low vapor pressure dampens the safety issues related to storage. Additionally, FT diesel is not soluble in water and is biodegradable [170].

FT synthesis can be classified according to the range of the processing temperature: *high temperature Fischer-Tropsch* (**HTFT**) in an approximate temperature range of $300-350$°C, and *low temperature Fischer-Tropsch* (**LTFT**) in the temperature range of $200-240$°C [177]. Primary product of HTFT is more branched and more olefinic than that of LTFT. The ASF distribution of HTFT products is more toward lighter products in the range of gasoline, consisting of hydrocarbons with between 4 and 12 carbon atoms per molecule. LTFT primary products can be classified in two groups: hydrocarbon condensate forming the light fraction–consisting of hydrocarbons of 5 to 6 carbons, which is liquid under ambient conditions, and a heavy fraction, known as wax, composed of heavy paraffins ($C_8 - C_{20}$) [178, 179]. LTFT process enables the production of large-scale, high quality diesel, with cetane number of approximately 75, whereas a big portion of the products in HTFT belongs to light alkenes. Additionally, the ratio of diesel to naphtha in the end product is higher in LTFT process revealing its superiority on HTFT process in diesel production. However, for production of gasoline, HTFT is a much better choice in terms of gasoline selectivity and octane number [174].

FT reactions can only be catalytically activated by metals from group VIII, namely, Fe, Co and Ru [166, 177]. Iron-based catalysts are commonly used because of their low costs in comparison to other metals. For iron-based catalysts high conversions ($\sim 90\%$) can be achieved, but this requires a two-stage operation that involves recycling of gas, which inevitably increases the capital and operational expenditures.

When utilizing syngas produced from coal, iron catalysts perform better compared with cobalt-based catalysts because of their resistance to possible poisoning [170].

In FT synthesis, the highest hydrocarbon yields are obtained with cobalt-based catalysts, and the product is abundantly made up of linear alkanes. Because water does not have an inhibiting effect on the catalyst, it is possible to achieve higher productivity at higher conversions. However, since they favor CH_4 at high temperatures, their usage is mostly limited to LTFT processes [166,177]. The sensitivity of conversion and product distribution to the H_2/CO ratio is higher during FT synthesis on cobalt [179].

2.3.1. Effect of Operating Conditions on FT Synthesis Product Distribution

FT synthesis results in a wide variety of products such as alkanes, alkenes, alcohols and oxygenates with carbon number in the $C_1 - C_{20+}$ range. Selective distribution of these products is strongly related to the operating conditions such as temperature, pressure and feed composition [166, 177].

2.3.1.1. Temperature. The reaction temperature has much more significance on FT synthesis product distribution than any other operating parameter [166,167,177]. Running the reaction at temperatures higher than the ascribed range for the particular catalyst leads to a shift toward lower-carbon products, producing more of secondary products like ketones and aromatics. More specifically, high temperature operation results in a distribution where light alkenes ($C_1 - C_7$) and light alkanes ($C_1 - C_7$) are abundant, and heavy alkenes ($C_9 - C_{26}$) and heavy alkanes (C_{15+}) are fractionally low. Thus, the average chain length decreases whereas branching increases. Additionally, methane selectivity increases, as the FT reaction mechanism favors methane production at high temperatures [167, 177]. The ratio of alkenes to alkanes (olefin-to-paraffin ratio) also increases with increasing temperature because hydrogenation becomes thermodynamically less favored at higher temperatures due to its exothermicity [179]. High temperatures lead to catalyst deactivation as well, especially in the case of using iron-based catalysts [167, 170].

2.3.1.2. Pressure. Total pressure is another parameter that significantly affects FT synthesis product distribution. It was shown that increase in total pressure results in a shift in product selectivity toward heavier products and more oxygenates [166]. It was also reported that the percent conversion remained constant when the pressure was increased while keeping other variables constant [177]. In LTFT process, selectivity of hard wax, which is most abundant, was not affected by any change in pressure. However, in HTFT process, it results in a shift to heavier products with decrease in methane selectivity [179].

2.3.1.3. Feed Composition. Syngas conversion increases as the molar H_2 : CO ratio in the feed is increased because steam production is favored, which enhances the WGS rate. In such a case, though, yields of heavier hydrocarbons are adversely affected [180]. An increase in H_2 : CO results in higher amounts of lighter hydrocarbons and a lower olefin content [177, 181]. When the ratio is smaller, on the other hand, hydrogen deficiency leads to a loss in process efficiency since required hydrogen is supplied by splitting of the water molecules by expending energy to break the bonds [170]. It was shown that the lower H_2 : CO ratio in the feed favored the production of heavier alkenes (C_{9+}). It was noted that the lowest H_2 : CO ratio led to the presence of a high amount of heavy alkenes up to about C_{26} in the product gas [182].

Injection of CO_2 and H_2O to the feed also affects product distribution. H_2O, with its increased partial pressure, inhibits the reactions, especially over iron-based catalysts. Increasing the partial pressure of CO_2 results in a decrease in methane selectivity [166]. Extra CO_2 shifts the WGS equilibrium to the left, limiting the consumption of CO, which is then converted into hydrocarbons at a higher rate [180].

2.4. Microchannel Reactors for Fuel Processing and Synthesis

Use of microchannels in reaction technology is introduced in this section by means of review of some of the major experimental and computer-based studies in the field. Two reaction systems are considered: gas-phase synthesis gas (syngas) production

from various fuels (e.g. hydrocarbons and alcohols) by different reaction schemes such as steam reforming, partial oxidation and autothermal reforming, and hydrocarbon production from synthesis gas by the Fischer-Tropsch synthesis.

2.4.1. Microchannel Reactors in Synthesis Gas Production

Synthesis gas can be used as feedstock for further chemicals production processes such as the Fischer-Tropsch, methanol and dimethyl ether syntheses, and can also be purified into fuel-cell-grade hydrogen. It can be obtained by steam reforming, catalytic partial oxidation or autothermal reforming of fossil fuels and alcohols, as described in detail in Section 2.2.

2.4.1.1. Experimental Studies. *Steam reforming of methane* (**SRM**) has been studied in catalytic microchannel reactors by several groups. Wang *et al.* [183] investigated methods of coating $Rh/MgO\text{-}Al_2O_3$ on Al-containing porous metal substrates that make up the engineered microchannel, and evaluated the SRM performances of the resulting reactors at 850°C. The catalyst was coated either on an interfacial oxide layer previously coated on the surface of the substrate or on the substrate itself a native aluminum oxide layer. They concluded that engineered catalysts with an interfacial layer provided flexibility in catalyst configuration, and that the resulting SRM activity and catalyst stability were higher. In another study [184], different metal alloy substrates making up the skeleton of the microchannel reactors and coating techniques were compared. FeCrAl, calcined at high temperature, and NiCrFeAl, washcoated with alumina, were used to support Rh. The reactors were tested for their stabilities and catalytic partial oxidation activities. The NiCrFeAl reactor did not yield any steam reforming conversion even at 800°C while the FeCrAl reactor remained active for 3 h, which began to deactivate possibly due to the migration and sintering of Rh particles. The reason for the lack of activity of the NiCrFeAl reactor was argued to be the coverage of the Rh particles by the Cr layer and Cr oxides.

Ryu *et al.* [185] compared the performances of Ni-based commercial catalysts

both washcoated onto metal monoliths and in powder form. They reported significantly increased activity on the monolith due to enhanced transport rates. The differences between the activities were notable at higher space velocities since the monolith also offered the advantage of much smaller pressure drop. Another highlight from this study was that doping a small amount (0.12wt%) of Ru, Pt or Ir onto the unreduced Ni catalyst promoted its activity which would otherwise be attained by pre-reduction in a stream of H_2 at 600°C. Tonkovich *et al.* [11] and Wang *et al.* [186] developed coating techniques for highly active and stable Rh/MgO-Al_2O_3 catalyst on metal (FeCrAl) substrates, and optimized the metal loading and dispersion. The microchannel reactor, operated at contact times between 1 and 25 ms, was observed to remain active and resistant to coke formation for 14 hours of time on stream [186]. Comparison between structured and conventional lab-scale packed-bed reactors was also made, and the former was found to demonstrate much higher volumetric productivity. In a follow-up work, Tonkovich *et al.* [187] succeeded to pull down the 1 ms barrier for SRM, and achieved ca. 98% approach to equilibrium methane conversion at 900 μs.

Izquierdo *et al.* [188] tested Ni-based catalysts, namely, Ni/MgO and Ni/Al_2O_3, Pd/Al_2O_3, and Pt/Al_2O_3 in a microchannel reactor and a conventional fixed bed for hydrogen production via SRM. With either reaction system, the Ni/Al_2O_3 catalyst gave high conversions; however, it suffered from rapid deactivation. The Ni/MgO catalyst, on the other hand, yielded the highest conversion at 1073 K and a steam-to-carbon ratio of 1.5 while preserving its activity. For all the catalysts, higher conversions were obtained in the microchannel reactor when compared with the fixed bed on an identical WHSV basis.

Work of Wichert *et al.* [189] involved the development and testing of a completely miniaturized LPG fuel processor for ca. 250 W of electric power output. The propane–model fuel for LPG–reformer was coupled to a catalytic burner. The reactor consisted of stainless steel sheets patterned by wet chemical etching. The elliptic microchannels (600 μm width, 800 μm depth) are separated by 250 μm fins. The microchannel shape and dimensions were determined by computer simulations in order to optimize the flow distribution and minimize pressure drop. The catalyst for propane steam reforming

was coated in a single step by filling the microchannels with the noble metal-containing alumina carrier suspension (undisclosed), removing the excess suspension followed by calcination. The prepared microchannel sheets were stacked and welded by laser for sealing. Long-term (1060 h) stable operation of the reformer was maintained despite many start-up/shutdown cycles. Neither the stainless steel skeleton of the reformer nor the welding seams were affected by the operating temperatures around 750°C. No effect of the elevated temperature on the mechanical integrity of the catalyst coating was observed. Complete conversion of propane was obtained for all experimental conditions.

Besides reforming of light hydrocarbons (e.g. CH_4, C_3H_8), reforming of liquid hydrocarbons such as gasoline and diesel is a very attractive, yet challenging, route for producing hydrogen-rich syngas for fuel cells. In order to understand the underlying mechanisms, Thormann *et al.* [190] examined isothermal reforming of gasoline and diesel in a microchannel reactor using a Rh/Al_2O_3 catalyst. The test reactor was filled with 14 micro-structured foils on which $200\,\mu m \times 200\,\mu m$ square microchannels were machined. Each foil contained 100 channels of 80 mm length which resulted in a geometric surface are of $6360\,mm^2$ including the top of the fins. The temperature of the reactor was controlled using eight heat cartridges, four on top and four on the bottom of the foil stack. Catalyst preparation involved the coating of the foils by Al_2O_3 using the sol-gel technique, followed by impregnation of the support with aqueous $RhCl_3$ solution. Each foil was coated with ~ 10 mg Al_2O_3 and ~ 2.7 mg Rh. The thickness of the coating was determined to be $2-3\ \mu m$. At 700°C, with a steam-to-carbon ratio of 4.0 and GHSV between 15000 and $25000\,h^{-1}$, the conversion of *iso*-octane–model fuel for gasoline–was nearly 100% that yielded a product gas composition of 9.7vol% CO, 4.2% CO_2, 0.6% CH_4, 33.9% H_2, 0.003% C_4H_{10}, balance water and nitrogen. Under such operating conditions, reforming conversion of hexadecane, the diesel surrogate, decreased from 95% to 65% over a 12-h period. The decrease is argued to be the result of soot formation, which was seen to be reversible by catalyst regeneration under air flow at 750°C. The product gas from hexadecane reforming, prior to deactivation of the catalyst, consisted of 3.8vol% CO, 4.4% CO_2, 25.2% H_2, 0.07% H_2, 0.03% C_2H_6, 0.02% $C_{16}H_{34}$, traces of pentane, hexane, and decane, as well as of water and nitrogen. Their results led the authors to speculate, and further investigate the statement that

iso-paraffins (e.g. *iso*-octane) are more active in steam reforming than *n*-paraffins.

Gawade *et al.* [191] evaluated the combustion as well as reforming kinetics of hexadecane over a Rh-Ni/Al_2O_3 catalyst in a micro heat exchanger/reactor system that enabled efficient heat transfer from the combustion channels to the reforming channels. Reforming data were obtained over a temperature range of $500 - 750$°C, and at high steam-to-carbon ratios (>3.0). Three different mechanistic models were used to model the kinetics: Eley–Rideal, Langmuir–Hinshelwood bimolecular adsorption, and Langmuir–Hinshelwood dual site. Among these, the Eley–Rideal model compared the best with the data. Combustion kinetics were also found to be well represented by a power-law model. Reforming of diesel (having an average chemical formula of $C_{14.37}H_{27.40}$) has also been investigated in a wall-coated microchannel reactor comprised of reforming and combustion compartments that have been arranged for co-current, counter-current and cross-flow configurations [192]. The results showed that the reactor design allows inlet temperatures below 500°C because of its internal superheating capacity due to excellent heat transfer between the exothermic and endothermic reactions.

The use of catalytic microchannel reactors offers potential solutions to problems encountered during ATR of fuels (such as those mentioned in Section 2.2.3.3), and additional benefit of increase in productivity per unit volume or mass of catalyst [186]. With characteristic dimensions less than 1 mm, microchannel reactors allow for high surface area-to-volume ratios and enhanced heat transfer coefficients that are one or two orders of magnitude greater than those in conventional tubular reactors [186]. This facilitates rapid delivery of the released heat throughout the microchannel and across the metallic channel walls, thus quenching the highly exothermic oxidation reactions and inhibiting local hot spots [193]. Moreover, since excessive pressure drop along the channels is not a concern, it is possible to operate at residence times below 1 ms [187]. Reduced residence times lead to increased production rates and can be manipulated so as to suppress undesired slow reactions leading to coke formation [8]. In view of these aspects, partial oxidation of methane in microchannel reactors has been studied over different metal-based catalysts. Fichtner *et al.* [194] used a honeycomb catalyst

made of Rh foils whose high thermal conductivity provided a good heat distribution in the flow direction that led to higher methane conversions and CO selectivities. Younes-Metzler *et al.* [195] demonstrated that POX of methane could be carried out over a Pd-based catalyst within safety margins due to good reaction control. Enger *et al.* [184] tested Fecralloy and Nicrofer as the material of construction of the Rh-impregnated microchannels in terms of stability and catalytic activity, and found out that the former resulted in a thin but stable layer of alumina, increasing the effective reactor surface area and providing more sites for the Rh particles. Makarshin *et al.* [196] compared two flow configurations, namely, co-current and counter- current flows. The latter outperformed the co-current configuration both in methane conversion and CO selectivity, especially at high heat loads, because it tended to spread out the heat over a wider catalytically active region. As for fuels other than methane, ATR of *iso*-octane over Pt [197], of methanol over Pd-Zn [198], and of ethanol over Rh [199] have been studied in microchannel reactors. The issue of carbon deposition over the microchannel catalysts during SR of methane has also been addressed in several works [200, 201] in which the catalysts' operational resistance even at very low steam-to-carbon ratios has been demonstrated.

Rh-impregnated metallic microchannel reactors were studied for production of hydrogen-rich syngas through short contact time catalytic partial oxidation and autothermal reforming of propane by Aartun *et al.* [193]. The metallic microchannel monolith was manufactured from Fecralloy (72.6% Fe, 22% Cr, 4.8% Al) and consisted of 676 channels of dimensions 120 μm $\times$ 130 μm $\times$ 20 mm. The monolith was oxidized in air at 1000°C to form a thin alumina surface layer. It was subsequently impregnated with Rh by passing an aqueous solution of $RhCl_3$ through the channels followed by drying at 120°C. The mass increase resulting from impregnation corresponded to 1 mg Rh. The Rh/Al_2O_3/Fecralloy monolith was reduced in situ at 800°C for 3 h in 10% H_2 in N_2.The monolith was placed in a quartz container. Schematic drawing of the experimental apparatus is shown in Figure 2.15.

The experiments were carried out using a continuous reactant flow at near-to-atmospheric pressure and furnace temperatures from 300 to 950°C. The concentration

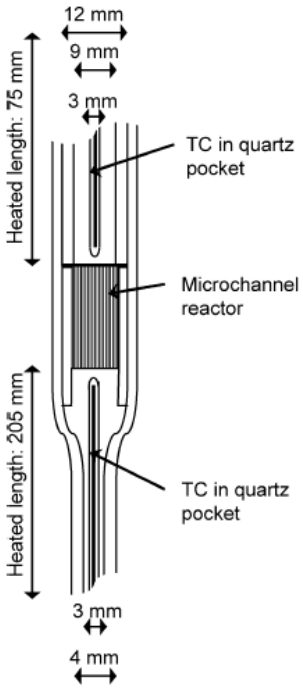

Figure 2.15. Schematic drawing of the quartz reactor loaded with microchannel monolith [193].

of propane was kept the same for both POX and ATR. The reactant mixture consisted of propane and air for POX, with a C : O ratio equal to 0.8. In case of ATR, steam was added to the feed and the C : O and H_2O : O_2 ratios were 0.5 and 2.0, respectively, with N_2 to balance. A total flow rate of 1000 Nml min^{-1} (at 0°Cand 1 atm) was chosen as reference.

The results showed that gas phase ignition at the monolith entrance occured at furnace temperatures above 700°C for both POX and ATR for a feed gas flow of 1000 Nml min^{-1}, corresponding to a residence time of 12.7 ms. Ignition observed at high temperatures was followed by a substantial decrease in the selectivity to the desired product of syngas, as well as increased hydrocarbon by-product formation. This behavior was ascribed to gas-phase reactions, especially formation of methane and ethene as cracking products. Lowering the residence time below 10 ms increased the syngas selectivity, probably due to quenching of the gas-phase reactions at high linear gas velocities, and suggested that direct formation of hydrogen and CO was

part of the reaction scheme. No catalyst deactivation was observed despite repeated temperature cycling under POX and ATR reactant exposure.

Another study by the same group [202] involved determination of the temperature profiles for both POX and ATR of propane taking place in the identical reaction system with Fecralloy microchannel monolith washcoated with Rh-containing alumina. The profiles along the reactor axis showed that the metallic microchannel reactor was able to minimize temperature gradients due to the exothermic reactions POX and ATR. Variation of the total flow rate at constant furnace temperature resulted in decreased propane and oxygen conversion along with increased H_2 and CO selectivity and reduced hydrocarbon by-product formation at residence times below 10 ms for both POX and ATR. This was recognized as an indication that gas phase ignition was suppressed at sufficiently high gas hourly space velocities (GHSV). The Rh/Al_2O_3/Fecralloy microchannel reactor also showed promising stability, since it was found not to deactivate after more than 70 experiments at POX or ATR conditions with temperature cycling from 300 to 1000°C.

Syngas production by POX of propane was also studied by the group of Pennemann [203]. Various catalysts based on rhodium, palladium and platinum on γ-alumina were washcoated into microstructured reactors. The experiments were carried out with sandwich-type reactors composed of two stainless steel plates each having 14 channels with 500 μm width and 250 μm depth. The microchannels were made by wet chemical etching using an aqueous iron chloride solution. The catalysts were introduced into the microchannels by a sequential procedure comprising washcoating, drying, calcination, impregnation and second calcination. The suspended support material of γ-Al_2O_3 was introduced into the channels by a fill-in wipe-off technique followed by a drying and a calcination step at 600°C. Subsequently, the support was impregnated with the respective metal salt solutions and calcined a second time at 450°C. After passivation layers and catalysts had been coated into the channels, the sandwich-type reactors were sealed by laser welding. The reactor was placed into a metal block equipped with a heating cartridge. At the beginning of each run, the freshly prepared catalyst was reduced at 700°C at a hydrogen flow rate of 20 $\mathrm{Nml\,min^{-1}}$ for 1 h. Without further

pretreatment, partial oxidation was initiated at 700 °C. After a sample had been taken online for analysis the reactor temperature was increased by 10°C. This procedure was repeated until a final temperature of 850°C was reached. Experiments were carried out at O : C ratios in the range of $1.0 - 1.3$. Flow rates were adjusted to a total flow rate of 400 $\mathrm{Nml\,min^{-1}}$ with respect to the reactants, resulting in a GHSV of 274000 $\mathrm{h^{-1}}$ and an overall pressure drop of approximately 0.8 bar. Product gases were analyzed by an online gas chromatograph.

The results of the experiments showed that propane conversion was strongly dependent on the catalyst type. In the case of rhodium, complete conversion and high selectivities towards hydrogen and carbon monoxide close to thermodynamic equilibrium were achieved. In contrast, over platinum and palladium, products of total oxidation, such as water and carbon dioxide were favored. Only in the case of platinum and palladium trace quantities of ethylene and propylene were detected. Furthermore, bimetallic rhodium/platinum catalysts were investigated and turned out to be as selective as a pure rhodium catalyst when the rhodium concentration of the bimetallic catalysts was higher than 0.5 wt%. In general, it was determined that in the case of complete or nearly complete propane conversion, the experiment had to be terminated after a certain time due to an increase in the pressure drop. By opening of the reactor coke formation was found to be the cause of plugging. Although both the reaction plates and the connection tubes were made of stainless steel, coke formation in the reactor outlet tube was the crucial factor. For prevention of deactivation due to coking, protective coating of the active surfaces was suggested.

Reforming of alcohols, as well as of hydrocarbons, are widely investigated in the literature for the purpose of production of hydrogen to be used in small- to medium-scale power applications. In their work, Park and coworkers [204] investigated methanol steam reforming in a microchannel reactor coated with $\mathrm{Cu/ZnO/Al_2O_3}$ catalyst. The reactor was constructed from stainless steel plates the channels on which were patterned by wet chemical etching (Figure 2.16). The microchannels were 500 μm wide, 200 μm deep and 33 mm long. The catalyst slurry was made of ICI Synetix 33-5 catalyst, 20% alumina sol, distilled water and 2-propanol. In order to enhance the adhesion between

Figure 2.16. Microchannel sheets for methanol steam reforming [204].

catalyst powders and the substrate structure, alumina was undercoated on the surface of the microchannels and then the suspension of powdered catalysts was coated on the preformed alumina layer. After drying in air, catalyst-coated metal structure was calcined at $350-400$°C. About 0.1 g of catalyst was coated on each microchannel basic structure. The plates were bonded together by a brazing process and were heated by rod-type electric heaters. The reforming reaction was conducted in the temperature range $200-260$°C. Methanol was evaporated in a vaporizer before mixing with steam. The feed flow rate was 0.1 mL min^{-1}. The product stream was separated using a cold trap maintained at 5°C and the composition of the dry reformed gas was analyzed by a gas chromatograph.

The performance of the reactor is shown in Figure 2.17a. The H_2 production rate was enhanced with increasing temperature. However, the amount of produced H_2 decreased with increasing steam-to-carbon ratio. This was mainly due to the decrease of absolute amount of methanol in the feed of methanol-water mixture with increasing steam-to-carbon ratio. Therefore, a high reaction temperature and a low steam-to-carbon ratio were more favorable for high amount of H_2 production during methanol steam reforming. The effect of reaction temperature and steam-to-carbon ratio on CO formation is shown in Figure 2.17b. The concentration of H_2 and CO_2 was less sensitive to the reaction temperature and steam-to-carbon ratio revealing $72-75\%$ H_2 and $24-25\%$ CO_2 in all runs. However, CO concentration increased from 0.17 to 1.6%

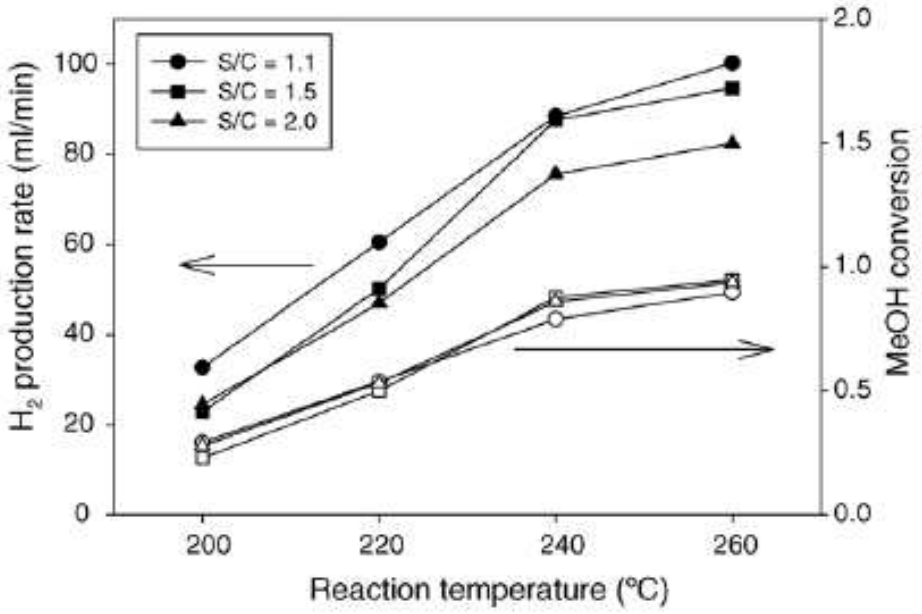

(a)

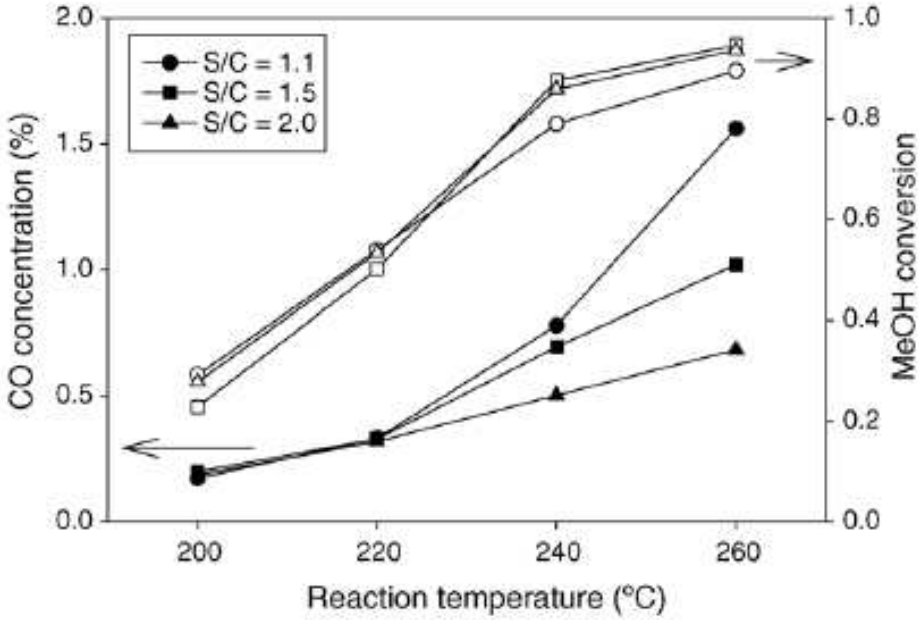

(b)

Figure 2.17. (a) Effect of temperature and S : C on H_2 production (b) Effect of temperature and S : C on CO concentration [204].

as the reforming temperature increased from 200 to 260°C. This was mainly because of the reverse water-gas shift reaction which was enhanced by increased temperature. CO concentration also decreased as the steam-to-carbon ratio increased.

Men *et al.* [205] designed, constructed and studied the performance of a microstructured methanol reformer to be installed into a completely miniaturized fuel processor that is to function as hydrogen supplier for low-power applications. The reactor consisted of stainless steel sheets patterned by wet chemical etching. The elliptic microchannels (600 μm width, 800 μm depth) are separated by 250 μm fins, and are 44 mm long. The microchannel shape and dimensions were determined by computer simulations for optimizing the flow distribution and minimizing pressure drop. The Cu/ZnO catalyst was coated in a single step by filling the microchannels with the metal-containing alumina carrier suspension, removing the excess suspension followed by calcination. The prepared microchannel sheets were stacked and welded by laser for sealing. Both sides of the end plates had two holes for rod-type electric heaters. The effects of temperature (in the range $235 - 275$°C), contact time ($W/F = 1.425 \times 10^{-3} - 5.7 \times 10^{-3}\,\mathrm{g_{cat}\,min\,ml^{-1}}$), and steam-to-carbon ratio ($\mathrm{S : C} = 1.1 - 2.0$) on conversion, H_2 yield, and CO and CO_2 selectivities were examined. At $\mathrm{S : C} = 2.0$, full methanol conversion was achieved at 275°C and $W/F = 2.85 \times 10^{-3}\,\mathrm{g_{cat}\,min\,ml^{-1}}$ whereas 0.35% CO containing reformate was obtained.

Steam reforming of methanol, together with the side reaction of methanol decomposition, was studied in a reactor with dimensions 40 mm × 40 mm × 8 mm comprising 125 microchannels coated with a $Cu/ZnO/Al_2O_3$ catalyst [206]. The continuous and stable operation for 100 h showed that the microchannel reactor could generate enough hydrogen for a power output of 11 W.

Peela *et al.* [90] performed a kinetic investigation of steam reforming of ethanol over $2\%Rh/20\%CeO_2/Al_2O_3$ in a microchannel reactor in the temperature range $450 - 550$°C. The microchannels were etched on a stainless steel sheet with 1 mm thickness by laser micromachining. The plate had 60-mm long 25 microchannels each with a depth of 400 μm and width 500 μm, separated by 300 μm fins. A binder (polyvinyl

alcohol) was coated beneath the support layer. Thickness of the catalyst layer was $\sim 30\,\mu$m. After joining the catalyst-coated sheet to a plain stainless steel plate by laser spot-welding, four cartridge heaters were inserted into the assembly to maintain the temperature at the value set. The steam-to-carbon ratio was varied between 2 and 4, and the weight of the catalyst deposited on the plate was $\sim$ 70 mg. The contact time, based on ethanol flow rate, was between 0.07 and 1.28 $g_{cat}\,h\,mol^{-1}$. The reaction scheme was determined to consist of reaction of steam with ethanol, decomposition of ethanol, steam reforming of methane, and the water-gas shift. The proposed kinetic model that is based on Langmuir–Hinshelwood kinetics satisfactorily predicted the conversion and product distribution.

2.4.1.2. Modeling and Simulation Studies. Detailed and accurate modeling and simulation of flows at the microscale has gained momentum with the widespread availability of commercial flow modeling softwares such as ANSYS FLUENT™, ANSYS CFX™ and COMSOL Multiphysics™ that also provide the opportunity to couple the flow field with global/elementary transport phenomena and reaction kinetics. This is the reason why the number of works involving modeling of microchannel reactors for the specific purpose of simulating heterogeneous reaction systems has arisen immensely in the last couple of years. This section gives an overview of the studies that have solely considered steam reforming of various fuels in which *the required heat is supplied by means of electrical power*. Works that comprise *different schemes of coupling of steam reforming and a heat source*–whether it be the combustion reaction of same or another fuel or simply a stream of hot gas–are introduced in Section 2.5.

The work of Cao and coworkers [207] involved developing a heterogeneous three-dimensional model in order to simulate reforming of methane in a microchannel reactor. The reactor consisted of two aligned FeCrAlY felts with identical dimensions (250 μm $\times$ 9 mm $\times$ 51 mm). About 14 mg of 10 wt% $Rh/MgO/Al_2O_3$ catalyst was washcoated onto each square centimeter of the felt surface. Heat was supplied by means of a furnace. Mixtures of methane and steam at varying compositions were introduced at GHSVs varying in the range $144000 - 3600000\,h^{-1}$.

The model assumed that the variations in washcoat effective diffusivity, effective thermal conductivity and heat capacity were small, and the axial conduction and diffusion were negligible compared to convection. The empirical kinetic rate constant and apparent activation energy were used to express the first-order reaction with respect to methane. The following fundamental equations represented the conservation laws of mass and energy in rectangular coordinates (x-y-z) with dependent variables temperature and methane concentration:

Gas phase:

$$u\frac{\partial c}{\partial z} = D_{\text{mix}}\left(\frac{\partial^2 c}{\partial z^2} + \frac{\partial^2 c}{\partial y^2}\right) \tag{2.38}$$

$$u\rho C_p\frac{\partial T}{\partial z} = k_{\text{mix}}\left(\frac{\partial^2 T}{\partial z^2} + \frac{\partial^2 T}{\partial y^2}\right) \tag{2.39}$$

Washcoat:

$$D_{\text{eff}}\left(\frac{\partial^2 c}{\partial x^2} + \frac{\partial^2 c}{\partial y^2}\right) = k\left(c, T\right)c \tag{2.40}$$

$$k_{\text{eff}}\left(\frac{\partial^2 T}{\partial x^2} + \frac{\partial^2 T}{\partial y^2}\right) = k\left(c, T\right)c\left(-\Delta H_{\text{r}}\right) \tag{2.41}$$

The set of equations were solved by the finite element method using the FEMLAB (now COMSOL™) Multiphysics environment. Figure 2.18a shows the temperature profile at the axial position $z = 2.54$ mm. It can be seen that the temperature distribution is very narrow in the cross section at a typical operating condition (850°C,

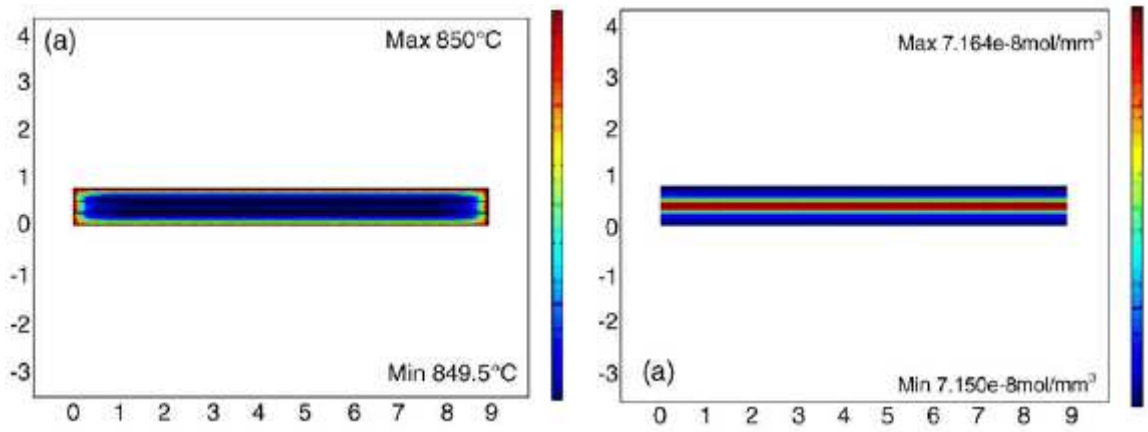

(a) (b)

Figure 2.18. (a) Temperature distribution in SRM microchannel reactor (b) Methane concentration profile at $z = 2.54$ mm [207].

20 atm, S : C = 2.0, 13.8 ms contact time, 72% methane conversion). The local cold spots typically inherent in conventional fixed bed reforming reactors were eliminated. Such improved heat transfer ensures the catalyst is being operated at an average high temperature that is close to the reactor wall temperature. Figure 2.18b shows the local methane concentration profiles at a certain distance from the reactor inlet. It can be seen that the conversion is uniform in neither phase. The local conversion is directly associated with the local temperature distribution shown in Figure 2.18a.

The amount of catalyst deposited on the walls of microchannels can have great effect on reactor performance. In light of this claim, Stutz and coworkers [208] investigated numerically the effect of catalyst surface site density (catalyst amount) and reactor geometry on the POX of methane in a wall-coated, single-channel microreactor. Such a reactor, consisting of a tubular flow channel and a thermally conductive channel, was considered to be a good representation of microfabricated channels and monoliths. It was found that hydrogen selectivity changed significantly with varying catalyst loading, which was a noteworthy result. This was ascribed to the splitting rate of methane and water, which is a function of catalyst density. Furthermore, the study showed the significance of scaling the inlet volume not only with the reactor volume (GHSV) but also with the catalyst amount (catalyst space velocity).

In the more recent work by Stutz and Poulikakos [209], syngas production was investigated by a numerical model of an adiabatic monolith reformer in which POX of methane took place. The study included the thermal and diffusive properties of a washcoat of finite thickness that was modeled as a porous layer composed of a ceramic support containing catalytically active Rh sites. It was combined with a two-dimensional radially symmetric model of a single tubular minichannel, considering both the thermal and diffusive transport phenomena in all domains. The channel diameter was taken to be 1 mm. CFD calculations combined with detailed surface reaction mechanisms were carried out. It was found that both the methane conversion and the hydrogen yield depended markedly on the washcoat thickness. An interesting result was that if the inlet volumetric flow and the amount of catalyst per washcoat volume were constant, an optimum washcoat thickness of 70 μm was found, where the hydrogen yield was maximal. For a thinner washcoat, the smalller amount of catalyst was limiting, leading to a low methane conversion. For a thicker washcoat, the limiting effect was the reduced residence time, which stemmed inherently from the constraint of constant volume flow, rather than the increased diffusive resistance.

As the continuation of their experimental study (Section 2.4.1.1), Thormann *et al.* [210] investigated hexadecane–the chosen diesel surrogate–reforming in microchannels coated with Rh/CeO_2. Developing a detailed kinetic model that also comprises the steam reforming of methane and propane for a better understanding of conversion of hexadecane fragments, they found out, using experimental data, that the turnover frequencies of the linear alkanes were inversely proportional to the number of carbon atoms per hydrocarbon molecule. These results were the basis for the kinetic model that links a global reaction equation for the dissociative adsorption of long-chain hydrocarbons with an elementary surface reaction mechanism of steam reforming of methane over Rh/Al_2O_3 catalysts. The model was seen to predict the correlation between turnover frequency and the number of carbon atoms. Even more, the ceria support was observed to have significant impact on the reformate composition.

The large number of modeling studies of reforming of methanol in microchannel reactors is representative of the importance of methanol in the fuel processing

literature such that it features low reforming temperatures and low carbon monoxide content [63, 206, 211–217]. Hsueh *et al.* [213, 214] performed numerical simulations of steam reforming of methanol in a plate-type microreactor. The effects of channel size and aspect ratio (ratio of channel height to channel width) on the transport characteristics and reactor performance were analyzed. It was found that as the aspect ratio decreases, methanol conversion and H_2 yield increase. Moreover, the temperature distribution throughout the channel becomes more uniform. As for the effect of channel size, use of smaller microchannels resulted in more uniform temperature distributions that led to reduced thermal entrance lengths, which translate to improved fuel utilization efficiencies.

Jang *et al.* [215] performed a similar CFD simulation study of methanol steam reforming in which they investigated the effects of wall temperature, channel geometry and inlet/outlet manifold configurations on fuel conversion and product distribution. The featured finding was that the manifold configuration of central inlet/two outlets not only results in $\sim 30\%$ increase ($32.4\% \rightarrow 42.3\%$) in conversion but it also yields a $\sim 30\%$ decrease ($0.39\% \rightarrow 0.27\%$) in carbon monoxide content.

Ethanol is another promising fuel for hydrogen production due to its high hydrogen content, availability, low toxicity and easy storage [219, 220]. Steam reforming of ethanol obtained from biomass has great potential in fuel processing particularly because bioethanol comes as a dilute aqueous solution (12 wt% ethanol) that can directly be used in reforming [220]. Uriz *et al.* [221] carried out a three-dimensional CFD simulation study of reforming of ethanol in microreactors with square channels over Co_3O_4-ZnO catalyst. The kinetic model implemented included ethanol dehydrogenation to acetaldehyde, ethanol decomposition to CO and CH_4, acetaldehyde reforming to H_2 and CO_2, and the water-gas shift reaction. The simulation results indicated that at high reaction temperatures (>625°C) ethanol decomposition–due to its higher activation energy and lower reaction enthalpy–competed with its dehydrogenation to acetaldehyde, which was the key intermediate of the reforming process. The net result was the reduction in the hydrogen yield and increase in the carbon monoxide content. It was shown that by increasing the surface area-to-volume ratio and the catalyst load-

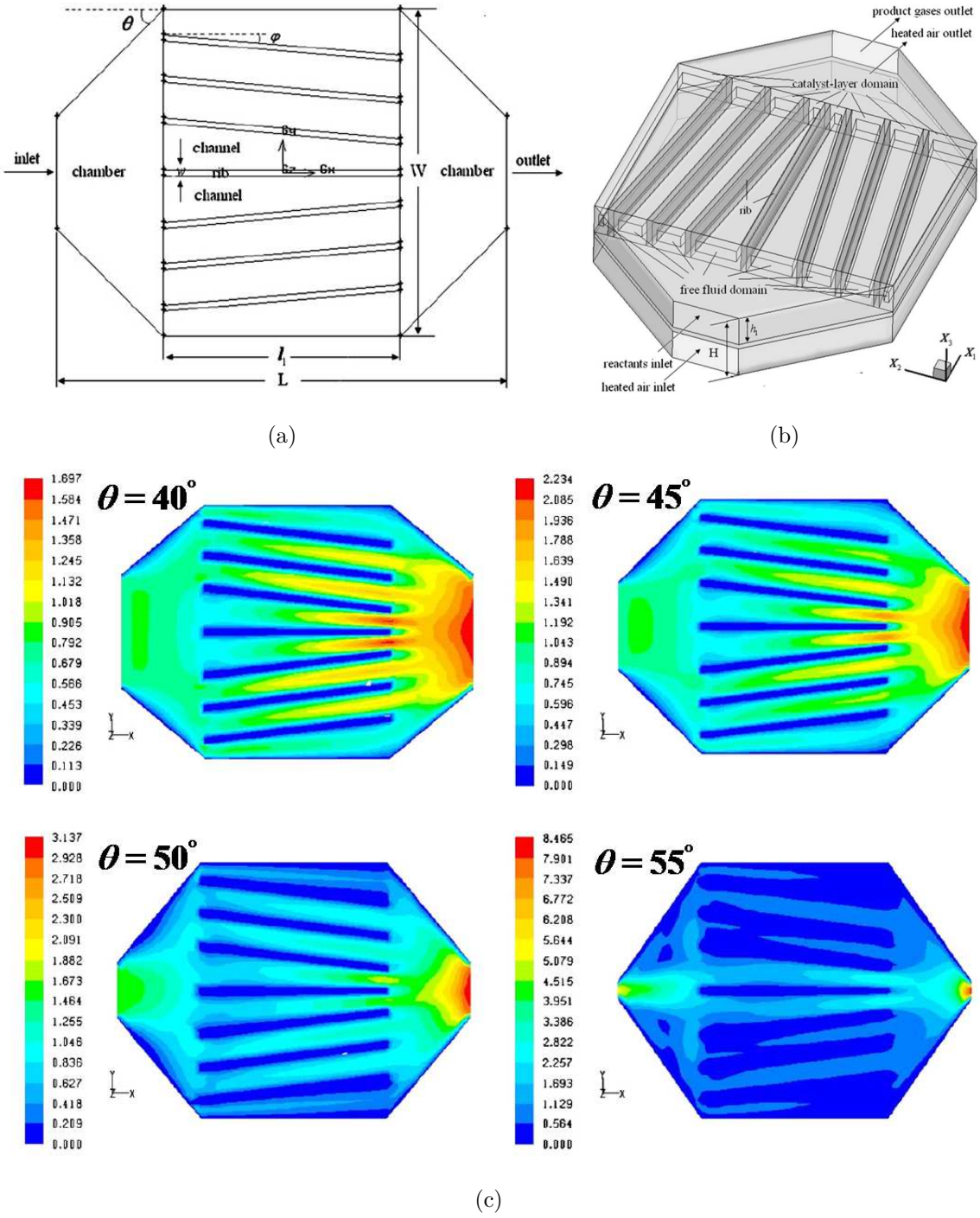

Figure 2.19. (a) 2D and (b) 3D schematic diagrams of the microreactor (c) Velocity distributions under different entrance angles θ [218].

ing, it was possible to allow a reduction in the operating temperature while increasing the selectivity. Parametric study of the channel sidelengths showed that microchannels with sidelength between 0.10 and 0.35 mm resulted in nearly isothermal flow with high hydrogen yields.

Up until this point in the review, the microchannel reactors, whether they be part of experimental test rigs or objects of purely theoretical design, consisted of single or a multitude of straight, parallel catalytic channels. Hao *et al.* [218] proposed a very interesting and promising microreactor design that involved eight non-parallel channels (Fig. 2.19a) in order to improve the performance of steam reforming of methanol. The widths of some channels were taken as variable along the reactor length by manipulating the entrance inclination angle θ and the channel inclination angle φ. Channels $\underline{\text{no}}$4 and 5 gradually narrow down along the flow direction. In contrast, widths of channels $\underline{\text{no}}$1 and 8 increase while the widths of the remaining channels are unchanged (Fig. 2.19b). Two-dimensional velocity contours under different entrance angles were plotted (Fig. 2.19c). Based on the criterion that all eight channels were to have similar velocity distributions, the optimal flow uniformity was obtained when θ and φ were equal to 55° and 9°, respectively, which also yielded the maximum conversion values.

2.4.2. Microchannel Reactors in Fischer-Tropsch Synthesis

The number of works in the open literature in which the Fischer-Tropsch synthesis had been carried out in the submillimeter range has shown a steady rise since 2008. The principal reason is the continuous development of micromanufacturing and micromachining technologies, which has enabled researchers to come up with new and robust designs of micro devices. On the other hand, as already mentioned in Section 2.4.1.2, ubiquity of CFD flow modeling softwares and increasing processor and memory power has made it possible to work with detailed reactor models at the micro scale.

2.4.2.1. Experimental Studies. One of the earliest works in literature as concerns the FT synthesis at the micro scale has been published by Chin *et al.* [222]. They synthe-

sized and tested a novel micro-structured catalyst based on aligned multiwall carbon nanotube arrays (Figure 2.20a). An Al_2O_3 thin film was deposited over FeCrAlY foam first to enhance the adhesion between the ceramic-based catalyst and the metal substrate. The nanotubes were deposited uniformly over the substrate by controlled catalytic decomposition of ethylene. The outer surfaces of the nanotubes with the active catalyst layer (Co-Re/Al_2O_3) formed a unique hierarchical structure. The catalyst possessed superior thermal conductivity due to the carbon nanotube, which allowed efficient heat removal from catalytic active sites during the exothermic FT synthesis reactions. The experiments were carried out in a microchannel reactor made of stainless steel, with a channel dimension of 3.56 cm × 0.90 cm × 0.15 cm. The metal foams used for preparing the structured catalysts were machined to match the internal geometry of the reactor channel, where bypass between the catalyst and the channel wall was minimized. The reactor temperature and pressure were adjusted to 240°C and 1.5 MPa, respectively, prior to the FT reaction. The feed composition was set to $CO : H_2 : Ar = 32 : 64 : 4$. Total feed flow rate was set to achieve a desired GHSV of 14400 h^{-1}. The stream leaving the reactor (unreacted syngas and hydrocarbon products) was separated into condensed and non-condensable products. A pressurized cold trap operated at 0°C was installed to capture majority of the condensable products (C_{4+}). Gaseous products were analyzed by a gas chromatograph to obtain CO conversion and product selectivity. CO conversion and product selectivity were calculated based on feed and product flow rates and a carbon balance.

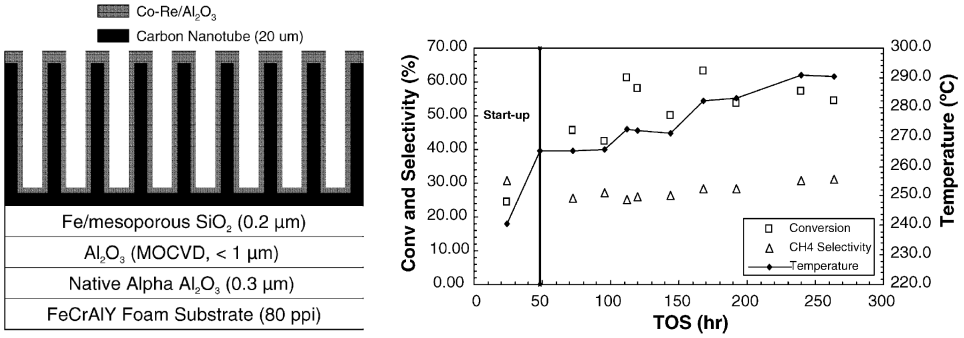

(a) (b)

Figure 2.20. (a) Schematic and (b) performance of the microstructured catalyst based on carbon nanotube arrays for FT synthesis [222].

Heat generated during the FTS reactions can be conducted along the length of the carbon nanotubes, and then quickly removed from active sites, thus lowering methane selectivity (Figure 2.20b). It was shown that the CH_4 selectivity was stable in the temperature range of $240 - 290°C$. For comparison, the authors carried out the FT reactions over the same active catalyst and microstructure, but without the carbon nanotube arrays. With the nanotube array, two- and four-fold enhancement was observed respectively in CO conversion and specific activity ($mmol_{COconv}\, g_{Co}{}^{-1}\, h^{-1}$). This was attributed to the improved mass and heat transfer which allowed the FT synthesis to be operated at higher temperatures without selectivity runaway that favors methane formation.

Guillou *et al.* [223] used a Co/SiO_2 catalyst grafted on a stainless steel substrate for FT synthesis (FTS) in a micro-chamber reactor. The reactor consisted of a stacking of a single catalytic plate between two mechanically engineered steel blocks. Upper and lower blocks were equipped with a thermocouple and power cartridges to ensure electrical heating and temperature control. The upper block acted as a gas distributor and collector. Inlet and outlet were located in perpendicular to the catalytic plate (Figure 2.21). The reaction chamber of 200 μl volume was obtained by engraving the upper block with a 40 mm $\times$ 20 mm $\times$ 250 μm rectangular groove. A similar groove was engraved in the lower block and received the catalyst coated plate.

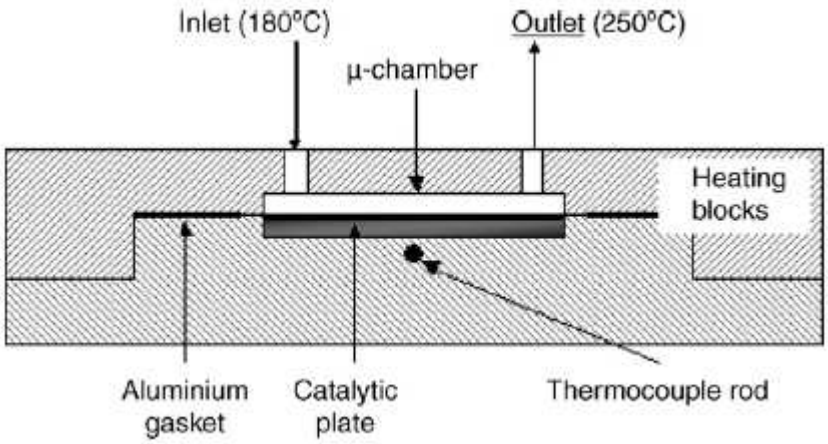

Figure 2.21. Micro-chamber test reactor for stainless steel supported catalysts [223].

Leakage from the stacking was prevented by means of an aluminum metallic joint. The working pressure was set at 0.1 MPa. Prior to FTS, catalyst was activated *in situ* under pure H_2 (680 ml h^{-1}) for 4 h at 450°C. After reduction, the reactor was cooled down to the required reaction temperature and gas flow was switched to the proper syngas composition at 0.1 MPa. Total flow rate was set to achieve a desired constant contact time of 1 s. Outlet stream was heated at 250°C to avoid product condensation. Gaseous products were analyzed online by a gas chromatograph.

Table 2.11. FTS reaction parameters and influence over activity and product distribution [223].

Experimental Conditions			**Analytical results**			
H_2:CO	e (μm)	T (°C)	X_{CO} (%)	$C_1 - C_4$ (%)	$C_5 - C_9$ (%)	C_{10+} (%)
1.5	50	180	10.01	46	24.9	29.1
1.75	50	180	11.04	46.7	26.2	27.1
2	50	180	12	52.5	27.9	19.6
2	50	180	12.5	50	28.3	21.6
2.5	50	180	15	53.6	24.2	21.2
3	50	180	16.02	59	26.7	14.3
2	70	150	1.03	45.2	25.6	28.9
2	70	170	13.5	43	29.1	27.9
2	70	180	15.1	51.4	28.9	19.7
2	70	200	18.7	66	28.1	6
2	70	220	24.1	85.5	14.4	0.1

Table 2.11 shows the FTS conditions, CO conversion (X_{CO}) and product distribution ($C_{1-4}, C_{5-9}, C_{10+}$ selectivities) obtained for various inlet compositions (H_2 : CO inlet partial pressures ratio), catalyst thicknesses (e) and reaction temperature (T). Results obtained on a 50 μm thick catalyst showed that conversion increases with hydrogen partial pressure. The variation of the rate-related X_{CO} shows the influence of syngas composition on the activity; the highest conversion levels were obtained for the H_2 richest inlet feeds. Product distribution showed a similar sensitivity to H_2 : CO. Higher relative hydrogen partial pressure caused a progressive shift of the distribution toward shorter hydrocarbons. However, the relationship between product distribution and conversion did not exhibit any clear trend: most CO_{10+} yields for constant tem-

perature experiments were closely distributed around a constant yield level curve at 2.5%.

The group of Guillou also investigated the FTS in a microchannel reactor [224]. The stacked single channel microstructured reactor was made up of an engineered stainless steel foil arranged between two housing devices. The housing was equipped with inlets (gas distributor) and outlet connections, as well as heating devices and a thermocouple. The temperature was adjusted with a PID controller. The engineered foil was the channel plate. The channel dimensions were 80 mm × 1 mm. It was mechanically engraved in a 250 μm thick steel foil. It was stacked between the upper and lower distributors. A 20wt% Co/SiO_2 catalyst was used for the FTS. It was obtained by a sol-gel modified method. A classical sol made out of the catalyst and support precursors ($Co(NO_3)_2$ and $Si(C_2H_5O)_4$) acidified with HNO_3 was used. Coating was applied by a continuous hot spraying process. The freshly-coated catalysts were then treated under air at 350°C for 1 h. The reactor was operated at $P = 0.1$ MPa and $T = 180$°C. The activity and product distribution results were comparable with the ones previously observed (Table 2.11) for the same catalyst for a different microreactor flow configuration [223].

Zhao *et al.* [225] studied the effect of ruthenium (Ru, 0.4wt%) as a promoter on silica-supported iron and cobalt nanocatalysts for syngas conversion to higher alkanes in a silicon microchannel reactor. Fe-Co/SiO_2 catalysts with and without Ru were synthesized by a sol-gel method. The reactor (Figure 2.22) consisted of a feed inlet, product outlet and 239 straight channels with 25 μm width and 100 μm depth. The volume of the reactor was approximately 9 mm^3. The multi-entry (16 ports) microreactor inlets and outlets were designed for better distribution of reactant and product gases passing through the microchannels. The microchannels on the silicon wafers were opened using photolithographic techniques and dry plasma etching. The packaging of the microreactor was completed using anodic bonding to avoid leakage of reactants. The catalyst slurry was coated on the reactor microchannels using a drop coating method (Figure 2.23).

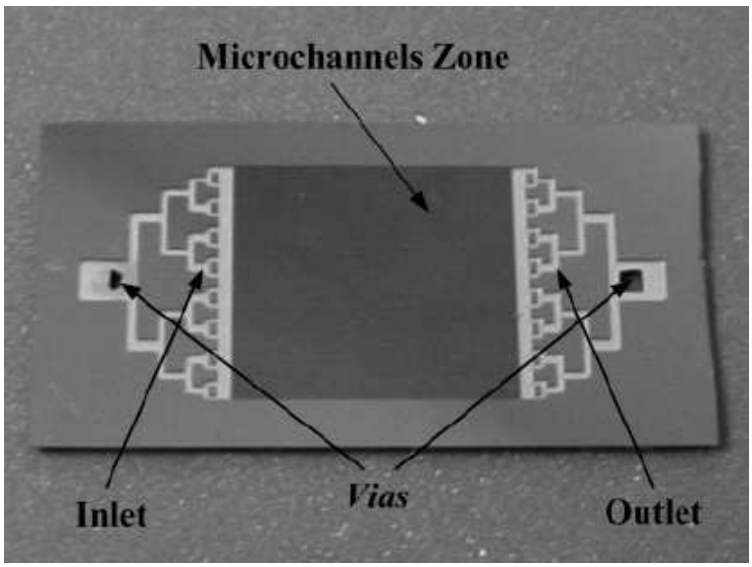

Figure 2.22. Typical silicon microreactor (3.1 cm × 1.6 cm) containing 239 channels, 25 μm wide and 100 μm deep, used for FT synthesis [225].

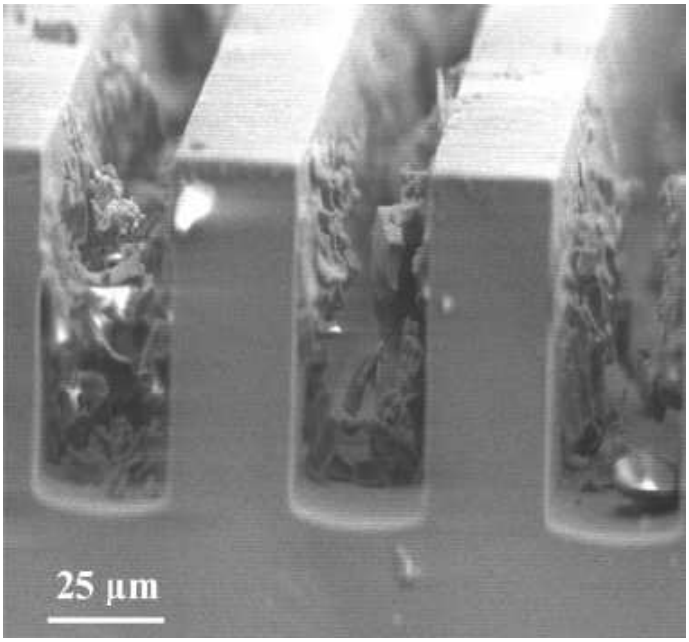

Figure 2.23. SEM image of silica-supported Fe-Co catalyst deposited in 25 μm wide and 100 μm deep microchannels [225].

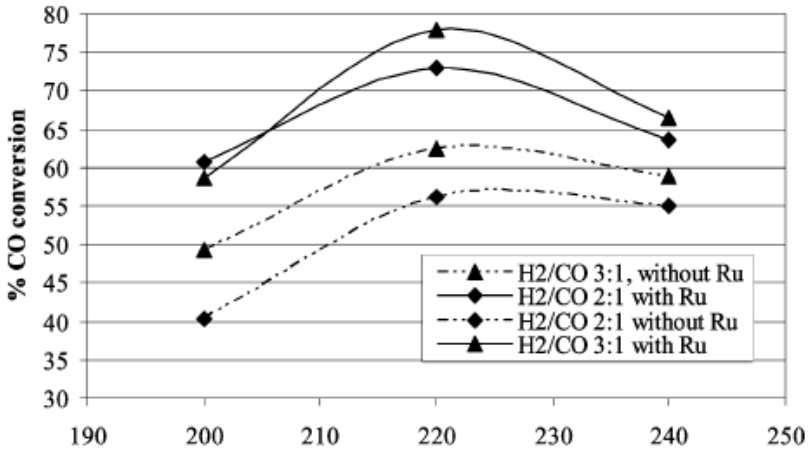

Figure 2.24. Comparative studies on CO conversion to alkanes at different temperatures and two H_2 : CO ratios, using silica-supported Fe-Co catalysts with and without Ru [225].

CO hydrogenation for silica-supported Fe-Co catalysts with and without Ru in 25 μm wide channel microreactors was carried out at atmospheric pressure, using a total flow rate of 0.4 sccm at different temperatures and ratios of H_2 : CO $(2-3:1)$. The highest CO conversion on the Ru-Fe-Co/SiO_2 catalyst reached ca. 78% at 220°C by adding only 0.4wt% Ru at a H_2 : CO ratio of 3 : 1. This was much higher than that observed for the Fe-Co/SiO_2 catalyst (63%), although the loadings of iron and cobalt were less in the Ru-Fe-Co/SiO_2 catalysts. The general trend was that 220°C was the optimum temperature for all the catalysts and H_2 : CO ratios (Figure 2.24). In addition, except at 200°C, a H_2 : CO ratio of 3 : 1 was better for syngas conversion than the ratio of 2 : 1, which was consistent with syngas conversion using alumina-supported catalysts. Furthermore, the ratio effect on CO conversion was less with Ru than that observed without Ru. With Ru, CO conversion was almost same for both 3 : 1 and 2 : 1 ratios of H_2 : CO at 200°C, whereas the H_2 : CO ratio effect was significant without Ru (40% at 2 : 1 to 49% at 3 : 1). This indicates that the role of Ru is more important in CO conversion than that of the H_2 : CO ratio.

Addition of the Ru promoter not only increased CO conversion significantly, but it also affected the selectivity to alkanes. While the Ru-Fe-Co/SiO_2 catalyst at a

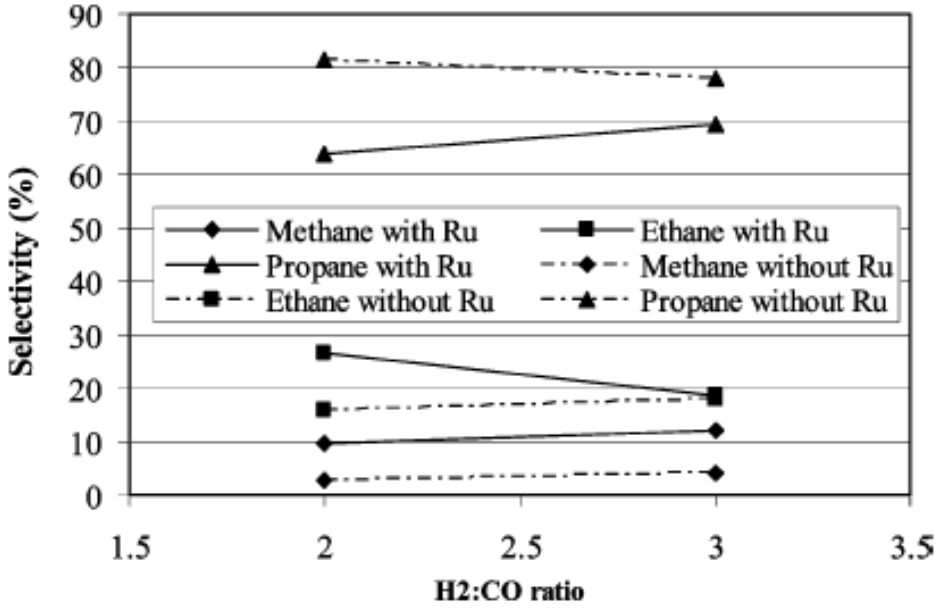

Figure 2.25. Selectivity to various alkanes at different H_2 : CO ratios using silica-supported Fe-Co catalysts with and without Ru [225].

H_2 : CO ratio of 3 : 1 yielded ∼70% selectivity to propane, ∼20% to ethane and ∼10% to methane (Figure 2.25), these values with the Fe-Co/SiO_2 catalyst were ∼80, 17 and 3%, respectively.

Apart from the well-established parallel microchannel configuration, several groups investigated different microstructuring methods. The reactor whose schematic is shown in Figure 2.26a consisted of eight parallel catalyst sections sandwiched between cross-flow oil channels for heat exchange. Each catalyst section was comprised of two foils with an etched 400 μm deep pillar structure, hexagonally arranged with 800 μm distance between the pillars. The foils were stacked opposite to each other, giving 800 μm channel height. Three thermocouples in the reactor body measured the reactor wall temperature and were regulated against temperature in the oil circulator bath during the experiments.

The milli-structured fixed-bed slit reactor (Figure 2.26b) studied by Knochen *et al.* [226] consisted of channels for the heat transfer medium and the catalyst bed.

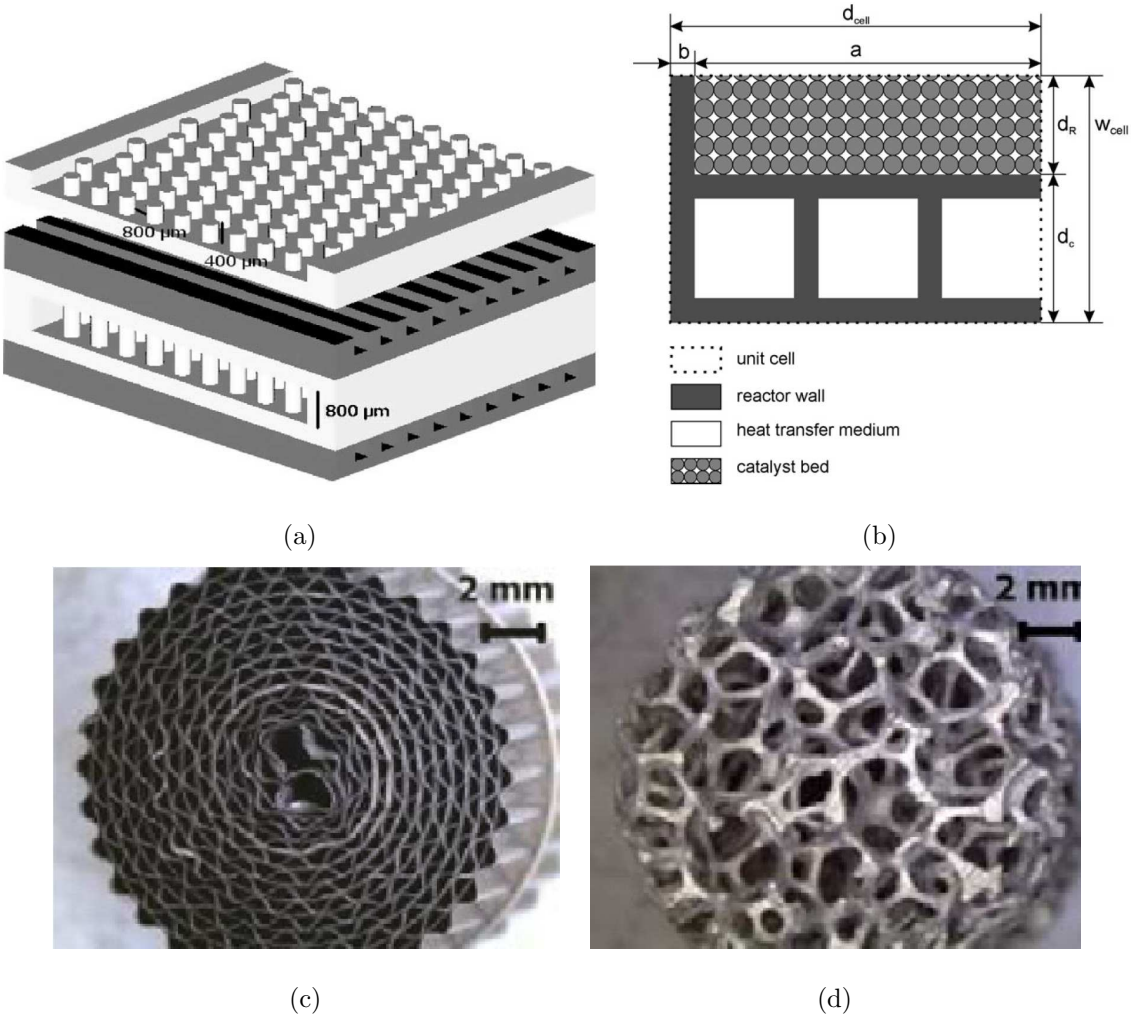

Figure 2.26. (a) Pillar structured catalyst foils and the cross-flow rectangular oil channels [227] (b) Milli-structured fixed-bed slit reactor [226] (c) Micromonolith (FeCrAlY) and (d) Foam (aluminum) reactors [228].

The dimensions of these channels and the walls could be chosen independently, which offered degrees of freedom for reactor optimization and maximization of the catalyst inventory. A larger slit width for the catalyst bed d_R resulted in higher ratio of catalyst and reactor volume while on the other hand the radial temperature gradient increased as well. Almeida *et al.* [228] used several types of structured supports in the work: parallel channel monoliths, foams and a microchannels block. Homemade parallel channel monoliths consisting of 50 μm FeCrAlY sheets, corrugated using rollers, were fabricated. Monoliths (Figure 2.26c) were made by rolling around a spindle alternate flat and corrugated sheets. Aluminum foils (Figure 2.26d) were cut out from slabs by a

hollow drill with a diamond saw border. Both monoliths and foams were cylindrical. In order to improve the interaction between the Al_2O_3-based washcoat layer and the metallic supports, the surfaces of both monoliths and foams were modified. The monoliths were heat-treated in air to generate α-alumina whiskers whereas the foams were pretreated by anodization in 1.6M oxalic acid at 50°C for obtaining a rough alumina surface. All the structured reactors and catalysts shown in Figure 2.26 were compared with conventional fixed-bed reactors for production on the basis of syngas conversion, product (methane and C_{5+}) selectivities, temperature control and overall pressure drop, and were found to perform much better with regard to these criteria.

2.4.2.2. Modeling and Simulation Studies. Transport limitations inherent in the gas-liquid-solid phase reactions taking place during the FTS play a significant role in the product selectivity. For instance, strong exothermic effect in the synthesis process enhances methanation, and diffusion limitations on reactants or products control the chain growth and affects secondary reactions. Conventional lab reactor testing uses a microtubular fixed bed which still shows large exothermicity in a wide range of conditions, particularly at short residence times (< 1 s) and high temperatures (above 210°C). As an example, Cao and coworkers [229] simulated Fischer-Tropsch synthesis in a microtubular reactor with an i.d. of 4 mm on a Co-based catalyst at 210°C and 20 atm with a GHSV of 18000 h^{-1} ($H_2 : CO = 2.0$). Figure 2.27a shows the bed temperature profile in such a microtubular reactor by finite element modeling at an overall CO conversion of 62%. The temperature gradient shows local hot spots in the bed. The maximum temperature excursion can be as high as 29°C even at moderate synthesis conditions such as GHSV of 18000 h^{-1} and wall temperature of 210°C. In such cases, intrinsic catalyst activity is overestimated as the catalyst sees a high average temperature. When various catalyst compositions are investigated, performance differences could be masked by such temperature non-uniformity. In order to reduce such heat transfer resistances, bed dilution using inert materials with high thermal conductivity such as SiC is usually employed to mitigate temperature gradients. However, catalyst dilution may change the hydrodynamic behavior and cause a large pressure drop. In addition, the dilution introduces foreign materials and gives unnecessary trouble in

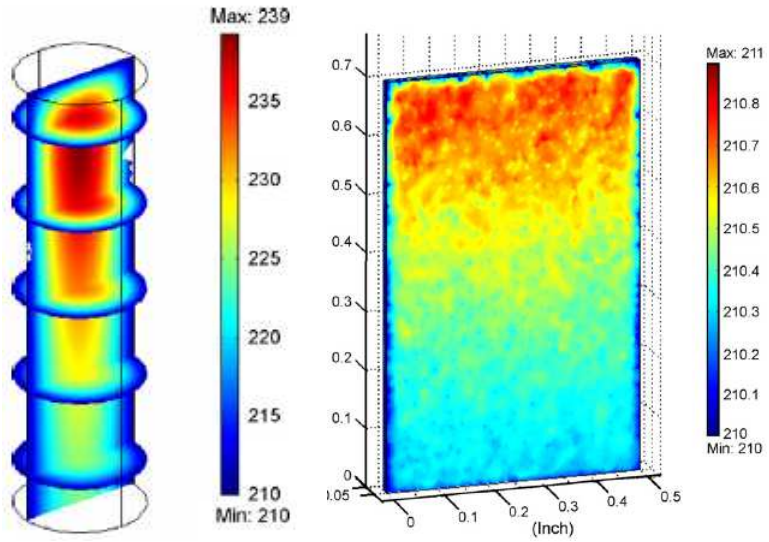

(a) (b)

Figure 2.27. (a) Temperature profiles in a conventional tubular reactor for FTS. Overall CO conversion is 62% (b) Temperature profiles in a microchannel reactor for FTS. Overall CO conversion is 50% (In both cases, $P = 20$ atm, reactor wall temperature at 210°C, $H_2 : CO = 2.0$, GHSV $= 18,000\ h^{-1}$) [229].

separating them from the spent catalysts for post-reaction characterization. The microchannel reactor approach provides a unique solution to such problems. For example, modeling results shown in Figure 2.27b indicate that the hot spots can be largely eliminated under the identical conditions as that used in the 4 mm microtubular reactor. The maximum temperature gradient was found to be less than 1°C in comparison to 29°C in the case of using microtubular reactor at the same wall temperature.

CFD analysis can help determine the optimal shape and geometry of reactor microchannels. This was demonstrated in the numerical and experimental work by Yu and coworkers [230] in which a novel microreactor with a network of omega-shaped microchannels was designed, fabricated and tested for enhanced chemical species mixing and reaction conversion for FTS. Fluidic and mixing properties of the omega channel reactor were investigated by means of CFD simulations. Also, a stochastic model describing particle transport in the axial direction was applied to characterize the residence time distribution or the cumulative probability of a particle exiting the mi-

croreactor over time. Both fluidic simulation and stochastic model approaches revealed the advantage of the omega-shaped microchannels as compared to straight or zig-zag-shaped microchannels (Figure 2.28).

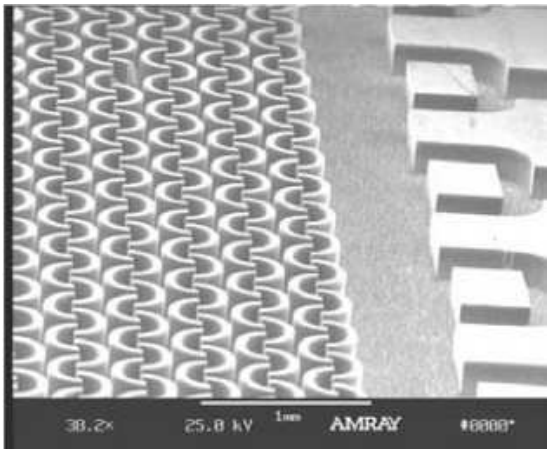

Figure 2.28. SEM image of an omega channel microreactor [230].

The so-called omega channel microreactor consisted of a network of omega-shaped channels, and these channels were integrated with one another to simulate a cellular structure of honeycombs. The omega configuration produced flow obstables that led to high velocities. The obstacles formed by the omega channel force the flow to commingle back and forth between the center and the channel wall. The velocity of flow in the omega channel varied significantly from point to point and its variance was large. It was shown that the velocity variance in the microreactor with omega channels was larger than that with straight or zig-zag channels. The flow in the straight and zig-zag channels was almost laminar and the velocity was about 200 μm per second. On the other hand, flow velocity in the omega channels varied from 200 to 700 μm per second. This played an important role in the enhancement of mixing and increased residence time.

Heat transfer phenomenon during low-temperature FTS was studied by Arzamendi *et al.* [231] in a microchannel reactor with the aid of three-dimensional CFD simulations. The microreactor consisted of 80 square microchannels of 1 mm side-length for syngas in cross flow with the coolant water. The syngas (H_2 : CO = 2.0)

GHSV was in the range of $5000 - 30000\,\mathrm{h}^{-1}$ at standard temperature and pressure. The thermal effect of the exothermic FTS was simulated as a uniform heat source in the catalytic layers. For a specified rate of CO flow ($F_{\mathrm{CO},0}\,\mathrm{mol\,s}^{-1}$) and CO conversion at the reactor outlet (X_{CO}), the heat generated ($\dot{Q}_g$) by the FTS was calculated using

$$\dot{Q}_g\ \left[\mathrm{kW\,m}^{-2}\right] = \frac{F_{\mathrm{CO},0} X_{\mathrm{CO}}\,(-\Delta H_R)}{40 \times (4 \times 1 \times 21) \times 10^{-6}} = 49107 F_{\mathrm{CO},0} X_{\mathrm{CO}} \tag{2.42}$$

The results indicated that when processing up to $30000\,\mathrm{h}^{-1}$ of syngas, FTS operation in the temperature range of $483 - 513\,\mathrm{K}$ could be achieved by setting the pressure between 5 and 35 atm, and adjusting the cooling water flow rate in the range $0.25 - 250\,\mathrm{g\,min}^{-1}$. Due to the importance of buoyancy effects, very low steam content (1%) in the coolant stream was sufficient to improve the heat exchange efficiency.

Hydrodynamics plays an important role in the FT synthesis because of the liquid products formation and their interaction with the syngas and also with the gaseous products. Derevich *et al.* [232] developed a theoretical hydrodynamics model in a microchannel reactor that considered the downward movement of liquid and gaseous products in annular flow regime. A geometry that was comprised of irregular internal walls coated with a cobalt-based catalyst was investigated using cylindrical coordinates. System of equations of two-phase hydrodynamics was obtained on the basis of generalized equations for mass continuity and momentum conservation in each phase. Moreover, a stable algorithm for calculation of the thermodynamic equilibrium of the gas-liquid phases was proposed. The hydrodynamics was modeled by considering the conjugation of gas and liquid flows, and also variations of mass fractions and thermophysical properties of liquid and gaseous products along the microchannel. One of the analysis results of this work that presented a complete hydrodynamics investigation of FTS in a microchannel for the first time was that the pressure gradient depended strongly on the roughness of the microchannel walls that varied with the catalyst coating shape. Another finding was that inertial and capillary forces had a strong influence

on the shape of the liquid-gas interface. The liquid film thickness also depended weakly on the syngas flow rate.

2.5. Integrated Reactor/Heat Exchanger Systems

Improved heat utilization is essential to the design of efficient chemical process equipments at macro- and microscales. Extensive academic and industrial research is being conducted on integration methods of reaction and heat exchange systems. Focus of many works has been the coupling of an exothermic combustion reaction with an endothermic synthesis reaction such that both reactions either take place in *adjacent* channels (*spatially segregated*), whether they be of conventional fixed-bed or of microchannel type, or in the same compartment (*spatially integrated*), and heat is exchanged simultaneously. This approach has pros and cons, the latter of which arise mainly from heat transfer limitations due to the nature of the walls between the compartments and the nature of the catalysts. The more recently realized approach of *decoupling* reaction and heat transfer processes claims to solve this issue, but it also poses certain design problems in the construction stage. The literature survey aims at reviewing recent experimental and computer-based works on integration of reaction and heat exchange systems by means of coupling and decoupling, thereby providing an outlook to the contents of the work performed by the author.

2.5.1. Coupled Reaction/Heat Exchange Systems

Thermal coupling between an exothermic (e.g. combustion) and an endothermic (e.g. steam reforming) reaction can be achieved in a number of ways. One strategy is to use "direct" coupling where both reactions are carried out simultaneously in the same reactor using a suitable bifunctional catalyst or a pair of different catalysts [70]. This idea has been limited to "one-fuel" systems on account of the complexity of the process. A second strategy is "temporal" coupling of the two reactions, where the exothermic and endothermic reactions are alternately carried out in the same reaction chamber [158]. Direct and temporal coupling are classified under the term "spatial integration". The final heat integration strategy involves "spatial segregation". In

Table 2.12. Summary of literature investigations on spatially coupled reactors.

Conditions	**Reactor dimensions**	**Type of study (Model/Experiments)**	**Reference**
CH_4 steam reforming (WGS and reverse methanation) on Ni-Mg-Al_2O_3 coupled with CH_4 oxidation (homogeneous and catalytic)	$L = 50\,\text{cm}$	1-D steady-state dispersion model	[233]
CH_4 reforming coupled with CH_4 oxidation (using proprietary catalysts)	$L = 25\,\text{cm}$	experiments $T_{\text{in}} = 653$ K (reformer) $T_{\text{in}} = 803$ K (combustor)	[234]
C_2H_6 dehydrogenation on Pd coupled with CH_4 combustion on Pd	$L = 1\,\text{m}$ $W = 2\,\text{mm}$ $T = 2\,\text{mm}$ $H = 1\,\text{m}$	2D steady-state dispersion model $T_{\text{in}} = 923$ K	[235]
CH_4 steam reforming (WGS and reverse methanation) on Ni-MgO-Al_2O_3 coupled with CH_4 oxidation on Pt-Al_2O_3	$L = 40\,\text{cm}$ (bench scale) $L = 12\,\text{m}$ (industrial)	experiments and 1-D steady-state model $T_{\text{in}} = 650 - 800$ K	[158]
CH_4 steam reforming coupled with CH_4 catalytic oxidation (homogeneous and catalytic)	$L = 1\,\text{m}$	1-D steady-state model	[236]
CH_3OH steam reforming on Cu/ZnO coupled with CH_3OH combustion on cobalt oxide	$L = 3\,\text{cm}$ $W = 0.32\,\text{mm}$ $T = 0.2\,\text{mm}$	experiments	[10]
C_4H_{10} combustion on Pt-Al_2O_3 coupled with NH_3 cracking on Ir-Al_2O_3	$L = 3\,\text{cm}$ $W = 200\,\mu\text{m}$ $H = 500\,\mu\text{m}$ $T = 2\,\mu\text{m}$	experiments in a suspended tube reactor and heat transfer modeling	[237]

this approach, the exothermic and endothermic reactions are carried out in different chambers that are separated by a heat-conducting medium. Spatial segregation allows an independent choice of fuel, of catalysts and of reaction conditions for the exothermic and endothermic reactions. This flexibility in conjunction with the small feature size of a microdevice, which facilitates heat transfer, renders this approach suitable for microdevices.

A summary of investigations on spatially segregated multifunctional reactors is presented in Table 2.12. Several issues are worth pointing out. Energy has usually been generated via catalytic combustion. Most of the works have focused on macroscale. Additionally, heat- and mass-transfer correlations have often been employed in one-dimensional (1-D) models to capture the underlying physics. L stands for the length, W and D are the width or inner diameter of the reactor channel, T is the wall thickness and H the height.

2.5.1.1. Parallel microchannel reactors. Microchannel reactors offer opportunities for the development of compact fuel processors for PEMFCs. In their work, Ryi and coworkers [13] proposed the design of a microdevice for the methane steam reforming with hydrogen catalytic combustion and investigated its performance at various operating conditions. Novel flow channels on reformer sheets and microholes on combustor sheet to inhibit the hot spot formation, which takes place at the reactor entrance.

The designed microchannel reactor consisted of a cover plate, a base plate and 25 sets (50 plates) of microchannel sheets. Figure 2.29 shows the schematic representation of the microchannel sheets and flow paths. Inconel plate was used to fabricate the microchannel sheets and stainless steel for cover and base plates. Microchannels were patterned on a plate using a wet chemical etching method. The cover plate had three conduits and the base plate, two conduits, which act as flow inlet and outlet. Each microchannel sheet had two conduits and two flow distribution chambers for uniform distribution. Each sheet had 22 channels with the following dimensions: 500 μm width, 250 μm depth and 17 mm length. Combustion and reforming sheets were stacked

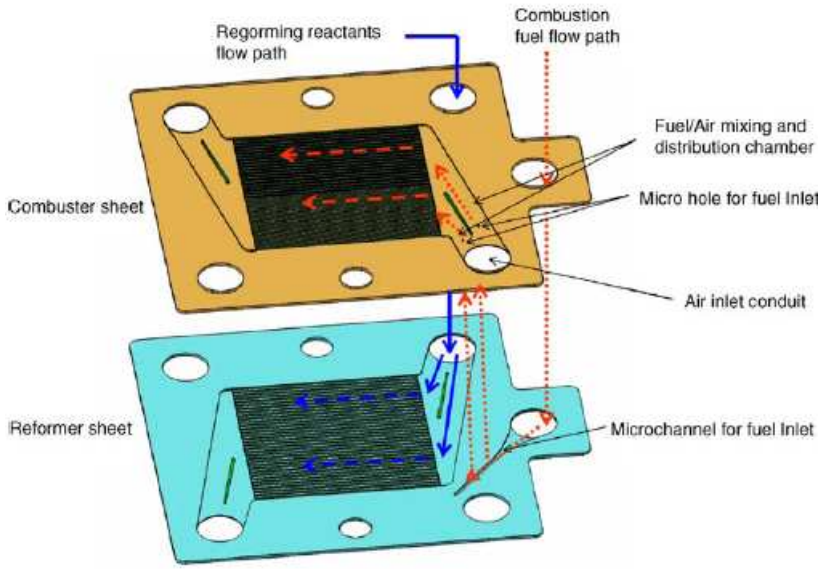

Figure 2.29. Schematic representation of the novel microchannel sheets and flow paths. Red dotted line: fuel for combustion flow path; red dashed line: fuel/air mixture and combustion off-gas flow path; blue solid line: reforming reactants flow path; blue dashed line: reformate flow path [13].

alternately and then bonded by a brazing method. The dimensions of the combustor and reformer unit excluding fittings were about 40 mm × 40 mm × 30 mm. Pt-Sn/Al_2O_3 catalyst for hydrogen combustion and Rh-Mg/Al_2O_3 catalyst for methane steam reforming were prepared by alumina washcoating followed by the subsequent impregnation of Pt-Sn and Rh-Mg solution in the combustor and reformer sheets, respectively.

Initial flow rates of the hydrogen and air were 3.8 and 9.9 × 10^{-3} mol min^{-1}, respectively. At the same time, N_2 of 4.9 × 10^{-3} mol min^{-1} and steam of 1.5 × 10^{-2} mol min^{-1} were introduced into the reformer. Water was introduced when the temperature of the reformer reached 120°C. When the combustor outlet temperature reached 800°C, hydrogen and air flow rates were increased to 4.2 and 1.1 × 10^{-2} mol min^{-1}, respectively. Then methane of 4.9 × 10^{-3} mol min^{-1} was introduced for methane steam reforming instead of N_2 when the reformer outlet temperature was 750°C. Out of numerous results, the most important ones were that the reformer

generated hydrogen for a PEM fuel cell output of 26 W, and that it took about 2.5 h for start-up of the fuel processor.

Petrachi *et al.* [12] investigated, using a 2D mathematical model, the coupling dynamics of *iso*-octane, steam reforming and catalytic combustion in a multifunctional reactor consisting of one combustion and one reforming channel separated by a steel wall. They also considered the flow of flue gas from an external burner as the heat source for steam reforming and reported that the latter configuration was more advantageous for use in on-board applications due to shorter start-up times.

Deshmukh and Vlachos [15] numerically investigated counter-current coupling of combustor/reformer microdevices for hydrogen production. They used two-dimensional CFD simulations to study spatially coupled, multifunctional microchemical devices. In particular, coupling between homogeneous propane combustion and catalytic ammonia decomposition on a Ru catalyst was studied in a microdevice consisting of alternating combustion and decomposition channels as a function of flow rate and materials conductivity in the counter-current flow configuration. A premixed, stoichiometric propane/air mixture was fed to the inlet of the combustion channel. The homogeneous propane combustion was modeled as an irreversible, one-step reaction

$$\mathrm{C_3H_8} + 5\mathrm{O_2} \rightarrow 3\mathrm{CO_2} + 4\mathrm{H_2O} \tag{2.43}$$

with the rate expression

$$\begin{aligned} \sigma_{\mathrm{C_3H_8}} \left[\mathrm{kmol\,m^{-3}\,s^{-1}}\right] = 4.836\times \\ 10^9 \exp\left(-\frac{1.256\times 10^8\ \mathrm{J\,kmol^{-1}}}{RT}\right) C_{\mathrm{C_3H_8}}^{0.1} C_{\mathrm{O_2}}^{1.65} \end{aligned} \tag{2.44}$$

where the concentrations were in $\mathrm{kmol\,m^{-3}}$.

Pure ammonia flowed counter-currently into the reforming channel, which had Ru catalyst deposited on the channel walls. The ammonia decomposition reaction occurred at the catalytic channel wall resulting in hydrogen production

$$2NH_3 \rightarrow N_2 + 3H_2 \tag{2.45}$$

The following reduced rate expression derived using a microkinetic model of elementary-like reaction steps was used to calculate the conversion of ammonia

$$\sigma_{NH_3} = \frac{-2\left(k_4\omega^2 - k_3 P_{N_2}\right)}{\left(1 + \frac{k_{11}}{k_{12}} P_{NH_3} + \sqrt{\frac{k_1}{k_2} P_{H_2}} + \omega\right)^2} \tag{2.46}$$

where

$$\omega = \sqrt{\frac{k_3}{k_4} P_{H_2} + \frac{k_2}{k_1} \frac{k_7 k_9 k_{11}}{2 k_4 k_{10} k_{12}} P_{NH_3} P_{H_2}^{-0.5}}$$

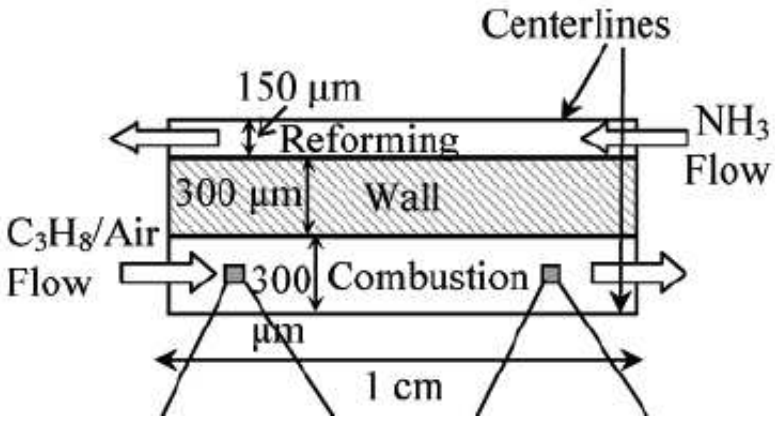

Figure 2.30. Schematic of a multifunctional microreformer/microcombustor device [15].

The simulated microreactor was a parallel plate reactor with alternating combustion and reforming channels separated by walls, as shown schematically in Figure 2.30. The device was 1 cm long. The combustion channel was 600 μm wide, the reforming channel 300 μm wide, and the wall separating the two channels was 300 μm thick. The

height of the channel was typically in the order of $5 - 10$ mm. A 2D representation of the system was reasonable because of the large aspect ratio. The alternating channel configuration allowed solving only half of each channel due to symmetry. It was found that the high temperatures generated via homogeneous combustion led to high conversions in short contact times and thus to compact devices. Sufficiently high ammonia flow rates served a dual purpose by lowering device temperatures and enabling more production of hydrogen. It was also shown that device operation was limited only to high conductivity materials and fast ammonia flows.

A turning point in integrated microchannel reactor/heat exchanger technology was the development and testing of a complete fuel processor, which was designed to supply a 5-kW fuel cell with purified reformate applying *iso*-octane as fuel [243]. *iso*-Octane had been chosen as a model substance for gasoline. The reactors were built as cross-flow plate heat-exchangers. It was composed of the autothermal reformer reactor (ATR), a heat exchanger for cooling the reformate downstream the ATR, a cross-flow cooled high-temperature water-gas shift reactor, a low-temperature water-gas shift reactor and a PrOx reactor again cooled by a cross-flow arrangement. The autothermal reformer was composed of 200 micro-structured metal foils of 400 μm thickness carrying a total of 25000 channels each 400 μm wide and 250 μm deep. A 1 wt% Rh on alumina sol carrier catalyst was coated onto the micro-structured plates, which were then sealed by laser welding and put into a stainless steel housing to assure mechanical stability at the maximum operating temperature of 800°C. The total amount of catalyst incorporated into the reactor was 19.8 g, which corresponds to 0.2 g of the active Rh species. The reactor was operated at a WHSV of $330\,\mathrm{Ndm^3\,g_{cat}^{-1}\,h^{-1}}$. Analysis of the outlet streams showed that near complete conversion of *iso*-octane was achieved. Besides the desired and expected products CO, CO_2, H_2 and CH_4, also small amounts of ethylene and propylene were found in the reformer product. A degradation of the reactor performance was not observed over the total operation time of 20 h.

Summary of select and recent modeling works in the literature on multifunctional microchannel reactors that comprise spatially segregated combustion and reforming reactions running over pertinent catalysts is given in Table 2.13.

Table 2.13. Summary of works on spatially segregated microchannel reactors for coupling of exo- and endothermic reactions.

Reaction/ Catalyst	**Coupled with/ Catalyst**	**Flow configuration**	**Channel dimensions**	**Temperature range**	**Model remarks**	**Reference**
CH_3OH steam reforming Pd-ZnO/Al_2O_3	CH_3OH combustion ——	parallel annular flow	$V = 0.3\,cm^3$	300°C (inlet)	3D CFD	[238]
C_3H_8 combustion homogeneous	NH_3 decomposition Ru-based	co-current counter-current	$L = 1\,cm$ $H = 0.6\,mm$ (COMB) $H = 0.3\,mm$ (DECOMP)	300 K (inlet)	2D CFD	[14, 15]
CH_4 steam reforming Rh-MgO/Al_2O_3	H_2 combustion Pd/Al_2O_3	cross-flow	$L = 11.4\,mm$ $W = 10.7\,mm$ $H = 0.356\,mm$	745 − 810°C	2D CFD	[187]
CH_4 steam reforming Ni-based	CH_4 combustion Pd/Al_2O_3	co-current, cross-flow	$L = 20\,mm$ $W = H = 0.35 - 2.80\,mm$	600°C (inlet)	3D CFD	[239, 240]
CH_4 steam reforming Rh-based	CH_4 combustion Pt-based	co-current	$L = 5 - 10\,cm$ $H = 0.2\,mm$ (SR) $H = 0.3\,mm$ (COMB) $T = 0.75\,mm$	400 K (SR inlet) 340 K (COMB inlet)	2D CFD	[20, 21]
CH_3OH steam reforming Cu-based	CH_3OH combustion Pd-based	co-current	$L = 10\,cm$ $H = 0.2\,mm$ (SR) $H = 0.3\,mm$ (COMB) $T = 0.75\,mm$	400 K (SR inlet) 340 K (COMB inlet)	2D CFD	[21]
CH_3OH steam reforming Cu-ZnO/Al_2O_3	CH_3OH combustion Cu-ZnO/Al_2O_3	co-current, cross-flow	$L = 20\,mm$ $W = H = 0.70\,mm$	150°C (SR inlet) 200°C (COMB inlet)	3D CFD	[239]
CH_4 steam reforming Pt/Al_2O_3	CH_4 combustion Rh/Al_2O_3	co-current	$L = 10\,mm$ $W = 10\,mm$ $H = 0.5\,mm$ $T = 1\,mm$	800°C (inlet)	2D CFD	[241]
$C_{16}H_{34}$ steam reforming Rh-Ni/Al_2O_3	$C_{16}H_{34}$ combustion Rh-Ni/Al_2O_3	co-current	$V = 0.615\,cm^3$	800°C (SR inlet) 377°C (COMB inlet)	Series of CSTRs	[191]
CH_3OH steam reforming Cu/ZrO_2/CeO_2	CH_3OH combustion Pt/Al_2O_3	co-current, serpentine	$L = 4\,mm$ $W = 10\,mm$ $W = H = 0.45\,mm$ $T = 0.45\,mm$	120°C (inlet)	3D CFD	[214, 242]
Fischer-Tropsch synthesis Co-based	Water (coolant) ——	cross-flow	$L = 21\,mm$ $W = H = 1.00\,mm$	250°C (Syngas inlet)	3D CFD	[231]
C_2H_5OH steam reforming Rh/CeO_2/Al_2O_3	Hot flue gas	co-current	$L = 60\,mm$ $W = 0.50\,mm$ $H = 0.40\,mm$ $T = 0.30\,mm$	450 − 550°C (inlet)	2D CFD	[90]

2.5.2. Decoupled Reaction/Heat Exchange Systems

The benefits of process integration by decoupling of the reaction and heat exchange systems have been demonstrated by Seris and coworkers [24, 25] at the University of Sydney, Australia and Heatric Ltd. (UK). They have designed and operated a scaleable, microstructured plant for syngas production by methane steam reforming. After laying out the reasons why such a technology is necessary, they describe the plant design. The plant is composed of four main modules:

- pre-reforming module including the high-temperature water-gas shift reactor
- reforming and combustion module
- low temperature shift reactor
- steam drum

The only heat input to the process is provided by the catalytic combustion reactions in the reforming and combustion module. A highly complex network of printed circuit heat exchangers (PCHEs) distributes the heat to the other parts of the process (pre-reformer module, steam generation, pre-heat of the reactants).

Printed circuit heat exchangers are compact, industrial-scale heat exchangers widely employed under extreme processing conditions, including highly corrosive fluids at high temperatures and pressures. PCHEs are single- material (usually metal) matrices formed by diffusion bonding together plates into which fluid flow passages have been formed by photochemical machining. Complex fluid circuitry is readily implemented with this technique, with characteristic passage dimensions in the range $100 - 2000$ μm as dictated by the cleanliness of the fluids and allowable pressure drops [37, 43].

The design basis of the steam reforming pilot plant, designed for a PEMFC, is taken to be

- 2 bar (abs) process side pressure, atmospheric combustion side pressure
- low-CO hydrogen required

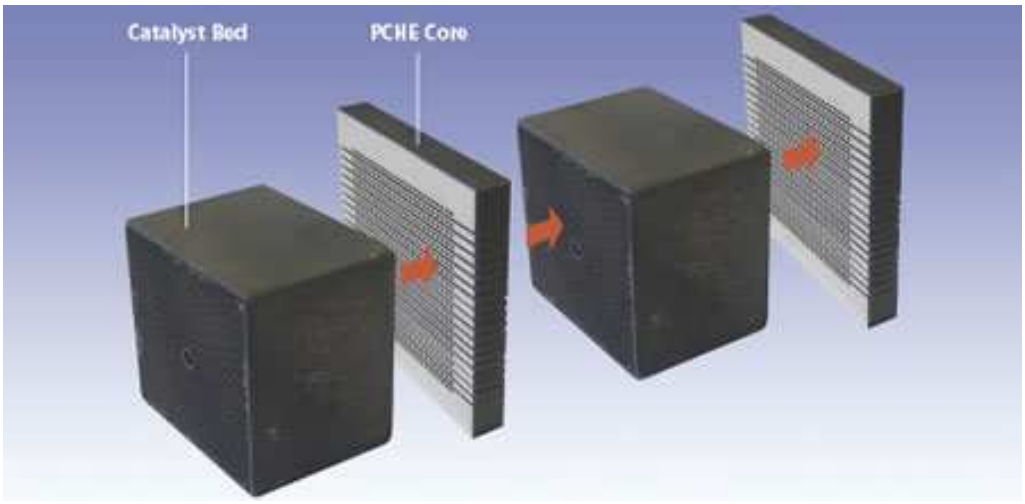

Figure 2.31. Assembly of adiabatic beds and PCHEs (www.heatric.com).

- typical levels of hydrogen conversion ($\sim 78\%$) in the fuel cell

Methane fed to the module has to be sulphur-free in order to prevent catalyst deactivation. Crushed catalyst pellets or monoliths are used in the reactors for ease of catalyst deployment. Material of construction is austenitic stainless steel for testing purposes. The base shape of the pre-reformer and reformer modules is a rectangular block, similar to the base shape of the commercialized PCHE (Figure 2.31). The scale-up of PCHEs can be achieved on three levels by multiplication of

- the number of channels (or size of the plate)
- the number of plates, stacked to create a block
- the number of blocks, combined under common headers

This linear scale-up on three levels allows a great flexibility in the size of the final plant. This compact geometry offers two advantages:

- Easy scale-up by multiplication. The size of the local plant can be matched to the local demand in a single step.
- Low cost manufacturing through the production of the same base unit.

In conventional fixed-bed tubular reactors, maintaining the radial and axial temperature profiles within acceptable bounds require the striking of a delicate balance between reaction and heat transfer within the tubes, heat transfer to the outside of the tubes, and pressure drop. One outcome of this balance is that tubular reformers are bulky since relatively large catalyst particles with low effectiveness are employed. Xu and Froment [134, 135] calculate an effectiveness of the active catalyst of less than 3% for the reforming reactions, with the active catalyst applied to only the outer 2 mm of the catalyst particles they considered. The implication is that the reforming catalyst bed could be two orders of magnitude smaller if effectiveness could be held near 1 simply by the use of small catalyst particles, without any improvement of intrinsic activity. Small particles are incompatible with tubular reformers, however, because pressure drop constraints would dictate the use of many parallel, short tubes.

There is the possibility of applying a thin layer of reforming catalyst onto the surfaces of micro-reactors. There is no doubt that PCHE cores would constitute an excellent matrix for such an approach. However, whilst this technique has great promise in appropriate circumstances, certain difficulties remain, including

- adhesion of the catalyst to the metal substrate
- difficulties associated with catalyst life and replacement
- coupling of the heat transfer and catalyst areas–generally requiring very high activity catalyst if heat exchange surface is to be kept as small as possible

An alternative approach, put into practice in the pilot plant, is the use of *multiple adiabatic beds* (**MAB**s), with heat interchangers between the beds. This is quite a traditional approach to temperature control in chemical reactions [244,245], but combined with PCHEs certain advantages arise:

- The flexibility of PCHEs allows them to be configured cost-effectively as panels between the beds, avoiding interconnecting piping and the need to redistribute the reactants to each bed after heat exchange. Thus many stages of adiabatic reaction and heat exchange can be employed, making the approach applicable to

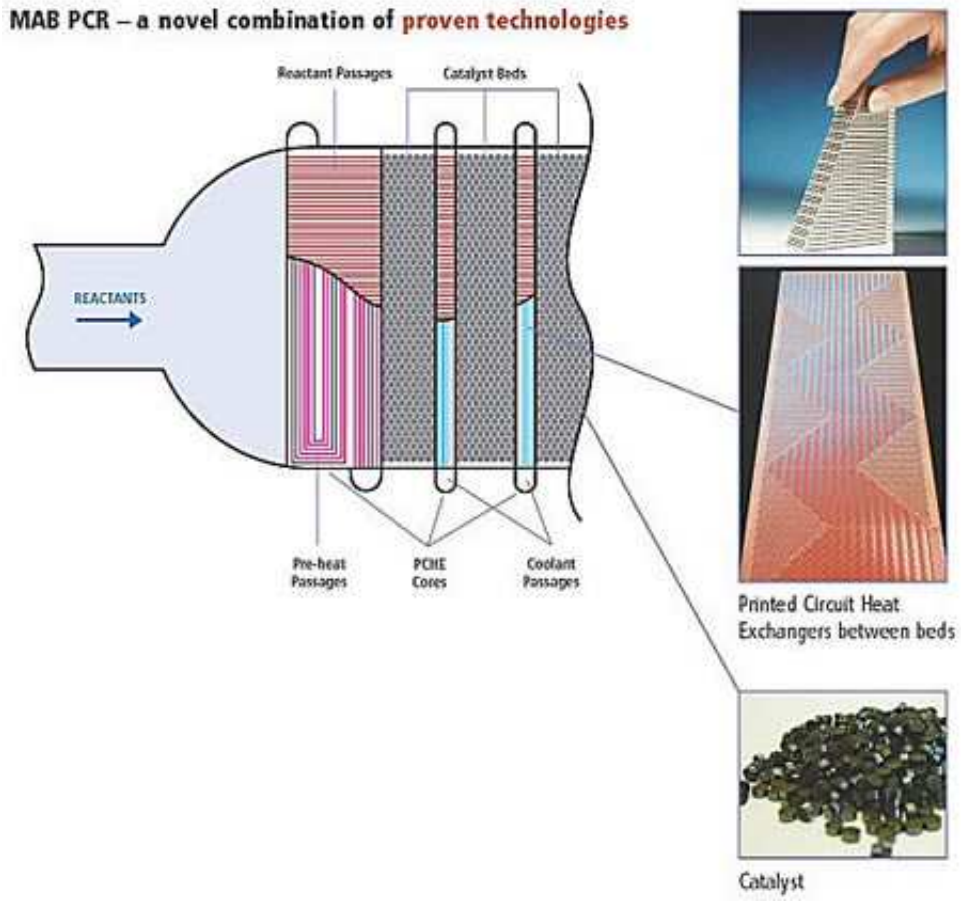

Figure 2.32. Schematic representation of catalyst bed and PCHE arrangement (www.heatric.com)

high heat load reactions such as reforming. A saw-tooth temperature pattern will result, with the size of the teeth inversely proportional to the number of them, so that temperatures can be held between any required bounds (Figure 2.32). Overall isothermal, ascending or descending temperature profiles can be applied to the reaction.

- The catalyst beds can be presented to the reactants with a short flow path and large face area, allowing the use of small catalyst particles with high effectiveness.
- Conventional, proven catalyst forms can be employed in configurations which allow ready replacement of the catalyst in accessible, "large" slots. The only variation which might be preferred for the catalyst is smaller particle sizes than for tubular reactors to assist process intensification. Crushing of conventional

sizes is a makeshift option. In many cases, a preferred catalyst form would be coated ceramic monolith, in order to minimize pressure drop. In the present case, the combustion, water-gas shift and reforming reactions are carried out over monolith catalyst with low pressure drop (e.g. 0.02 bar for the overall pressure drop in the combustion air stream). Crushed pellets ($1 - 2$ mm) employs higher but still acceptable pressure drops.

- The heat transfer volume and the catalyst volume in the reactor are decoupled. Depending on the heat loads and heat transfer fluid temperature, the ratio between the two volumes can be varied at will.
- Flow patterns within the PCHE panels can be configured to produce flat temperature profiles in the reactants avoiding hot spots.
- Periodic injection of fresh reactants is readily incorporated, thereby allowing the extent of exothermic reactions to be safely limited in each stage.

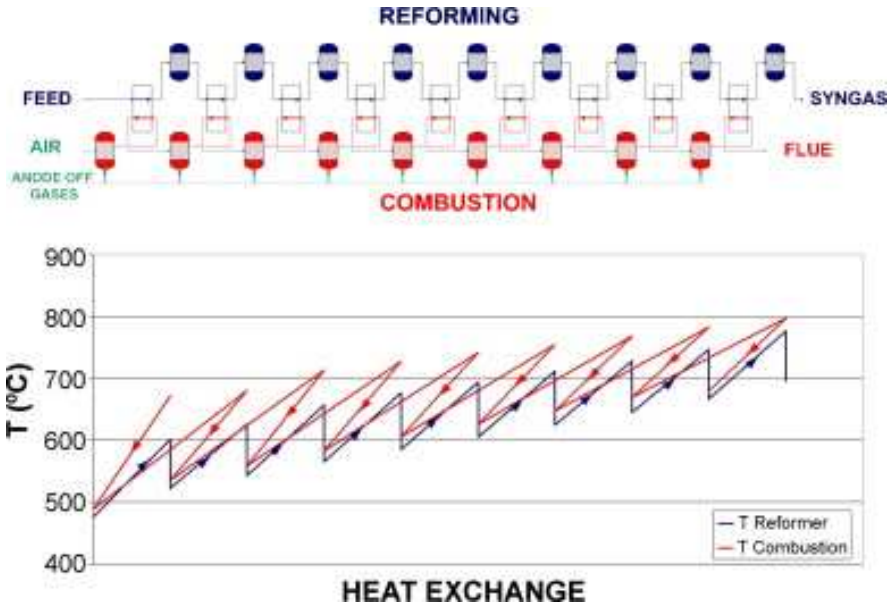

Figure 2.33. Saw-tooth pattern for the temperature profile in the reforming and combustion module [24]

In the present test unit, both the steam reforming reaction and the combustion reaction supplying heat to the reformer are carried out using multiple adiabatic beds. Figure 2.33 describes the combustion and reforming temperature profiles arising. The low pressure (200 kPa) in the reformer means that satisfactory conversions of methane

(90%) are achievable at much lower temperatures than in higher-pressure industrial reformers operating.

The plant consisting of the above-mentioned cascade of monolith reactors and PCHEs produced a stream containing 80% hydrogen at a rate of 5 $Nm^3\,h^{-1}$. The process intensity is approximately one order of magnitude greater than is achievable in conventional large-scale reformers and there are no efficiency penalties in achieving this because of process intensification. The PCHE construction technique means that the system is scaleable and provides the basis for hydrogen production over a wide range of applications and market sizes.

3. EXPERIMENTAL

3.1. Materials

3.1.1. Chemicals

All the chemicals used for catalyst preparation are presented in Table 3.1.

Table 3.1. Chemicals used for catalyst synthesis.

Chemicals	**Specification**	**Source**	**Molecular weight**
Nickel nitrate	$Ni(NO_3)_2 \cdot 6H_2O$ extra pure	Sigma-Aldrich	290.81
Rhodium(III) nitrate	$Rh(NO_3)_3$ $\sim$ 10wt%Rh in $>$ 5wt%nitric acid	Sigma-Aldrich	288.92
Ruthenium(III) nitrosyl nitrate	$Ru(NO)(NO_3)_x(OH)_y$ 1.5wt%Ru in dilute nitric acid	Sigma-Aldrich	318.10
Tetraammineplatinum(II) nitrate	$[Pt(NH_3)_4](NO_3)_2$ 50.4wt%Pt	Sigma-Aldrich	387.22
Gamma alumina	$\gamma - Al_2O_3$ $225\,m^2\,g^{-1}$	Alfa Aesar	——
Gamma alumina (3μm)	$\gamma - Al_2O_3$ $120 - 190\,m^2\,g^{-1}$	Merck	——
FeCrAlY	FeCrAlY sheets	Goodfellow Cambridge, Ltd.	——

3.1.2. Gases and Liquids

All of the cylinder gases used in this research were supplied by Linde Turkey, Istanbul. Table 3.2 lists the specification and application of each gas. Deionized water with conductivity less than $0.1\,\mu S\,cm^{-1}$ is used in all experiments.

Table 3.2. Specifications and applications of the gases used.

Gas	**Specification**	**Application**
Argon	99.999% (Linde)	GC carrier gas
Helium	99.999% (Linde)	GC carrier gas
Nitrogen	99.998% (Linde)	Inert
Hydrogen	99.99% (Linde)	GC calibration, reduction
Carbon monoxide	99.999% (Linde)	GC calibration
Carbon dioxide	99.999% (Linde)	GC calibration
Dry air	78.4% N_2 + 21.5% O_2 (Linde)	GC calibration, reactant
Methane	99.9% (Linde)	GC calibration, reactant

3.2. Experimental Systems

The systems used in this work can be classified into four groups:

- **Catalyst Preparation System**: the setup used for synthesizing the catalysts by the incipient-to-wetness impregnation technique
- **Catalyst Characterization Systems**: X-ray diffraction (XRD) and scanning electron microscopy (SEM) for crystal structure and surface morphology of the catalysts
- **Catalytic Reaction System**: the assembly, which is used for assessing catalytic activity/selectivity, consists of gas and liquid flow control units, electric heat tracing, reaction chamber, and feed/product sampling sections
- **Product Analysis System**: gas chromatograph (GC) for quantitative determination of the composition of the feed and product streams

3.2.1. Catalyst Preparation System

The system used for catalyst synthesis by incipient-to-wetness impregnation method (Figure 3.1) consists of a Retsch UR1 ultrasonic mixer, a vacuum pump, a Büchner flask and a Masterflex computerized-drive peristaltic pump.

3.2.2. Catalyst Characterization Systems

The structural analyses of the catalyst samples were carried out at Boğaziçi University Advanced Technologies R&D Center through Backscattering Electron-Scanning Electron Microscopy (**BSE-SEM**) and Energy Dispersive X-ray Analysis (**EDX**) using a Philips XL30 ESEM-FEG unit, and through X-ray Diffraction (**XRD**) using a Rigaku D/MAX-Ultima+ equipment.

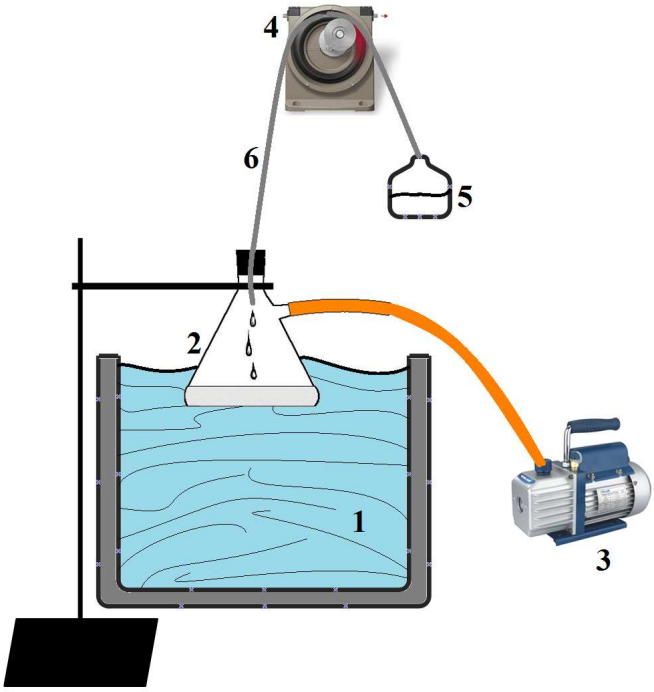

Figure 3.1. Schematic diagram of the impregnation system. 1. Ultrasonic mixer, 2. Büchner flask, 3. Vacuum pump, 4. Peristaltic pump, 5. Aqueous catalyst solution, 6. Silicon tubing (1.6 mm ID) [246].

3.2.3. Catalytic Reaction System

The in-house reaction system was designed and constructed at the Department of Chemical Engineering. It consists of three characteristic sections:

- Feed section
- Reaction section
- Product analysis section

The feed section consists of mass flow control units, 1/4", 1/8" and 1/16" stainless steel tubes and fittings for precise feeding of water and the gases. Gases in pressurized cylinders are regulated in gas flow regulators (items 1 in Figure 3.2). Flow rates of the gases are measured and controlled by Bronkhorst F-201CV series digital mass flow

controllers (items 2 in Figure 3.2) whose calibration curves are given in Appendix A. On-off valves (items 3 in Figure 3.2) are placed downstream the line to prevent possible back-pressure fluctuations. Using a different line for each gas makes it possible to meter their flow independently and adjust the desired feed ratios.

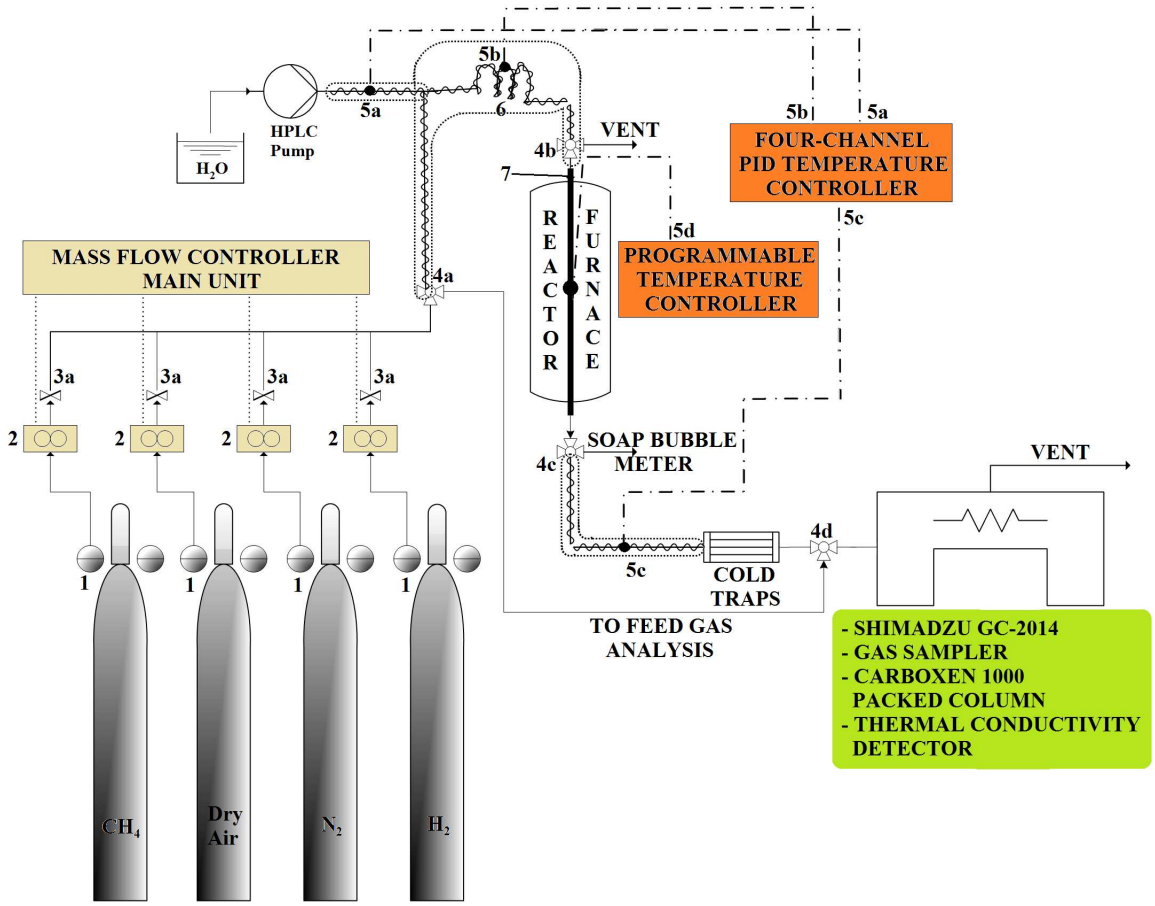

Figure 3.2. Schematic diagram of the reaction system. 1. Gas regulators, 2. Mass flow controllers, 3. On-off valves, 4. Three-way valves, 5. Thermocouple locations, 6. Mixing zone, 7. Quartz tube.

Shimadzu LC-20AD HPLC pump is used to feed the system with constant and pulse-free flow of deionized water. Water is vaporized before mixing with the gases in the 1/16" tube, which is kept at 120±3°C using a 1 m heating tape, a 16-gauge wire K-type sheathed thermocouple (at 5a in Figure 3.2) and a four-channel temperature controller. Steam and the gas mixture are then allowed to mix (in zone 6 in Figure 3.2) in order to introduce a homogeneous mixture into the reactor. Temperature of the

mixing zone, which is also heat traced, is measured and controlled by a thermocouple (at 5b in Figure 3.2) and the temperature controller.

Installation of three-way valves are necessary for diverting the flow upon need. To perform a feed gas analysis, i.e. to determine the composition of the reactive stream prior to reaction, the gases should be directed to the gas chromatograph, which is undertaken by Valves 4a and 4d in Figure 3.2). Valve 4b switches the flow between the reactor line and the vent. The mixture is vented off for 30 min so that steady and well-mixed flow is established before the reaction is initiated. The reaction section is described in detail in Section 3.4.

In order to prevent condensation of water vapor present in the product stream leaving the reactor, the line between Valve 4c and the cold traps are kept at 120°C. The soap bubble meter is necessary for gas calibration before system testing and for monitoring the flow during the reaction tests. Two salt-ice cold traps held in Dewar flasks are placed before the GC unit to remove water vapor in the product mixture, which may be detrimental for the Carboxen column. Details concerning product analysis using the GC are given in the following section.

3.2.4. Product Analysis System

The product stream contains–on a dry basis–unconverted methane, hydrogen, carbon monoxide and dioxide, inert nitrogen, and probably other light hydrocarbons such as ethane and propane. Shimadzu GC-2014 gas chromatograph, equipped with a Carboxen 1000 packed column and a thermal conductivity detector (TCD), is able to separate and quantify all the said species.

Before proceeding with the reaction tests, the gas chromatograph is calibrated by injecting known volumes of the species through the injection ports to the column under the conditions given in Table 3.3. Area of the peaks that correspond to each species in the chromatogram are then calculated by integration and plotted against the known volumes. The calibration curves are presented in Appendix B.

Table 3.3. GC conditions for product analysis.

GC Parameter	**Shimadzu GC-2014**
Detector type	TCD
Column temperature	40°C (0 → 13.5 min) 40 → 150°C (13.5 → 15.5 min) 150°C (15.5 → 23.5 min)
Injector temperature	110°C
Detector temperature	175°C
Detector current	50 μA
Carrier gas	Ar
Carrier gas flow rate	25 ml min^{-1}
Column packing material	Carboxen 1000
Column tubing material	Stainless steel
Column length & ID	6 m & 3 mm
Sampling loop	1 ml kept at 25°C

3.3. Catalyst Preparation and Pretreatment

3.3.1. Support Preparation

Catalytic oxidation and steam reforming of hydrocarbons, specifically those of methane, occur at elevated temperatures. Therefore, the catalyst supports should not only have high surface areas but also have good thermal stabilities. γ-Al_2O_3 is a commonly used support material due to its high surface area. However, it has been reported to have lower stability at temperatures greater than 600°C and tendency to facilitate carbon formation in the presence of steam due to its high acidity [116]. The most thermally stable phase of alumina is obtained when the γ phase is transformed into the α phase at temperatures greater than 1127°C [247]. However, its low surface area, which is less than 5 m^2 g^{-1}, is likely to result in poor catalytic activities. Using a support such as δ-alumina–an intermediate phase between γ and α–, having relatively high thermal stability and a decent surface area, can be the optimum in terms of catalytic performance [116].

Avci and coworkers investigated three different support preparation procedures that are given in Table 3.4 [248]. They basically involved the calcination of γ-Al_2O_3 (BET surface area: 279 m^2 g^{-1}) at various temperatures. Comparison of the resulting materials was based on their BET surface areas.

Table 3.4. Al_2O_3 support preparation procedures [248].

Procedure	**BET surface area** ($m^2\,g^{-1}$)
Calcination at 1000°C for 4 h	46.8
Drying of Al_2O_3 at 150°C for 2 h followed by calcination at 900°C for 4 h	81.6
Drying of Al_2O_3 at 105°C overnight followed by calcination at 875°C for 4 h	73.2

The second procedure in Table 3.4 resulted in the highest BET surface area, possibly due to the low temperature removal of bonded water. It is likely that the duration of drying is important, since a longer period of drying at a lower temperature resulted in a lower surface area, even though the calcination temperature was less than that for the second procedure.

The experimental tests in this research comprise steam and autothermal reforming of methane for the comparative and parametric study of packed-bed (PB) and microchannel (MC) reactor configurations. A set of Xwt% M/δ-Al_2O_3 catalysts (M = Ni, Rh, Ru, Pt) with varying metal loadings (X = 10 for Ni, 2 for others) are prepared by the incipient-to-wetness impregnation method for the steam reforming experiments. Methane ATR experiments in the microchannel reactor are conducted over a combination of 0.2wt%Pt/δ-Al_2O_3 and 2wt%Rh/δ-Al_2O_3 catalysts. Alumina particles (Table 3.1), crushed and sieved to $45-60$ mesh ($250-354\,\mu$m) size range are used as support for the PB catalysts. Alumina powder of 3-μm size (Table 3.1) is used for synthesizing the MC catalysts. Thermally stable δ phase of both supports are obtained by drying at 150°C for 2 h and calcination at 900°C for 4 h in accordance with the procedural guidelines given in Table 3.4.

3.3.2. Preparation of Active Catalysts

The incipient-to-wetness impregnation method is common to both packed-bed and microchannel catalyst syntheses. The latter involves another and different route after the catalyst powders are prepared (Section 3.3.2.1) while the as-synthesized particulate catalysts are used in the PB experiments.

3.3.2.1. Incipient-to-wetness Impregnation of Active Metals. Aqueous solutions of the metal precursors given in Table 3.1 are prepared by dissolving/mixing the calculated amount of the precursor salts/solutions in definite amounts of deionized water (ca. $1\,\mathrm{ml}_{\mathrm{solution}}\,\mathrm{g}_{\mathrm{support}}^{-1}$). The support, either $45-60$ mesh- or 3 μm-size δ-Al_2O_3, is put into the Büchner erlen and mixed ultrasonically for 25 min under vacuum. The aqueous solution is then impregnated over the support via a peristaltic pump (Figure 3.1). The resulting slurry is allowed to mix ultrasonically under vacuum for another 1.5 h, and is dried overnight at 120°C. All the catalysts except Ni/δ-Al_2O_3 are calcined at 500°C at a ramping rate of $5\,^{\circ}\mathrm{C\,min}^{-1}$ for 3 h. The calcination temperature for Ni/δ-Al_2O_3 is set to 600°C.

3.3.2.2. Catalytic Microchannel Synthesis. Several mechanical and chemical treatment methods are required for the preparation of the catalytic microchannel. The first of these is wire electro discharge machining of FeCrAlY sheets (Table 3.1) into 2 mm × 5 mm × 20 mm plates, and 310-grade stainless steel into a cylindrical housing with diameter $D = 18.6$ mm, and length $L = 30$ mm. As a next step, in order to enhance the adhesion of the coated plates, a native alumina layer on the plates are formed by calcining them in air at 900°C at a ramping rate of $20\,^{\circ}\mathrm{C\,min}^{-1}$ for 2 h. Then, the calcined 3-μm powders are mixed with deionized water at a water-to-powder weight ratio of $5-8:1$. The resulting slurries are blade-coated repeatedly onto the 5 mm × 20 mm plates until the weight per surface area reaches ca. $0.02\,\mathrm{g}_{\mathrm{cat}}\,\mathrm{cm}^{-2}$. The coated plates are dried overnight at 120°C and calcined for 3 h either at 500 (others) or 600°C (Ni).

The last step in catalytic microchannel preparation is the insertion of the catalyst coated plates into the cylindrical housing. The interior of the housing is engineered by wire electro discharge machining to have a combined opening for the plate(s) and the microchannel. The plate(s) (single plate coated with M/δ-Al_2O_3 for SRM, two plates coated with Pt/δ-Al_2O_3 and Rh/δ-Al_2O_3 for ATR of methane) is inserted with 0.5 mm fitting to the grooves at each side to give one microchannel with dimensions 0.75 mm (H_j) × 4 mm (W_j) × 20 mm depth, with height including the thickness of the coated catalyst layers. The net weight of catalysts used are determined after insertion

of the plate(s) into the housing, and then removing them since the grooves strip off some coating on the sides during insertion. Possible displacement of the plate(s) is prevented by stuffing ceramic wool into the remaining 10 mm gap between the bottom of the catalytic plate(s) and the bottom of the housing.

Figure 3.3a shows the orthographic drawing of the cylindrical housing and the synthesized catalytic microchannel used in the steam reforming of methane (SRM). The catalyst arrangement is shown in Figure 3.3b, where the reactive mixture consisting of methane, steam and nitrogen flows top down through the microchannel reactor. Figure 3.4a,b show the drawing of the "H-type" cylindrical housing and the microchannel used in autothermal reforming (ATR) of methane, and the catalyst arrangement, respectively.

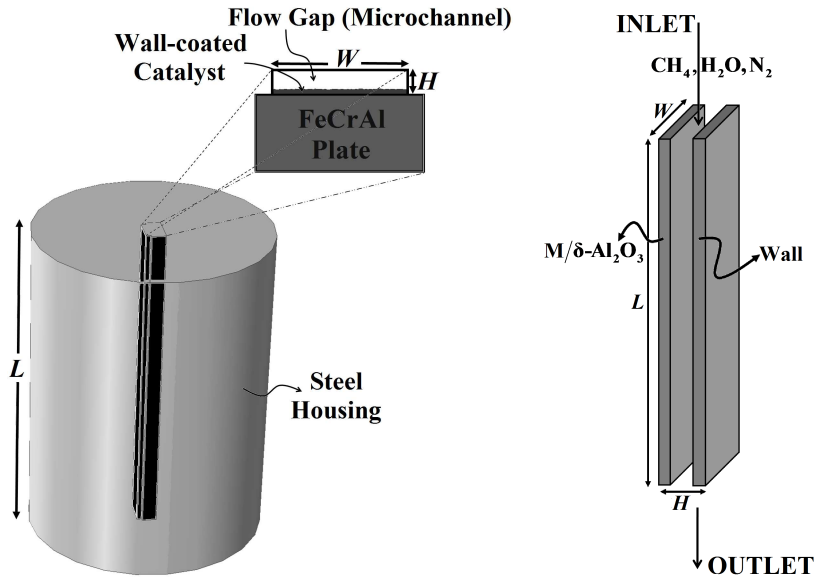

Figure 3.3. (a) Orthographic drawing of the steel housing and the microchannel used in the SRM experiments, (b) details of the catalytic microchannel configuration (M = Ni, Rh, Ru, Pt).

3.3.3. Pretreatment

It is usually required to activate the catalysts after calcination, which means that the active metals should be reduced from their oxidized states to the metallic state.

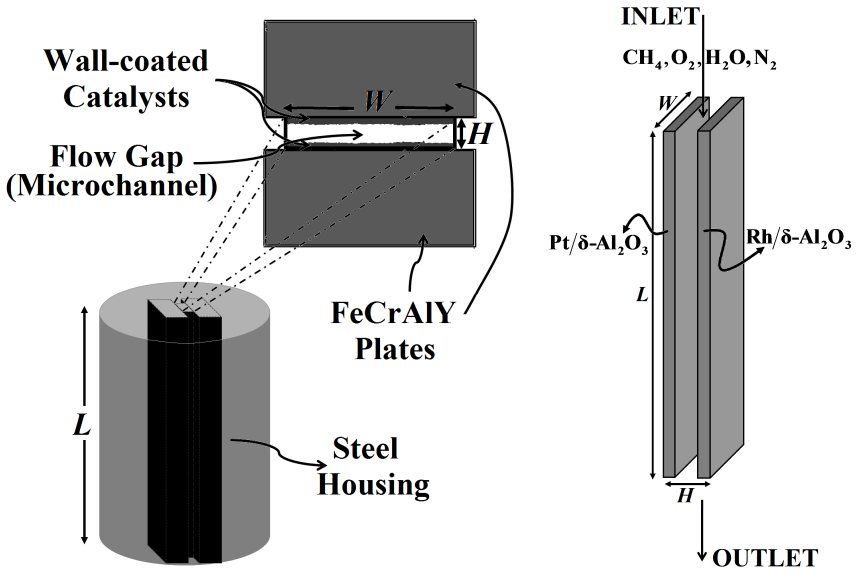

(a) (b)

Figure 3.4. (a) Orthographic drawing of the steel housing and the microchannel used in methane ATR, (b) details of the catalytic microchannel configuration.

Catalysts for the PB and MC configurations are reduced in situ (Section 3.4) under 40 Nml min^{-1} hydrogen flow at 800°C for 2 h before the reaction tests.

3.4. Reaction Tests

3.4.1. Blank Tests

Blank tests are conducted to ensure that the materials of construction (stainless steel and FeCrAlY), glass and ceramic wools, and δ-Al_2O_3 (used as diluent) are inert toward the reactants. GC analysis of the reactor effluents in blank runs that are carried out using particulate alumina and uncoated plates respectively in PB and MC experiments do not indicate any oxidation or steam reforming activity.

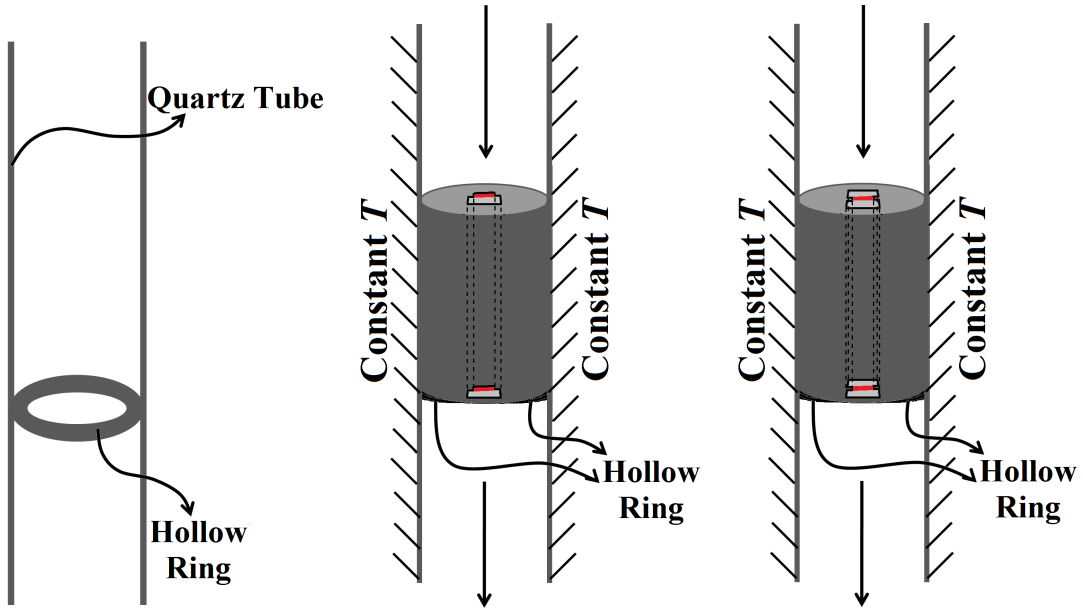

(a) (b) (c)

Figure 3.5. (a) The hollow ring inside the quartz tube, the microchannel reactor arrangement inside the quartz tube (b) for steam and (c) autothermal reforming of methane.

3.4.2. Steam Reforming of Methane in Packed-bed and Microchannel Reactors

In the PB experiments 100 mg of each particulate catalyst is diluted with δ-Al_2O_3 (both at $45-60$ mesh size) at a catalyst:diluent weight ratio of $1:6$. The mixture is then placed into the center of a 10 mm $\times$ 80 cm (inner diameter $\times$ length) quartz tube, and fixed underneath by a ceramic wool plug. In the MC experiments, the housing, including the catalytic plate, is placed into the center of a 20 mm$\times$80 cm (inner diameter $\times$ length) quartz tube, and is supported underneath by a hollow ring that is wide enough to ensure sufficient circumferential overlap (Figure 3.5a). The designed overlap keeps the housing fixed in position and prevents bypass through the annulus between the housing and the tube (Figure 3.5b). The possibility of bypass is further diminished during the experiments due to the thermal expansion of the steel housing at high ($>$ 500°C) temperatures that reduces the annular gap. Temperature of the catalytic zone is controlled and measured to $\pm$0.1°C by a Shimaden FP-23 programmable temperature

controller and a K-type sheathed thermocouple, which is positioned inside the tube furnace to have immediate contact with the central point of the quartz tube (item 7 in Figure 3.2), where the catalytic microchannel is located (at 5d in Figure 3.2). The tube is placed in the furnace such that the catalytic zone at its midst remains within the 10-cm constant-temperature zone.

Table 3.5. SRM operating conditions in the microchannel reactor[a].

τ (**ms**)	**S : C**						***T*** (°C)				
	0.5	1	1.5	2	2.5	3.0[b]	600	650	700	750[b]	800
12.86	▲	▲	×	×	×	×	×	×	×	×	▲
19.28						×				×	
38.57						×				×	
51.43						×				×	
77.14	▲	▲	×	×	×	×	×	×	×	×	▲

[a] (×) denotes all metals whereas (▲) denotes Rh only.

[b] Identical runs for $T = 750$°C and S : C = 3.0.

The MC experiments are conducted in the following parameter ranges: (i) residence time τ between 12.86 ms (210 Nml min^{-1}) and 77.14 ms (35 Nml min^{-1}), (ii) reaction temperature T between 600 and 800°C, and (iii) steam-to-carbon ratio S : C between 0.5 and 3.0. Here residence time τ is defined as the entire flow-by volume (including the coating volume) divided by the total volumetric flow rate (v_{MC}) at normal conditions (25°C, 1 atm). Steam-to-carbon ratio is defined as the number of moles of steam divided by that of methane at the inlet. Mole fraction of inlet methane is kept constant at 0.143 in all runs. The feed gas composition of 1 : 3 : 3 ($CH_4 : H_2O : N_2$) is preserved at each residence time change. The S : C ratio is adjusted by varying the N_2 flow rate such that the residence time and the partial pressure of methane remain unchanged. Analyses that involve the parametric variations of temperature and the S : C ratio are done only at the highest and lowest residence times. The matrix shown in Table 3.5 summarizes this experimental program. In order to ensure reproducibility, all runs are repeated at least twice using different coated plates.

Steam reforming of methane in the MC and PB configurations are compared at 750°C and S : C = 3.0 on the basis of identical weight hourly space velocity (WHSV),

Table 3.6. Flow rates for the packed-bed configuration[a].

Metal	w_{MC}/ w_{PB} (mg/mg)	v_{PB} ($Nml\,min^{-1}$)	v/w ($Nml\,min^{-1}\,mg^{-1}$)
Ni	14.2/100	246	2.46
Rh	13.5/100	259	2.59
Ru	15.7/100	223	2.23
Pt	18.6/100	188	1.88

[a] $CH_4 : H_2O : N_2 = 1 : 3 : 3$; $T = 750°C$, $S : C = 3.0$.

which is defined as the ratio of the total inlet volumetric flow rate to the catalyst weight. WHSV for the MC configuration is calculated by dividing the total inlet volumetric flow rate ($35\,Nml\,min^{-1}$) by the weight of catalyst deposited on the plates (w_{MC}) which is different for each catalyst due to the different densities of the active metals (Table 3.6). Inlet volumetric flow rates in the PB configuration (v_{PB}) are then determined by multiplying the WHSV value with 100 mg, the weight of active catalysts used in the PB experiments (Table 3.6). The w_{MC} values reported in Table 3.6 are net amounts of the catalysts remaining upon scraping. Due to excessive pressure drop along the bed, it is not possible to operate at higher flow rates in the PB configuration.

Carbon balance between the reactant CH_4 and the gaseous products CO and CO_2 gives the conversion of methane (χ_{CH_4}) (Equation 3.1), which is also calculated by the percent difference between inlet and outlet CH_4 (Equation 3.2):

$$\chi_{CH_4} = 100 \times \frac{x_{CO} + x_{CO_2}}{x_{CO} + x_{CO_2} + x_{CH_4}} \tag{3.1}$$

$$\chi_{CH_4} = 100 \times \frac{F^{in}_{CH_4} - F^{out}_{CH_4}}{F^{in}_{CH_4}} \tag{3.2}$$

Proximity of the results obtained from Equations 3.1 and 3.2 implies coke-free operation since all the methane reacted is already converted to the detectable gaseous products CO and CO_2. The other significant result of the analyses, CO selectivity (S_{CO}), is

defined as

$$S_{\mathrm{CO}} = 100 \times \frac{x_{\mathrm{CO}}}{x_{\mathrm{CO}} + x_{\mathrm{CO_2}}} \tag{3.3}$$

In Equations 3.1 and 3.3, x_i's denote the species mole fractions on a dry basis. Reactor productivity is expressed in terms of moles of methane reacted per weight of catalyst per time ($\mathrm{mol_{CH_4}\,kg_{cat}^{-1}\,s^{-1}}$).

3.4.3. Autothermal Reforming of Methane in the Microchannel Reactor

The difference between steam reforming (Section 3.4.2) and autothermal reforming of methane in the microchannel reactor is two-fold: the structural difference comes from the use of a "H-type" housing (Figure 3.4a), and two coated plates (with 0.2wt%Pt/δ-Al_2O_3 and 2wt%Rh/δ-Al_2O_3) instead of one (Figure 3.3a). Reactor operation strategy, which is exactly the same as that for SRM, has already been described in the first paragraph of Section 3.4.2 (see Figure 3.5c for the microchannel reactor arrangement in the quartz tube in methane ATR). The second difference is the presence of oxygen in the feed stream, which necessitates methodical quantification of its amount so as to allow a parametric study. This quantification is done by use of the oxygen-to-carbon (O_2 : C) ratio, which is defined as the ratio of molecular oxygen to methane at the inlet.

The experiments are carried in the following parameter ranges: (i) residence time τ between 12.86 ms (210 $\mathrm{Nml\,min^{-1}}$) and 25.72 ms (105 $\mathrm{Nml\,min^{-1}}$), (ii) reaction temperature T between 500 and 650°C, (iii) steam-to-carbon ratio S : C between 0 and 3.0, and (iv) oxygen-to-carbon ratio O_2 : C between 0.47 and 0.63. Definitions of the residence time and the steam-to-carbon ratio are the same as those for the SRM experiments. Mole fraction of inlet methane is kept constant at 0.143 in all runs, and the feed gas composition of 2.12 : 6.36 : 1 : 5.36 (CH_4 : H_2O : O_2 : N_2) is preserved at each residence time change. The S : C or O_2 : C ratio is adjusted by varying the N_2 flow rate such that all other parameters (i.e., O_2 : C or S : C and τ) and the partial pressure of methane remain unchanged. Analyses that involve the parametric

variations of temperature, S : C and O_2 : C ratios are done only at the lowest residence time. The matrix shown in Table 3.7 summarizes the experimental program. All runs are repeated at least twice using different pairs of coated Pt and Rh plates in order to ensure reproducibility. Equation 3.1-3 are used for CH_4 conversion and CO selectivity calculations.

Table 3.7. Methane ATR operating conditions in the microchannel reactor.

τ (**ms**)	S : C							O_2 : C			***T*** (°C)			
	0	0.5	1.0	1.5	2.0	2.5	3.0[a]	0.47[a]	0.54	0.63	500	550	600	650[a]
12.86	×	×	×	×	×	×	×[b]	×[b]	×	×	×	×	×	×[b]
14.84							×	×						×
19.28							×	×						×
25.72							×	×						×

[a] Marked columns denote identical runs with S : C = 3.0, O_2 : C = 0.47 and $T = 650$°C.

[b] Base-case values with $\tau = 12.86$ ms, S : C = 3.0, O_2 : C = 0.47 and $T = 650$°C.

4. MODELING AND SIMULATION

This section of the work is concerned with the construction and development of mathematical models that represent the physical models of *compact catalytic reaction systems* including parallel microchannel reactors and reactor/heat exchanger cascades. Computational fluid dynamics (CFD) model of reactive flow, heat and mass transfer in the microchannels leads to a large set of conservation and constitutive equations, which are presented in a form applicable to any general catalytic reaction system. Simulation of the compact catalytic systems is done within the context of *fuel conversion* for hydrogen production for fuel cells and for commodity chemicals production. System-specific information such as reaction kinetics, physical properties, microchannel geometry and flow configuration (e.g. co- or counter-current) is handled separately.

4.1. Hydrocarbon and Alcohol Conversion Processes

Processing of gaseous or liquid fuels for conversion into fuel-cell-grade hydrogen in catalytic microchannel reactors is investigated on the basis of several parametric (operating conditions) and structural variations (geometry). The gaseous fuel is propane (LPG component). *n*-Heptane (model hydrocarbon for petroleum naphtha), *iso*-octane (model hydrocarbon for gasoline), methanol (due to its widespread availability) and ethanol (bioethanol component) are the fuels in liquid form at standard temperature and pressure (273.15 K, 1 bar). Fuel-to-hydrogen conversion is carried out by combustion-assisted steam reforming, where part of the fuel to be reformed or a different fuel (methane) undergoes catalytic combustion in order to generate the heat required by endothermic reforming (Section 4.1.1). While *n*-heptane reforming is demonstrated both in coupled (parallel microchannel reactors, Section 4.2) and decoupled (cascades, Section 4.3) reaction/heat exchange systems, reforming of all the rest takes place in coupled systems.

Production of syngas, which is an intermediate product that is used as feedstock in Fischer-Tropsch and methanol syntheses, is demonstrated via combustion-assisted

steam reforming of methane in coupled and decoupled systems, where combustion of part of the fuel provides the heat (Section 4.1.2). A comparison between the two systems, based on overall size and precision of temperature control, is drawn. Autothermal reforming of methane in a spatially integrated microchannel is also modeled using elementary reaction kinetics (Section 4.2.2).

The other process that has industrial relevance is ethane dehydrogenation, which is one of the well-established practices of paraffins-to-olefins production. The reaction requires good temperature control due to the possibility of coke formation. Combustion-assisted ethane dehydrogenation is modeled in coupled and decoupled reaction/heat exchange systems (Section 4.1.3).

4.1.1. Production of Hydrogen for Fuel Cells

4.1.1.1. Steam Reforming of Propane, Methanol and Ethanol. Heat required by the steam reforming of a hydrocarbon or alcohol fuel can be supplied by combustion of part of that fuel. This is demonstrated via coupling of catalytic reforming and combustion reactions of propane, methanol and ethanol. The stoichiometric reactions, heats of reactions and the catalysts used are presented in Tables 4.1 and 4.2.

Table 4.1. Catalytic combustion reactions of propane, methanol and ethanol.

	Reaction	ΔH^0_{298} ($\mathrm{kJ\,mol^{-1}}$)	**Catalyst**	**Reference**
(4.1)	$CH_3OH + 1.5O_2 \rightarrow CO_2 + 2H_2O$	-676	Pt/Al_2O_3	[249]
(4.2)	$C_2H_5OH + 3O_2 \rightarrow 2CO_2 + 3H_2O$	-1278	$Cu\text{-}CrO/Al_2O_3$	[250]
(4.3)	$C_3H_8 + 5O_2 \rightarrow 3CO_2 + 4H_2O$	-2044	$Pt/\delta\text{-}Al_2O_3$	[107]

Table 4.2. Steam reforming reactions of propane, methanol and ethanol.

	Reaction	ΔH^0_{298} ($\mathrm{kJ\,mol^{-1}}$)	**Catalyst**	**Reference**
(4.4)	$CH_3OH + H_2O \rightleftharpoons CO_2 + 3H_2$	49.5	$Cu/ZnO\text{-}Al_2O_3$	[251]
(4.5)	$C_2H_5OH + H_2O \rightleftharpoons 2CO + 4H_2$	255	Ni/Al_2O_3	[84]
(4.6)	$C_3H_8 + 3H_2O \rightleftharpoons 3CO + 7H_2$	498	$Ni/MgO\text{-}Al_2O_3$	[68]

4.1.1.2. Steam Reforming of *n*-Heptane and *iso*-Octane. The hydrocarbon fuel, *n*-heptane–surrogate for petroleum naphtha–can be converted to high purity, fuel-cell-grade hydrogen in a series of catalytic steps involved in the fuel processor/PEM fuel cell system shown in Figure 4.1. In this system, *n*-heptane conversion takes place in the reformer unit via the steam reforming (SR) reaction which is considered to run over a Ni/Mg-Al_2O_4 catalyst [252]:

$$n\text{-}C_7H_{16} + 7H_2O \rightleftharpoons 7CO + 15H_2 \qquad \Delta H^0_{298} = 1108\,\mathrm{kJ\,mol^{-1}} \tag{4.7}$$

The major side reactions accompanying steam reforming are the methanation of syngas (reverse of Equation 4.8), steam reforming of methane to CO_2 (Equation 4.9) and the water-gas shift reaction (Equation 4.10):

$$CH_4 + H_2O \rightleftharpoons CO + 3H_2 \qquad \Delta H^0_{298} = -206.2\,\mathrm{kJ\,mol^{-1}} \tag{4.8}$$

$$CH_4 + 2H_2O \rightleftharpoons CO_2 + 4H_2 \qquad \Delta H^0_{298} = 165\,\mathrm{kJ\,mol^{-1}} \tag{4.9}$$

$$CO + H_2O \rightleftharpoons CO_2 + H_2 \qquad \Delta H^0_{298} = -41.2\,\mathrm{kJ\,mol^{-1}} \tag{4.10}$$

The heat required to drive the endothermic steam reforming is provided by catalytic combustion of methane, the model compound for natural gas, over a Pt/δ-Al_2O_3 catalyst [107]. Effective integration of these reactions can be achieved in two intensified reactor configurations, namely the microchannel (Section 4.2) and the cascade (Section 4.3) systems. Methane combustion can be represented by its total oxidation:

$$CH_4 + 2O_2 \rightarrow CO_2 + 2H_2O \qquad \Delta H^0_{298} = -802.3\,\mathrm{kJ\,mol^{-1}} \tag{4.11}$$

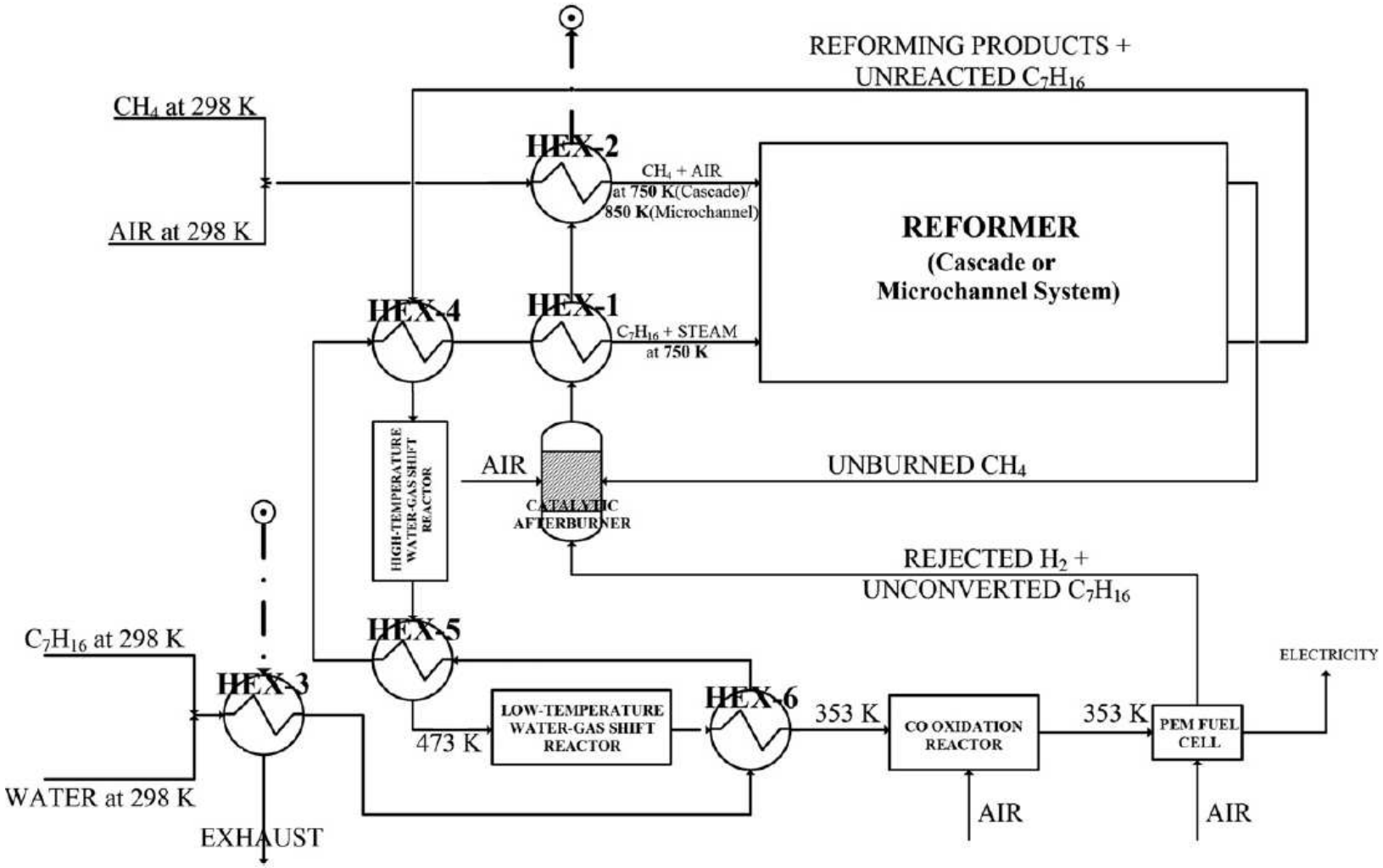

Figure 4.1. Process flow diagram of the fuel processor/PEM fuel cell assembly.

The hydrogen-rich stream leaving the reformer contains carbon monoxide whose concentration must be reduced to below 10 ppm since it is a poison for the Pt-based catalysts of the PEM fuel cell [74, 253, 254]. The clean-up operation of the hydrogen-rich stream is considered to be undertaken in three stages. The first two stages involve the water-gas shift reaction (Equation 4.10) run in fixed-bed adiabatic reactors at high- and low-temperature modes, respectively. The high-temperature water-gas shift (HTS) reaction takes place over a Fe-based catalyst and reduces the CO concentration to ca. 10% by mole [255]. The low-temperature water-gas shift (LTS) reaction runs over a Cu-based catalyst and reduces the CO concentration to less than 1% [256]. Preferential CO oxidation (Equation 4.12) as the final stage of cleaning-up has been reported to achieve CO removal at the desired level [60, 67].

$$\mathrm{CO} + 1/2\mathrm{O_2} \rightarrow \mathrm{CO_2} \qquad \Delta H^0_{298} = -283\,\mathrm{kJ\,mol^{-1}} \tag{4.12}$$

The reformer feed, consisting of inputs for steam reforming (liquid n-heptane and water) and for combustion (methane and air) needs to be evaporated and heated from room temperature to the relevant reaction temperatures, and this can be achieved in the context of heat integration depicted in Figure 4.1. Unburned methane from the combustion reaction, unconverted n-heptane from the reforming reactions and purged hydrogen from the fuel cell, which corresponds to ca. 25% of the hydrogen fed to the PEMFC [257], are catalytically burned in an afterburner, whose exhaust is then used to preheat, and if necessary, evaporate the feed streams through several heat exchange stages (HEX 1, 2 and 3 in Figure 4.1). Furthermore, the product stream that leaves the reformer at temperatures around 763 K has to be cooled down to 673 K before being fed into the high-temperature water-gas shift (HTS) reactor, so another exchange takes place between the stream mentioned and the reforming feed stream (HEX-4). Even though the HTS reactor alone reduces the CO content substantially, the CO removal unit accepts streams with CO concentration less than 1%, which calls for another intermediate operation, namely the low-temperature water-gas shift (LTS) [258]. However, the LTS operation runs at temperatures between 473 and 600 K [256], therefore, an

exchanger (HEX-5) is installed between the high- and low-temperature water-gas shift reactors, which facilitates heat transfer from the SR/HTS product stream to the SR feed stream. The final heat exchange stage (HEX-6) applied down the process line is required to cool the outlet stream from the LTS reactor from 600 to 353 K, the operating temperature of the CO oxidation reactor [259], and to preheat the SR feed stream. This configuration enables, at steady state, the autothermal operation of the fuel processor/PEMFC assembly and eliminates the need for external heat supply.

Process intensification can be achieved through the compact design of all the reactor and heat exchanger units described above. However, integration of the exothermic and endothermic reactions in the reforming unit makes the major contribution to the size and efficiency of the fuel processor (reformer + hydrogen clean-up units + heat exchangers)/fuel cell assembly shown in Figure 4.1. Therefore, the size comparison simply takes its roots from the integration (coupled or decoupled) scheme itself. The remaining parts of the fuel processor are considered to be of the same design, if not the same size, for both schemes. The basis flow rate used to determine the reformer size is set as the amount of hydrogen required to drive a 2-kW PEM fuel cell, which corresponds to $2.2 \times 10^{-2}\,\mathrm{mol_{H_2}\,s^{-1}}$ [260]. However, when assessing the effectiveness of the fuel processing unit in terms of productivity, the amount of hydrogen that enters the fuel cell is used as the basis: in either reformer scheme, whether of microchannel (coupled) or of cascade (decoupled), hydrogen is also produced in the subsequent water-gas shift stages, so that the overall amount of hydrogen produced can drive a PEMFC-based auxiliary power unit (APU) in the 2-3 kW range, as desired.

n-Heptane flows in the process flow diagram of Figure 4.1 can be replaced by streams of any liquid hydrocarbon for the purpose of CO-free H_2 production, provided that the sizes of the reactors and the exchanger duties are duly adjusted. Conversion of gasoline, which can be described by the steam reforming of its surrogate, *iso*-octane, over a Ni/Al_2O_3 catalyst is represented by [261, 262]:

$$\textit{iso}\text{-}C_8H_{18} + 8H_2O \rightleftharpoons 8CO + 17H_2 \qquad \Delta H^0_{298} = 1274.8\,\mathrm{kJ\,mol^{-1}} \tag{4.13}$$

Steam reforming of *iso*-octane also harnesses the heat released by methane combustion (Equation 4.11). This time, integration of these two reactions takes place in a coupled reaction/heat exchange system consisting of parallel microchannels, where the effects of their geometric variations on fuel conversion and hydrogen selectivity are sought.

4.1.2. Production of Syngas

Syngas ($CO + H_2$) is an important feedstock in chemicals production processes such as Fischer-Tropsch (FT), methanol and dimethyl ether (DME) syntheses. Steam reforming of methane (SRM) is one of the commercial routes to producing syngas. Tubular reactors packed with Ni-based catalysts are used for carrying out SRM, for which the heat is supplied either by a direct-firing furnace or by heat exchange with a hot stream [76].

Autothermal reforming (ATR) of methane is another well-established industrial practice of producing syngas, which involves the spatial integration of exothermic partial oxidation (POX) and endothermic steam reforming (SR) of the fuel that is co-fed into the reactor with steam and oxygen. Due to the immediate and effective supply of heat from the oxidation to the reforming reactions, external heating requirements are minimal. ATR of methane is carried out also over Ni-based catalysts at temperatures in excess of 1173 K in order to affect the syngas feed ratio in favor of the methanol ($H_2 : CO \approx 3.00 : 1$) or FT ($2.00 : 1 < H_2 : CO < 2.15 : 1$) syntheses [140].

4.1.2.1. Steam Reforming of Methane. The overall production of methanol from natural gas, represented by methane, involves two steps: the endothermic reforming of natural gas and the exothermic synthesis reaction [263]:

$$CH_4 + H_2O \rightleftharpoons CO + 3H_2 \qquad \Delta H^0_{298} = 206.2\,\mathrm{kJ\,mol^{-1}} \tag{4.8}$$

$$CH_4 + 2H_2O \rightleftharpoons CO_2 + 4H_2 \qquad \Delta H^0_{298} = 165\,\mathrm{kJ\,mol^{-1}} \tag{4.9}$$

$$CO + 2H_2 \rightleftharpoons CH_3OH \qquad \Delta H^0_{298} = -90.6\,\mathrm{kJ\,mol^{-1}} \tag{4.14}$$

The desired heat to drive the endothermic reforming reactions is provided by catalytic combustion:

$$CH_4 + 2O_2 \rightarrow CO_2 + 2H_2O \qquad \Delta H^0_{298} = -802.3\,\mathrm{kJ\,mol^{-1}} \tag{4.11}$$

The overall description of the methanol synthesis process is shown in Figure 4.2. Methane and steam are fed to the reformer which is heated by catalytic combustion of a second stream of methane. The reforming reactor is operated at about 1123 K to produce a gas suitable for the methanol synthesis ($H_2 : CO : CO_2 = 75 : 24 : 1$ per cent by mole) [263]. Since the synthesis reaction (Equation 4.14) requires only two moles of hydrogen per carbon monoxide, carbon dioxide coming from combustion (Equation 4.11) can be injected into the methanol synthesis reactor (not shown in Figure 4.2) to convert the excess hydrogen to a mixture of carbon monoxide and steam via the reverse water-gas shift reaction:

$$CO_2 + H_2 \rightleftharpoons CO + H_2O \qquad \Delta H^0_{298} = 41.2\,\mathrm{kJ\,mol^{-1}} \tag{4.15}$$

Such a route can help in approaching the stoichiometric $H_2 : CO$ ratio, and can therefore favor methanol formation. Copper-based catalysts used for synthesis deactivate at temperatures much in excess of 570 K [104, 263], and the inlet gases to the synthesis reactor must be cooled, the exchanged heat being used to warm the reformer inlet feed. Since the conversion per pass is around 3% [263], recycle of the unconverted reactants is essential to give a total of 10% conversion after recycle.

Typical temperatures involved in the methanol synthesis are presented in Figure 4.2. Inlet and outlet temperatures of steam reforming, 785 and 1123 K, respectively, and the inlet temperature and pressure to the methanol synthesis reactor (523 K, 50 bar) are adapted from actual process practice reported in [263]. Temperature at the inlet of catalytic combustion is set as the light-off temperature of methane, 900 K [107].

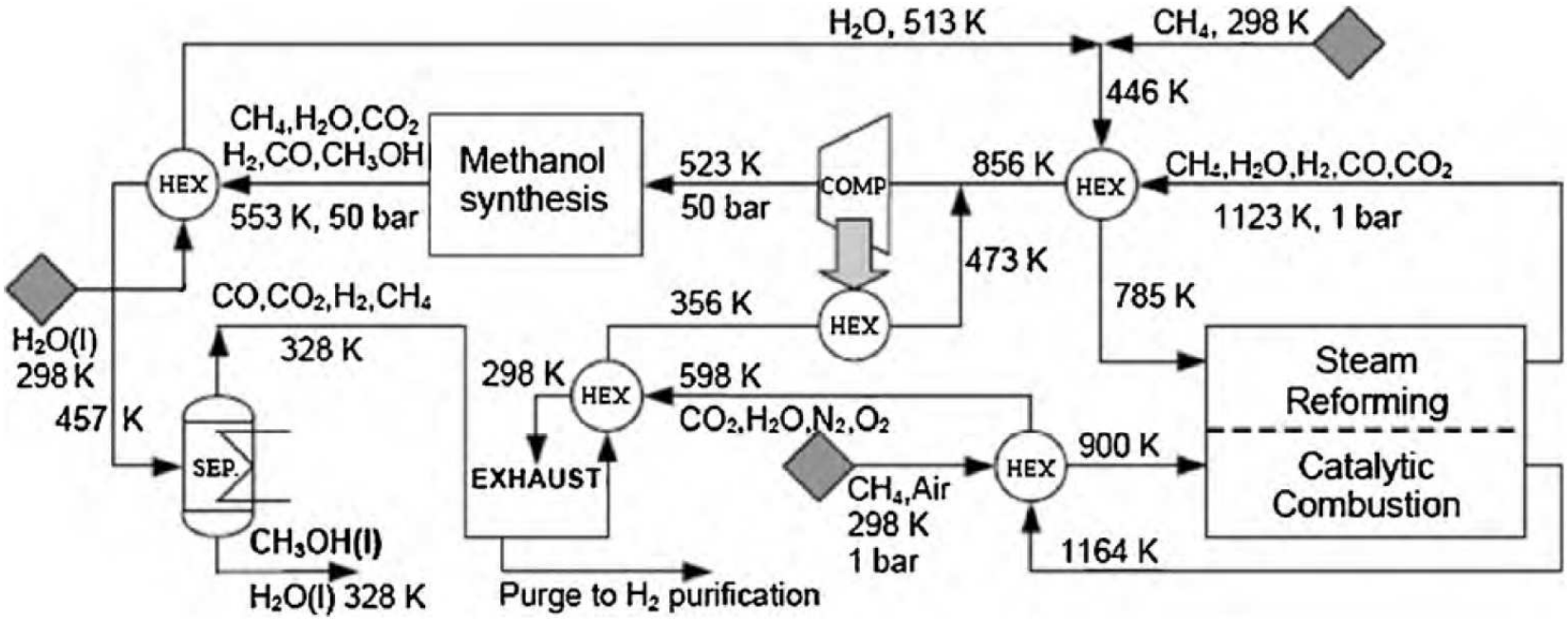

Figure 4.2. Process flow diagram of methanol production.

Temperature at the outlet of the separator, 328 K, is set to less than the boiling point of methanol (338 K) so that all the methanol can be obtained in the liquid phase. Finally, the inlet streams entering the process and exhaust streams leaving the process (except methanol exit from the separator) are assumed to be at 298 K. Rest of the stream temperatures shown in Figure 4.2 are calculated by mole and energy balances around the specific control volumes. The molar flow rates are calculated by the mole balances around the units by taking a basis of 1 kmol h^{-1} of methane entering the steam reformer, and by assuming 90% steam reforming conversion [263], complete conversion of methane in combustion [107], and the molar ratio of methane reformed-to-methane combusted as 3. The calculated flow rates are then adapted to the desired throughput by flowsheet scaling. The material and energy balance equations are solved by ChemCad process simulation software. The necessary thermochemical data such as reaction enthalpy and heat capacity of the species are used directly from the ChemCad database. Combustion-assisted steam reforming of methane for the purpose of syngas production is investigated in coupled (microchannel reactor) and decoupled (cascade) reaction/heat exchange systems using CFD and reactor modeling techniques.

4.1.2.2. Autothermal Reforming of Methane. A CFD-based model of the spatially integrated system (microchannel reactor) designed and tested for autothermal reforming of methane in Section 3.4.3 is also constructed in order to develop an essential design and analysis tool that has capability to predict experimental results.

4.1.3. Dehydrogenation of Paraffins to Olefins

In the case of ethane dehydrogenation,

$$C_2H_6 \rightleftharpoons C_2H_4 + H_2 \qquad \Delta H^0_{298} = 136.9\,\text{kJ mol}^{-1} \tag{4.16}$$

which is an important route to production of olefins from paraffins, temperature control is essential to avoid coke deposition over the catalyst. The olefin-to-paraffin equilibrium is favored only at high temperatures (ca. 1000 K), which also favor coking [264],

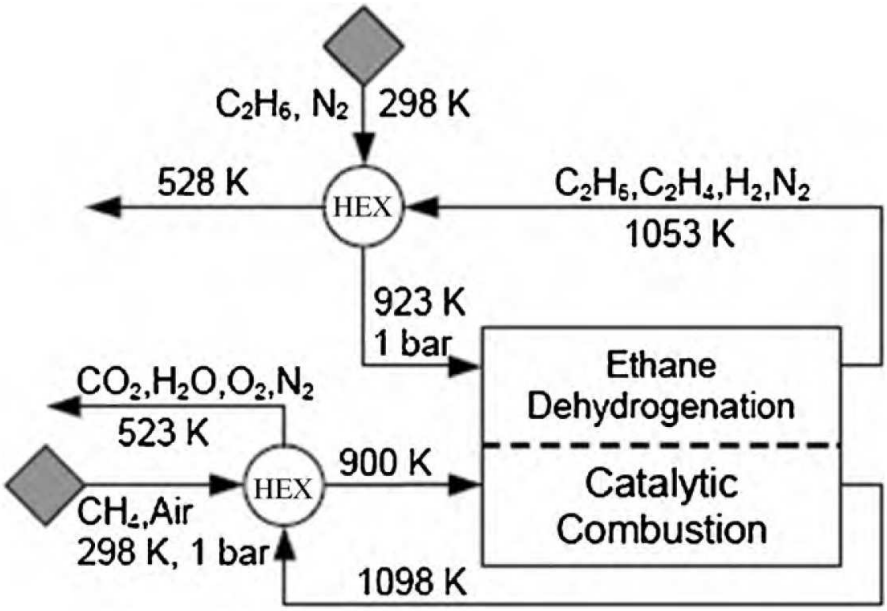

Figure 4.3. Process flow diagram of ethane dehydrogenation.

and diluents, often used to minimize coking, tend to deactivate the catalysts. As a result, commercial processes are often based on a dehydrogenation-regeneration cycle, dehydrogenation being optimized when temperature control limits the coke formation. Since coking is particularly deleterious in microchannel systems and channel blockage can occur, minimization of coking demands careful control of temperature, which, in the microsystems, necessitates careful control of heat generated by the catalytic combustion. The process flow diagram for ethane dehydrogenation (Figure 4.3) is much simpler than is the case for methanol (Figure 4.2), in which the inlet streams entering the process are assumed to be at 298 K. Inlet temperature of the catalytic combustion unit is set as the light-off temperature of methane (900 K) [107]. Inlet and outlet temperatures of ethane dehydrogenation is taken as 923 and 1053 K, respectively [235], and the molar ratio of ethane dehydrogenated-to-methane combusted is set as 3. These values are expected to be high enough to give reasonable conversions–62% in dehydrogenation (Equation 4.16) and ca. 100% in oxidation (Equation 4.11) [107]–and low enough to avoid very significant coking. The remainder of the stream temperatures are obtained using ChemCad. Temperature control during ethane dehydrogenation is demonstrated in coupled (microchannel reactor) and decoupled (cascade) reaction/heat exchange systems.

4.2. Coupled Reaction/Heat Exchange Systems

4.2.1. Spatially Segregated Microchannel Reactors

The microchannel reactor geometry used in modeling combustion-assisted steam reforming of propane, *n*-heptane, *iso*-octane, methanol and ethanol, shown in Figure 4.4, involves a repeating unit that consists of two parallel channels, called the **unit cell**, in which the exothermic and the endothermic reaction streams flow in either co-current or counter-current mode, and in which heat is transferred through the wall between the channels. The respective catalysts washcoated on the channel walls, with washcoat thickness being assumed to be uniform on all sides, facilitate the combustion and reforming reactions. Any given channel is part of a horizontal array of channels, each of which has the same reaction occurring within, as shown in the frontal view of the microchannel array on the x-y plane in Figure 4.5. Considering the shaded combustion channel in the figure, heat released due to the reaction is transferred in all directions. However, for two reasons the direction of net heat flow is toward the endothermic reforming channels, as indicated by the solid vertical arrows in Figure 4.5: (i) lateral heat flow in the x-direction (shown by the dashed horizontal arrows) out of the shaded channel is counter-balanced by heat flow from the respective combustion channels to its left and right, and (ii) the lateral temperature gradients column-wise are much smaller than those gradients row-wise due to the fact that the reactions taking place in a given row are identical (either combustion or reforming). Another implication of the alternating and symmetrical arrangement of the exothermic and endothermic channel groups is that inbound and outbound heat fluxes (solid vertical arrows) essentially cancel each other out, hence that the unit cell is adiabatic. Moreover, the microchannel array is thought to be ideally insulated on the sides, thus heat loss to the surroundings is negligible. Convenience gained by the symmetric arrangement of the channels gives way to using a 2D mathematical model for analyzing the integration of combustion and reforming reactions in catalytic microchannel or plate reactors, as has been demonstrated widely in the literature [14, 15, 19, 20, 207, 235, 265, 266]. Arzamendi *et al.* [239] performed a three-dimensional simulation of coupled methanol combustion and reforming in a multi-channel reactor system, and their graphical results indicate

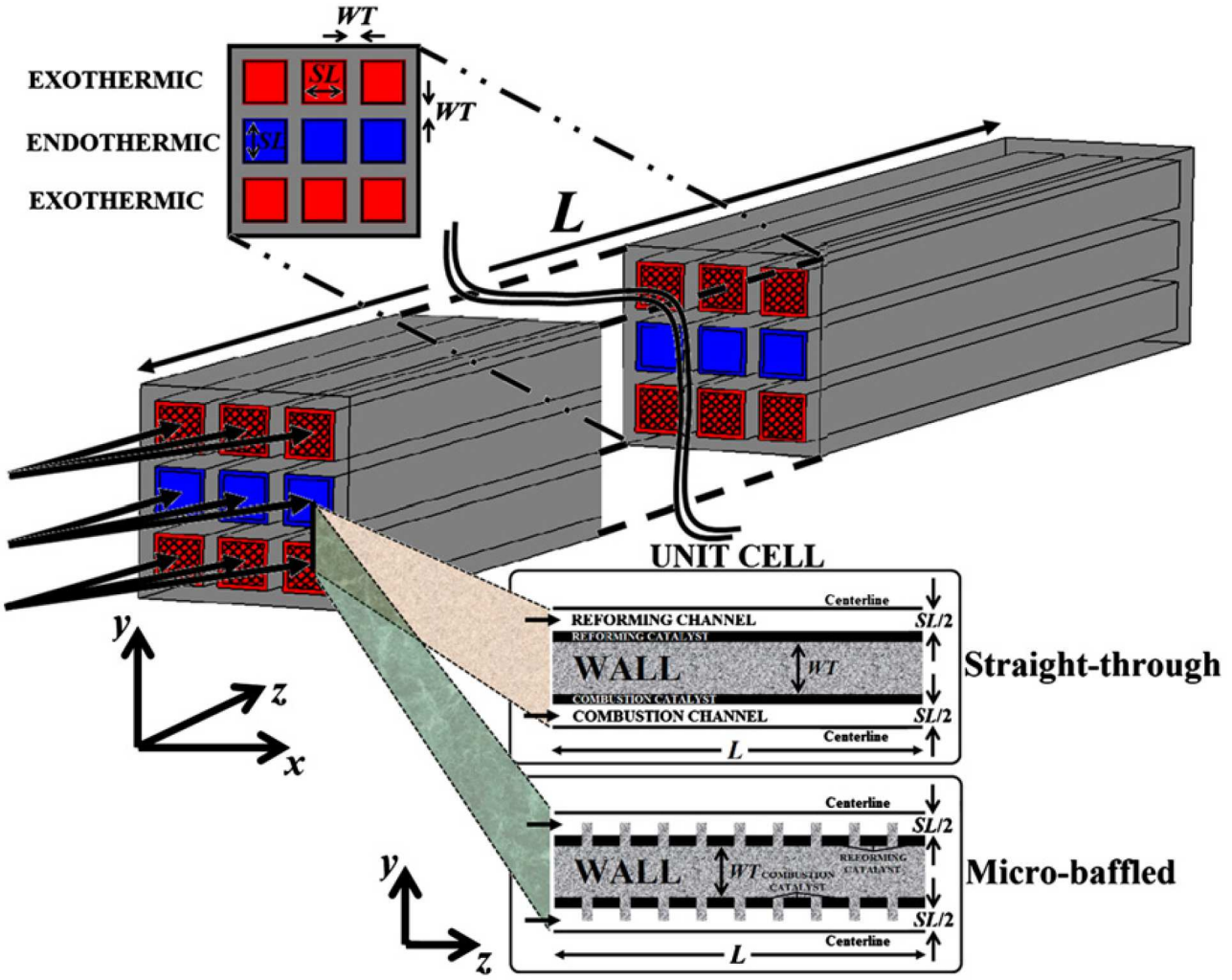

Figure 4.4. Depiction of the parallel microchannel reactor, the unit cell (lower inset) used in the 2D mathematical model and cross-sectional view of the microchannels (upper inset).

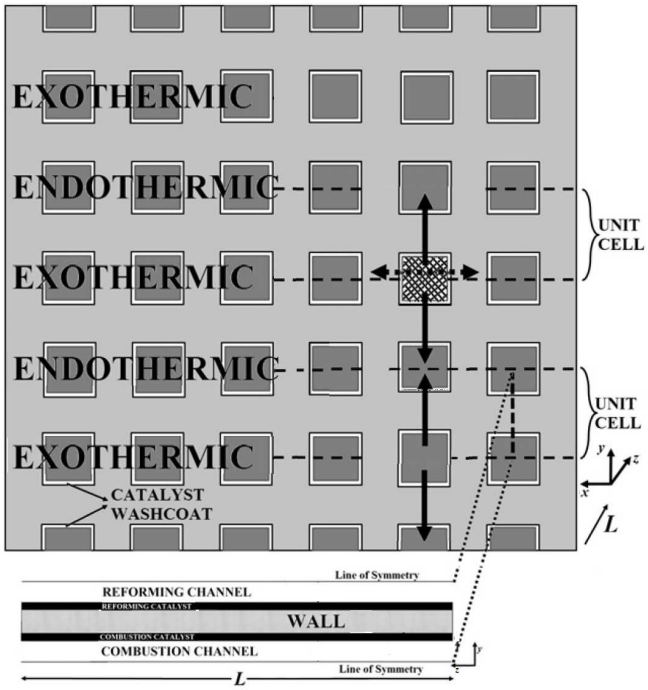

Figure 4.5. Frontal view of the microchannel array shown in Figure 4.4.

that lateral variations of temperature and species concentrations are not significant. Therefore, a two-dimensional domain that excludes any variation in velocity, pressure, concentration or temperature across the channel width (in the x-direction) suffices to model the microchannel reactor.

Variations in the structure of microchannel reactors are common. These involve, for instance, increasing or decreasing the cross-sectional area over some portion of or the whole length of the channels in order to affect the residence time and to induce static mixing. Changing the thickness of the separating fins affect the heat transfer rate between the channels. An example of a textural variation is seen in Figure 4.4 in which the micro-baffled configuration is depicted against the straight-through configuration.

The microchannel reactor geometry used in modeling combustion-assisted steam reforming of methane for syngas production, and ethane dehydrogenation for olefins production is shown in Figure 4.6. In many aspects it is similar to the reactor (Figure 4.4) used in modeling steam reforming of other hydrocarbons and alcohols such

that it consists of arrays of parallel channels separated by walls (fins). The geometry involves a repeating unit composed of the co-current flow of exothermic (methane combustion) and endothermic (steam reforming or ethane dehydrogenation) reaction streams in two parallel, cylindrical channels between which heat is transferred through the wall. Due to the symmetry, the behavior of this unit resembles the response of the multichannel reactor in which the exothermic and endothermic channels are grouped in horizontal layers as shown in Figure 4.6. In order to obtain desired steam reforming and ethane conversions ($> 80\%$ and $> 60\%$, respectively), and the syngas feed composition for methanol synthesis, high temperatures in excess of 1100 K are needed. For this purpose, the channel-wall boundaries are to be coated with a thin insulating layer along the first halves of the channels (Figure 4.6), and the insulated zones are assumed to behave adiabatically. Moreover, the catalytic washcoats are present only along the first half of the combustion channel, and along the second half of the reforming/dehydrogenation channel. Such a scheme conserves the heat released by combustion within the channel to induce methane light-off and allows combustion to proceed until the temperature rises up to ca. 1200 K. Preliminary simulations have shown that when the uninsulated parallel channels are completely coated with catalysts, heat generated by combustion at the inlet (first 0.5 cm) is immediately transferred to the endothermic reaction channel, thus, methane light-off cannot occur. In this case the maximum temperatures obtained are ca. 920 K. The presence of insulation in the combustion channel is seen to have no effect on axial conduction. It is worth noting that, in actual practice, it may not be possible to ensure perfect adiabatic conditions along the half of the microchannels. However, the use of ceramic-based materials having a thermal conductivity of ca. $10 - 20$ times smaller than that of steel may help in providing a thermal response at near-adiabatic scale.

Even though the microchannel diameters are in the submillimeter range, temperature and concentration variation in the lateral direction have to be accounted for since the reactions take place in the wall-coated catalyst layers. 3D cylindrical models offer accuracy at the expense of increased computational cost, therefore, the 2D axisymmetric model that neglects angular variations are employed in microchannel modeling.

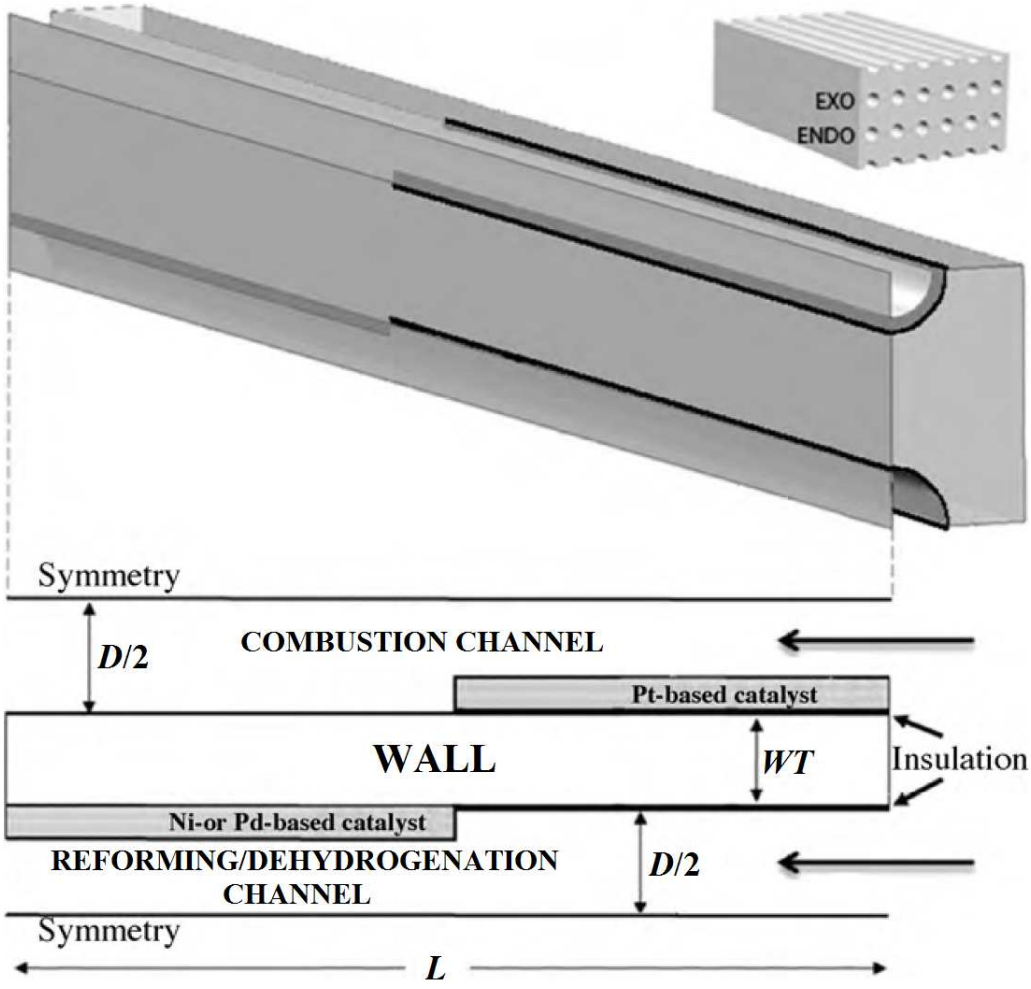

Figure 4.6. Description of the microchannel configuration used in combustion-steam reforming and combustion-dehydrogenation couplings.

4.2.2. Spatially Integrated Microchannel Reactors

Autothermal reforming of methane for syngas production is modeled on the microchannel geometry shown in Figure 4.7 whose width, height and length are the same as those of the reactor tested (Section 3.4.3). From a modeling perspective, the only difference between such an integrated system and the segregated systems explained above originates from the absence of an impermeable wall. The flow and transport equations in 3D Cartesian coordinates are applicable to integrated systems with slight modifications.

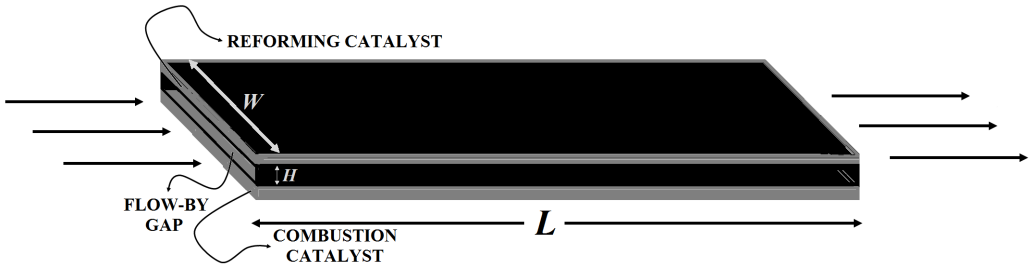

Figure 4.7. Schematic of the microchannel reactor used in methane ATR.

4.2.3. Working Equations, Implications and Simplifications

Combined model of the reactive flows in the wall-coated microchannels and heat transfer across the fins (walls separating the channels) (Figure 4.4) is described by the three-dimensional (3D) Navier-Stokes equations which form a set of partial differential equations (PDE) for the total mass, momentum, species mass conservation and energy (Section 4.2.3.2). Their solution gives the velocity, pressure, species concentration and temperature fields in the microchannel. Physical properties (i.e., fluid viscosity, species diffusivities, effective thermal conductivities) are estimated using correlations from the literature. Rates and heats of reactions are introduced to the model as source terms in the species mass and energy equations. Flow in porous media (catalytic washcoats) is modeled by the modification of the momentum equations that will be explained in detail. Certain assumptions are made that apply to all hydrocarbon conversion processes (steam and autothermal reforming of the fuels) that are considered in this work.

4.2.3.1. Assumptions.

- Incompressible, Newtonian, laminar flow
- Gravitational and external body forces are neglected
- The reactive gas mixtures enter the microchannels with uniform inlet velocities
- Only the designated reaction(s) takes place over a given catalyst, i.e., propane combustion over a Pt-based catalyst, propane reforming and water-gas shift over

a Ni-based catalyst

- Gas-phase reactions are neglected since in all conversion processes, homogeneous reactions require much longer ignition times than the heterogeneous reactions [137, 267]
- The fluid and catalyst properties are isotropic, i.e., they are uniform in all directions

4.2.3.2. Generalized Transport Equations. Hydrodynamics, mass and heat transfer inside the spatially segregated microchannels, and heat flow across the segregating fins are governed by three-dimensional (3D) Navier-Stokes equations given in Table 4.3.

Table 4.3. Generalized transport equations describing spatially segregated microchannel operation with reaction over catalytic washcoats.

Continuity equation
$$\frac{\partial \rho_{fj}}{\partial t} + \nabla \cdot (\rho_{fj} \vec{\mathbf{v}}_j) = 0 \quad (4.17)$$
Momentum conservation
$$\frac{\partial}{\partial t} (\rho_{fj} \vec{\mathbf{v}}_j) + \nabla \cdot (\rho_{fj} \vec{\mathbf{v}}_j \vec{\mathbf{v}}_j) = \vec{\mathbf{F}}_j - \nabla p_j + \nabla \cdot \bar{\bar{\tau}}_j + \rho_{fj} \vec{g} \quad (4.18)$$
Species mass conservation
$$\frac{\partial}{\partial t} (\rho_{fj} Y_{ij}) + \nabla \cdot (\rho_{fj} \vec{\mathbf{v}}_j Y_{ij}) = -\nabla \cdot \vec{J}_{ij} + M_i \Re_{ij}^{\mathrm{v}} + M_i \Re_{ij}^{\mathrm{s}} A_{sj} \quad (4.19)$$
Energy equation
$$\epsilon_j \frac{\partial}{\partial t} \left(\rho_{fj} c_{p_{fj}} T_j \right) + (1 - \epsilon_j) \frac{\partial}{\partial t} \left(\rho_{sj} c_{p_{sj}} T_j \right) + \nabla \cdot \left(\rho_{fj} c_{p_{fj}} \vec{\mathbf{v}}_j T_j \right) = \nabla \cdot \left(k_{\mathrm{eff},j} \nabla T_j - \sum_i h_{ij} \vec{J}_{ij} + (\bar{\bar{\tau}}_j \vec{\mathbf{v}}_j) \right) + S_{hj} \quad (4.20)$$
Energy equation in the fins
$$\frac{\partial}{\partial t} (\rho_w c_{p_w} T_w) = \nabla \cdot (k_w \nabla T_w) \quad (4.21)$$

The symbols used in Equation 4.17-21 are given in Table 4.4. The same nomenclature will be followed throughout the rest of the work. The subscripts i and j denote the species and the flow channel, respectively, while f, s and w refer to the fluid, the catalytic washcoat and the wall separating the channels. The superscripts s and v are used to distinguish between reactions that are formulated on volumetric and wall-surface bases. Note, however, that the volumetric reactions, which still take place over the catalyst volume, should not be confused with homogeneous gas-phase reactions. The subscripts "gas" and "solid" denote the gas phase and the porous washcoat.

Table 4.4. List of symbols used in the generalized transport equations (Equation 4.17-21).

Symbol	**Meaning**	**Unit**
A_{sj}	Active surface area of catalytic washcoat in channel j	m^{-1}
$c_{p_{fj}}$	Heat capacity of fluid in channel j	$\mathrm{J\,kg^{-1}\,K^{-1}}$
$c_{p_{sj}}$	Heat capacity of catalytic washcoat in channel j	$\mathrm{J\,kg^{-1}\,K^{-1}}$
c_{p_w}	Heat capacity of solid wall (fin)	$\mathrm{J\,kg^{-1}\,K^{-1}}$
f	Fluid property	—
$\vec{\mathbf{F}}_j$	Momentum source/sink term in channel j	$\mathrm{kg\,m^{-2}\,s^{-2}}$
$\vec{g}$	Gravitational acceleration	$\mathrm{m\,s^{-2}}$
h_{ij}	Sensible enthalpy of species i in channel j	$\mathrm{J\,kg^{-1}}$
i	Species index	—
j	Channel index (combustion or reforming)	—
$\vec{J_{ij}}$	Diffusive mass flux of species i in channel j	$\mathrm{kg\,m^{-2}\,s^{-1}}$
$k_{\mathrm{eff},j}$	Effective thermal conductivity of fluid in channel j	$\mathrm{W\,m^{-1}\,K^{-1}}$
k_w	Thermal conductivity of solid wall (fin)	$\mathrm{W\,m^{-1}\,K^{-1}}$
M_{ij}	Molecular weight of species i in channel j	$\mathrm{kg\,mol^{-1}}$
p_j	Pressure field in channel j	bar, Pa
$\Re^{\mathrm{s}}_{ij}$	Source of species i in channel j due to surface reaction	$\mathrm{mol\,m^{-2}\,s^{-1}}$
$\Re^{\mathrm{v}}_{ij}$	Source of species i in channel j due to volumetric reaction	$\mathrm{mol\,m^{-3}\,s^{-1}}$
S_{hj}	Heat source due to chemical reaction in channel j	$\mathrm{W\,m^{-3}}$
$\vec{\mathbf{v}}_j$	Velocity field in channel j	$\mathrm{m\,s^{-1}}$
t	Time	s
T_j	Temperature in channel j	K, °C
T_w	Wall (fin) temperature	K, °C
Y_{ij}	Mass fraction of species i in channel j	—
ϵ_j	Porosity of catalytic washcoat in channel j	—
ρ_{fj}	Fluid density in channel j	$\mathrm{kg\,m^{-3}}$
ρ_{sj}	Solid density of catalytic washcoat in channel j	$\mathrm{kg\,m^{-3}}$
ρ_w	Solid wall (fin) density	$\mathrm{kg\,m^{-3}}$
$\bar{\bar{\tau}}_j$	Stress tensor in channel j due to flow	$\mathrm{kg\,m^{-2}\,s^{-2}}$

Below is a thorough overview of the equations that describe every phenomenon (e.g. momentum, species and heat transport, flow in washcoats, source terms originating from the reactions) in microchannel reactors. The equations presented in Table 4.3 are given in three- and two-dimensional Cartesian coordinates in hierarchically simplified forms. They are also presented for 2D axisymmetric geometries.

4.2.3.3. Continuity Equation. Equation 4.17 is the general form of the continuity equation whose 2D and 3D Cartesian and 2D axisymmetric forms for incompressible flows (constant ρ_{fj}, $\partial\rho_{fj}/\partial t = 0$) are shown in Table 4.5.

Table 4.5. The continuity equation in 2D and 3D Cartesian coordinates, and in 2D axisymmetric (AS) geometries for incompressible flows.

2D	$\frac{\partial}{\partial x}\left(\rho_{fj}v_{xj}\right) + \frac{\partial}{\partial y}\left(\rho_{fj}v_{yj}\right) = 0$	(4.22)
3D	$\frac{\partial}{\partial x}\left(\rho_{fj}v_{xj}\right) + \frac{\partial}{\partial y}\left(\rho_{fj}v_{yj}\right) + \frac{\partial}{\partial z}\left(\rho_{fj}v_{zj}\right) = 0$	(4.23)
AS	$\frac{\partial}{\partial z}\left(\rho_{fj}v_{zj}\right) + \frac{\partial}{\partial r}\left(\rho_{fj}v_{rj}\right) + \frac{\rho_{fj}v_{rj}}{r} = 0$	(4.24)

4.2.3.4. Momentum Conservation Equation. Conservation of momentum in channel j in an inertial (non-accelerating) reference frame is described by Equation 4.18. The stress tensor $\bar{\bar{\tau}}_j$ is given by

$$\bar{\bar{\tau}}_j = \mu_j \left[\left(\nabla\vec{\mathbf{v}}_j + \nabla\vec{\mathbf{v}}_j^{\mathrm{T}} \right) - \frac{2}{3}\nabla\cdot\vec{\mathbf{v}}_j\mathbf{I} \right] \tag{4.30}$$

where μ_j is the molecular viscosity of the gas mixture in channel j, $\mathbf{I}$ is the unit tensor, and the second term on the right-hand side is the effect of volume dilation that contributes to dissipation of momentum due to viscous forces. However, its effect on the velocity field and the viscous heating of the fluid is small, therefore, it can be dropped out from the stress tensor term. The 3D Cartesian and 2D axisymmetric

Table 4.6. The momentum conservation equation in 3D Cartesian coordinates, and in 2D axisymmetric (AS) geometries.

3D	$\boldsymbol{x}$**:** $\frac{\partial}{\partial t}(\rho_{fj}v_{xj}) + v_{xj}\frac{\partial}{\partial x}(\rho_{fj}v_{xj}) + v_{yj}\frac{\partial}{\partial y}(\rho_{fj}v_{xj}) + v_{zj}\frac{\partial}{\partial z}(\rho_{fj}v_{xj}) = \vec{F}_x - \frac{\partial p_j}{\partial x} + \frac{\partial}{\partial x}\left(\mu_j\frac{\partial v_{xj}}{\partial x}\right) + \frac{\partial}{\partial y}\left(\mu_j\frac{\partial v_{xj}}{\partial y}\right) + \frac{\partial}{\partial z}\left(\mu_j\frac{\partial v_{xj}}{\partial z}\right)$	(4.25)
	$\boldsymbol{y}$**:** $\frac{\partial}{\partial t}(\rho_{fj}v_{yj}) + v_{xj}\frac{\partial}{\partial x}(\rho_{fj}v_{yj}) + v_{yj}\frac{\partial}{\partial y}(\rho_{fj}v_{yj}) + v_{zj}\frac{\partial}{\partial z}(\rho_{fj}v_{yj}) = \vec{F}_y - \frac{\partial p_j}{\partial y} + \frac{\partial}{\partial x}\left(\mu_j\frac{\partial v_{yj}}{\partial x}\right) + \frac{\partial}{\partial y}\left(\mu_j\frac{\partial v_{yj}}{\partial y}\right) + \frac{\partial}{\partial z}\left(\mu_j\frac{\partial v_{yj}}{\partial y}\right)$	(4.26)
	$\boldsymbol{z}$**:** $\frac{\partial}{\partial t}(\rho_{fj}v_{zj}) + v_{xj}\frac{\partial}{\partial x}(\rho_{fj}v_{zj}) + v_{yj}\frac{\partial}{\partial y}(\rho_{fj}v_{zj}) + v_{zj}\frac{\partial}{\partial z}(\rho_{fj}v_{zj}) = \vec{F}_z - \frac{\partial p_j}{\partial z} + \frac{\partial}{\partial x}\left(\mu_j\frac{\partial v_{zj}}{\partial x}\right) + \frac{\partial}{\partial y}\left(\mu_j\frac{\partial v_{zj}}{\partial y}\right) + \frac{\partial}{\partial z}\left(\mu_j\frac{\partial v_{zj}}{\partial y}\right)$	(4.27)
AS	$\boldsymbol{z}$**:** $\frac{\partial}{\partial t}(\rho_{fj}v_{zj}) + v_{rj}\frac{\partial}{\partial r}(\rho_{fj}v_{zj}) + v_{zj}\frac{\partial}{\partial z}(\rho_{fj}v_{zj}) = \vec{F}_z - \frac{\partial p_j}{\partial z} + \frac{1}{r}\frac{\partial}{\partial r}\left(r\mu_j\frac{\partial v_{zj}}{\partial r}\right) + \frac{\partial}{\partial z}\left(\mu_j\frac{\partial v_{zj}}{\partial z}\right)$	(4.28)
	$\boldsymbol{r}$**:** $\frac{\partial}{\partial t}(\rho_{fj}v_{rj}) + v_{rj}\frac{\partial}{\partial r}(\rho_{fj}v_{rj}) + v_{zj}\frac{\partial}{\partial z}(\rho_{fj}v_{zj}) = \vec{F}_r - \frac{\partial p_j}{\partial r} + \frac{\partial}{\partial r}\left[\frac{1}{r}\frac{\partial}{\partial r}(r\mu_j v_{rj})\right] + \frac{\partial}{\partial z}\left[\mu_j\frac{\partial v_{rj}}{\partial z}\right]$	(4.29)

forms after simplification are shown in Table 4.6. The 2D form in Cartesian coordinates is not given since it can easily be obtained from the 3D form by dropping the terms associated with the z-direction.

4.2.3.5. Flow in Porous Media. The approach to model flow in porous catalytic washcoats is twofold:

(i) either by the addition of a momentum source term to the standard fluid flow equations
(ii) or by replacement of standard fluid flow equations with Brinkman-extended Darcy equations in the porous media

(i) The source term in channel j is composed of two parts: a viscous loss term (Darcy, the first term on the right-hand side of Equation 4.31, and an inertial loss term (the second term on the right-hand side of Equation 4.31:

$$\vec{\mathbf{F}}_j = -\left(\mathbf{D}_j \mu_j \vec{\mathbf{v}}_j + \mathbf{C}_j \frac{1}{2} \rho_j |\vec{\mathbf{v}}_j| \vec{\mathbf{v}}_j\right) \tag{4.31}$$

where $\vec{\mathbf{F}}_j$ is vector of source terms, $|\vec{\mathbf{v}}_j|$ is the magnitude of the velocity, and $\mathbf{D}_j$ and $\mathbf{C}_j$ are prescribed matrices. This momentum sink contributes to the pressure gradient in the porous cell, creating a pressure drop that is proportional to the fluid velocity (or velocity squared) in the cell.

The case of simple homogeneous porous media is

$$\vec{\mathbf{F}}_j = -\left(\frac{\mu_j}{\alpha_j} \vec{\mathbf{v}}_j + C_{2j} \frac{1}{2} \rho_j |\vec{\mathbf{v}}_j| \vec{\mathbf{v}}_j\right) \tag{4.32}$$

where α_j is the permeability of the washcoat, and C_{2j} is the inertial resistance factor.

(ii) The use of Brinkman-extended Darcy model equations for flow in a porous medium (Table 4.7) is also common. In accordance with the Darcy model, the second

Table 4.7. The Brinkman-extended Darcy equation in 3D Cartesian coordinates, and in 2D axisymmetric (AS) geometries for flow in porous media.

3D	$\boldsymbol{x}$**:** $\frac{1}{\epsilon_j}\frac{\partial}{\partial t}\left(\rho_{fj}v_{xj}\right)+\left(\frac{\mu_j}{\alpha_j}\right)v_{xj}=-\frac{\partial p_j}{\partial x}+\frac{\partial}{\partial x}\left[\left(\frac{\mu_{\text{eff},j}}{\epsilon_j}\right)\frac{\partial v_{xj}}{\partial x}\right]+\frac{\partial}{\partial y}\left[\left(\frac{\mu_{\text{eff},j}}{\epsilon_j}\right)\frac{\partial v_{xj}}{\partial y}\right]+\frac{\partial}{\partial z}\left[\left(\frac{\mu_{\text{eff},j}}{\epsilon_j}\right)\frac{\partial v_{xj}}{\partial z}\right]$	(4.33)
	$\boldsymbol{y}$**:** $\frac{1}{\epsilon_j}\frac{\partial}{\partial t}\left(\rho_{fj}v_{yj}\right)+\left(\frac{\mu_j}{\alpha_j}\right)v_{yj}=-\frac{\partial p_j}{\partial y}+\frac{\partial}{\partial x}\left[\left(\frac{\mu_{\text{eff},j}}{\epsilon_j}\right)\frac{\partial v_{yj}}{\partial x}\right]+\frac{\partial}{\partial y}\left[\left(\frac{\mu_{\text{eff},j}}{\epsilon_j}\right)\frac{\partial v_{yj}}{\partial y}\right]+\frac{\partial}{\partial z}\left[\left(\frac{\mu_{\text{eff},j}}{\epsilon_j}\right)\frac{\partial v_{yj}}{\partial z}\right]$	(4.34)
	$\boldsymbol{z}$**:** $\frac{1}{\epsilon_j}\frac{\partial}{\partial t}\left(\rho_{fj}v_{zj}\right)+\left(\frac{\mu_j}{\alpha_j}\right)v_{zj}=-\frac{\partial p_j}{\partial z}+\frac{\partial}{\partial x}\left[\left(\frac{\mu_{\text{eff},j}}{\epsilon_j}\right)\frac{\partial v_{zj}}{\partial x}\right]+\frac{\partial}{\partial y}\left[\left(\frac{\mu_{\text{eff},j}}{\epsilon_j}\right)\frac{\partial v_{zj}}{\partial y}\right]+\frac{\partial}{\partial z}\left[\left(\frac{\mu_{\text{eff},j}}{\epsilon_j}\right)\frac{\partial v_{zj}}{\partial z}\right]$	(4.35)
AS	$\boldsymbol{z}$**:** $\frac{1}{\epsilon_j}\frac{\partial}{\partial t}\left(\rho_{fj}v_{zj}\right)+\left(\frac{\mu_j}{\alpha_j}\right)v_{zj}=-\frac{\partial p_j}{\partial z}+\frac{1}{r}\frac{\partial}{\partial r}\left[r\left(\frac{\mu_{\text{eff},j}}{\epsilon_j}\right)\frac{\partial v_{zj}}{\partial r}\right]+\frac{\partial}{\partial z}\left[\left(\frac{\mu_{\text{eff},j}}{\epsilon_j}\right)\frac{\partial v_{zj}}{\partial z}\right]$	(4.36)
	$\boldsymbol{r}$**:** $\frac{1}{\epsilon_j}\frac{\partial}{\partial t}\left(\rho_{fj}v_{rj}\right)+\left(\frac{\mu_j}{\alpha_j}\right)v_{rj}=-\frac{\partial p_j}{\partial r}+\frac{\partial}{\partial r}\left[\frac{1}{r}\frac{\partial}{\partial r}\left\{r\left(\frac{\mu_{\text{eff},j}}{\epsilon_j}\right)v_{rj}\right\}\right]+\frac{\partial}{\partial z}\left[\left(\frac{\mu_{\text{eff},j}}{\epsilon_j}\right)\frac{\partial v_{rj}}{\partial z}\right]$	(4.37)

term on the left-hand side of each equation corresponds to viscous fluid motion due to the pressure gradient. The Darcy number ($\mathrm{Da}_j = \alpha_j/\delta_{sj}$) is between 1 and 4, which is quite large as to make the flow non-Darcian. Therefore, an extension to the model is necessary. The viscous Brinkman terms appear on the right-hand sides of Equations 4.33-4.37. These equations lack the inertial (convective) terms, which are replaced by those accounting for the boundary frictional drag on the impermeable walls of the channels. Flow within the porous medium is not due to inertial effects but due to the combination of viscous and pressure effects. Inertial losses during flow in the medium can be accounted for by the Brinkman-Forchheimer extension of the Darcy equation through the dimensionless term $C_{Fj}|\vec{\mathbf{v}}_j|\vec{\mathbf{v}}_j/\mathrm{Da}_j^{1/2}$ [268]. However, due to the high value of the Darcy number, inertial effects, thus the Forchheimer term, can be neglected. The Brinkman-extended Darcy model makes use of an effective viscosity $\mu_{\mathrm{eff},j}$. Studies in the literature report varying and sometimes inconsistent results as to the magnitude of the effective viscosity ($\mu_{\mathrm{eff},j} < 1 \,\mathrm{and}\, 1 < \mu_{\mathrm{eff},j} < 10$) [269, 270]. Moreover, its value strongly depends on the geometry of the medium [271]. Therefore, it is taken to be equal to the fluid viscosity in the gas phase.

The coupling between the full set of Navier-Stokes equations in the gas phase and the Brinkman-extended Darcy equations in the catalyst is made possible by means of the conditions that the velocity and the normal component of the stress tensor are continuous across the gas-solid boundary.

4.2.3.6. Species Mass Conservation. Equation 4.19 is the general form of the species mass conservation equation whose 3D Cartesian and 2D axisymmetric forms are shown in Table 4.8. Note that the species concentrations c_{ij} or mole fractions x_{ij} can always be substituted for the mass fractions Y_{ij} in the equations through appropriate relations and the ideal gas assumption.

The Fickian diffusive mass flux of species i in channel j, $\vec{J}_{ij}$, is given by

$$\vec{J}_{ij} = -\rho_{fj} D_{\mathrm{eff},i,mj} \nabla Y_{ij} \qquad i = 1, 2, \ldots, N_g \tag{4.40}$$

Table 4.8. The species conservation equation in 3D Cartesian coordinates, and in 2D axisymmetric (AS) geometries.

3D	$\frac{\partial}{\partial t}\left(\rho_{fj}Y_{ij}\right)+v_{xj}\frac{\partial}{\partial x}\left(\rho_{fj}Y_{ij}\right)+v_{yj}\frac{\partial}{\partial y}\left(\rho_{fj}Y_{ij}\right)+v_{zj}\frac{\partial}{\partial z}\left(\rho_{fj}Y_{ij}\right)=$ $\frac{\partial}{\partial x}\left[D_{\text{eff},i,mj}\frac{\partial}{\partial x}\left(\rho_{fj}Y_{ij}\right)\right]+\frac{\partial}{\partial y}\left[D_{\text{eff},i,mj}\frac{\partial}{\partial y}\left(\rho_{fj}Y_{ij}\right)\right]$ $+\frac{\partial}{\partial z}\left[D_{\text{eff},i,mj}\frac{\partial}{\partial z}\left(\rho_{fj}Y_{ij}\right)\right]+M_{ij}\Re_{ij}^{\text{v}}+M_{ij}\Re_{ij}^{\text{s}}A_{sj}$ (4.38)
AS	$\frac{\partial}{\partial t}\left(\rho_{fj}Y_{ij}\right)+v_{rj}\frac{\partial}{\partial r}\left(\rho_{fj}Y_{ij}\right)+v_{zj}\frac{\partial}{\partial z}\left(\rho_{fj}Y_{ij}\right)=$ $\frac{1}{r}\frac{\partial}{\partial r}\left[rD_{\text{eff},i,mj}\frac{\partial}{\partial r}\left(\rho_{fj}Y_{ij}\right)\right]+\frac{\partial}{\partial z}\left[D_{\text{eff},i,mj}\frac{\partial}{\partial z}\left(\rho_{fj}Y_{ij}\right)\right]$ $+M_{ij}\Re_{ij}^{\text{v}}+M_{ij}\Re_{ij}^{\text{s}}A_{sj}$ (4.39)

where $D_{\text{eff},i,mj}$ is the effective diffusivity of species i in the mixture, and N_g is the number of gas-phase species. If the flow is in the gas phase, $D_{\text{eff},i,mj}$ simply equals $D_{i,mj}$. If flow in porous media is under consideration, $D_{\text{eff},i,mj}$ is calculated using $D_{i,mj}$ and the Knudsen diffusion in the pores of the medium. In Equations 4.39 and 4.40, the consumption/production rate of species i in channel j during volumetric and wall-surface reactions is given respectively by $\Re_{ij}^{\text{v}}$ and $\Re_{ij}^{\text{s}}$. M_{ij} is the molecular weight of species i, and A_{sj} is the active surface area-to-volume ratio of the catalyst in channel j. In a given channel j, if there is a reaction or group of reactions taking place, it follows either the volume- or wall-surface-based catalytic mechanism.

4.2.3.7. Energy Equation. In the generalized energy equation (Equation 4.20) in Table 4.3, several terms can be dropped out due to their negligible effect on temperature variation. The second and third terms on the right-hand side, $\sum_i h_{ij}\vec{J}_{ij}$, which accounts for the heat transfer by the diffusive flux of all the species, and $\bar{\bar{\tau}}_j\vec{\mathbf{v}}_j$, which accounts for heat exchange due to viscous dissipation are such terms while the first term that represents conduction heat transfer is retained (Table 4.9).

Table 4.9. The energy equation in 3D Cartesian coordinates, and in 2D axisymmetric (AS) geometries.

3D	$\epsilon_j \frac{\partial}{\partial t}\left(\rho_{fj} c_{p_{fj}} T_j\right) + \left(1-\epsilon_j\right) \frac{\partial}{\partial t}\left(\rho_{sj} c_{p_{sj}} T_j\right) + v_{xj} \frac{\partial}{\partial y}\left(\rho_{fj} c_{p_{fj}} T_j\right)$ $+ v_{yj} \frac{\partial}{\partial x}\left(\rho_{fj} c_{p_{fj}} T_j\right) + v_{zj} \frac{\partial}{\partial z}\left(\rho_{fj} c_{p_{fj}} T_j\right) = \frac{\partial}{\partial x}\left[k_{\text{eff},j} \frac{\partial}{\partial x}\left(\rho_{fj} T_j\right)\right]$ $+ \frac{\partial}{\partial y}\left[k_{\text{eff},j} \frac{\partial}{\partial y}\left(\rho_{fj} T_j\right)\right] + \frac{\partial}{\partial z}\left[k_{\text{eff},j} \frac{\partial}{\partial z}\left(\rho_{fj} T_j\right)\right] + S_{hj}$ (4.41)
AS	$\epsilon_j \frac{\partial}{\partial t}\left(\rho_{fj} c_{p_{fj}} T_j\right) + \left(1-\epsilon_j\right) \frac{\partial}{\partial t}\left(\rho_{sj} c_{p_{sj}} T_j\right) + v_{rj} \frac{\partial}{\partial r}\left(\rho_{fj} c_{p_{fj}} T_j\right)$ $+ v_{zj} \frac{\partial}{\partial z}\left(\rho_{fj} c_{p_{fj}} T_j\right) = \frac{1}{r} \frac{\partial}{\partial r}\left[r k_{\text{eff},j} \frac{\partial}{\partial r}\left(\rho_{fj} T_j\right)\right]$ $+ \frac{\partial}{\partial z}\left[k_{\text{eff},j} \frac{\partial}{\partial z}\left(\rho_{fj} T_j\right)\right] + S_{hj}$ (4.42)

4.2.3.8. Treatment of the Energy Equation in Porous Media. Effective thermal conductivity of the fluid in the catalytic washcoats is calculated using the volume average of the fluid and solid conductivities:

$$k_{\text{eff},j} = \epsilon_j k_{fj} + \left(1-\epsilon_j\right) k_{sj} \tag{4.43}$$

Thus, when flow and transport in the gas phase are being solved for, the porosity is taken to be equal to 1, which, in 3D Cartesian coordinates, reduces Equation 4.41 to

$$\begin{aligned} &\frac{\partial}{\partial t}\left(\rho_{fj} c_{p_{fj}} T_j\right) + v_{xj} \frac{\partial}{\partial x}\left(\rho_{fj} c_{p_{fj}} T_j\right) \\ &+ v_{yj} \frac{\partial}{\partial y}\left(\rho_{fj} c_{p_{fj}} T_j\right) + v_{zj} \frac{\partial}{\partial z}\left(\rho_{fj} c_{p_{fj}} T_j\right) = \frac{\partial}{\partial x}\left[k_{f,j} \frac{\partial}{\partial x}\left(\rho_{fj} T_j\right)\right] \\ &+ \frac{\partial}{\partial y}\left[k_{f,j} \frac{\partial}{\partial y}\left(\rho_{fj} T_j\right)\right] \frac{\partial}{\partial z}\left[k_{f,j} \frac{\partial}{\partial z}\left(\rho_{fj} T_j\right)\right] + S_{hj} \end{aligned} \tag{4.44}$$

The source of energy, S_{hj}, in Equations 4.41 and 4.42 consists of the sum of

enthalpies of all volumetric and surface reactions in channel j:

$$S_{hj} = \sum_{k_v=1}^{N_{\text{vrxn}}} \left(-\Delta H_{k_v}\right) \mathcal{R}^{\text{v}}_{k_v,j} + \sum_{k_s=1}^{N_{\text{srxn}}} \left(-\Delta H_{k_s}\right) A_{sj} \mathcal{R}^{\text{s}}_{k_s,j} \tag{4.45}$$

4.2.3.9. Energy Equation in the Fins. Equation 4.21 that describes heat flow in the fins is obtained when the terms associated with convective heat transfer in Equation 4.23 are dropped out, and the physical properties equated to those of the fin. In 3D Cartesian coordinates, the energy equation in the fins is

$$\begin{aligned} \frac{\partial}{\partial t}\left(\rho_w c_{p_w} T_w\right) = & \frac{\partial}{\partial x}\left[k_w \frac{\partial}{\partial x}\left(\rho_w T_w\right)\right] \\ & + \frac{\partial}{\partial y}\left[k_w \frac{\partial}{\partial y}\left(\rho_w T_w\right)\right] + \frac{\partial}{\partial z}\left[k_w \frac{\partial}{\partial z}\left(\rho_w T_w\right)\right] \end{aligned} \tag{4.46}$$

4.2.4. Boundary Conditions

The generalized transport equations given in Table 4.3 are solved subject to the boundary conditions in Table 4.10.

4.2.4.1. Channel Entrance. The flow velocity is assumed to be unidirectional at the channel entrances $z_j = 0$, therefore, a normal inflow velocity ($v_{zj} = U_j^{\text{in}}$) is specified. Concentration or mass fraction of each species i fed to the channel j is also prescribed. A constant, time-independent temperature inlet condition in each channel inlet is used.

4.2.4.2. Symmetry Lines. Across a symmetry boundary, flux of all quantities are assumed to be zero. There is no convective flux across a symmetry plane or line, thus the normal velocity component is zero. There is no diffusion flux across a symmetry plane or line either, therefore, gradients of all flow variables are zero. Since the shear stress is zero at a symmetry boundary, it can also be interpreted as a "slip" wall when used in viscous flow calculations.

Table 4.10. Boundary conditions associated with the generalized transport equations given in Table 4.3.

Channel entrance	$z_j = 0; \quad \forall x_j, y_j$ or $\forall r_j$	
Velocity $v_{zj} = U_j^{\text{in}}$	Species $c_{ij} = c_{ij}^{\text{in}}$ or $Y_{ij} = Y_{ij}^{\text{in}}$	Temperature $T_j = T_j^{\text{in}}$
Symmetry at the channel centerline	$\forall z_j$	
Velocity $\vec{\mathbf{n}} \cdot \vec{\mathbf{v}}_j = 0$	Species $\vec{\mathbf{n}} \cdot \left(\vec{J}_{ij} + \rho_{fj} \vec{\mathbf{v}}_j Y_{ij} \right) = 0$	Temperature $\vec{\mathbf{n}} \cdot \left(-k_{\text{eff},j} \nabla T_j + \rho_{fj} c_{p_{fj}} \vec{\mathbf{v}}_j T_j \right) = 0$
Fin-channel interface	$\forall z_j$	
Velocity $\vec{\mathbf{n}} \cdot \vec{\mathbf{v}}_j = 0$	Species $\vec{\mathbf{n}} \cdot \left(\vec{J}_{ij} + \rho_{fj} \vec{\mathbf{v}}_j Y_{ij} \right) = 0$	Temperature $\vec{\mathbf{n}} \cdot (-k_w \nabla T_w) = \vec{\mathbf{n}} \cdot \left(-k_{\text{eff},j} \nabla T_j + \rho_{fj} c_{p_{fj}} \vec{\mathbf{v}}_j T_j \right) = 0$
Gas-solid interface	$\forall z_j$	
Velocity & Stress tensor $\vec{\mathbf{v}}_j\|_{\Gamma_{\text{gas}}} = \vec{\mathbf{v}}_j\|_{\Gamma_{\text{solid}}}$ $\vec{\mathbf{n}}_j \cdot \bar{\bar{\tau}}_j\|_{\Gamma_{\text{gas}}} = \vec{\mathbf{n}}_j \cdot \bar{\bar{\tau}}_j\|_{\Gamma_{\text{solid}}}$	Species $Y_{ij}\|_{\Gamma_{\text{gas}}} = Y_{ij}\|_{\Gamma_{\text{solid}}}$ $\vec{\mathbf{n}} \cdot \left(\vec{J}_{ij} + \rho_{fj} \vec{\mathbf{v}}_j Y_{ij} \right)\Big\|_{\Gamma_{\text{gas}}} =$ $\vec{\mathbf{n}} \cdot \left(\vec{J}_{ij} + \rho_{fj} \vec{\mathbf{v}}_j Y_{ij} \right)\Big\|_{\Gamma_{\text{solid}}}$	Temperature $T_j\|_{\Gamma_{\text{gas}}} = T_j\|_{\Gamma_{\text{solid}}}$ $\vec{\mathbf{n}} \cdot \left(-k_{\text{eff},j} \nabla T_j + \rho_{fj} c_{p_{fj}} \vec{\mathbf{v}}_j T_j \right)\big\|_{\Gamma_{\text{gas}}} =$ $\vec{\mathbf{n}} \cdot \left(-k_{\text{eff},j} \nabla T_j + \rho_{fj} c_{p_{fj}} \vec{\mathbf{v}}_j T_j \right)\big\|_{\Gamma_{\text{solid}}}$
Channel exit	$z_j = L; \quad \forall x_j, y_j$ or $\forall r_j$	
Pressure $p_j = p_j^{\text{out}}$ $\dot{m}_j = \dot{m}_j{}^{\text{out}}$ (optional)	Species $\vec{\mathbf{n}} \cdot \vec{J}_{ij} = 0$ $Y_{ij} = Y_{ij}^{\text{out}}$ (backflow condition)	Temperature $\vec{\mathbf{n}} \cdot (-k_{\text{eff},j} \nabla T_j) = 0$ $T_j = T_j^{\text{out}}$ (backflow condition)
All other boundaries		
Velocity $\vec{\mathbf{n}} \cdot \vec{\mathbf{v}}_j = 0$	Species $\vec{\mathbf{n}} \cdot \left(\vec{J}_{ij} + \rho_{fj} \vec{\mathbf{v}}_j Y_{ij} \right) = 0$	Temperature $\vec{\mathbf{n}} \cdot \left(-k_{\text{eff},j} \nabla T_j + \rho_{fj} c_{p_{fj}} \vec{\mathbf{v}}_j T_j \right) = 0$

4.2.4.3. Fin-Channel Interface. In viscous flows, the no-slip boundary condition is prescribed at the walls, meaning that the fluid velocity is zero at a solid, impermeable, stationary boundary, which, in this case is the fin-channel interface(s). Due to the impermeability of the fins, mass flux of species is also zero at the interface. Heat flux across the boundary, however, is continuous except for the insulated portions of the channels in the combustion-reforming/dehydrogenation coupling (Figure 4.6).

4.2.4.4. Gas-Solid Interface. The common choice of conditions associated with a gas-solid boundary are the continuity of the vector or scalar quantity (e.g. velocity, mass fraction, temperature), and continuity of the normal component of the diffusion tensor (e.g. momentum, mass, heat).

4.2.4.5. Channel Exit. At the channel exit, gauge pressure is set to a value. In order to double-check the converged results, it is good practice to also set a target mass flow rate for steady-state flow. While using the finite volume method (FVM), in case reversed flow occurs at the exit, backflow conditions consistent with the flow model assist in minimizing convergence difficulties. Diffusive mass and heat fluxes are prescribed to be zero while using the finite element method (FEM).

4.2.4.6. All Other Boundaries. The system or unit cell boundaries other than the ones explained above are treated as insulated walls or symmetry boundaries where the velocity falls down to zero, and there are no mass or heat fluxes.

4.2.5. Reaction Kinetics

The rates and heats of reactions are needed in the species mass conservation and energy equations (Equations 4.19 and 4.20). In Table 4.12-22, global kinetics and kinetic parameters of all volumetric reactions ($\mathcal{R}^{v}_{k_v,j}$) used in this work are given either as power-law or Langmuir-Hinshelwood-Hougen-Watson-type expressions. The kinetic parameters (rate and adsorption constants) are calculated by Arrhenius-type expressions. Steam reforming kinetics considered during simulation of methane ATR

is handled by a detailed surface reaction mechanism that takes place over a Rh/Al_2O_3 catalyst whose composition is proprietary [272].

Table 4.11. Index of rates of volumetric reactions taking place over washcoated catalysts in the microchannels.

$\mathcal{R}^{v}_{k_v,j}$	**Combustion Reactions**	$\mathcal{R}^{v}_{k_v,j}$	**Steam Reforming Reactions**
1	$CH_4 + 2O_2 \rightarrow CO_2 + 2H_2O$	**5a**	$CH_4 + H_2O \rightleftharpoons CO + 3H_2$
		5b	$CH_4 + 2H_2O \rightleftharpoons CO_2 + 4H_2$
		5c	$CO + H_2O \rightleftharpoons CO_2 + H_2$
2	$C_3H_8 + 5O_2 \rightarrow 3CO_2 + 4H_2O$	**6**	$C_3H_8 + 3H_2O \rightleftharpoons 3CO + 7H_2$
3	$CH_3OH + 3/2O_2 \rightarrow CO_2 + 2H_2O$	**7**	$CH_3OH + H_2O \rightleftharpoons CO_2 + 3H_2$
4	$C_2H_5OH + 3O_2 \rightarrow 2CO_2 + 3H_2O$	**8**	$C_2H_5OH + H_2O \rightleftharpoons 2CO + 4H_2$
		9	$n\text{-}C_7H_{16} + 7H_2O \rightleftharpoons 7CO + 15H_2$
		10	$iso\text{-}C_8H_{18} + 8H_2O \rightleftharpoons 8CO + 17H_2$
		11	$C_2H_6 \rightleftharpoons C_2H_4 + H_2$

4.2.5.1. Global Kinetics of Volumetric Reactions. Table 4.11 shows enumeration of the rates of volumetric reactions that take place over catalytic washcoats in the microchannels, where k is the index of volumetric reactions. Each reaction or group of reactions (as in the case of steam reforming of methane over Ni, item 5 in Table 4.11) are handled separately in Table 4.12-22.

Table 4.12. Kinetic rate expression for (1) methane combustion.

$CH_4 + 2O_2 \rightarrow CO_2 + 2H_2O$	$\Delta H^0_{298} = -802.3\,\mathrm{kJ\,mol^{-1}}$		$Pt/\delta\text{-}Al_2O_3$ [107]
$\mathcal{R}^{v}_{1j} = \dfrac{k^{v}_{1j} K_{CH_4} p_{CH_4} \sqrt{K_{O_2} p_{O_2}}}{\left(1 + K_{CH_4} p_{CH_4} + \sqrt{K_{O_2} p_{O_2}}\right)^2}$		$[\mathrm{mol\,m^{-3}\,s^{-1}}]$	(4.47)
$k^{v}_{1j} = k^{v}_{1_0} \exp\left(-\dfrac{E_1}{RT}\right)$	k_{1_0}	43.9	$[\mathrm{mol\,m^{-3}\,s^{-1}}]$
	E_1	35.257	$[\mathrm{kJ\,mol^{-1}}]$
$K_{CH_4} = K_{CH_{4_0}} \exp\left(-\dfrac{\Delta H_{CH_4}}{RT}\right)$	$K_{CH_{4_0}}$	4324	$[\mathrm{bar^{-1}}]$
	ΔH_{CH_4}	46.554	$[\mathrm{kJ\,mol^{-1}}]$
$K_{O_2} = K_{O_{2_0}} \exp\left(-\dfrac{\Delta H_{O_2}}{RT}\right)$	$K_{O_{2_0}}$	4.41×10^{-3}	$[\mathrm{bar^{-1}}]$
	ΔH_{O_2}	-61.939	$[\mathrm{kJ\,mol^{-1}}]$

Table 4.13. Kinetic rate expression for (2) propane combustion.

$C_3H_8 + 5O_2 \rightarrow 3CO_2 + 4H_2O$	$\Delta H^0_{298} = -2044\,\mathrm{kJ\,mol^{-1}}$		Pt/δ-Al_2O_3 [107]
$\mathcal{R}^{\mathrm{v}}_{2j} = k^{\mathrm{v}}_{2j}\left(100 \cdot p_{C_3H_8}\right)^{1.1}\left(100 \cdot p_{O_2}\right)^{-0.6}$		$[\mathrm{mol\,m^{-3}\,s^{-1}}]$	(4.48)
$k^{\mathrm{v}}_{2j} = k_{2_0}\exp\left(-\dfrac{E_2}{RT}\right)$	k_{2_0}	1.87×10^8	$[\mathrm{mol\,m^{-3}\,s^{-1}\,bar^{-0.5}}]$
	E_2	104.318	$[\mathrm{kJ\,mol^{-1}}]$

Table 4.14. Kinetic rate expression for (3) methanol combustion.

$CH_3OH + 3/2O_2 \rightarrow CO_2 + 2H_2O$	$\Delta H^0_{298} = -676\,\mathrm{kJ\,mol^{-1}}$		Pt/Al_2O_3 [249]
$\mathcal{R}^{\mathrm{v}}_{3j} = k^{\mathrm{v}}_{3j} c_{CH_3OH}$		$[\mathrm{mol\,m^{-3}\,s^{-1}}]$	(4.49)
$k^{\mathrm{v}}_{3j} = \begin{cases} 1000\exp\left(-\dfrac{5.9\times10^4}{RT} + 22.45\right) & T < 380\,\mathrm{K} \\ 1000\exp\left(-\dfrac{6.4\times10^3}{RT} + 5.8\right) & T > 380\,\mathrm{K} \end{cases}$		$[\mathrm{s^{-1}}]$	

Table 4.15. Kinetic rate expression for (4) ethanol combustion.

$C_2H_5OH + 1/2O_2 \rightarrow CH_3CHO + H_2O$ $CH_3CHO + 5/2O_2 \rightarrow 2CO_2 + 2H_2O$	Cu-CrO/Al_2O_3 $\Delta H^0_{298} = -1278\,\mathrm{kJ\,mol^{-1}}$		[250]
$\mathcal{R}^{\mathrm{v}}_{4a,j} = k^{\mathrm{v}}_{4a,j} c_{C_2H_5OH} c^{0.5}_{O_2}$		$[\mathrm{mol\,m^{-3}\,s^{-1}}]$	(4.50)
$\mathcal{R}^{\mathrm{v}}_{4b,j} = k^{\mathrm{v}}_{4b,j} c_{CH_3CHO} c^{0.5}_{O_2}$		$[\mathrm{mol\,m^{-3}\,s^{-1}}]$	(4.51)
$k^{\mathrm{v}}_{4a,j} = k_{4a_0}\exp\left(-\dfrac{E_{4a}}{RT}\right)$	k_{4a_0}	2.06×10^8	$[\mathrm{mol^{-0.5}\,m^{1.5}\,s^{-1}}]$
	E_{4a}	79.1	$[\mathrm{kJ\,mol^{-1}}]$
$k^{\mathrm{v}}_{4b,j} = k_{4b_0}\exp\left(-\dfrac{E_{4b}}{RT}\right)$	k_{4a_0}	3.33×10^{15}	$[\mathrm{mol^{-0.5}\,m^{1.5}\,s^{-1}}]$
	E_{4b}	157.7	$[\mathrm{kJ\,mol^{-1}}]$

Table 4.16. Kinetic rate expression for (5) steam reforming of methane.

$CH_4 + H_2O \rightleftharpoons CO + 3H_2$ $CH_4 + 2H_2O \rightleftharpoons CO_2 + 4H_2$ $CO + H_2O \rightleftharpoons CO_2 + H_2$	$\Delta H^0_{298} = 206.2\,\mathrm{kJ\,mol^{-1}}$ $\Delta H^0_{298} = 165\,\mathrm{kJ\,mol^{-1}}$ $\Delta H^0_{298} = -41.2\,\mathrm{kJ\,mol^{-1}}$		$Ni/MgO\text{-}Al_2O_4$ [134]
$\mathcal{R}^{\mathrm{v}}_{5a,j} = \dfrac{k^{\mathrm{v}}_{5a,j}/p^{2.5}_{H_2}\left(p_{CH_4}p_{H_2O} - p^3_{H_2}p_{CO}/K^{\mathrm{I}}_{\mathrm{eq}}\right)}{\mathrm{DEN}^2}$		$[\mathrm{mol\,kg^{-3}_{cat}\,s^{-1}}]$	(4.52)
$\mathcal{R}^{\mathrm{v}}_{5b,j} = \dfrac{k^{\mathrm{v}}_{5b,j}/p^{3.5}_{H_2}\left(p_{CH_4}p^2_{H_2O} - p^4_{H_2}p_{CO_2}/K^{\mathrm{II}}_{\mathrm{eq}}\right)}{\mathrm{DEN}^2}$		$[\mathrm{mol\,kg^{-3}_{cat}\,s^{-1}}]$	(4.53)
$\mathcal{R}^{\mathrm{v}}_{5c,j} = \dfrac{k^{\mathrm{v}}_{5c,j}/p_{H_2}\left(p_{CO}p_{H_2O} - p_{H_2}p_{CO_2}/K^{\mathrm{III}}_{\mathrm{eq}}\right)}{\mathrm{DEN}^2}$		$[\mathrm{mol\,kg^{-3}_{cat}\,s^{-1}}]$	(4.54)
$k^{\mathrm{v}}_{5a,j} = k_{5a_0}\exp\left(-\dfrac{E_{5a}}{RT}\right)$	k_{5a_0}	1.17×10^{15}	$[\mathrm{mol\,kg^{-1}_{cat}\,s^{-1}\,bar^{-0.5}}]$
	E_{5a}	240.1	$[\mathrm{kJ\,mol^{-1}}]$
$k^{\mathrm{v}}_{5b,j} = k_{5b_0}\exp\left(-\dfrac{E_{5b}}{RT}\right)$	k_{5b_0}	2.83×10^{14}	$[\mathrm{mol\,kg^{-1}_{cat}\,s^{-1}\,bar^{-0.5}}]$
	E_{5b}	243.9	$[\mathrm{kJ\,mol^{-1}}]$
$k^{\mathrm{v}}_{5c,j} = k_{5c_0}\exp\left(-\dfrac{E_{5c}}{RT}\right)$	k_{5c_0}	5.43×10^{5}	$[\mathrm{mol\,kg^{-1}_{cat}\,s^{-1}\,bar^{-1}}]$
	E_{5c}	67.13	$[\mathrm{kJ\,mol^{-1}}]$
$K^{\mathrm{I}}_{\mathrm{eq}} = 4.707 \times 10^{12}\exp\left(-\dfrac{224000}{RT}\right)$ $K^{\mathrm{III}}_{\mathrm{eq}} = 1.142 \times 10^{-2}\exp\left(-\dfrac{37300}{RT}\right)$ $K^{\mathrm{II}}_{\mathrm{eq}} = K^{\mathrm{I}}_{\mathrm{eq}}K^{\mathrm{III}}_{\mathrm{eq}}$			
$\mathrm{DEN} = (1 + K_{CO}p_{CO} + K_{H_2}p_{H_2} + K_{CH_4}p_{CH_4} + K_{H_2O}p_{H_2O}/p_{H_2})$			
$K_{CH_4} = K_{CH_{4_0}}\exp\left(-\dfrac{\Delta H_{CH_4}}{RT}\right)$	$K_{CH_{4_0}}$	6.65×10^{-4}	$[\mathrm{bar^{-1}}]$
	ΔH_{CH_4}	-38.28	$[\mathrm{kJ\,mol^{-1}}]$
$K_{H_2O} = K_{H_2O_0}\exp\left(-\dfrac{\Delta H_{H_2O}}{RT}\right)$	$K_{H_2O_0}$	1.77×10^{5}	$[\mathrm{bar^{-1}}]$
	ΔH_{H_2O}	88.68	$[\mathrm{kJ\,mol^{-1}}]$
$K_{CO} = K_{CO_0}\exp\left(-\dfrac{\Delta H_{CO}}{RT}\right)$	K_{CO_0}	8.23×10^{-5}	$[\mathrm{bar^{-1}}]$
	ΔH_{CO}	-70.65	$[\mathrm{kJ\,mol^{-1}}]$
$K_{H_2} = K_{H_{2_0}}\exp\left(-\dfrac{\Delta H_{H_2}}{RT}\right)$	$K_{H_{2_0}}$	6.12×10^{-9}	$[\mathrm{bar^{-1}}]$
	ΔH_{H_2}	-82.90	$[\mathrm{kJ\,mol^{-1}}]$

Table 4.17. Kinetic rate expression for (6) steam reforming of propane.

$C_3H_8 + 3H_2O \rightleftharpoons 3CO + 7H_2$	$\Delta H^0_{298} = 498\,\mathrm{kJ\,mol^{-1}}$		$Ni/MgO\text{-}Al_2O_3$ [68]
$\mathcal{R}^{\mathrm{v}}_{6j} = k^{\mathrm{v}}_{6j} \dfrac{(100 \cdot p_{C_3H_8})^{0.93} (100 \cdot p_{H_2O})^{-0.53}}{1 + \theta (100 \cdot p_{H_2})^{0.86}}$		$[\mathrm{mol\,m^{-3}\,s^{-1}}]$	(4.55)
$k^{\mathrm{v}}_{6j} = k_{6_0} \exp\left(-\dfrac{E_6}{RT}\right)$	k_{6_0}	2.14×10^{13}	$[\mathrm{mol\,m^{-3}\,s^{-1}\,kPa^{-0.4}}]$
	E_6	189.556	$[\mathrm{kJ\,mol^{-1}}]$
$\theta = 1$			$[\mathrm{kPa^{-0.86}}]$

Table 4.18. Kinetic rate expression for (7) steam reforming of methanol.

$CH_3OH + H_2O \rightleftharpoons CO_2 + 3H_2$	$\Delta H^0_{298} = 49.5\,\mathrm{kJ\,mol^{-1}}$		$Cu/ZnO\text{-}Al_2O_3$ [251]
$\mathcal{R}^{\mathrm{v}}_{7j} = k^{\mathrm{v}}_{7j} \left(10^5 \cdot p_{CH_3OH}\right)^{0.564} \left(11600 + 10^5 \cdot p_{H_2O}\right)^{-0.647}$		$[\mathrm{mol\,m^{-3}\,s^{-1}}]$	(4.56)
$k^{\mathrm{v}}_{7j} = k_{7_0} \exp\left(-\dfrac{E_7}{RT}\right)$	k_{7_0}	2.19×10^9	$[\mathrm{mol\,m^{-3}\,s^{-1}\,bar^{0.083}}]$
	E_7	103.0	$[\mathrm{kJ\,mol^{-1}}]$

Table 4.19. Kinetic rate expression for (8) steam reforming of ethanol.

$C_2H_5OH + H_2O \rightleftharpoons 2CO + 4H_2$	$\Delta H^0_{298} = 255\,\mathrm{kJ\,mol^{-1}}$		Ni/Al_2O_3 [84]
$\mathcal{R}^{\mathrm{v}}_{8j} = k^{\mathrm{v}}_{8j} \cdot A/B$		$[\mathrm{mol\,m^{-3}\,s^{-1}}]$	(4.57)
$k^{\mathrm{v}}_{8j} = k_{8_0} \exp\left(-\dfrac{E_7}{RT}\right)$	k_{8_0}	3.26×10^{16}	
	E_8	55.4	$[\mathrm{kJ\,mol^{-1}}]$
$A = \dfrac{(c_{C_2H_5OH}/1000) - (c_{CO_2}/1000)^2 (c_{H_2}/1000)^6}{K_{p,8} (c_{H_2O}/1000)^3}$			
$B = 1 + K_{8a} (c_{CO_2}/1000) + \dfrac{K_{8b} (c_{CO_2}/1000) (c_{H_2}/1000)^{0.5}}{(c_{H_2O}/1000)}$			
$K_{8a} = 4.48 \times 10^{10}$			
$K_{8b} = 7.28 \times 10^6$			
$K_{p,8} = \exp\left(\dfrac{\Delta S_8}{R} - \dfrac{\Delta H_8}{RT}\right)$			

Table 4.20. Kinetic rate expression for (9) steam reforming of *n*-heptane.

$n\text{-}C_7H_{16} + 7H_2O \rightleftharpoons 7CO + 15H_2O$ $\quad \Delta H^0_{298} = 1108\,\mathrm{kJ\,mol^{-1}}$			Ni/MgO-Al_2O_4 [252]
$\mathcal{R}^{\mathrm{v}}_{9j} = k^{\mathrm{v}}_{9j} \dfrac{k_9 p_{C_7H_{16}}}{\left[1 + K_{9a}\left(\frac{p_{C_7H_{16}} p_{H_2}}{p_{H_2O}}\right) + K_{9b}\left(\frac{p_{H_2O}}{p_{H_2}}\right)\right]^2}$		$[\mathrm{mol\,m^{-3}\,s^{-1}}]$	(4.58)
$k^{\mathrm{v}}_{9j} = k_{9_0} \exp\left(-\dfrac{E_9}{RT}\right)$	k_{9_0}	2.22×10^{-5}	$[\mathrm{mol\,kg^{-1}_{cat}\,s^{-1}\,bar^{-1}}]$
	E_9	67.8	$[\mathrm{kJ\,mol^{-1}}]$
$K_{9a} = 25.2$			$[\mathrm{bar^{-1}}]$
$K_{9b} = 0.077$			—

Table 4.21. Kinetic rate expression for (10) steam reforming of *iso*-octane.

$iso\text{-}C_8H_{18} + 8H_2O \rightleftharpoons 8CO + 17H_2$ $\quad \Delta H^0_{298} = 1274.8\,\mathrm{kJ\,mol^{-1}}$			Ni/Al_2O_3 [261]
$\mathcal{R}^{\mathrm{v}}_{10j} = \dfrac{k^{\mathrm{v}}_{10j}\sqrt{(100 \cdot p_{C_8H_{18}})\,(100 \cdot p_{H_2O})}}{1 + K_{C_8H_{18}} p_{C_8H_{18}} + K_{H_2O} p_{H_2O}}$		$[\mathrm{mol\,kg^{-1}_{cat}\,s^{-1}}]$	(4.59)
$k^{\mathrm{v}}_{10j} = k_{10_0} \exp\left(-\dfrac{E_{10}}{RT}\right)$	k_{10_0}	141	$[\mathrm{mol\,kg^{-1}_{cat}\,s^{-1}\,kPa^{-1}}]$
	E_9	46.079	$[\mathrm{kJ\,mol^{-1}}]$
$K_{C_8H_{18}} = K_{C_8H_{18}0} \exp\left(-\dfrac{\Delta H_{C_8H_{18}}}{RT}\right)$	$K_{C_8H_{18}0}$	2.16×10^{-2}	$[\mathrm{kPa^{-1}}]$
	$\Delta H_{C_8H_{18}}$	-18.525	$[\mathrm{kJ\,mol^{-1}}]$
$K_{H_2O} = K_{H_2O_0} \exp\left(-\dfrac{\Delta H_{H_2O}}{RT}\right)$	$K_{H_2O_0}$	2.64×10^{-3}	$[\mathrm{kPa^{-1}}]$
	ΔH_{H_2O}	-51.733	$[\mathrm{kJ\,mol^{-1}}]$

Table 4.22. Kinetic rate expression for (11) ethane dehydrogenation.

$C_2H_6 \rightleftharpoons C_2H_4 + H_2$ $\quad \Delta H^0_{298} = 136.9\,\mathrm{kJ\,mol^{-1}}$			Pd/Al_2O_3 [273]
$\mathcal{R}^{\mathrm{v}}_{11j} = k^{\mathrm{v}}_{11j}\left(p_{C_2H_6} - \frac{p_{C_2H_6}p_{H_2}}{K_{p,11}}\right)$		$[\mathrm{mol\,kg^{-1}_{cat}\,s^{-1}}]$	(4.60)
$k^{\mathrm{v}}_{11j} = k_{11_0}\exp\left(-\frac{E_{11}}{RT}\right)$	k_{11_0}	4.39×10^3	$[\mathrm{mol\,kg^{-1}_{cat}\,s^{-1}\,bar^{-1}}]$
	E_{11}	75.58	$[\mathrm{kJ\,mol^{-1}}]$
$K_{p,11} = 1.096\times10^7\exp\left(-\frac{143410}{RT}\right)$			

4.2.5.2. Surface Reaction Kinetics of Steam Reforming of Methane. The detailed surface reaction mechanism for steam reforming of methane over a Rh/Al_2O_3 catalyst [272] is given in Table 4.23. The mechanism consists of 44 elementary reactions with 6 gas-phase and 13 surface-adsorbed site species. Even though the mechanism is elementary, it presents a complete model including the water-gas shift and carbon formation (Bouduard) reactions. The temperature dependence of the reaction rate constants are of Arrhenius-type. Their dependence on surface coverage of species m is also considered in the following modified Arrhenius expression [274]:

$$k_{k_s,j} = A_{k_s,j}T_j^{\beta_{k_s}}\exp\left[-\frac{E_{k_s}}{RT_j}\right]\times\prod_{m=1}^{N_s}10^{\theta_m\eta_{mk}}\theta_m^{\mu_{mk}}\exp\left[-\frac{\epsilon_{mk}\theta_m}{RT_j}\right], \qquad m = 1,2,\ldots,N_s \tag{4.61}$$

In Equation 4.61, $\eta_{mk} = \mu_{mk} = 0$ for all site species in all reactions whereas ϵ_{m,k_s}, the coverage-dependent activation energy assumes values different from zero in certain reactions, as shown in Table 4.23. Values of the parameters $A_{k_s,j}$, E_{k_s} and β_{k_s} are given in Table 4.23. The consumption/production rate of gas-phase and site species i due to steam reforming is then defined by

$$\Re^{\mathrm{s}}_{i,\mathrm{SR}} = \sum_{k_s=1}^{N_{\mathrm{srxn}}}\left(\nu''_{i,k_s,j} - \nu'_{i,k_s,j}\right)k_{k_s,j}\prod_{l=1}^{N_g+N_s}c_{lj}^{\nu'_{i,k_s,j}}, \qquad i,l = 1,2,\ldots,N_g+N_s \tag{4.62}$$

c_{lj} is equal to the product of the surface coverage θ_{lj} and the surface site density Γ_j.

Table 4.23. Reaction mechanism for steam reforming of methane over Rh [272] (continued on the next page).

k_s	**Reaction**	$A_{k_s,j}$ (cm, mol, s)	β_{k_s}	E_{k_s} (kJ mol^{-1})
	Adsorption			
1.	H_2+Rh(s)+Rh(s)→ H(s)+H(s)	1.000×10^{-02}[a]	0.0	0.00
2.	O_2+Rh(s)+Rh(s)→ O(s)+O(s)	1.000×10^{-02}[a]	0.0	0.00
3.	CH_4+Rh(s)→ CH_4(s)	8.000×10^{-03}[a]	0.0	0.00
4.	H_2O+Rh(s)→ H_2O(s)	1.000×10^{-01}[a]	0.0	0.00
5.	CO_2+Rh(s)→ CO_2(s)	1.000×10^{-05}[a]	0.0	0.00
6.	CO+Rh(s)→ CO(s)	5.000×10^{-01}[a]	0.0	0.00
	Desorption			
7.	H(s)+H(s)→H_2+Rh(s)+Rh(s)	$3.000 \times 10^{+21}$	0.0	77.80
8.	O(s)+O(s)→O_2+Rh(s)+Rh(s)	$1.300 \times 10^{+22}$	0.0	355.20
9.	H_2O(s)→H_2O+Rh(s)	$6.000 \times 10^{+13}$	0.0	45.00
10.	CO(s)→CO+Rh(s)	$1.000 \times 10^{+13}$	0.0	133.40
	$\theta_{CO(s)}$			50.0[b]
11.	CO_2(s)→CO_2+Rh(s)	$3.000 \times 10^{+08}$	0.0	21.70
12.	CH_4(s)→CH_4+Rh(s)	$2.000 \times 10^{+14}$	0.0	25.10
	Surface Reactions			
13.	H(s)+O(s)→OH(s)+Rh(s)	$5.000 \times 10^{+22}$	0.0	83.70
14.	OH(s)+Rh(s)→H(s)+O(s)	$3.000 \times 10^{+20}$	0.0	37.70
15.	H(s)+OH(s)→H_2O(s)+Rh(s)	$3.000 \times 10^{+20}$	0.0	33.50
16.	H_2O(s)+Rh(s)→H(s)+OH(s)	$5.000 \times 10^{+22}$	0.0	110.90
17.	OH(s)+OH(s)→H_2O(s)+O(s)	$3.000 \times 10^{+21}$	0.0	100.80
18.	H_2O(s)+O(s)→OH(s)+OH(s)	$3.000 \times 10^{+21}$	0.0	171.80
19.	C(s)+O(s)→CO(s)+OH(s)	$5.000 \times 10^{+23}$	0.0	97.90
20.	CO(s)+Rh(s)→C(s)+O(s)	$3.700 \times 10^{+21}$	0.0	169.00
	$\theta_{CO(s)}$			50.0[b]
21.	CO(s)+O(s)→CO_2(s)+Rh(s)	$1.000 \times 10^{+20}$	0.0	121.60
	$\theta_{CO(s)}$			50.0[b]
22.	CO_2(s)+Rh(s)→CO(s)+O(s)	$5.000 \times 10^{+21}$	0.0	115.30
23.	CO(s)+H(s)→C(s)+OH(s)	$3.700 \times 10^{+21}$	0.0	142.76
	$\theta_{CO(s)}$			50.0[b]
24.	C(s)+OH(s)→CO(s)+H(s)	$3.700 \times 10^{+20}$	0.0	25.54
25.	CO(s)+H(s)→HCO(s)+Rh(s)	$5.000 \times 10^{+19}$	0.0	108.90

[a] Sticking coefficient.

[b] Coverage-dependent activation energy.

Table 4.23. Reaction mechanism for steam reforming of methane over Rh (continued from the previous page).

k_s	**Reaction**	$A_{k_s,j}$ (cm, mol, s)	β_{k_s}	E_{k_s} (kJ mol^{-1})
26.	HCO(s)+Rh(s)→CO(s)+H(s)	$3.700 \times 10^{+21}$	0.0	0.00
	$\theta_{\mathrm{CO(s)}}$			-50.0[b]
27.	HCO(s)+Rh(s)→CH(s)+O(s)	$8.000 \times 10^{+23}$	0.0	59.50
28.	CH(s)+O(s)→HCO(s)+Rh(s)	$3.700 \times 10^{+21}$	0.0	167.50
29.	CH_4(s)+Rh(s)→CH_3(s)+H(s)	$5.500 \times 10^{+20}$	0.0	61.00
30.	CH_3(s)+H(s)→CH_4(s)+Rh(s)	$3.700 \times 10^{+21}$	0.0	51.00
31.	CH_3(s)+Rh(s)→CH_2(s)+H(s)	$3.700 \times 10^{+24}$	0.0	103.00
32.	CH_2(s)+H(s)→CH_3(s)+Rh(s)	$3.700 \times 10^{+21}$	0.0	44.00
33.	CH_2(s)+Rh(s)→CH(s)+H(s)	$3.700 \times 10^{+24}$	0.0	100.00
34.	CH(s)+H(s)→CH_2(s)+Rh(s)	$3.700 \times 10^{+24}$	0.0	68.00
35.	CH(s)+Rh(s)→C(s)+H(s)	$3.700 \times 10^{+21}$	0.0	21.00
36.	C(s)+H(s)→CH(s)+Rh(s)	$3.700 \times 10^{+21}$	0.0	172.80
37.	CH_4(s)+O(s)→CH_3(s)+OH(s)	$1.700 \times 10^{+24}$	0.0	80.34
38.	CH_3(s)+OH(s)→CH_4(s)+O(s)	$3.700 \times 10^{+21}$	0.0	24.27
39.	CH_3(s)+O(s)→CH_2(s)+OH(s)	$3.700 \times 10^{+24}$	0.0	120.31
40.	CH_2(s)+OH(s)→CH_3(s)+O(s)	$3.700 \times 10^{+21}$	0.0	15.06
41.	CH_2(s)+O(s)→CH(s)+OH(s)	$3.700 \times 10^{+24}$	0.0	114.50
42.	CH(s)+OH(s)→CH_2(s)+O(s)	$3.700 \times 10^{+21}$	0.0	36.82
43.	CH(s)+O(s)→C(s)+OH(s)	$3.700 \times 10^{+21}$	0.0	30.13
44.	C(s)+OH(s)→CH(s)+O(s)	$3.700 \times 10^{+21}$	0.0	136

[a] Sticking coefficient.

[b] Coverage-dependent activation energy.

Adsorption rate constants are calculated from the following expression that involves an initial sticking coefficient $S^0_{k_s,j}$ [274]:

$$k^{\mathrm{ads}}_{k_s,j} = \frac{S^0_{k_s,j}}{\Gamma_j}\sqrt{\frac{RT_j}{2\pi M_{ij}}} \tag{4.63}$$

4.2.6. Physical Properties

Physical properties of the fluid mixtures, the catalytic washcoats and the separating walls (fins) are needed for solution of the transport equations. The reacting

fluids are mixtures of a hydrocarbon fuel, steam, carbon oxides, hydrogen, nitrogen and oxygen in the case of methane ATR. The mixture-averaged fluid viscosity is given by [275]:

$$\mu_j = \sum_{i=1}^{N_g} \left. \frac{x_i \mu_i}{\sum_{l=1}^{N_g} x_{il} \Phi_{il}} \right|_j \tag{4.64}$$

with

$$\Phi_{il} = \frac{1}{\sqrt{8}} \left(1 + \frac{M_i}{M_l}\right)^{-1/2} \left[1 + \left(\frac{\mu_i}{\mu_l}\right)^{1/2} \left(\frac{M_l}{M_i}\right)^{1/4}\right]^2 \qquad i, l = 1, 2, \ldots, N_g$$

Dynamic viscosity of species i in channel j is calculated from [276]

$$\mu_{ij} = 2.6693 \times 10^{-6} \frac{\sqrt{10^3 M_{ij} T_{ij}}}{\varpi_i^2 \Omega_i} \tag{4.65}$$

where the values of the collision diameter ϖ_i and the collision integral Ω_i are taken from [276].

Thermal conductivity of the gaseous mixture in channel j is calculated using [277]

$$k_{fj} = \sum_{i=1}^{N_g} \left. \frac{x_i k_i}{\sum_{l=1}^{N_g} x_{il} \Phi_{il}} \right|_j \tag{4.66}$$

k_{ij}, is obtained from [276]

$$k_{ij} = 8.3224 \times 10^{-4} \frac{\sqrt{10^{-3} T_j / M_{ij}}}{\varpi_i^2 \Omega_i} \tag{4.67}$$

$D_{i,mj}$, is calculated by [277]

$$D_{i,mj} = \left. \frac{1 - Y_i}{\sum_{l=1}^{N_g} Y_i / D_{il}} \right|_j, \qquad l \neq i \tag{4.68}$$

D_{il}, for the multicomponent gas mixtures are given by [278]

$$D_{il,j} = \frac{10^{-3} T_j^{1.75} \left(\frac{1}{M_i} + \frac{1}{M_l}\right)^{1/2}}{p_j \left[\left(\sum v\right)_i^{1/3} + \left(\sum v\right)_l^{1/3}\right]^2} \tag{4.69}$$

Here, p_j is the operating pressure in channel j and $\left(\sum v\right)_i$ is the sum of the atomic diffusion volumes for species i. The effective diffusivity, $D_{\text{eff},i,mj}$, in the porous catalyst washcoats are calculated from [279]

$$D_{\text{eff},i,mj} = \frac{\epsilon_{\text{cat},j}}{\tau_{\text{cat},j}} \left[\frac{1}{D_{K,ij}} + \frac{1}{D_{i,mj}}\right]^{-1} \tag{4.70}$$

$D_{K,ij}$ is a function of the average pore diameter $d_{\text{pore},j}$, molecular weight of the species and the temperature [279]:

$$D_{K,ij} = 48.5 d_{\text{pore},j} \sqrt{\frac{T_j}{M_{ij}}} \tag{4.71}$$

Density of the gaseous mixtures are calculated using Eq. (4.72), assuming they behave ideally under atmospheric pressure and high temperatures:

$$\rho_{fj} = \frac{p_j^{\text{in}} M_j}{R T_j^{\text{in}}} \tag{4.72}$$

The surface area-to-volume ratio A_{sj} of the Rh catalyst used for steam reforming in modeling of methane ATR is determined by

$$A_{sj} = \frac{S_{\text{BET,j}} w_{sj}}{V_{sj}} \tag{4.73}$$

The viscous and inertial loss coefficients α_j and C_{2j} in Equation 4.32 can be

Table 4.24. Values and estimation methods of the physical properties of the fluids, catalysts and fin materials used in spatially segregated reactors for steam reforming of different fuels.

Property	**Value/Formula**	**Unit**	**Reference**
ρ_{fj}	$\rho_{fj} = \frac{p_j^{\text{in}} M_j}{R T_j^{\text{in}}}$	kg m^{-3}	This work
ρ_{sj}	1109.5 (Pt/δ-Al_2O_3), 1205.8 (Ni/δ-Al_2O_3)	kg m^{-3}	[280]
α_j	1×10^{-8}	m^2	[281]
$\epsilon_{\text{cat},j}$	0.4	—	[282]
$D_{i,mj}$, $D_{\text{eff},i,mj}$	1.8×10^{-5}, 5.35×10^{-7}	$\text{m}^2\,\text{s}^{-1}$	[207]
μ_j	Equation 4.64	$\text{kg m}^{-1}\,\text{s}^{-1}$	[275]
$\mu_{\text{eff},j}$	μ_j	$\text{kg m}^{-1}\,\text{s}^{-1}$	This work
k_{fj}	Equation 4.66	$\text{W m}^{-1}\,\text{K}^{-1}$	[277]
k_{sj} (Al_2O_3)	27	$\text{W m}^{-1}\,\text{K}^{-1}$	[280]
$k_{\text{eff},j}$	Equation 4.43	$\text{W m}^{-1}\,\text{K}^{-1}$	This work
$c_{p_{ij}}$	$c_{p_{ij}} = A + B \cdot T_j + C \cdot T_j^2 + D \cdot T_j^3$	$\text{J kg}^{-1}\,\text{K}^{-1}$	[283]
$c_{p_{fj}}$	$c_{p_{fj}} = \sum_i^{N_g} x_i \cdot c_{p_{ij}}$	$\text{J kg}^{-1}\,\text{K}^{-1}$	[283]
$c_{p_{sj}}$ (Al_2O_3)	900	$\text{J kg}^{-1}\,\text{K}^{-1}$	[280]
c_{p_w}	900 (Al_2O_3), 475 (AISI Steel), 440 (Iron)	$\text{J kg}^{-1}\,\text{K}^{-1}$	[280]
k_w	27 (Al_2O_3), 44.5 (AISI Steel), 76.2 (Iron)	$\text{W m}^{-1}\,\text{K}^{-1}$	[280]

obtained from

$$\alpha_j = \frac{d_{pj}^2}{150} \frac{\epsilon_j^3}{(1-\epsilon_j)^2} \tag{4.74}$$

$$C_{2j} = \frac{3.5}{d_{pj}} \frac{(1-\epsilon_j)}{\epsilon_j^3} \tag{4.75}$$

since the first and second terms on the right-hand side of Equation 4.32 can be matched to those in the Ergun equation for flow in pipes filled with spherical particles [284].

Even though the approach followed in modeling of spatially segregated and spatially integrated microchannel reactors are similar such that it involves simultaneous solution of momentum, mass of species and energy equations, slight differences in esti-

Table 4.25. Values and estimation methods of the physical properties of the fluids and catalysts used in spatially integrated reactors for autothermal reforming of methane.

Property	**Value/Formula**	**Unit**	**Reference**
ρ_{fj}	$\rho_{fj} = \dfrac{p_j^{\text{in}} M_j}{R T_j^{\text{in}}}$	$\text{kg}\,\text{m}^{-3}$	This work
α_j	7.37×10^{-11} using Equation 4.74	m^2	This work
C_{2j}	7.54×10^{4} using Equation 4.75	m^{-1}	This work
$\epsilon_{\text{cat},j}$, $\tau_{\text{cat},j}$ [a]	0.58, 8.1	—	[285]
$D_{i,mj}$, $D_{\text{eff},i,mj}$	Equations 4.68 and 4.70	$\text{m}^2\,\text{s}^{-1}$	This work
μ_j	Equation 4.64	$\text{kg}\,\text{m}^{-1}\,\text{s}^{-1}$	[275]
$S_{\text{BET},j}$, $d_{\text{pore},j}$ [b]	95, 2.61×10^{-8}	$\text{m}^2\,\text{g}^{-1}$, m	[286]
Γ_j	2.77×10^{-5}	$\text{mol}\,\text{m}^{-2}$	[287]
A_{sj}	1.24×10^{8}	m^{-1}	This work
V_{sj}	8×10^{-9}	m^{-3}	This work
w_{sj}	10.44×10^{-3} (Rh), 15.21×10^{-3} (Pt)	g	This work
δ_{sj}, d_{pj}	100×10^{-6}	m	This work

[a] Obtained with non-catalytic γ-Al_2O_3.

[b] Obtained with Rh/δ-Al_2O_3.

mates of the physical properties (e.g. $\epsilon_{\text{cat},j}$, α_j, $D_{i,mj}$) arise depending on how flow in porous media (Section 4.2.3) and reaction kinetics (Section 4.2.5)are incorporated into the models. Values of the physical properties of the fluid mixtures, catalytic washcoats and, material of the separating wall (fin), if present, are required for the solution of the model equations. These are provided in Table 4.24 for combustion-assisted steam reforming of methane, propane, methanol, ethanol, *n*-heptane and *iso*-octane, and ethane dehydrogenation in *spatially segregated systems*. Table 4.25, which presents physical property information for use with the *spatially integrated system*, has some extra properties listed (e.g. tortuosity, BET surface area). Since methane ATR, the reaction scheme taking place in the integrated system, is run isothermally, the thermal properties (e.g. $c_{p_{fj}}$, $c_{p_{sj}}$, k_{fj}) are not needed.

4.2.7. Microchannel, Catalyst and Flow Configurations for Coupled Systems

Table 4.26 shows reactor data and the operating conditions for each system modeled, the latter of which are listed in boldface in the second half of the table. Reactor data comprise the **length** (L_j), **width** (W_j) and **height** (H_j) **of the microchannels**, **separating wall** (fin) **thickness** (WT), **thickness of the catalytic washcoats** (δ_{sj}), specification of flow direction in each channel with respect to the other (**co-** or **counter-current**), and specification of presence or absence of **micro-baffles** within the flow-by volumes. Since methane ATR is carried out in a spatially integrated reactor, there are no entries in the cells corresponding to wall thickness and material, and flow configuration. A single value in a cell indicates that the property is common both to the exothermic and endothermic reaction channels in a unit cell. This is the default case with the channel dimensions and the thickness of the catalysts.

Temperatures, fuel flow rates, oxygen-to-carbon (O_2 : C) or steam-to-carbon (S : C) ratios at each channel inlet are the specified operating conditions along with the inlet pressures which are atmospheric (not shown in Table 4.26). The top entry in a cell is related to the exothermic reaction while the bottom entry relates to the endothermic reaction. Two different definitions exist for the **oxygen-to-carbon** and **steam-to-carbon** ratios. One definition states that they are equal to the *number of moles of molecular oxygen or steam divided by that of the fuel*. In the other definition, the number of moles of fuel is replaced by the *number of moles of carbon atoms in the fuel molecule*. Both definitions are frequently encountered, and hence the inlet ratios are given in terms of both. Since steam is not needed during ethane dehydrogenation, the S : C entry in Table 4.26 is replaced by N_2 : C.

In combustion-reforming integration of propane, methanol and ethanol, a total of nine 2 mm-wide, equally-spaced micro-baffles that are considered to be integral parts of the metallic walls, extend 190 μm into the microchannels on each side, as shown in Figure 4.4. Coupling of methane combustion and *iso*-octane reforming is also carried out in a reactor with nine pairs of micro-baffles of width 2 mm and length 100 μm.

Table 4.26. Reactor data and operating conditions for cases demonstrating **spatially coupled reactor/heat exchange systems**.

	CH_4 COMB CH_4 SR	**CH_4 COMB C_2H_6 DEHYD**	**C_3H_8 COMB C_3H_8 SR**	**CH_3OH COMB CH_3OH SR**	**C_2H_5OH COMB C_2H_5OH SR**	**CH_4 COMB n-C_7H_{16} SR**	**CH_4 COMB iso-C_8H_{18} SR**	**CH_4 ATR**
Model	2D AS	2D AS	2D	2D	2D	2D	2D & 3D	3D
L_j [m]	0.05	0.05	0.1	0.1	0.1	0.1	0.1	0.02
W_j [μm]	280[a]	280[a]	280 − 560	280 − 560	280 − 560	400	280 − 560	4000
H_j [μm]	280	280	280 − 560	280 − 560	280 − 560	400	280 − 560	750
WT [μm]	400	400	100 − 400	100 − 400	100 − 400	200	100 − 400	—
Wall [μm] material	AISI Steel	AISI Steel	AISI Steel	AISI Steel	AISI Steel	AISI Steel	AI_2O_3, AISI Steel, Iron	— Single channel
δ_{sj} [μm]	60	60	60	60	60	60	60	100
Flow config.	Co-current	Co-current	Co-current	Co-current	Co-current	Counter-current	Co-current	— Single channel
Micro-baffles	NO	NO	YES, 9 190μm×2 mm	YES, 9 190μm×2 mm	YES, 9 190μm×2 mm	NO	YES, 9 100μm×2 mm	NO
$\boldsymbol{T_j^{in}}$ [K]	**900** **785**	**900** **923**	**673** **623**	**473** **473**	**500** **473**	**850** **750**	**800** **800**	**500 − 650**
$\boldsymbol{F_{ij}^{in}}$ [mol s^{-1}]	$\mathbf{4 \times 10^{-7}}$ $\mathbf{1.24 \times 10^{-6}}$	$\mathbf{5.2 \times 10^{-7}}$ $\mathbf{1.16 \times 10^{-6}}$	$\mathbf{1.24 \times 10^{-7}}$ $\mathbf{1.24 \times 10^{-7}}$	$\mathbf{1.24 \times 10^{-7}}$ $\mathbf{1.24 \times 10^{-7}}$	$\mathbf{1.24 \times 10^{-7}}$ $\mathbf{1.24 \times 10^{-7}}$	$\mathbf{1.5 \times 10^{-8}}$ $\mathbf{1.5 \times 10^{-7}}$	$\mathbf{4 \times 10^{-9}}$ $\mathbf{4 \times 10^{-8}}$	$\mathbf{2.31 - 4.62}$ $\mathbf{\times 10^{-5}}$
$\boldsymbol{F_{O_2,j}^{in}}$ **:** $\boldsymbol{F_{ij}^{in}}$ (O_2 : C)	**2.0** **(2.0)**	**2.0** **(2.0)**	**6.0** **(2.0)**	**4.0** **(4.0)**	**6.0** **(3.0)**	**2.0** **(2.0)**	**2.0** **(2.0)**	**0.47 − 0.63** **(0.47 − 0.63)**
$\boldsymbol{F_{H_2O,j}^{in}}$ **:** $\boldsymbol{F_{ij}^{in}}$ (S : C)	**2.5** **(2.5)**	**0.25**[b] **(0.125)**[b]	**9.0** **(3.0)**	**1.0** **(1.0)**	**6.0** **(3.0)**	**21.0** **(3.0)**	**24.0** **(8.0)**	**0 − 3.0** **(0 − 3.0)**

[a] Cylindrical microchannels with $W_j = H_j = D_j$.

[b] $F_{N_2,j}^{in} : F_{ij}^{in} = 0.25$. Inert N_2 fed to dilute the stream. No steam fed in ethane dehydrogenation.

4.2.8. Sizing and Other Considerations

Sizing of the microchannel reactors is based on the principle of numbering-up of the catalytic microchannels. This is handled by dividing the targeted flow rate of the product (hydrogen, syngas or ethene) by the flow rate at the exit of a single steam reforming or dehydrogenation channel, which gives the number of reforming or dehydrogenation channels required. The total number of channels (combustion and reforming or dehydrogenation) is found by doubling this value, which is then used together with the channel dimensions and wall thickness to calculate the size of the microchannel block.

The water-gas shift and CO oxidation reactors, assumed to be of packed-bed type, are required to clean up the reformate stream leaving the reformer (Figure 4.1) during the fuel processing of *n*-heptane for fuel-cell-grade hydrogen production (Section 4.1.1). Their contributions to the overall fuel processor volume are determined by reactor simulations using the one-dimensional fixed-bed reactor model (see Equation 4.79-81): the catalyst weight in each of the reactors is calculated via a trial-and-error procedure until the effluent stream meets the termination criteria, which are set as the limits of CO exit concentrations in the pertinent units and their operating temperature ranges (Section 4.1.1.2). The high- and low-temperature water-gas shift reaction runs over Fe- and Cu-based catalysts, respectively. The preferential CO oxidation is considered to run over a Cu-based catalyst. The rate expressions for the high- and low-temperature water-gas shift reactions are adopted from [255] and [256], respectively,

$$\mathcal{R}^{\mathrm{v}}_{\mathrm{HTS}} = k^{\mathrm{v}}_{\mathrm{HTS}} \frac{p^{0.9}_{\mathrm{CO}} p^{0.31}_{\mathrm{H_2O}}}{p^{0.156}_{\mathrm{CO_2}} p^{0.05}_{\mathrm{H_2}}} \left(1 - \frac{1}{K^{\mathrm{WGS}}_{\mathrm{eq}}} \frac{p_{\mathrm{CO_2}} p_{\mathrm{H_2}}}{p_{\mathrm{CO}} p_{\mathrm{H_2O}}} \right) \tag{4.76}$$

$$\mathcal{R}^{\mathrm{v}}_{\mathrm{LTS}} = k^{\mathrm{v}}_{\mathrm{LTS}} \left(p_{\mathrm{CO}} p_{\mathrm{H_2O}} - \frac{p_{\mathrm{CO_2}} p_{\mathrm{H_2}}}{K^{\mathrm{WGS}}_{\mathrm{eq}}} \right) \tag{4.77}$$

and the kinetics of CO oxidation in a hydrogen-rich stream is described using the rate

expression proposed by Sedmak *et al.* [259]:

$$\mathcal{R}^{\mathrm{v}}_{\mathrm{PROX}} = \frac{k^{\mathrm{v}}_{\mathrm{PROX}} K_{\mathrm{CO}} K_{\mathrm{O_2}} p_{\mathrm{CO}} p^{0.2}_{\mathrm{O_2}}}{0.5 K_{\mathrm{CO}} p_{\mathrm{CO}} + K_{\mathrm{O_2}} p^{0.2}_{\mathrm{O_2}}} \tag{4.78}$$

The heat exchangers (HEX $1-6$) integrated into the processor/fuel cell assembly (Figure 4.1) are considered in terms of the heat load they are to undertake, instead of their sizes. The percentage of heat recovery is taken to be 50% for all of the exchangers, which is a reasonable assumption if they are to be comprised of parallel microchannels [288]. The unconverted reactants *n*-heptane and methane and purged hydrogen are assumed to be fully combusted over the Pt-based catalyst in the afterburner unit, so it is also treated as a heat exchanger working with 50% heat recovery.

4.3. Decoupled Reaction/Heat Exchange Systems

Although they have significant beneficial features, microchannel reactors can sometimes have disadvantages when their routine use in commercial practice, which is at its infancy, is considered. The catalysts buried in the microchannels cannot be easily replaced upon deactivation. Moreover, the small channels are subject to the risk of blockage due to effects such as carbon formation [76]. However, some of these difficulties can be avoided by the use of a second type of microchannel system, the cascade reactor array [24, 25]. This system consists of *multiple adiabatic beds containing catalysts linked by microchannels in which only heat exchange occurs* (Figure 4.8). One set of reactors and microchannels are associated with the desired reaction (e.g. steam reforming), and one set with catalytic oxidation, the channels connecting the reactors being arranged parallel to the reforming channels in order to facilitate heat transfer. The concept of using catalytic reactor beds with *interstage heat transfer* to achieve higher conversions is a classic approach, and has industrially established examples such as oxidation of SO_2 to SO_3. However, the cascade reactor system is novel since it employs microchannel technology in its heat exchangers, and is an intensified variant of an existing concept [25]. Combustion-assisted steam reforming of *n*-heptane and of methane, and ethane dehydrogenation to be used as demonstrative processes in

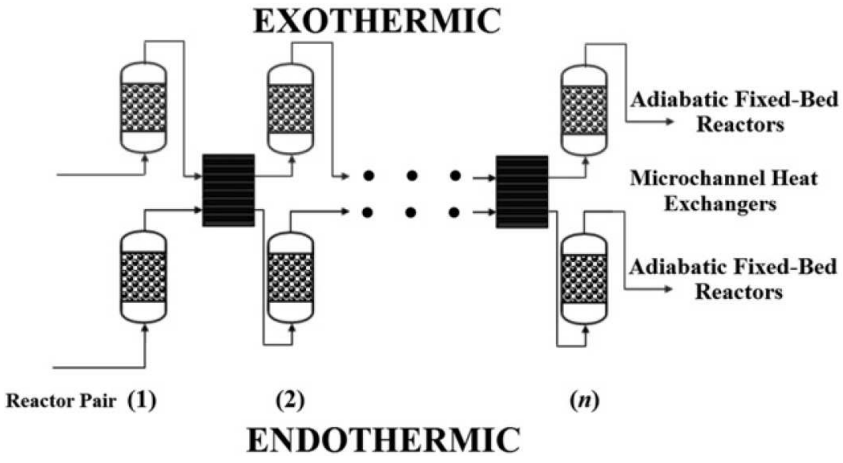

Figure 4.8. Description of the cascade reactor configuration.

decoupled reaction/heat exchange systems are detailed in Sections 4.1.1.2, 4.1.2.1 and 4.1.3, respectively.

The cascade configuration has some advantages over the microchannel reactors. Catalyst, particulate or monolithic type, is placed in slots within a heat exchange block, thus avoiding the need to redistribute the reactants after each heat exchange stage and allowing facile replacement of deactivated catalyst. The heat transfer zone and catalyst volume are decoupled, and can independently be varied. This system offers some operational advantages; it is beneficial for reactions demanding strict temperature control as the bed sizes can be arranged together with the amount and distribution of reactant flows to obtain the desired temperature profiles. Furthermore, it is possible, by appropriate design, to inject reactants as the fluid passes through the series of multiple beds. Desired conversion levels can be obtained by increasing the number of reactor-heat exchanger stages, which is limited only by excessive pressure drop along the array. The size of the cascade systems may be comparable to microchannel reactor arrays, and is certainly smaller than the conventional plants [24, 25].

4.3.1. Design of Cascade Reactors

The cascade design procedure primarily has a trial-and-error nature. Starting with assumed sizes of adiabatic packed-beds in the exothermic and endothermic re-

action arrays, the outlet temperatures from each bed pair are determined. The inlet temperatures to the subsequent pair are then assigned, which also dictates the amount of interstage heat transfer. The procedure is repeated until the number of bed pairs sufficient to achieve the desired conversion is calculated. If certain process constraints are violated or desired conversion cannot be achieved with an acceptable number of stages using the given configuration, the process is reiterated by varying the assumed bed size and amount of interstage heat transfer.

Among the constraints the most restrictive one is the upper allowable limit of methane combustion conversion, 20% [107], the exceeding of which creates conditions that lead to thermal runaway and make it impossible to control the temperature precisely. Yet another but less stringent constraint is the aspect ratio of the beds which dictates that the length-to-diameter ratio be in a reasonable range, and that the pressure drop not be so high as to permit process infeasibilities. Thus, the reactors should be sized such that combustion conversion and pressure drop in each bed are limited to 20% and 1%, respectively. A one-dimensional pseudohomogeneous reactor model is used for the simulation of the adiabatic operation in the fixed-bed reactors. The working equations are

$$\frac{dF_{ij}}{dw_{sj}} = \Re_{ij}^{\mathrm{v}} \tag{4.79}$$

$$\frac{dT_j}{dw_{sj}} = \frac{\sum_{k_v=1}^{N_{\mathrm{vrxn}}} \left(-\Delta H_{k_v}\right) \mathcal{R}_{k_v,j}^{\mathrm{v}}}{\sum_{i=1}^{N_g} F_{ij} c_{p_{ij}}} \tag{4.80}$$

$$\frac{dp_j}{dw_{sj}} = -\frac{\beta_0}{A_{cj}\left(1-\epsilon_j\right)\rho_{sj}} \frac{p_j^{\mathrm{in}}}{p_j} \frac{T_j}{T_j^{\mathrm{in}}} \frac{\sum_{i=1}^{N_g} F_{ij}}{\sum_{i=1}^{N_g} F_{ij}^{\mathrm{in}}} \tag{4.81}$$

subject to the initial conditions

$$F_{ij} = F_{ij}^{\mathrm{in}}, \quad T_j = T_j^{\mathrm{in}}, \quad p_j = p_j^{\mathrm{in}} \quad \text{at} \quad w_{sj} = 0$$

The notation is similar to that used in microchannel modeling such that i denotes the species, j, the exothermic or endothermic operation line, and k_v, the particular reaction(s) in each line. Rate expressions are the same as those for rate calculations in microchannel reactors (Section 4.2.5.1).

The design of microchannel heat exchangers linking the catalytic beds differs slightly from the microchannel reactor design in that only the fluid-phase momentum, species mass and energy equations, and energy equation in the walls are considered due to the absence of catalytic porous media (Eqs. (4.26)-(4.28), (4.38), (4.41) and (4.46)). The representative unit cell of the heat exchangers is similar to the straight-through microchannel configurations shown in Figures 4.4 and 4.6, and involves two adjacent square or cylindrical channels in which the hot and cold streams flow co-currently, and the separating steel wall. The variables available for adjustment are the lengths and cross-sectional areas of the channels. Inasmuch as heat loads at the intermediate exchange stages are variable, design is suited to the highest one. Sizing of the microchannel heat exchangers in the cascade system is done by dividing the total flow leaving each catalytic bed by flow through a single pair and by calculating the number of channels that meets the actual load. Owing to the interstage temperatures that are determined during the phase of sizing the beds, the heat load is known prior to heat exchanger design. Flow through a single pair of microchannels, or equivalently the number of microchannels is assumed initially. With the channel dimensions set, the transport equations are solved as explained above. The length and cross-sectional area are varied until the exit criteria (inlet temperatures to the subsequent pair of beds) are met. If the acceptable sets of variables cannot meet the criteria, the number of channels is changed and the procedure is started all over again.

4.4. Numerical Solution Techniques

This section focuses on the solution methods of the model equations set forth in Sections 4.2.3 and 4.3.1 describing transport phenomena and reaction in microchannels. Brief information is provided on the general use of *computational fluid dynamics* (CFD) techniques, and the *finite element* and *finite volume* methods are introduced in a

nutshell. Model solutions are obtained with two commercial CFD packages, Comsol Multiphysics™ and ANSYS FLUENT™, which make use of the finite element and finite volume methods, respectively.

4.4.1. What is CFD?

Computational fluid dynamics is the general term coined for the computer-based analysis of systems involving fluid flow, heat and mass transfer and associated phenomena such as flow in porous media and chemical reactions [289]. Catalytic reaction engineering is among the many application areas of the CFD analysis such that all the physical phenomena listed above occur and are intermingled. Ubiquity of high-performance computing and commercial softwares has led to a notable increase in the number of works that seek solutions to reaction engineering problems using CFD techniques. Moreover, CFD has several unique advantages over experimental rigs and pilot plants [289]:

- reduction in lead times and costs associated with new designs
- ability to analyze systems when controlled experiments are difficult or impossible to perform (e.g. very large systems, chemical systems near explosive limits)
- practically unlimited level of detail of results
- production of extremely large volume of parametric results at virtually no added expense

4.4.2. How Does CFD Work?

Numerical algorithms that are developed to handle fluid flow problems are at the heart of CFD codes [289], which discretize the problem on a given grid that represents the model geometry, and then solve the resulting system of equations in order to obtain the nodal values of the field variables, e.g. velocity. Even more, most commercial CFD packages are able to examine, display and visualize the results. A complete CFD code contains three main elements [289]: (i) a pre-processor, (ii) a solver, and (iii) a post-processor.

4.4.2.1. Pre-processor. The pre-processing stage involves:

- definition of the geometry (e.g. unit cell of the microchannel reactor) or the computational *domain*
- generation of a *grid* consisting of smaller, non-overlapping subdomains called *elements* or *cells*
- association of the physical and/or chemical phenomena with each group of subdomains and specification of the *boundary conditions*
- definition of fluid properties and incorporation of *constitutive and user-defined functions* (e.g. multicomponent diffusivities, rates of chemical reactions)

Solution to a flow problem is defined at nodes inside each element (cell). In general, it can be said that the larger the number of elements, the better the solution, since the accuracy of a CFD solution is governed by the number of elements in the grid. Moreover, some field variables go through rapid variations in certain regions in the domain, for example, as in the case of fast, exothermic combustion reactions. This necessitates the *refining* of the grid, or increasing the number of elements in that region. Refining continues until the solution is guaranteed to be *grid-free*. These add to the computational cost associated with the CFD solution of the problems, which itself sometimes needs to be optimized.

4.4.2.2. Solver. The solvers that come with commercial softwares such as Comsol Multiphysics™ and ANSYS Fluent™ essentially carry out the following tasks [289] using the finite element and finite volume methods:

- conversion of the resulting equations into a system of algebraic equations (discretization)
- solution of the algebraic equations by an iterative method

The following balance equation in an arbitrarily chosen element or cell can be written for a general flow variable ϕ, e.g. a velocity component or enthalpy:

$$\left[\begin{array}{l}\text{Rate of change}\\ \text{of } \phi \text{ in the}\\ \text{control volume}\\ \text{with respect to}\\ \text{time}\end{array}\right] = \left[\begin{array}{l}\text{Net rate of}\\ \text{increase of}\\ \phi \text{ due to}\\ \text{convection into}\\ \text{the control}\\ \text{volume}\end{array}\right] + \left[\begin{array}{l}\text{Net rate of}\\ \text{increase of}\\ \phi \text{ due to}\\ \text{diffusion into}\\ \text{the control}\\ \text{volume}\end{array}\right] + \left[\begin{array}{l}\text{Net rate of}\\ \text{creation of}\\ \phi \text{ inside the}\\ \text{control}\\ \text{volume}\end{array}\right] \quad (4.82)$$

CFD codes apply discretization schemes suitable for the treatment of transient transport phenomena, convection and diffusion as well as for handling source terms associated with consumption or production of species due to chemical reactions. The underlying physical phenomena are complex and highly nonlinear (owing to convection and source terms) so an iterative solution procedure is required.

4.4.2.3. Post-processor. Due to the increasing graphics capabilities of computers, major CFD packages now come with detailed data visualization tools that include

- display of domain geometry and the grid
- vector, 2D and 3D surface plots
- particle tracking
- translation, rotation and scaling of plots
- high-resolution PostScript output
- animation of time-variable results

4.4.3. The Finite Element Method

The finite element method is based on the integral formulation of the governing partial differential equations, which is proved to be advantageous in providing a more natural treatment of Neumann boundary conditions and discontinuous source terms due to the less stringent requirements of regularity and smoothness of the solution [290].

The general partial differential equation (PDE)

$$\mathcal{L}(u) \equiv \sum_{i,j=1}^{n} a^{ij}(x) \frac{\partial^2 u}{\partial x_i \partial x_j} + \sum_{i=1}^{n} b^i(x) \frac{\partial u(x)}{\partial x_i} + c(x)\, u(x) = s \tag{4.83}$$

in some domain $\Omega \subset \mathbb{R}^n$ is in its strong form. The integral form is given by

$$\int_0^1 \mathcal{L}(u)\, w(x) dx = \int_0^1 s w(x) dx \tag{4.84}$$

where the choice of the weight function $w(x)$ defines the type of scheme.

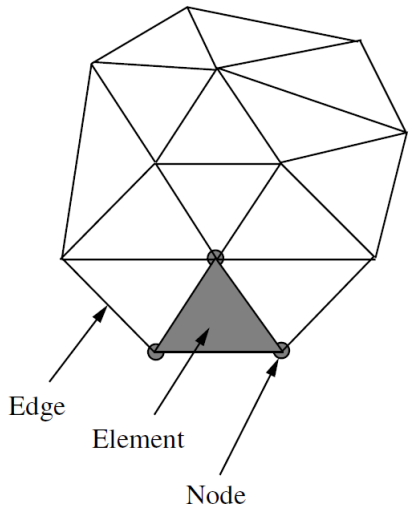

Figure 4.9. Typical finite element grid [291].

In the finite element method, the domain of interest $\Omega = \{x : 0 \leq x \leq 1\}$ is discretized into $N-1$ elements $\Omega_i = \{x : x_{i-1} \leq x \leq x_i\}$ of various shapes, e.g. triangles, quadrilaterals (Figure 4.9). Each element is formed by the connection of a certain number of nodes. The number of nodes forming an element depends on the type of element (or interpolation function).

The approximate solution is represented by

$$u^{\delta}(x,t) = \sum_{i=1}^{N} u_i(t)\, N_i(x) \tag{4.85}$$

where the set of functions $N_i(x)$ is known as the expansion basis. Its support is defined as the set of points where $N_i(x) \neq 0$. Expansion bases with compact support, which are piecewise continuous polynomials within each element are shown in Figure 4.10 [290].

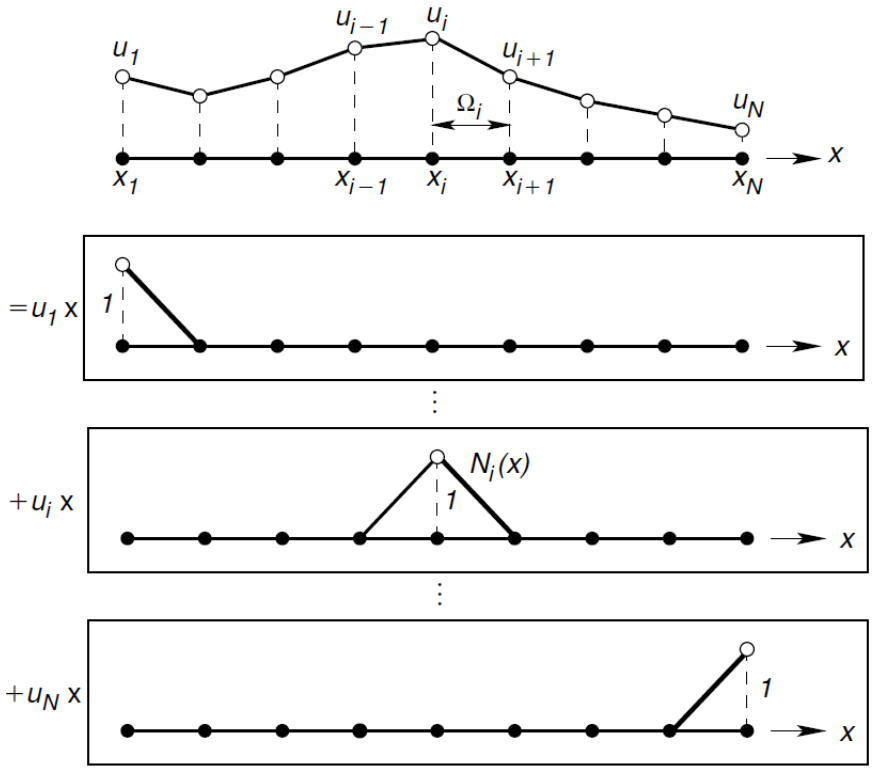

Figure 4.10. A piecewise linear approximation $u^{\delta}(x,t) = \sum_{i=1}^{N} u_i(t) N_i(x)$ [290].

The global shape functions $N_i(x)$ can be split within an element into two local contributions of the form shown in Figure 4.11. These individual functions are referred to as the *shape functions* [290, 291].

4.4.3.1. Galerkin FEM. The weight function in Equation 4.84 is set to be the same as the basis function $N_i(x)$, i.e., $w(x) = N_i(x)$. Assuming $\mathcal{L}(x) = u_{xx} = s(x)$ in the domain Ω with boundary conditions $u(0) = \alpha$ and $u_x(1) = g$, Equation 4.87 becomes

$$\int_0^1 w(x) u_{xx} dx = \int_0^1 w(x) s dx \tag{4.86}$$

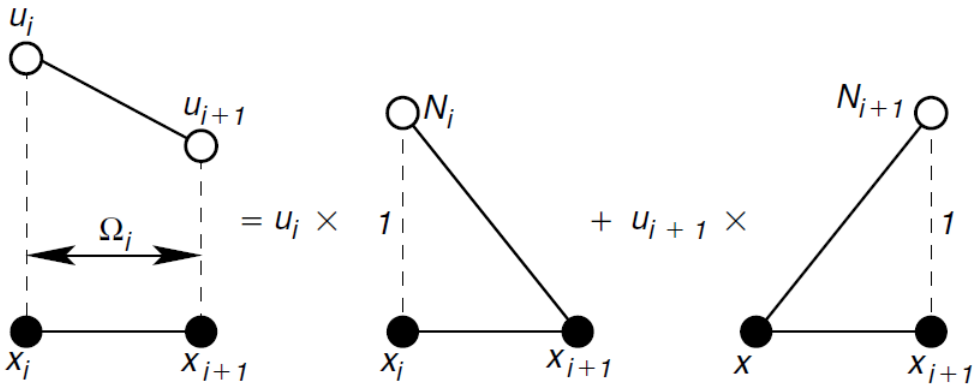

Figure 4.11. Shape functions for the finite element method [290].

Integrating the left-hand side by parts gives the weak form [290]

$$-\int_0^1 w_x u_x dx + w\left(1\right) u_x\left(1\right) - w\left(0\right) u_x\left(0\right) = \int_0^1 w\left(x\right) s\left(x\right) dx \tag{4.87}$$

In two and three dimensions, Gauss' divergence theorem is used to obtain a similar result.

Boundary conditions in the finite element method is implemented into the discretized equations rather conveniently. The Neumann boundary condition of $u_x\left(1\right) = g$ is simply substituted into Equation 4.87, which leads to symmetric matrices. The Dirichlet boundary condition $u\left(0\right) = \alpha$ can be applied by imposing $u_1 = \alpha$ and requiring that $w\left(0\right) = 0$. The weight functions $w\left(x\right)$ are, as a general rule, imposed to be zero at Dirichlet boundaries.

With $u\left(x\right) \approx u^{\delta}\left(x\right) = \sum_{j=1}^{N} u_j N_j\left(x\right)$ and $w\left(x\right) = N_i\left(x\right)$, Equation 4.87 becomes

$$-\int_0^1 \frac{dN_i}{dx}\left(x\right) \sum_{j=1}^{N} u_j \frac{dN_j}{dx}\left(x\right) dx = \int_0^1 N_i\left(x\right) s\left(x\right) dx \qquad i = 2, \ldots, N \tag{4.88}$$

which represents a linear system of $N-1$ equations with $N-1$ unknowns: $\{u_2, \ldots, u_N\}$. The integrals in Equation 4.88 are calculated as sums of integrals over the elements Ω_i. Since the basis functions have compact support, as shown in Figure 4.10, their value

and derivatives are different from zero only on the elements containing the node i, i.e.,

$$N_i(x) = \begin{cases} \dfrac{x - x_{i-1}}{\Delta x_{i-1}} & x_{i-1} < x < x_i \\ \dfrac{x_{i+1} - x}{\Delta x_i} & x_i < x < x_{i+1} \end{cases} \tag{4.89}$$

$$\frac{dN_i(x)}{dx} = \begin{cases} \dfrac{1}{\Delta x_{i-1}} & x_{i-1} < x < x_i \\ \dfrac{-1}{\Delta x_i} & x_i < x < x_{i+1} \end{cases} \tag{4.90}$$

with $\Delta x_{i-1} = x_i - x_{i-1}$ and $\Delta x_i = x_{i+1} - x_i$. Then the only integrals different from zero in Equation 4.88 are

$$\begin{aligned} &-\int_{x_{i-1}}^{x_i} \frac{dN_i}{dx}\left(u_{i-1}\frac{dN_{i-1}}{dx} + u_i\frac{dN_i}{dx}\right)dx \\ &-\int_{x_i}^{x_{i+1}} \frac{dN_i}{dx}\left(u_i\frac{dN_i}{dx} + u_{i+1}\frac{dN_{i+1}}{dx}\right)dx \\ &= \int_{x_{i-1}}^{x_i} N_i s dx + \int_{x_i}^{x_{i+1}} N_i s dx \end{aligned} \tag{4.91}$$

Using the equalities in Equation 4.89, the right-hand side is equal to

$$F = \int_{x_{i-1}}^{x_i} \frac{x - x_{i-1}}{\Delta x_{i-1}} s(x) dx + \int_{x_i}^{x_{i+1}} \frac{x_{i+1} - x}{\Delta x_i} s(x) dx \tag{4.92}$$

which, when integrated, becomes

$$F = \left(\frac{\Delta x_{i-1}}{2} + \frac{\Delta x_i}{2}\right) s_i \tag{4.93}$$

Upon required substitutions and algebraic manipulations, the discrete form of Equation 4.91 is obtained:

$$-\frac{u_i - u_{i-1}}{\Delta x_{i-1}} + \frac{u_{i+1} - u_i}{\Delta x_i} = \frac{\Delta x_{i-1} + \Delta x_i}{2} s_i \tag{4.94}$$

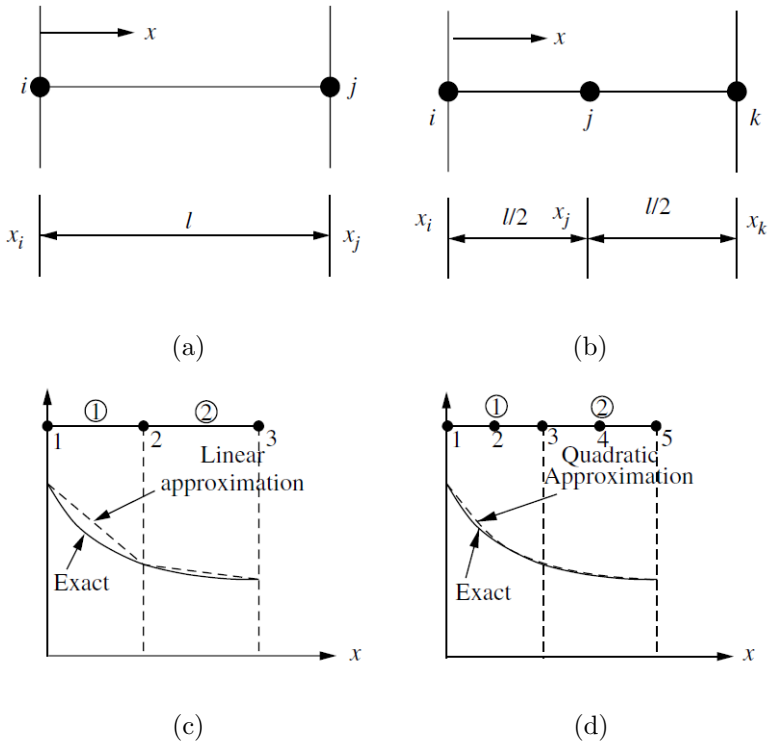

Figure 4.12. One dimensional finite elements. (a) A linear element, (b) a quadratic element, (c) linear and (d) quadratic variation of field variable ϕ over an element, ○–Element. •–Node [291].

4.4.3.2. Elements and Shape Functions. Polynomial-type shape functions are widely used because they can be integrated, or differentiated, easily and the accuracy of the results can be improved by increasing the order of the polynomial (Figure 4.12c,d).

(i) *One-dimensional linear elements*

Consider the variation of a field variable ϕ over a typical linear element with end nodes i and j, and with corresponding values of the variable denoted by ϕ_i and ϕ_j, respectively [291]. The linear variation in the element is represented by

$$\phi(x) = \alpha_1 + \alpha_2 x \tag{4.95}$$

where ϕ is the value at any location x and the parameters α_1 and α_2 are constants. As there are two arbitrary constants in the linear representation, it requires only two

nodes to determine α_1 and α_2 [291]:

$$\begin{aligned} \phi_i &= \alpha_1 + \alpha_2 x_i \\ \phi_j &= \alpha_1 + \alpha_2 x_j \end{aligned} \tag{4.96}$$

The parameters are then

$$\begin{aligned} \alpha_1 &= \frac{\phi_i x_j - \phi_j x_i}{x_j - x_i} \\ \alpha_2 &= \frac{\phi_j - \phi_i}{x_j - x_i} \end{aligned} \tag{4.97}$$

Substitution of α_1 and α_2 into Equation 4.95 gives

$$\phi = \phi_i \left[\frac{x_j - x}{x_j - x_i} \right] + \phi_j \left[\frac{x - x_i}{x_j - x_i} \right] \tag{4.98}$$

or

$$\phi = N_i \phi_i + N_j \phi_j = \begin{bmatrix} N_i & N_j \end{bmatrix} \begin{Bmatrix} \phi_i \\ \phi_j \end{Bmatrix} \tag{4.99}$$

where N_i and N_j are called *shape functions* [291].

Equation 4.99 can be rewritten as

$$\phi = [\mathbf{N}] \{\boldsymbol{\phi}\} \tag{4.100}$$

where

$$[\mathbf{N}] = \begin{bmatrix} N_i & N_j \end{bmatrix} \tag{4.101}$$

is the shape function and

$$\{\boldsymbol{\phi}\} = \left\{ \begin{array}{c} \phi_i \\ \phi_j \end{array} \right\} \tag{4.102}$$

is the vector of unknown values of ϕ.

Equation 4.99 shows that ϕ at any location x can be calculated using the shape functions N_i and N_j evaluated at x. The shape functions at different locations within an element are given in Table 4.27.

Table 4.27. Properties of linear shape functions.

Item	**Node**, i	**Node**, j	**Arbitrary** x
N_i	1	0	between 0 and 1
N_j	0	1	between 0 and 1
$N_i + N_j$	1	1	1

The two *essential requirements of the properties of the shape functions of any element in one, two or three dimensions* are that

- at the node of interest the shape function assumes a value of unity, and at all other nodes, zero
- sum of all the shape functions in an element is equal to unity anywhere within the element including the boundaries

Figure 4.13 shows the variation of the shape functions and their derivatives within a linear element. A typical linear variation of ϕ is also shown. The derivatives of the shape functions are evidently constant within an element.

One-dimensional quadratic, and two-dimensional triangular shape functions are explained in detail in Appendix C. Information on higher-order and three-dimensional elements can be found in [291].

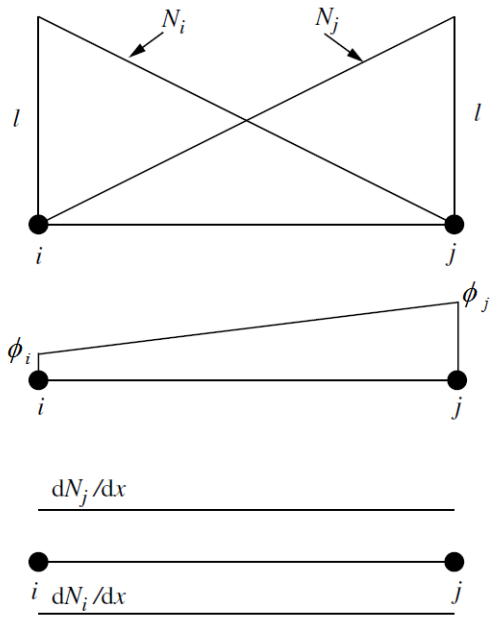

Figure 4.13. Variation of shape functions, ϕ and derivatives within a linear element [291].

4.4.3.3. Solvers. The solvers employed by Comsol Multiphysics™ (henceforth referred to as Comsol™) for the solution of the assembled matrices in the finite element method break down the problem–whether linear or nonlinear–into one or several linear systems of equations by approximating the given problem with a linearized problem [280]. Whether working on a stationary or time-dependent model, the solver spends most of its time solving one or several systems of linear equations. Because the number of unknowns in these systems is usually very large, the most important solver parameter setting concerns the choice of the *linear solver*. The linear solvers available in Comsol™ and their capabilities are tabulated in Table 4.28.

The direct solvers PARDISO, UMFPACK, SPOOLES and TAUCS Cholesky are preferable for 1D and 2D models, and for 3D models with the degrees of freedom between 100000 and 1000000. The direct solvers solve a linear system by Gaussian elimination. This stable and reliable process is well-suited for ill-conditioned systems. The *elimination process sometimes requires large memory resources and long computing times*, an effect particularly noticeable for 3D models [280]. The spatially segregated

Table 4.28. Linear system solvers in Comsol [280].

Linear system solver	**Usage**
Direct solvers	
UMFPACK	A highly efficient direct solver for nonsymmetric systems
SPOOLES	An efficient direct solver for symmetric and nonsymmetric systems which uses less memory than UMFPACK
PARDISO	A highly efficient direct solver for symmetric and nonsymmetric systems that often uses less memory than UMFPACK
PARDISO out of core	An out-of-core version of PARDISO that stores the LU-factors on disk
Cholesky (TAUCS)	An efficient direct solver for symmetric, positive-definite systems
Iterative solvers	
GMRES	An iterative solver for nonsymmetric problems
FMGRES	An iterative solver for nonsymmetric problems which can handle more general preconditioners but also uses more memory than GMRES
Conjugate gradients	An iterative solver for symmetric positive definite problems
BiCGStab	An iterative solver for nonsymmetric problems which uses a fixed amount of memory independent of the number of iterations.
Geometric multigrid	An iterative solver for elliptic or parabolic problems

microchannel reactor models introduced in Section 4.2.1 are solved using the finite element method on Comsol™ with the direct linear solvers UMFPACK [292, 293] and PARDISO [294].

4.4.4. The Finite Volume Method

Like the finite element method (Section 4.4.3), the finite volume method is based on the integral formulation of the partial differential equations describing the system. The solution strategy involves

- discretization of the solution domain into control volumes (cells)
- integration of the equations on the individual control volumes in order to reduce them to algebraic equations for the dependent (unknown) variables (e.g. velocity, pressure, etc.)
- linearization of the discretized equations and solution of the linear system(s) of equations in order to update the values of the variables until convergence criteria are met

The solution strategy is somewhat varied by the last step above since the approach used to linearize and solve the discretized equations differentiates from solver to solver.

The two commonly employed solvers in the finite volume method are [295]

- the pressure-based solver
- the density-based solver

In both methods the velocity field is obtained from the momentum equations. In the *density-based approach*, the continuity equation is used to obtain the density field while the pressure field is determined from an equation of state. On the other hand, the *pressure-based solver* extracts the pressure field by solving the pressure or pressure correction equation, which is obtained by manipulation of the momentum and continuity equations [295].

The methane ATR model (Section 4.2.2) is solved by the finite volume method employing the pressure-based solver that specifically uses the SIMPLE algorithm. Below is an overview of this solver and the required discretization schemes associated with it. For details of the density-based solver, the reader is referred to the ANSYS FLUENT 14.0 User's Guide [295].

4.4.4.1. Discretization and Solution of the General Scalar Transport Equation. Consider the unsteady conservation equation for transport of a scalar quantity ϕ written in integral form for an arbitrary control volume V [295]:

$$\int_V \frac{\partial \rho\phi}{\partial t} dV + \oint \rho\phi\vec{\mathbf{v}}\cdot d\vec{\mathbf{A}} = \oint \Gamma_\phi \nabla\phi \cdot d\vec{\mathbf{A}} + \int_V S_\phi dV \tag{4.103}$$

where ρ is the fluid density, $\vec{\mathbf{v}}$ the velocity vector, $\vec{\mathbf{A}}$, the surface area vector, Γ_ϕ, the diffusion coefficient for ϕ, $\nabla\phi$, the gradient of ϕ, and S_ϕ, the source of *phi* per unit volume. Discretization of Equation 4.103 on an arbitrary control volume, or cell (Figure 4.14), yields

$$\frac{\partial \rho\phi}{\partial t} V + \sum_f^{N_{\text{faces}}} \rho_f \vec{\mathbf{v}}_f \phi_f \cdot \vec{\mathbf{A}}_f = \sum_f^{N_{\text{faces}}} \Gamma_\phi \nabla\phi_f \cdot \vec{\mathbf{A}}_f + S_\phi V \tag{4.104}$$

where N_{faces} is the number of faces enclosing the cell, ϕ_f, the value of ϕ convected through face f, $\rho_f \vec{\mathbf{v}}_f \cdot \vec{\mathbf{A}}_f$, the mass flux through face f, $\vec{\mathbf{A}}_f$, the area of face f, $\nabla\phi_f$, the gradient of ϕ at face f, and V, the cell volume.

The discretized scalar transport equation (Equation 4.104) contains the unknown scalar variable ϕ at the cell center as well as the unknown values in the surrounding neighboring cells. This equation will, in general, be nonlinear with respect to these variables. A linearized form of Equation 4.104 can be written as [295]

$$a_P \phi = \sum_{\text{nb}} a_{\text{nb}} \phi_{\text{nb}} + b \tag{4.105}$$

where the subscript nb refers to neighboring cells, and a_P and a_{nb} are the linearized

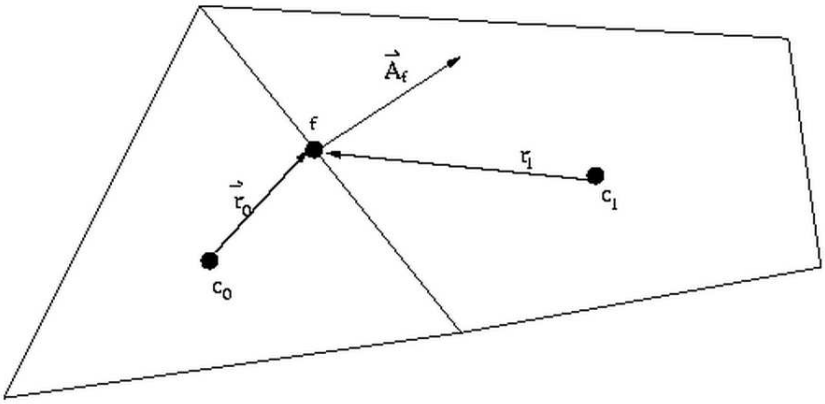

Figure 4.14. Control volume used to illustrate discretization of a scalar transport equation [295].

coefficients for ϕ and ϕ_{nb}. The number of neighbors for each cell depends on the grid, but will typically equal the number of faces enclosing the cell except for boundary cells. Similar equations can be written for each cell in the grid, which result in a set of algebraic equations with a sparse coefficient matrix.

- *Spatial discretization*

Discrete values of the scalar ϕ are stored at the cell centers (c_0 and c_1 in Figure 4.14) by default. However, face values ϕ_f are required for the convection terms in Equation 4.104, and must be interpolated from the cell center values. This is accomplished using an *upwind scheme*. Upwinding means that the face value ϕ_f is derived from quantities in the cell upstream relative to the direction of the normal velocity v_n in Equation 4.104. The diffusion terms in Equation 4.104 are discretized using the central differencing scheme, and are always second-order accurate.

(i) *First-order upwind scheme*

When first-order accuracy is sufficient, quantities at cell faces are determined by assuming that the cell-center values of any field variable represent a cell-average value and hold throughout the entire cell; i.e., the face quantities are identical to the cell

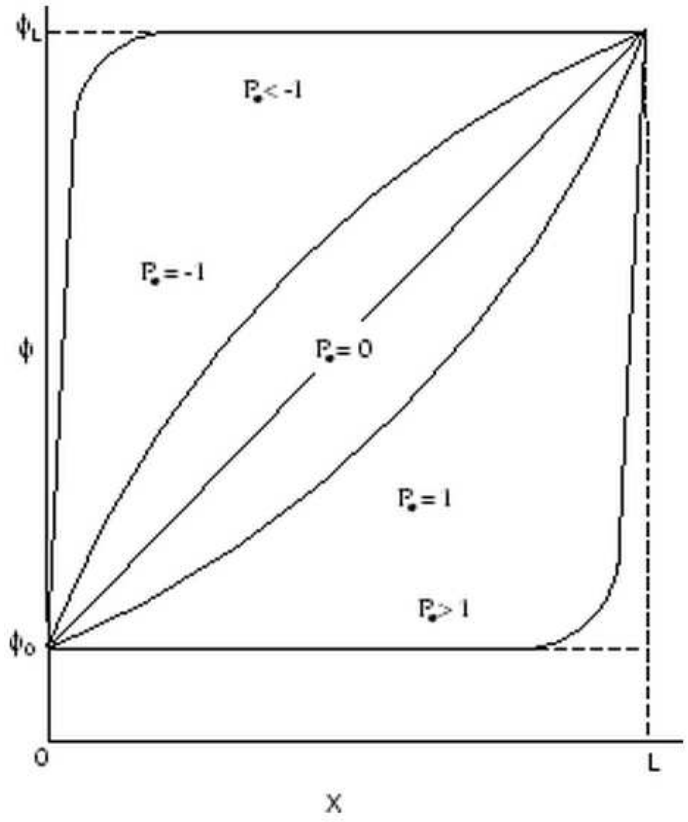

Figure 4.15. Variation of ϕ between $x = 0$ and $x = L$ for a one-dimensional convection-diffusion problem [295].

quantities. Thus, when first-order upwinding is applied, the face value ϕ_f is set equal to the cell-center value of ϕ in the upstream cell.

(ii) *Power-law scheme*

The power-law discretization scheme interpolates the face value of ϕ using the exact solution to a one-dimensional convection-diffusion equation [295]

$$\frac{\partial}{\partial x}(\rho u \phi) = \frac{\partial}{\partial x}\Gamma\frac{\partial \phi}{\partial x} \tag{4.106}$$

where Γ and ρu are constant across the interval ∂x. Equation 4.106 can be integrated

to yield the following solution describing how ϕ varies with x:

$$\frac{\phi(x) - \phi_0}{\phi_L - \phi_0} = \frac{\exp\left(\mathrm{Pe}\frac{x}{L}\right) - 1}{\exp(\mathrm{Pe}) - 1} \tag{4.107}$$

where $\phi_0 = \phi|_{x=0}$, $\phi_L = \phi|_{x=L}$, and Pe is the Peclet number, $\mathrm{Pe} = \rho u L/\Gamma$.

The variation of $\phi(x)$ betwen $x = 0$ and $x = L$ is depicted in Figure 4.15 for a range of Pe, which shows that for large Pe, the value of ϕ at $x = L/2$ is approximately equal to the upstream value. This implies that when the flow is dominated by convection, interpolation can be accomplished by letting the face value of a variable be equal to its upstream value.

(iii) *Second-order upwind scheme*

When second-order accuracy is desired, quantities at cell faces are computed using a multidimensional linear reconstruction approach [295], where higher-order accuracy is achieved at cell faces through a Taylor series expansion of the cell-centered solution about the cell centroid. The face value ϕ_f is computed using the following expression:

$$\phi_{f,\mathrm{SOU}} = \phi + \nabla\phi \cdot \vec{\mathbf{r}} \tag{4.108}$$

where ϕ and $\nabla\phi$ are the cell-centered value of ϕ and its gradient in the upstream cell, and $\vec{\mathbf{r}}$ is the displacement vector from the upstream cell centroid to the face centroid. This formulation requires the determination of the gradient $\nabla\phi$ in each cell, whose value is limited so that no new maxima or minima are introduced.

For discussion of other higher-order upwinding schemes employed during discretization of the partial differential equations in the finite volume method (e.g. central differencing, QUICK, third-order MUSCL), the reader is referred to the ANSYS FLUENT User's Guide [295].

- *Evaluation of gradients and derivatives*

In the finite volume method, gradients are needed for constructing values of a scalar at the cell faces, and also for computing secondary diffusion terms and velocity derivatives. The gradient of a given variable, $\nabla\phi$, is used to discretize the convection and diffusion terms in the flow conservation equations. The Green-Gauss theorem is commonly used to calculate the gradient of a scalar at the cell center c_0, whose discrete form is given as

$$(\nabla\phi)_{c_0} = \frac{1}{V}\sum_f \bar{\phi}_f \vec{\mathbf{A}}_f \tag{4.109}$$

where $\bar{\phi}_f$ is the value of ϕ at the cell face centroid, computed using two different techniques below. The summation is over all the faces enclosing the cell.

(i) *Green-Gauss cell-based gradient evaluation*

The face value $\bar{\phi}_f$ in Equation 4.109 is calculated from the arithmetic average of the values at the neighboring cell centers, i.e.,

$$\bar{\phi}_f = \frac{\phi_{c_0} + \phi_{c_1}}{2} \tag{4.110}$$

(ii) *Green-Gauss node-based gradient evaluation*

Alternatively, $\bar{\phi}_f$ can be computed by the arithmetic average of the nodal values on the face.

$$\bar{\phi}_f = \frac{1}{N_f}\sum_n^{N_f} \bar{\phi}_n \tag{4.111}$$

where N_f is the number of nodes on the face. The nodal values $\bar{\phi}_n$ are constructed from the weighted average of the cell values surrounding the nodes. In this technique,

exact values of a linear function are reconstructed at a node from surrounding cell-centered values on arbitrary grids by solving a constrained minimization problem, thus preserving second-order spatial accuracy [289, 295].

(iii) *Least squares cell-based gradient evaluation*

This technique assumes that the solution varies linearly. In Figure 4.16, the change in cell values between cell c_0 and c_i along the vector $\delta \boldsymbol{r}_i$ from the centroid of cell c_0 to cell c_i can be expressed as

$$(\nabla \phi)_{c_0} \cdot \Delta \boldsymbol{r}_i = (\phi_{c_i} - \phi_{c_0}) \tag{4.112}$$

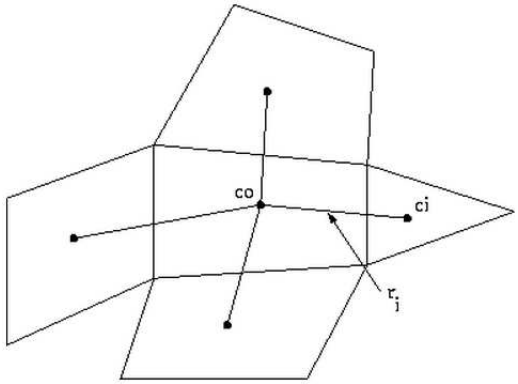

Figure 4.16. Cell centroid evaluation.

If similar equations are written for each cell surrounding the cell c_0, the following system is obtained in compact form [295]:

$$[\boldsymbol{J}] (\nabla \phi)_{c_0} = \Delta \phi \tag{4.113}$$

where $[\boldsymbol{J}]$ is the coefficient matrix which is purely a function of geometry.

The objective here is to determine the cell gradient by solving the minimization problem for the system of the non-square coefficient matrix in a least-squares sense. The linear system of equations is over-determined and can be solved by decomposing

the coefficient matrix using the Gram-Schmidt process [295]. This decomposition yields a matrix of weights for each cell. Thus, for the cell-centered scheme this means that the three components of the weights ($\boldsymbol{W}_{i0}^{x}, \boldsymbol{W}_{i0}^{y}, \boldsymbol{W}_{i0}^{z}$) are produced for each of the faces of cell c_0.

Therefore, the gradient at the cell center can be computed by multiplying the weight factors by the difference vector $\Delta\phi = (\phi_{c_i} - \phi_{c_0})$,

$$(\phi_x)_{c_0} = \sum_{i=1}^{n} \boldsymbol{W}_{i0}^{x} \cdot (\phi_{c_i} - \phi_{c_0}) \tag{4.114}$$

$$(\phi_y)_{c_0} = \sum_{i=1}^{n} \boldsymbol{W}_{i0}^{y} \cdot (\phi_{c_i} - \phi_{c_0}) \tag{4.115}$$

$$(\phi_z)_{c_0} = \sum_{i=1}^{n} \boldsymbol{W}_{i0}^{z} \cdot (\phi_{c_i} - \phi_{c_0}) \tag{4.116}$$

When a flow solution is required on polyhedral grids, the cell-based least squares gradients are recommended for use over the default cell-based gradients, particularly if a more accurate solution is desired [295].

4.4.4.2. Pressure-based Solver. The generalized transport equations (Equation 4.17-20) governing fluid flow in microchannels are all functions of the velocity field $\vec{\mathbf{v}}$, which is an unknown in CFD calculations. In order to compute the entire flow field, certain strategies should be developed.

Consider the momentum transport equations given in Table 4.6 for each velocity component. Every component appears in each equation, and the velocity field must also satisfy the continuity equation in Table 4.5. The pressure gradient term is present in all the momentum equations but there is no equation for the pressure. If the pres-

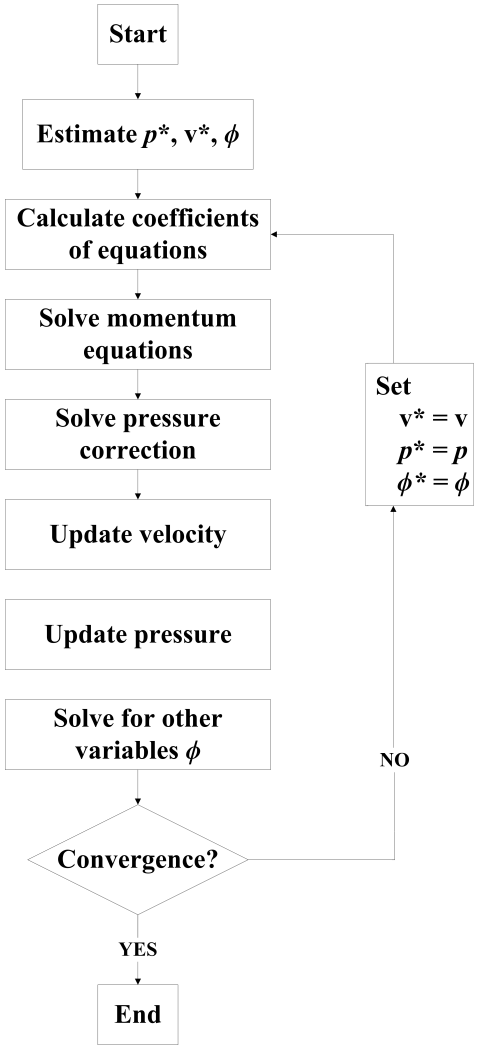

Figure 4.17. Flowchart of the SIMPLE algorithm.

sure gradient is known, the momentum equations can readily be discretized using the schemes explained in Section 4.4.4.1 as has been done for any other scalar. If the flow is compressible, the continuity and energy equations may be used as the transport equations for density and temperature, respectively, which allows for the calculation of pressure through an equation of state $p = \mathfrak{p}(\rho, T)$. However, since the flows considered in this work are incompressible, the density is constant, and, by definition, not linked to pressure. In this case pressure-velocity coupling introduces a constraint in the solution of the flow field: if the correct pressure field is applied in the momentum equations, the resulting velocity field should satisfy the continuity equation. By adopting an iterative solution strategy such as the SIMPLE algorithm [296, 297], the pressure-

velocity coupling can be resolved. In this algorithm the mass fluxes through face f, $\vec{J}_f = \rho\vec{\mathbf{v}}_n$, are evaluated from so-called guessed velocity components. Furthermore, a guessed pressure field is used to solve the momentum equations, and a pressure correction equation, deduced from the continuity equation, is solved to obtain a pressure correction field, which is in turn used to update the velocity and pressure fields. The SIMPLE algorithm, whose algorithm is shown in Figure 4.17, may be summarized as follows [289, 295, 297]:

(i) set the boundary conditions and the initial guesses $(p^*, \vec{\mathbf{v}}^*, \phi^*)$
(ii) compute the gradients of velocity and pressure
(iii) calculate coefficients of the equations and solve the discretized momentum equation to compute the intermediate velocity field $(\vec{\mathbf{v}}^*)$
(iv) solve the pressure correction equation, and update velocity and pressure and any other scalars $(p, \vec{\mathbf{v}}, \phi)$
(v) check for convergence; if not converged, store the computed values and go back to step (ii)

Other pressure-velocity coupling algorithms, e.g. SIMPLEC, a variant of SIMPLE [298], the Pressure-Implicit with Splitting of Operators (PISO), part of the SIMPLE family of algorithms, and Coupled, are explained in detail in the references [289, 295].

The PRESTO! (PREssure STaggering Option) scheme [297] is used to interpolate the pressure values at the cell faces for discretization of the momentum equation.

In this work GAMBIT 2.4.6 is used to create the spatially integrated microchannel geometry and the computational grid for the problem. The relevant details are outlined in Section 5.6.

5. RESULTS AND DISCUSSION

5.1. Simulation of On-board Fuel Conversion in Catalytic Microchannel Reactor-Heat Exchanger Systems

Catalytic conversions of propane, methanol and ethanol are simulated in spatially segregated microchannel reactors that involve successive exothermic combustion and endothermic reforming channels in order to investigate the effect of design parameters on hydrogen yield. The parameters investigated are the channel opening dimensions, thickness of the wall segregating the channels, and absence/presence of built-in micro-baffles that extend normally into the flow zone. Time required to reach steady state for methanol and ethanol reforming is determined by time-dependent analyses. Size of an actual microchannel reactor to produce enough hydrogen to run a 2-kW PEMFC is calculated based on simulation results.

The reactions taking place in the microchannels are given in Tables 4.1 and 4.2 in Section 4.1.1.1. The 2D model geometry is shown in Figure 4.4 in Section 4.2.1. Kinetics for each reaction are presented in Table 4.13-15 and Table 4.17-19. Physical properties of the fluid mixtures and the segregating wall are given in Table 4.24. Operating conditions are presented in condensed form in Table 4.26. The governing equations for free flow and flow in porous media together with the species and energy equations (Section 4.2.3), subject to the boundary conditions outlined in Section 4.2.4, are solved using the finite element method (Section 4.4.3) on the CFD package Comsol^{TM} [280]. The unstructured grids for straight-through flows consist of $13675 - 50735$ two-dimensional, quadratic triangular elements (Figure 5.1). At regions near the channel inlets and in the subdomain where combustion is modeled (combustion catalyst), the grid is refined so that it can resolve sharp concentration and temperature gradients. Unstructured grids are used for flows in microchannel configurations with micro-baffles as well. The solutions are tested to be grid-free. UMFPACK solver is employed for solution of the linear system of equations with the tolerance set to 1×10^{-6}. Typical run times until convergence are $2 - 4$ minutes.

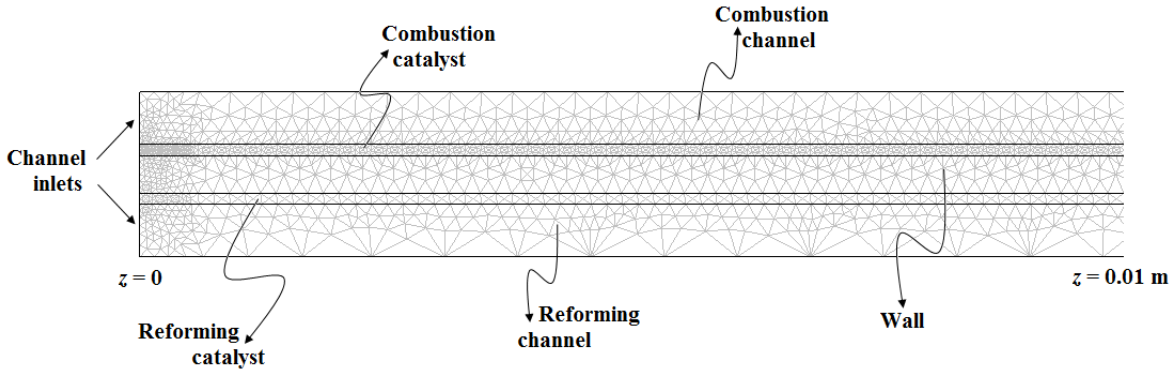

Figure 5.1. The first one-tenth of the computational grid used in the simulation of the parallel microchannel reactor for coupling of combustion and steam reforming of propane ($SL = 560\,\mu$m, $WT = 200\,\mu$m).

Several cases that involve variation of *either* the wall thickness *or* the side lengths of both channels are investigated for each fuel (Table 5.1). The last case which aims to determine the effect of using micro-baffles is not considered for methanol. The results of combustion/steam reforming coupling of propane, methanol and ethanol are presented in Figure 5.2a,b,c, which show the effects of geometric parameters on H_2 yield at the steam reforming channel exit, which is defined as the moles of H_2 produced per mole of fuel fed.

Table 5.1. Cases involving the variations of the wall thickness and side length.

Case	**Wall thickness, WT (μm)**	**Side length, SL (μm)**
1	100	560
2	200	560
3	300	560
4	400	560
5	200	280
6	200	420
7	200	560 (micro-baffles)

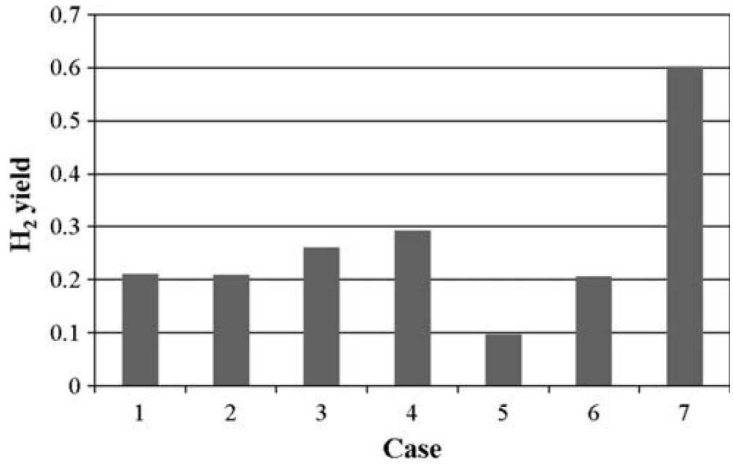

(a)

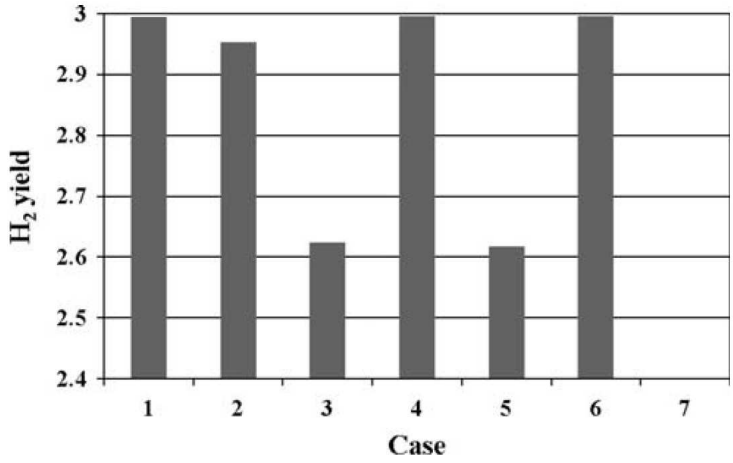

(b)

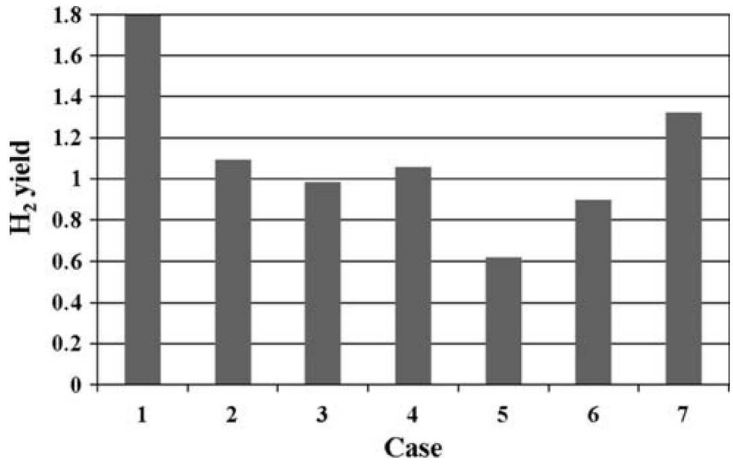

(c)

Figure 5.2. H_2 yields for different wall thicknesses and channel side lengths when (a) propane, (b) methanol, (c) ethanol is used as the fuel.

5.1.1. Effect of Wall Thickness

Methanol is known for having the advantage of requiring mild conditions for being reformed. This fact is in alignment with the simulations which predict near complete reforming and combustion conversion for feed temperatures of 473 K, and give H_2 yields close to 3 (Figure 5.2b), the maximum theoretical value dictated by the stoichiometry. This value is obtained at $560 \times 560\,\mu m^2$ channels segregated by a $100\,\mu$m wall. When the channel side lengths are kept constant and wall thickness is increased gradually up to $300\,\mu$m, a decrease in H_2 yield down to 2.62 is observed. As the increased wall thickness brings about more resistance to heat flow to the reforming zone from the combustion zone, and causes reduced steam reforming temperatures, lower yields can be expected. However, the decreasing trend is then changed by a thicker, $400\,\mu$m wall that increases the yield again up to ca. 3 (Figure 5.2b). Such a response can be explained by analyzing the heat transfer between the channels: at the microscale heat exchange takes place immediately at the entrance (first 0.01 m) of the channels. Fast heat removal from the combustion zone suppresses the light-off and prevents further temperature rise. Considering this fact, the increase in wall thickness from 300 to $400\,\mu$m makes the combustion channel more "adiabatic", i.e., tends to preserve the temperature by reducing the rate of heat removal and, therefore, allows more methanol to be combusted. As a result, amount of heat produced and transferred to methanol reforming increases, thus leading to higher H_2 yields. The 400-μm wall certainly increases the resistance to heat flow between the channels (as in the $300 - 400\,\mu$m range), but also lets the combustion to produce more heat to overcome the resistance effect and increase the conversion of endothermic methanol reforming.

The response of combustion/steam reforming of ethanol-to-hydrogen conversions against increased wall thickness, shown in Figure 5.2c, are found to be similar to that observed for methanol. However, conversion of propane shows a slightly different trend: H_2 yields are found to be almost the same in the case of 100 and $200\,\mu$m walls and are increased at the $200 - 400\,\mu$m wall range (Figure 5.2a). Propane differs from the alcohols with its high heat of combustion. The corresponding value of $-2044\,kJ\,mol^{-1}$

makes the "adiabatic" effect explained above more pronounced for propane, as the retardation of heat removal from combustion channel even at small levels can lead to higher combustion conversions, and produce excess heat that suppresses the wall resistance. This fact leads to the clear domination of the "adiabatic" effect, as it is valid in a wider, $200 - 400\,\mu$m range. Moreover, it can balance the opposing wall resistance in the $100 - 200\,\mu$m range, in which the latter phenomenon is clearly dominant in the case of alcohols (Figure 5.2a,b).

5.1.2. Effect of Side Length

The effect of channel side length on H_2 yields are shown in Figure 5.2a,b,c. Simulations involving a constant wall thickness of $200\,\mu$m reveal that reducing the side length from 560 to $420\,\mu$m causes changes in H_2 yield only below ca. 20%, whereas an equivalent size reduction leading to $280\,\mu$m results in yield losses up to 50%. Considering the fact that the molar flow rates do not change, reduction in channel cross-sectional areas increases the superficial velocities in both channels, decreases the residence times amd reduces the conversions and yields. However, although the side lengths are changed at equal intervals ($140\,\mu$m), the residence time effect is reflected less and more respectively in the $560 - 420\,\mu$m and $420 - 280\,\mu$m ranges. The difference can be explained by the opposing effect of convective heat transfer that is favored by improved mixing induced by higher superficial velocities: mixing can favor heat flow between the channels by increasing the convective heat transfer coefficients in both channels to a certain extent. This mechanism seems to be more effective in the former range and even dominates the residence time effect slightly in the case of methanol where the yield obtained in the $560\,\mu$m channel is incrementally lower than that in $420\,\mu$m (Figure 5.2b). Below this, however, yields are adversely affected (Figure 5.2a,b,c). Pressure drop is found to be negligible in all cases and is estimated to vary between 72 and 205 Pa upon decreasing the channel side length from 560 to $280\,\mu$m.

5.1.3. Effect of Using Micro-baffles

The possibility of improving H_2 yields via the mixing effect is further investigated by considering wall-integrated micro-baffles that extend normally into the flow zones (Figure 4.4). Since methanol conversion gives near theoretical yields, simulations are conducted only for propane and ethanol conversions running in $560 \times 560\,\mu m^2$ channels segregated by 200-μm-thick walls. The results show that, compared with the straight-through flow configuration, presence of micro-baffles increases the H_2 yield by $\sim 190\%$ and by $\sim 21\%$ in the case of combustion/reforming of propane and ethanol, respectively (Figure 5.2a,c) at the expense of only $\sim$ 20 Pa increase in pressure drop. Micro-baffles act as static mixers and improve the convective heat transfer coefficients, which eventually favors the rate of heat transfer into the reforming zone. These findings are in accordance with the relevant works in the literature that report improved heat transfer characteristics as the result of use of structured microchannels [299].

5.1.4. Time-dependent behavior

Dynamics of the parallel microchannel system is also investigated to gain insight about the start-up behavior of a multichannel fuel processor. Transient CFD simulations are run only for alcohols in $560 \times 560\,\mu m^2$ straight-through channels segregated by 200-μm-thick walls. Results show that combustion/steam reforming couplings of methanol and ethanol require 1000 s and 1350 s, respectively, for reaching steady state (Figure 5.3a,b). For such flows at the micro-scale, the start-up times are somewhat prolonged: once the reactor operation is initiated, compact nature of the system lets continuous and rapid use of exothermal heat by steam reforming which slows down the take-off of combustion and the whole system. However, due to the fact that the fuel processor serves to supply hydrogen for a PEM-based auxiliary power unit, the start-up period can be compensated by other means such as use of hydrogen stored from previous cycles.

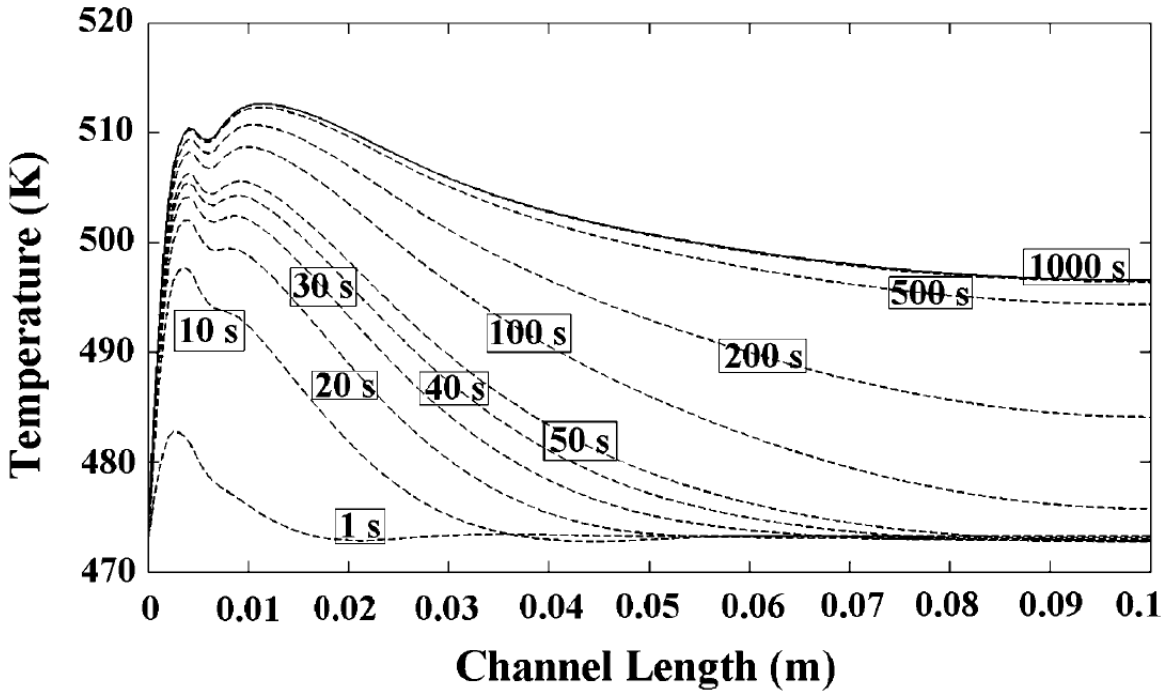

(a)

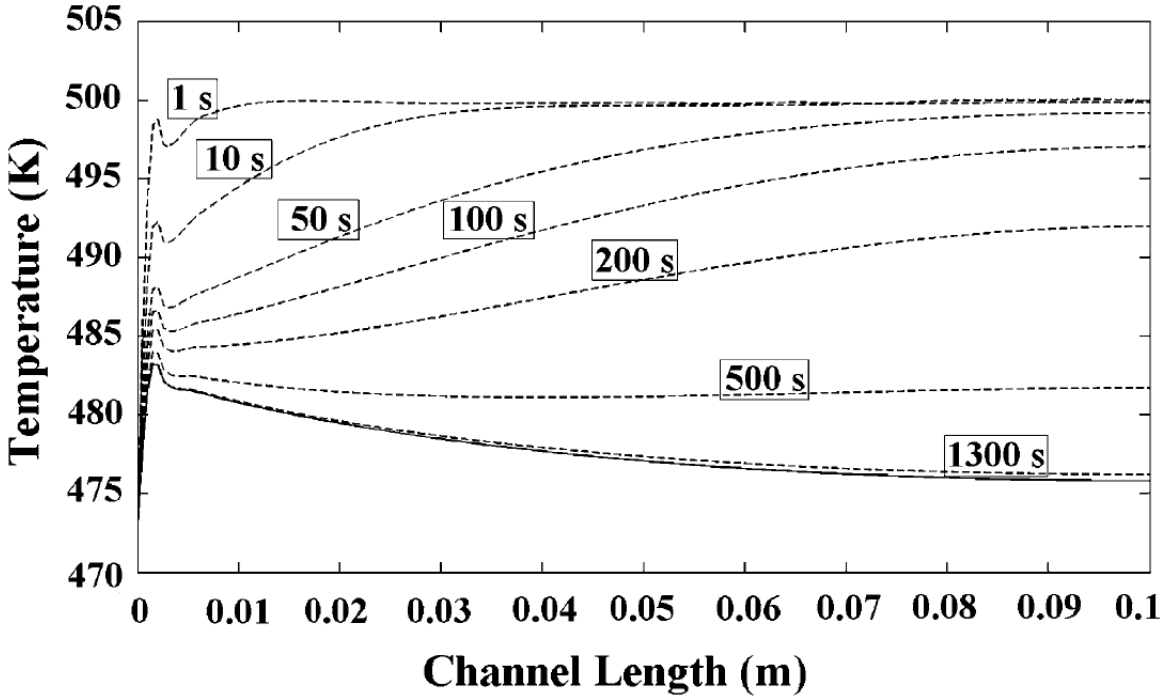

(b)

Figure 5.3. Temporal and spatial profiles of steam reforming of (a) methanol and (b) ethanol.

5.1.5. Sizing

Sizing of an actual fuel conversion unit is also carried out by taking methanol as the fuel of choice. The basis value of $40\,\mathrm{mol\,h^{-1}}$ of H_2 per kW of PEM power [300] together with single channel H_2 yield (Case 2, Figure 5.2b) gives a total of ca. 120000 channels for generating H_2 to drive a 2-kW PEM fuel cell. Considering that a single plate contains 400 microchannels, 300 plates are required. For such a microchannel assembly, the dimensions are $0.3 \times 0.1 \times 0.4\,\mathrm{m^3}$, totaling to a volume of $1.2 \times 10^{-2}\,\mathrm{m^3}$.

5.1.6. Summary

Catalytic oxidation and steam reforming of methanol, ethanol and propanol are studied in two parallel, wall-segregated, square microchannels. Effects of wall thickness, channel side length and use of a non-uniform geometry within the channels on hydrogen yield are investigated by steady-state and transient CFD simulations. Change in the wall thickness leads to different behaviors of steam reforming of propane and alcohols. Decrease in side length, i.e., increase in superficial fluid velocities, tends to increase H_2 yields, most likely by mixing-driven improvements in the heat transfer coefficients. However, further reduction in side length results in abruptly declining residence times and thus H_2 yields. Use of micro-baffles, which are known to act as static mixers, leads to notable increase in steam reforming conversions and H_2 yields. Duration of the start-up is found to vary between 1000 and 1350 s. Number of channels and size of a multichannel fuel processor that can drive a 2-kW PEM fuel cell are respectively estimated to be 120000 and $1.2 \times 10^{-2}\,\mathrm{m^3}$.

5.2. Microchannel Reactor Modeling for Combustion Driven Reforming of *iso*-Octane

In this section coupled methane combustion/*iso*-octane steam reforming in spatially segregated, parallel microchannels are parametrically studied for analyzing the effects of different geometric and material configurations on temperature distribution and hydrogen yield. Side lengths of the square microchannels, thickness and material of construction of the wall segregating them, and the use of micro-baffles are the parameters investigated. The 2D unit cell model of the system is employed for carrying out the simulations after reduction from the 3D to 2D model is justified.

Reaction kinetics of methane combustion (represented by Equation 4.11) and *iso*-octane reforming (represented by Equation 4.13) are given in Table 4.12 and Table 4.21, respectively. The 3D and 2D model geometries are shown in Figure 4.4 in Section 4.2.1. Physical properties of the reactive mixtures and of the wall are tabulated in Table 4.24. Reactor and catalyst data, and the operating conditions are summarized in Table 4.26. Momentum, species mass and energy equations describing fluid flow in the microchannels, coupled with the energy equation governing heat flow through the wall (Section 4.2.3) that are subject to the pertinent boundary conditions in Section 4.2.4 are solved by the finite element method on the CFD package Comsol™ v3.5a [280] running on a HP z800 workstation equipped with 8×2.67 GHz Xeon™ processors and 32 GB of DDR3 memory.

In all simulations, length of the microchannels (L) is set as 1×10^{-1} m. Thickness of the wall is varied in 1×10^{-4} m increments from 1×10^{-4} to 4×10^{-4} m while keeping the microchannel side length constant at 5.6×10^{-4} m. For every wall thickness variation, straight-through (ST) and micro-baffled (BF) channel configurations are also tested (Figure 4.4, lower inset). The equally-spaced micro-baffles with 1×10^{-4} m length and 2×10^{-3} width are thought of as being integral parts of the metallic plates. In addition to wall thickness and channel texture, side lengths (SL) of the square microchannels are studied by varying them from 2.8×10^{-4} to 5.6×10^{-4} m in increments of 1.4×10^{-4} m for the 2×10^{-4} m thick wall. The above-mentioned plans of the

parametric studies addressing geometric variations involve the use of AISI steel as the default wall material. Importance of wall material in reactor behavior is explored by changing the material to α-Al_2O_3 and iron in the configuration with the 2×10^{-4} m thick wall segregating straight-through microchannels with 5.6×10^{-4} m side length. This parametric approach amounts to performing 12 grid-independent simulations in 3D, each of which is expected to take several tens of hours till convergence. For instance, as a base trial, the geometry for 5.6×10^{-4} m straight-through channels and 2×10^{-4} m thick steel walls, when discretized using quadratic tetrahedral elements, is comprised of 70388 elements. That many elements are required for the grid-independent solution, which has been sought only for this given set of geometric parameters by increasing the number progressively from 25800 to 84923. Due to the particular configuration of the microchannels within the reactor block shown in Figure 4.4, however, it is possible to obtain nearly the same results using a 2D model with considerably lower computational cost. The bases of this simplification, together with a comprehensive comparison of 2D and 3D models are outlined in Section 5.2.1. This simplified approach is employed in conducting the parametric studies whose results are presented and discussed in Sections 5.2.2 to Sections 5.2.5.

5.2.1. Comparison of 2D and 3D Models

In a parallel microchannel geometry, any given channel is part of a horizontal array of channels, which has the same reaction occurring within, as shown in the cross-sectional view on the $x - y$ plane (Figure 4.4). Considering one of the combustion (exothermic) channels, heat released due to the reaction is transferred in all directions. However, for two reasons the direction of net heat flow is toward the endothermic reforming channels: (i) lateral heat flow in the x-direction is counter-balanced by heat flow from adjacent combustion channels, and (ii) the temperature gradients in the x-direction are much smaller than those in the y-direction due to the fact that the reactions taking place in a given row are identical (either combustion or reforming). This reasoning gives way to constructing a mathematical model in 2D, i.e., a model excluding x as an independent variable. Further simplification of the model is possible

because another implication of the alternating and symmetrical arrangement of the reaction channel arrays is that inbound and outbound heat fluxes into and out of any repeating pair of exo- and endothermic channels essentially cancel each other out so long as the number of channels is sufficiently high in the y-direction. Then the 2D model reduces to the repeating unit cell that consists of two parallel semi-channels segregated by a wall (Figure 4.4, lower inset) with the co-current flow of the exo- and endothermic reactive streams. This approach is particularly useful for comparative and parametric analyses of coupling of combustion and reforming in spatially segregated microchannel or plate reactors, as the inclusion of the third dimension affects the results negligibly.

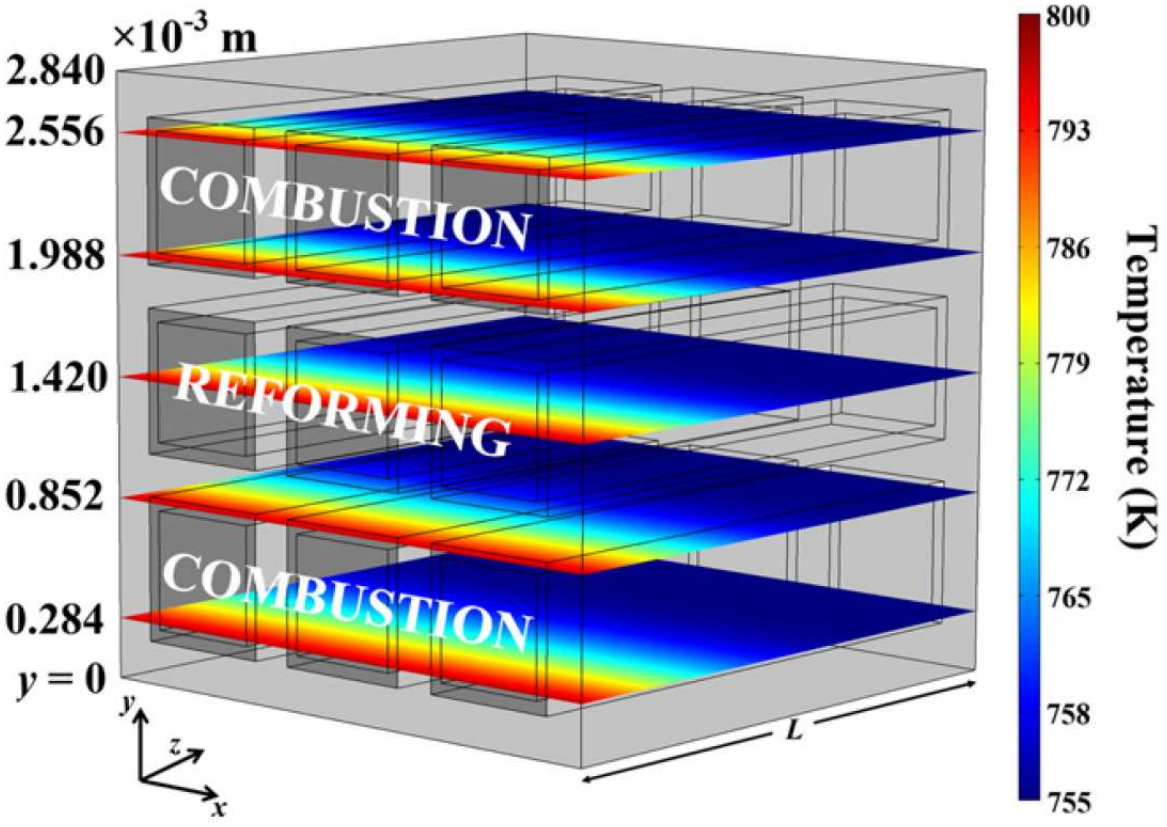

Figure 5.4. Temperature variation in x- and z-directions at different levels of y-coordinate for the base case ($SL = 5.6 \times 10^{-4}$ m, $WT = 2 \times 10^{-4}$ m, material: AISI steel) using the 3D 9-channel model.

Figure 5.4 shows the plot of the temperature variation with x and z at 5 different evenly-spaced y values for the base trial run ($SL = 5.6 \times 10^{-4}$ m, $WT = 2 \times 10^{-4}$ m, material: AISI steel), which indicates that there is no variation laterally (in the x-direction). The difference between temperatures predicted by the 2D unit cell and 3D 9-channel models, averaged over the entire domains, is 4 K. Even though this corresponds to $\sim$ 10% of the difference between the inlet (800 K) and outlet (755 K) temperatures obtained by the 3D model, the trends of axial temperature evolution are the same. The difference between the outlet temperatures is even smaller (755 K and 753 K). Thus, it is safe to assume that the 2D unit cell model can be substituted for the current 3D model, considering that the 2D model results are acceptable for the scope of this work.

The 2D unit cell approach is also attractive on the basis of memory and CPU requirements, both of which increase immensely with the inclusion of the third dimension [20, 207, 235, 265, 266]. To illustrate, simulation of the base case using the 3D model requires a grid consisting of 70388 tetrahedral elements and 32 h of CPU time for obtaining the result in Figure 5.4. On the other hand, the base case simulations are executed with a CPU time of less than only 3 min when the 2D model is used with the number of quadratic triangular elements ranging between 22674 and 40251. 33980 elements are found to be sufficient to secure a grid-independent solution for the given set of parameters (Figure 5.5). The longest side of the triangular elements varies between 385×10^{-4} and 392×10^{-4} m. The grids for microchannel geometries with micro-baffles are comprised of more elements that are needed to resolve the flow field around the corners of the microbaffles (Figure 5.5). The grid-independent solution for $SL = 5.6 \times 10^{-4}$ m, $WT = 2 \times 10^{-4}$ m and AISI steel is obtained using 35676 triangular elements.

5.2.2. Effect of Wall Thickness

In this series of simulations, thickness of the steel wall (WT) is increased from 1×10^{-4} to 4×10^{-4} m at 1×10^{-4} m increments both for straight-through (ST) and micro-baffled (BF) channels by keeping the side length of the square microchannels (SL)

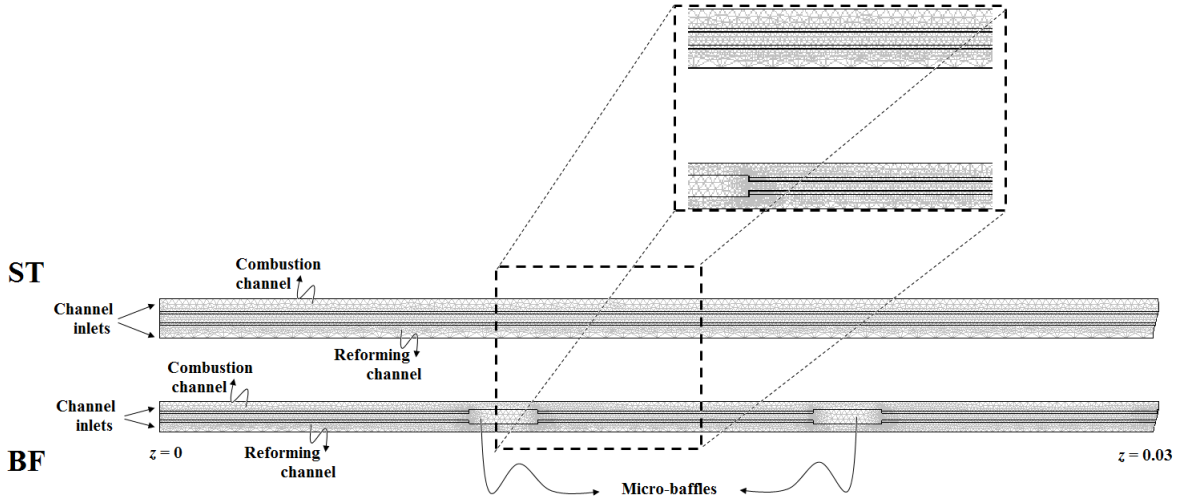

Figure 5.5. The grids used in the simulations of the 2D unit cell model for straight-through (ST) and micro-baffled (MF) configurations ($SL = 5.6 \times 10^{-4}$ m, $WT = 2 \times 10^{-4}$ m, material: AISI steel).

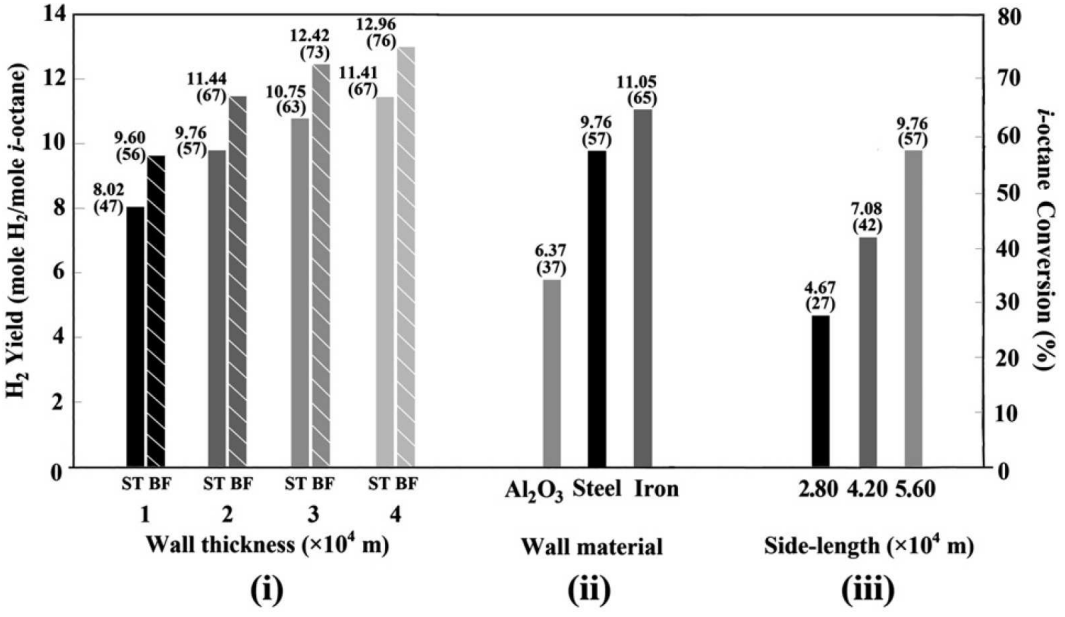

Figure 5.6. Hydrogen yields and *iso*-octane conversions (in parentheses) obtained for different (i) wall thickness, (ii) wall materials, and (iii) microchannel side lengths.

constant at 5.6×10^{-4} m. The first group of bar plots (Case (i)) in Figure 5.6 shows that when the wall thickness is increased from 1×10^{-4} to 4×10^{-4} m, the increase in the hydrogen yield, defined as the number of moles of hydrogen produced in the reforming channel per number of moles of *iso*-octane fed, is 42% and 35% for the straight-through and micro-baffled channels, respectively. This follows directly from the increase in the rate of reaction, hence the fuel conversion–defined as the ratio of number of moles of *iso*-octane converted to the number of moles of *iso*-octane fed—whose evolution along the channel for different wall thicknesses mimics the temperature profiles. In contrast to what is given by the plots, a thicker wall that poses a larger resistance to heat transfer between combustion and reforming zones is actually expected to lead to lower reforming temperatures and hinder the yield. According to the average channel temperatures along the reforming channel shown in Figure 5.7a, as the steel wall gets thicker, the temperature drop due to the endothermic reaction is more severe over the first few millimeters into the entrance of the channel. However, along the remainder of the channel length, the reverse trend is observed: the rate of temperature decline is smaller for a thicker wall. For a plausible explanation of the phenomenon, one should resort to axial evolution of heat flux through the wall-reforming channel boundary, shown in Figure 5.7b. At the reforming channel entrance, for the thinnest wall, the component of the heat flux normal to the wall-steam reforming washcoat boundary (in y-direction) is greatest, which provides the largest partial compensation for the heat lost, resulting in the comparatively mild decrease in temperature (Figure 5.7a, inset). Once the entrance effect is surpassed, the heat transmitted to the reforming channel begins to decrease, though at a smaller rate for a wall of relatively smaller thickness. This is the reason why the overall reforming channel temperature associated with a thicker wall turns out to be higher, thereby leading to higher conversions. The variation of heat flux along the distance down the channel (Figure 5.7b) for different wall thicknesses reveals that influence of axial heat conduction within the wall becomes greater as it get thicker. The amount of heat transferred into the reforming channel within the first few millimeters upstream diminishes with increasing thickness, because axial conduction that spreads the transverse heat wave along the length of the wall becomes more effective with a larger share of the wall material.

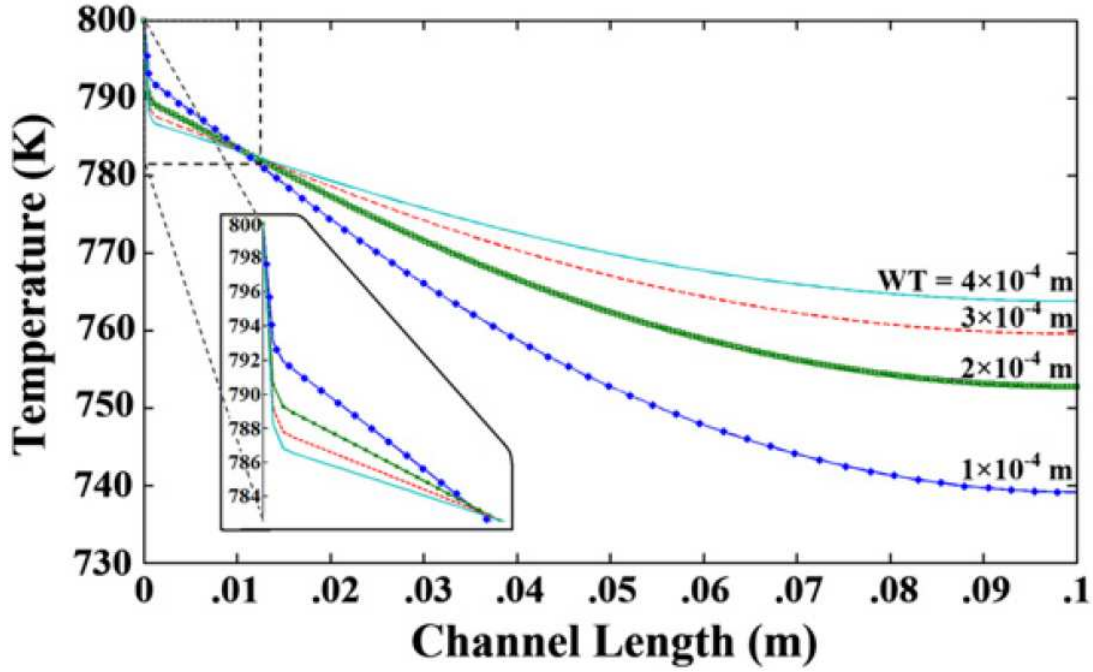

(a)

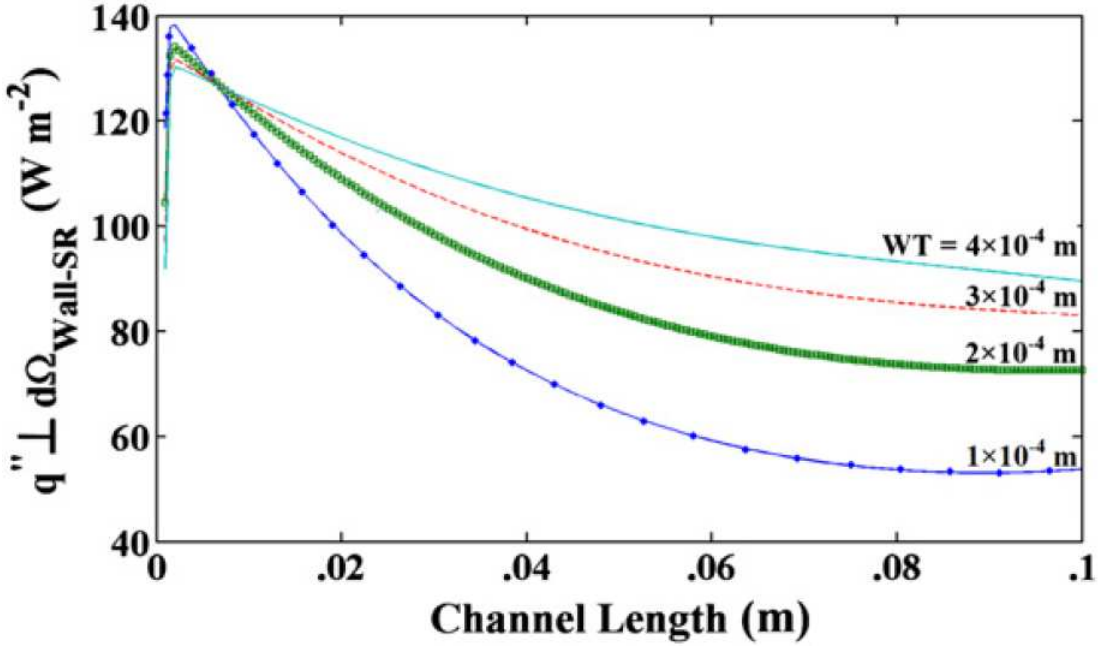

(b)

Figure 5.7. Variation of (a) the average bulk temperature along the steam reforming channel, and (b) the normal component of heat flux through the steel wall-steam reforming washcoat boundary for different wall thickness values.

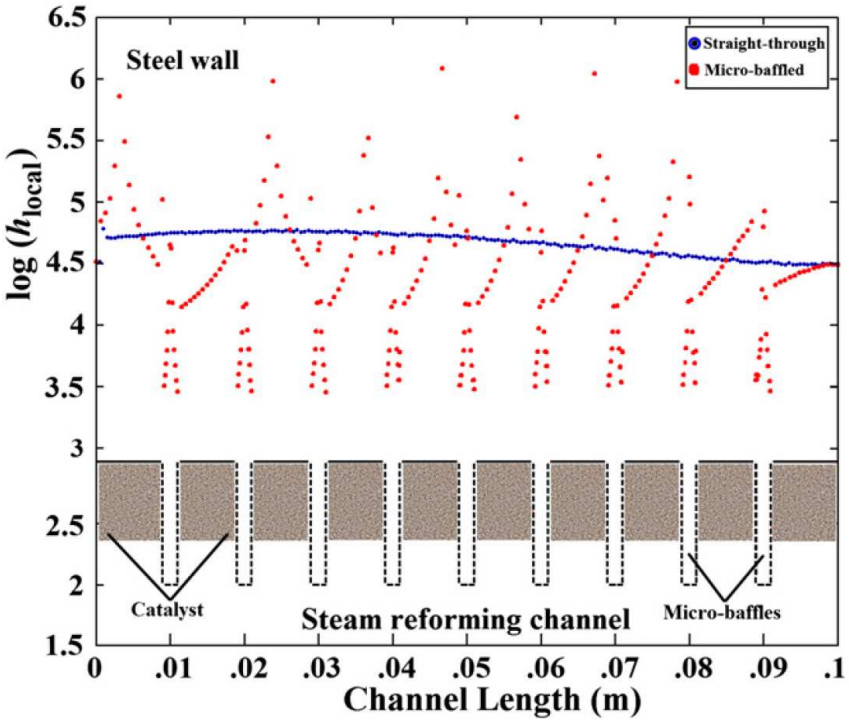

Figure 5.8. Local heat transfer coefficients along the steel wall-reforming washcoat interface for straight-through and micro-baffled geometries.

5.2.3. Effect of Channel Wall Texture

The channel wall texture has effect on hydrogen yield as well. Referring to Figure 5.6 and the results for Case (i), in the range of steel wall thicknesses investigated (1×10^{-4} to 4×10^{-4} m, the yield obtained with the micro-baffled (BF) configuration is 16.5% higher, on average, than that obtained with the straight-through (ST) configuration. Micro-baffles act as static mixers, induce further mixing in the vicinity of catalytic regions and improve the convective heat transfer coefficients, which eventually expedite heat transfer. These findings are in agreement with results in the literature that report improved heat transfer upon use of non-uniform structures in microchannels [299]. Figure 5.8 shows the logarithmic variation of the local convective heat transfer coefficients along the 2×10^{-4} m steel wall/5.6×10^{-4} m reforming channel boundary for the straight-through and micro-baffled configurations. The dashed lines and the shaded regions, both shown not-to-scale, denote the micro-baffles and the catalytic porous washcoat, respectively. Despite lacking a general trend, the heat transfer

coefficient associated with the micro-baffled configuration is far higher than that associated with the straight-through configuration over the catalytic regions, a desired situation that results in higher reforming rates. Share of the wall material is also larger due to the finned nature of the wall, thus axial heat conduction is expected to be more effective compared with the straight-through configuration. This is indeed confirmed by the yield results shown in Figure 5.6. For instance, while there is a 10% increase in yield in changing the wall thickness from 2×10^{-4} to 3×10^{-4} m for the straight-through configuration, the increase in going from a straight-through to a micro-baffled configuration (with wall thickness equal to 2×10^{-4} m) is 17%. Therefore, it can be inferred that the micro-baffles serve the dual purpose of enhancing the heat transfer coefficient and axial heat conduction.

5.2.4. Effect of Wall Material

The wall material is also of concern to the reformer design because of its role in heat transfer between the channels and also because of its strength and durability under rigorous operating conditions, such as high temperatures and pressures. Owing to its importance, three different materials–α-Al_2O_3, AISI steel and iron–having thermal conductivities of 18, 44.5 and 76.2 $W\,m^{-1}\,K^{-1}$, respectively, are tested with 5.6×10^{-4} m straight-through microchannels and 2×10^{-4} m thick wall. According to the second group of bar plots (Case (ii)) in Figure 5.6, hydrogen yield is found to increase by 53% and 73%, respectively, when steel and iron are used instead of alumina, which is the direct result of elevated reforming channel temperatures upon material change. Temperature increase can be accounted for by the same line of reasoning used for explaining the system behavior with changing wall thickness. Referring to Figure 5.9a, average bulk temperature of the reforming channel decreases at a faster rate over the first few millimeters into the reforming channel entrance as the wall thermal conductivity is increased. However, an opposite trend is observed after $\sim$ 1 cm from the entrance: for a wall of higher thermal conductivity, more sluggish decrease in temperature is noted, which results in relatively higher channel temperatures from $\sim$ 1 cm up until the exit. Once again it is necessary to check how the heat flux from the wall to the

reforming channel varies with axial distance (Figure 5.9b). Within the entrance region, normal component of the flux is greatest for the wall material with the lowest thermal conductivity. After axial conduction begins to dominate over transverse conduction, however, the more thermally conductive wall facilitates higher fluxes and temperatures (Figure 5.9a). This is due to the fact that axial heat conduction is enhanced, and it works to spread the incoming heat from the combustion region over the entire body.

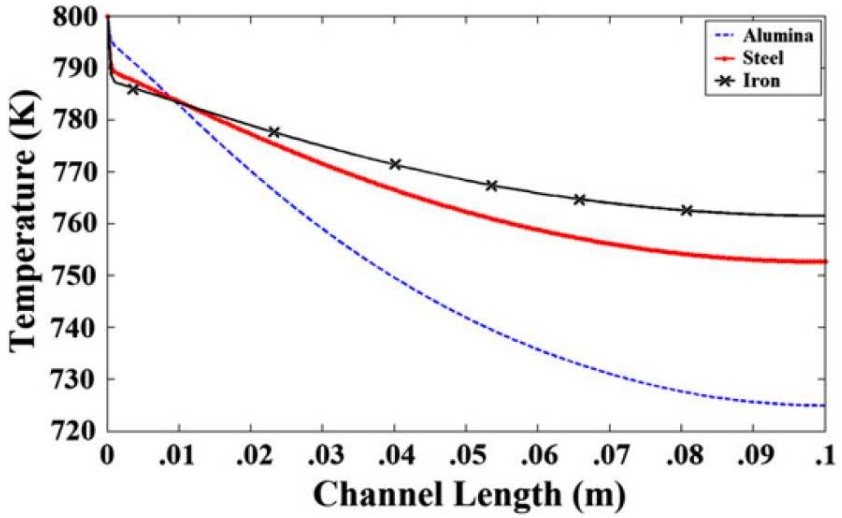

(a)

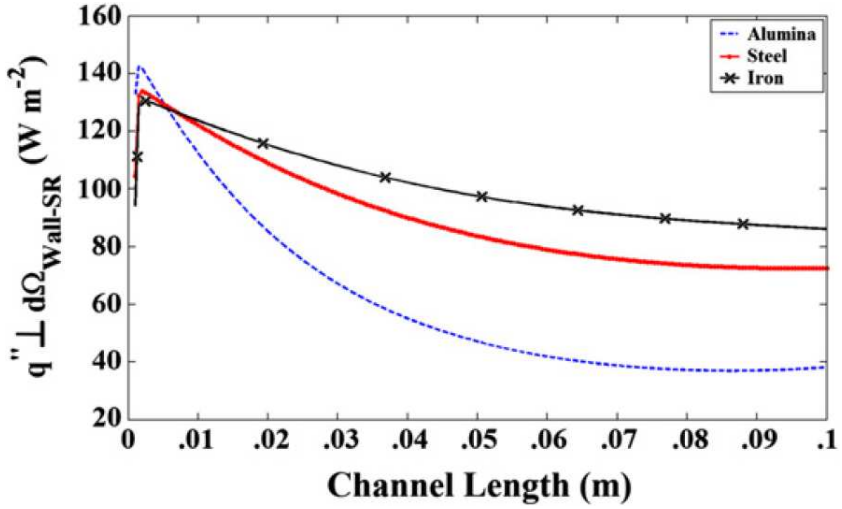

(b)

Figure 5.9. Variation of (a) the average bulk temperature along the steam reforming channel, and (b) the normal component of heat flux through the steel wall-steam reforming washcoat boundary for different wall materials.

5.2.5. Effect of Side Length of the Microchannels

The effect of channel side length on hydrogen yield is shown in Figure 5.6. Simulation results indicate that, for the constant steel wall thickness of 2×10^{-4} m, increasing the side length will increase the contact time–defined as the ratio of open channel volume to the volumetric flow rate–in both combustion and reforming channels, and will enhance the hydrogen yield. If one also considers that the flow is hydrodynamically developed and that the Nusselt number is constant [301], an increase in side length will lead to a decrease in the convective heat transfer coefficients that reduces the heat transfer rate between the combustion and reforming channels, and thus the hydrogen yield. The counteracting consequences of varying the side length can be illustrated such that in the $2.8 - 4.2 \times 10^{-4}$ m interval, the contact time is enhanced by a factor of 1.25 while the local heat transfer coefficients decrease by 0.5. Upon increasing the side length from 4.2×10^{-4} to 5.6×10^{-4} m, the contact time increases by 0.78, and the heat transfer coefficients decrease by 0.33. The respective 52% and 38% increases in hydrogen yield in the $2.8 - 4.2 \times 10^{-4}$ m and $4.2 - 5.6 \times 10^{-4}$ m intervals indicate that the effect of contact time is more pronounced in the former interval.

5.2.6. Summary

Coupling of catalytic combustion of methane and steam reforming of *iso*-octane for hydrogen production in a reformer composed of square microchannels is studied by computer simulations. Validity of a 2D unit cell model is justified, which is used to carry out the parametric study that involves varying geometric and material properties of the microchannels and of the wall. Effects of wall thickness, channel dimensions, a non-uniform geometry and wall material are investigated. Increasing the wall thickness and the channel side length leads to improvements in hydrogen yields due to pronounced axial heat conduction in the wall and due to residence time effects, respectively. Use of micro-baffles, which act as static micro-mixers, leads to considerable improvements in hydrogen yields through the enhancement of heat transfer coefficients. The performance–with respect to H_2 yield only–of iron as the wall material is superior to those of α-Al_2O_3 and stainless steel as it has the largest thermal conductivity.

5.3. Comparison of Compact Reformer Configurations for On-board Fuel Processing

This section presents the results of computer-aided analyses of two compact reaction systems for production of CO-free hydrogen via steam reforming of n-heptane in order to drive a PEM fuel cell based APU in the $2-3$ kW range. The size, efficiency and fuel requirements of a complete fuel processor based on a microchannel reactor for reforming of the fuel is explored in comparison to those of a fuel processor based on a cascade reactor (Figure 4.1). The spatially segregated microchannel reactor exemplifies a coupled reaction/heat exchange system, which is considered in detail in Section 4.2.1 whereas the cascade reactor is an example of a decoupled reaction/heat exchange system, and is explained in Section 4.3. In both systems the heat needed to drive the endothermic steam reforming reactions are supplied by exothermic methane combustion.

Reaction kinetics of methane combustion (represented by Equation 4.11) and n-heptane reforming (represented by Equation 4.7) are given in Tables 4.12 and 4.20, respectively. The 2D model geometry is shown in Figures 4.4 and 4.5 in Section 4.2.1, and the physical properties of the reactive mixtures and of the microchannel wall are tabulated in Table 4.24. Reactor and catalyst data, and the operating conditions are presented concisely in Table 4.26. The transport equations for fluid flow in the microchannels and heat flow across the segregating wall (Section 4.2.3), subject to the boundary conditions given in Section 4.2.4, are solved by the finite element method on the CFD package Comsol™ v3.5a [280] running on a HP xw8400 workstation equipped with 4×2.00 GHz Xeon™ processors and 4 GB of memory. The solution domain shown in Figure 4.5 is discretized using quadratic triangular elements. The number of elements comprising the unstructured grid is increased progressively from 2529 to 6555 to find the grid-independent solution, which is obtained with 4411 elements.

The cascade reactor design procedure is explained in Section 4.3.1 where the one-dimensional pseudohomogeneous reactor model (Eqs. (4.79)- (4.81)) is used for predicting the reactor performance. The resulting set of ordinary differential equations

(ODE) are solved on MATLAB™ using a stiff solver. Integration of the peripherals of the proposed fuel processor such as the subsequent CO clean-up units and heat exchangers, is elaborated in Section 4.1.1.2. Scale-up of microchannel reactors and heat exchangers and sizing of the peripherals are performed following the procedures given in Section 4.2.8.

5.3.1. Steam Reforming of *n*-heptane in the Microchannel Reactor

The results of the simulations for the microchannel reformer configuration are presented in Table 5.2 and Figure 5.10. It can be observed that the combustion and reforming channel temperatures equilibrate at a small distance down the channel length ($\sim$ 0.01 m) at around 730 K. This is the direct result of the high rate of heat flow between the reactive flow zones, which is one of the superior characteristics of microchannel reactors compared with their conventional counterparts: the overall heat transfer coefficient between the combustion and reforming channels are calculated to be 9270 $\mathrm{W\,m^{-2}\,K^{-2}}$ (Nu = 59 based on channel side length), whereas coupling of exothermic and endothermic reactions arranged in a similar fashion (adjacent reaction compartments, counter-current flow) but with catalysts packed in channels instead of being coated on the walls, results in overall heat transfer coefficients around 50 $\mathrm{W\,m^{-2}\,K^{-2}}$ [236]. Owing to the mean channel temperatures of $\sim$ 740 K, 87% steam reforming conversion of *n*-heptane (Figure 5.10) and 43% combustion conversion of methane are obtained. The stream leaving the reforming channel contains 1.52×10^{-6} $\mathrm{mol\,s^{-1}}$ H_2 ($\sim$ 33% by mole), 7.74×10^{-7} $\mathrm{mol\,s^{-1}}$ CO ($\sim$ 17%), trace amounts of CO_2 and CH_4, unconverted *n*-heptane and excess water ($\sim$ 50%). The molar H_2 : CO ratio of 1.96 is lower than the stoichiometric ratio dictated by the reforming of *n*-heptane (Equation 4.7), and implies the effect of reverse water-gas shift reaction ($CO_2 + H_2 \rightleftharpoons CO + H_2O, \Delta H^0_{298} = 41.2\,\mathrm{kJ\,mol^{-1}}$) at elevated temperatures. Formation of trace quantities of methane can also be related to the temperature effect, which does not favor the thermodynamics of exothermic methanation (reverse of Equation 4.8). Pressure drop along the microchannel unit is found to be negligible and turned out to be 700 Pa in the reforming channel and 100 Pa in the combustion channel.

Table 5.2. Comparison of the results of microchannel and cascade systems for the combustion-assisted steam reforming of n-heptane.

		Inlet[a]					**Outlet**[a]			**Total volume** (m^3)
		CH_4 ($mol\,s^{-1}$)	n-C_7H_{16} ($mol\,s^{-1}$)	C : O_2	S : C	T (K)	χ_{HC} (%)	H_2 ($mol\,s^{-1}$)	T (K)	
Microchannel (per channel)	**COMB**	1.5×10^{-8}	—	0.5	—	850	43	—	734	
	SR	—	1.5×10^{-7}	—	3.0	750	87	1.52×10^{-6}	764	
Microchannel (28900 channels)	**COMB**	2.17×10^{-4}	—	0.5	—	850	43	—	734	1.04×10^{-3}
	SR	—	2.17×10^{-3}	—	3.0	750	87	2.2×10^{-2}	764	
Cascade	**COMB**	1.8×10^{-3}	—	0.25	—	750	86	—	496	1.39×10^{-3}
	SR	—	1.5×10^{-3}	—	3.0	750	88	2.2×10^{-2}	764	

[a] Inlet and Outlet refer to the reformer in Figure 4.1.

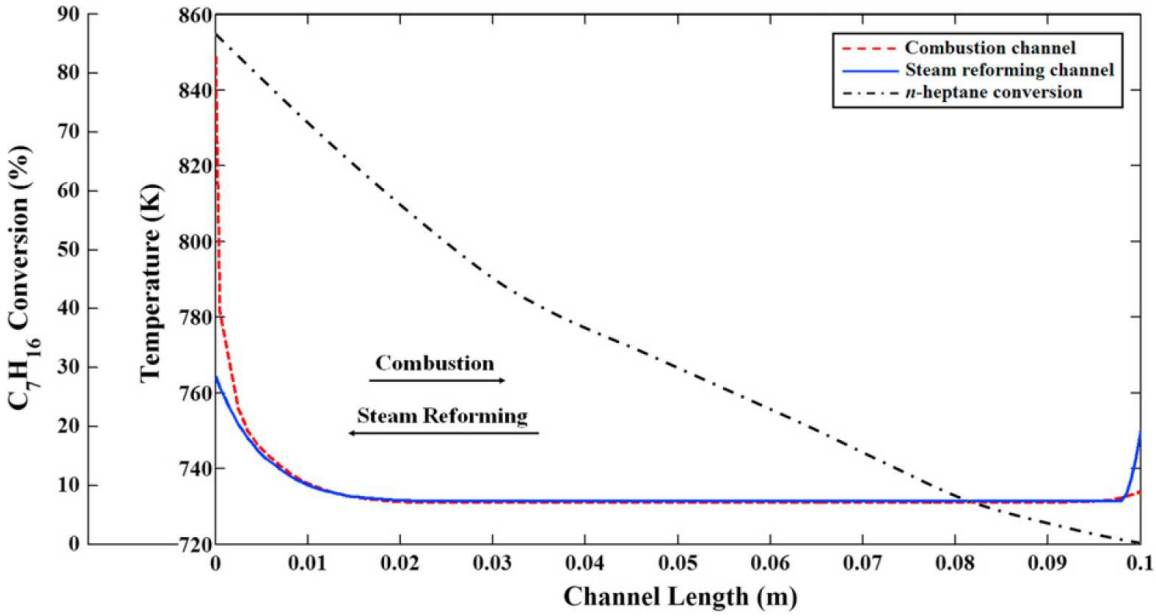

Figure 5.10. Simulation results of the methane combustion-*n*-heptane steam reforming coupling in the microchannel configuration.

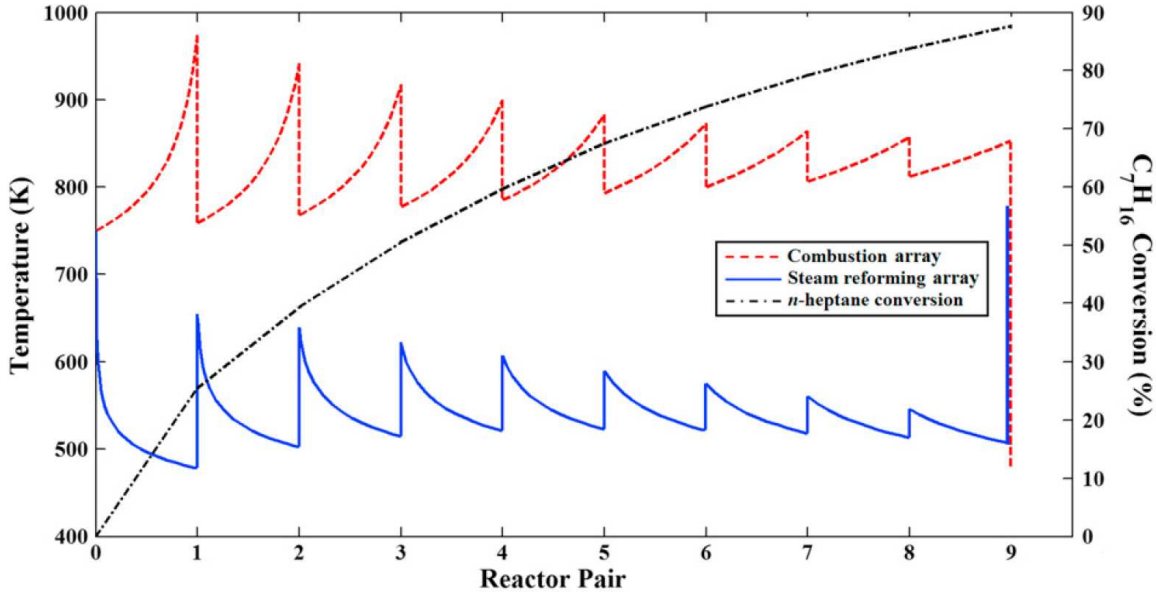

Figure 5.11. Simulation results of combustion-assisted steam reforming of *n*-heptane in the cascade configuration.

5.3.2. Steam Reforming of n-heptane in the Cascade Reactor

Combustion-assisted steam reforming of n-heptane is also demonstrated using the cascade system. Heat generated in a catalytic combustion bed is transferred to the steam reforming gas stream through a microchannel heat exchanger. The cooled stream is then fed to the next combustion bed to generate heat for the subsequent reforming bed. Upon heat exchange, each designated by the vertical lines in Figure 5.11, the heated reformer stream is fed to the next catalytic bed in which further reforming conversion takes place adiabatically (Figure 4.8). Such heating-cooling cycles lead to saw-tooth temperature profiles along the combustion and reforming arrays. The resulting saw-tooth pattern and evolution of the cumulative n-heptane conversion are shown in Figure 5.11. Even though conversion in a combustion bed is limited to 20%, the heat generated is enough to drive the endothermic reactions in the corresponding reforming bed, as indicated by 88% conversion of n-heptane and 86% conversion of methane (Table 5.2). The reformer stream leaving the cascade is comprised of $\sim$ 39% H_2 ($2.2 \times 10^{-2}\,\mathrm{mol\,s^{-1}}$), 18% CO ($9.4 \times 10^{-3}\,\mathrm{mol\,s^{-1}}$), trace CO_2 and CH_4 ($< 1\%$), unconverted n-heptane and excess water ($\sim$ 42%). The H_2 : CO ratio at the exit is higher than that in the microchannel reactor configuration because lower temperatures are encountered in the last three reforming beds, a situation favored by the forward water-gas shift reaction (Equation 4.10). By the same token of lower bed temperatures, methanation reaction (reverse of Equation 4.8) is more favored due to its exothermic nature, and, therefore, the exit methane concentration, although small, is 12 times that for the microchannel configuration. The total pressure drop across the combustion and reforming arrays are respectively 21% and 10% of the inlet pressure. Pressure drop values are observed to originate from the packed beds of the individual arrays. The contribution of the microchannel heat exchanger sections to the overall pressure drop is found to be negligible.

5.3.3. Sizing and Comparison of the Proposed Designs

Following the procedures given in Section 4.2.8, sizing of both reformer configurations is carried out on the basis of producing hydrogen at a rate of $2.2 \times 10^{-2}\,\mathrm{mol\,s^{-1}}$.

In the microchannel configuration, sizing is based on the H_2 exit flow rate from a single steam reforming channel and turned out to be 14450 microchannels for producing $2.2 \times 10^{-2}\,\mathrm{mol_{H_2}\,s^{-1}}$. The total number of microchannels (combustion plus reforming) is twice this quantity, i.e., 28900. For the given channel length of 0.1 m, a nearly cubical arrangement can be made by a 170×170 array of microchannels. The dimensions of this arrangement, excluding the inlet and outlet manifolds, are 0.1 m (length) $\times$ 0.102 m (height) $\times$ 0.1022 m (width), and the corresponding volume is $1.04 \times 10^{-3}\,\mathrm{m^3}$. In the cascade configuration, pairs of combustion and reforming catalyst beds are designed for side-by-side placement in single slots, therefore, they are assumed to be of the same length, differing only in diameter. Based on this constraint and the iterative technique explained in Section 4.3.1, the hydraulic diameter and length of each of the combustion beds are found to be $2.64 \times 10^{-2}\,\mathrm{m}$ and $5.28 \times 10^{-2}\,\mathrm{m}$, respectively. The Pt-based catalyst loading per bed is 0.032 kg. Each of the steam reforming beds has $5.48 \times 10^{-2}\,\mathrm{m}$ diameter and $5.28 \times 10^{-2}\,\mathrm{m}$ length, and contains 0.15 kg of Ni-based catalyst. Controlled temperatures and desired conversion values are found to be achieved by the use of 9 beds per gas stream, summing up to a total of 18 catalytic beds. The use of a lower number of beds violates the combustion conversion constraint so that the operation ceases to be feasible. On the other hand, using more beds brings only incremental improvements in conversion while the overall pressure drop becomes intolerable. Dimensions of the linking microchannel heat exchangers, based on 270 W, the largest duty of interstage heat exchange, are $7.5 \times 10^{-3}\,\mathrm{m}$ (length) $\times$ $6.45 \times 10^{-3}\,\mathrm{m}$ (height) $\times$ $2.84 \times 10^{-2}\,\mathrm{m}$ (width). Each heat exchanger houses a total of 1024 channels: the hot stream flows in channels of 360 μm height (H) while the cold stream channels have a height (H) of 240 μm. Both the hot and cold channels are 240 μm wide (W), are separated by 200 μm-thick walls (WT), and they are arranged into an array of 64×16. The cascade configuration, consisting of 18 catalytic beds and 9 microchannel heat exchangers, occupies a block volume of $1.39 \times 10^{-3}\,\mathrm{m}$, 81% of which comes from the reforming beds alone.

Size of the alternate reformer designs is used to estimate the total volume of the fuel processing system by adding up volumes of the CO clean-up units (Section 4.1.1.2). When the microchannel reactor configuration is used in the primary hydrogen gener-

ation step via the steam reforming of n-heptane, the total volume of the reactors–including the high- and low-temperature water-gas shift converters and the CO oxidation reactor–is calculated to be $1.53 \times 10^{-3}\,\mathrm{m}^3$. In the case of using the cascade reactor configuration, that volume is found to be $1.73 \times 10^{-3}\,\mathrm{m}^3$, 1.12 times that for the microchannel reactor case even though the reactors involved in the cleaning steps are substantially smaller for the cascade configuration because of lower CO content in the reformate (1.12×10^{-2} versus $9.4 \times 10^{-3}\,\mathrm{mol\,s^{-1}}$).

Other comparison criteria between the reaction systems are the total size of the heat exchangers installed and the overall efficiency. Since the exchangers are thought to be of the same design, comparison based on heat load, calculated by multiplication of the mass flow rates, average specific heats and temperature differences across the heat exchangers, should suffice. The total heat exchange carried out across the six heat exchangers (Figure 4.1) amounts to 4100 W and 3480 W for the microchannel and cascade reactor systems. The efficiency is defined as the ratio of the lower heating values (LHV) of the product hydrogen and the fuels methane and n-heptane:

$$\eta = 100 \times \frac{n_{\mathrm{H_2}} \times \mathrm{LHV}_{\mathrm{H_2}}}{n_{\mathrm{CH_4}} \times \mathrm{LHV}_{\mathrm{CH_4}} + n_{\mathrm{C_7H_{16}}} \times \mathrm{LHV}_{\mathrm{C_7H_{16}}}} \tag{5.1}$$

The lower heating values of methane, hydrogen and n-heptane are 47.1, 120.2 and $44.9\,\mathrm{MJ\,kg^{-1}}$, respectively [302]. $n_{\mathrm{H_2}}$ refers to hydrogen fed to the fuel cell while $n_{\mathrm{CH_4}}$ and $n_{\mathrm{C_7H_{16}}}$ are amounts of methane and n-heptane fed to the fuel processor. The amount of hydrogen at downstream processing is different for the microchannel and cascade reformer configurations. Hydrogen that is rejected by the PEM fuel cell, corresponding to ca. 25% of the hydrogen fed [257], is sent to the afterburner unit as part of the heat integration (Figure 4.1). Based on this configuration, the efficiency of the cascade reactor system is found to be higher than that of the microchannel reactor, i.e., 73.5% versus 68.2%. The difference can be attributed to the amount of n-heptane consumed in the cascade system, which is $\sim 30\%$ less than that used in the microchannel configuration. Data relevant to comparison criteria and the results are summarized in Table 5.3.

Table 5.3. Comparison of the microchannel and cascade systems based on the amount of fuel consumed, overall efficiency, fuel processor size and total heat load.

	CH_4 fed ($mol\,s^{-1}$)	n-C_7H_{16} fed ($mol\,s^{-1}$)	**H_2 produced** ($mol\,s^{-1}$)	**Efficiency**	**Reactor volume** (m^3)	**Total volume of reactors** (m^3)	**Total heat load** (W)
Microchannel	2.17×10^{-4}	2.17×10^{-3}	3.26×10^{-2}	68.2%	1.04×10^{-3}	1.53×10^{-3}	4100
Cascade	1.8×10^{-3}	1.5×10^{-3}	2.86×10^{-2}	73.5%	1.39×10^{-3}	1.71×10^{-3}	3480

Even though n-heptane conversions in both systems are nearly identical (Table 5.2), the number of moles of hydrogen produced per mole of n-heptane fed is 15 for the microchannel reactor and 19 for the cascade configuration (Table 5.3). Extra hydrogen is the product of the exothermic water-gas shift reaction that is favored by the distinctly lower average temperatures in the cascade (Figures 5.10 and 5.11). Higher reforming temperatures, attainable by adjusting the inlet temperatures of the combustion beds, are automatically restricted by the process limitations imposed on the combustion reactors (allowable methane conversion of 20% per bed). In the microchannel configuration, on the other hand, heat from the combustion channel is immediately drawn into the steam reforming channel that constitutes a large sink due to the very high heat of reaction ($1108\,\mathrm{kJ\,mol^{-1}}$) and presence of excess steam (21 moles of steam per mole of n-heptane, S : C of 3.0). At lower inlet temperatures than the specified one (850 K for combustion, 750 K for reforming), the reduction in the combustion stream temperature at the very upstream of the channel becomes so drastic that the reaction extinguishes before reaching the light-off value of conversion (10% of methane fed). Even after combustion initiates, continuous heat removal along the microchannels is so fast that the rate of methane conversion remains low only to give 43% conversion at the outlet although the mixture is stoichiometric. Therefore, the option of operating the microchannel reactor at lower temperatures to take advantage of higher water-gas shift reaction rates is ruled out.

Increased hydrogen production per unit amount of fuel in the cascade configuration, however, comes with the cost of using larger reforming reactors and feeding methane that is 8.3 times that used in the microchannel reactor. Because of the presence of interstage heat transfer and cyclic nature of the cascade configuration, heat generated in a combustion bed upon 20% conversion at a maximum is transferred to the next reforming bed in the sequence. Therefore, each successive combustion step experiences low-temperature inlet conditions (Figure 5.11). In order to compensate for the interrupted heat generation and to sustain the adiabatic reforming reactions in successive adiabatic beds, more methane must be combusted. The combustion and reforming processes in the microchannel reactor, however, run in single compartments (channels) and proceed uninterruptedly. Therefore, less methane will be required to

drive the endothermic reactions in the microchannel reactor configuration. The comparable results presented in Table 5.3 show that the microchannel reactor offers an advantage in case of a stringent size restriction. In addition to its higher efficiency, the benefit of using the cascade reactor configuration lies in easy replacement of deactivated catalyst and decoupling of reaction and heat transfer for much better temperature control.

5.3.4. Summary

Two intensified catalytic reactor configurations, parallel microchannels and cascades, are compared, using computer-based techniques, in the context of production of fuel-cell-grade hydrogen to drive a $2-3$ kW PEMFC-based APU via steam reforming of surrogate naphtha (n-heptane). Both of the processes involve the integration of endothermic n-heptane steam reforming with exothermic methane combustion. It is shown that fast heat transfer between the two reactions can lead to n-heptane conversions in excess of 87% in either reaction system. Comparison of the proposed designs, based on the amount of hydrogen produced at the reforming step, reveals the benefit of microchannel configuration due to the lesser size (1.53×10^{-3} versus $1.71 \times 10^{-3}\,\mathrm{m}^3$) of the fuel processor comprised of the reformer and subsequent clean-up units. However, based on the ratio of the lower heating value of hydrogen produced to the lower heating value of the total fuel (methane + n-heptane) consumed, a fuel processor with the cascade system is more efficient (73.5% versus 68.2%). Higher efficiency is mainly associated with the n-heptane consumption in the cascade being ca. 30% lower than that in the microchannel system. The presence of catalyst in packed-bed form allows its facile replacement in case of any deactivation, and therefore makes the cascade configuration the choice of the designer in terms of ease of operability and efficiency.

5.4. Microreactor Catalytic Combustion for Chemicals Processing

In this section computer-aided case studies of coupled and decoupled reaction/heat exchange systems are conducted in order to explore their possible benefits such as reduction in equipment size and compatibility with reaction schemes that demand precise temperature control. The coupled system is comprised of parallel microchannels that are segregated by metallic walls (Section 4.2.1), and the decoupled system is the cascade arrangement comprised of adiabatic packed-bed reactors interlinked by microchannel heat exchangers (Section 4.3). The specific case studies are combustion-assisted steam reforming of methane for production of syngas that is to be used in methanol synthesis (Figure 4.2), and combustion-assisted ethane dehydrogenation (Figure 4.3) as a solid example of conversion of paraffins to olefins. Sizes of the microchannel and cascade configurations are compared on the basis of 1000 $Sm^3\,day^{-1}$ of methane being fed to steam reforming. In the case of ethane dehydrogenation, the basis is set as 1000 $Sm^3\,day^{-1}$ of ethane being fed to the dehydrogenation reactor.

Reaction kinetics of methane combustion (Equation 4.11) and steam reforming (Equation 4.8-10), and of ethane dehydrogenation (Equation 4.16) are given in Tables 4.12, 4.16 and 4.22, respectively. The 2D axisymmetric model geometry is shown in Figure 4.6. Physical properties of the reactive fluids and of the microchannel wall are tabulated in Table 4.24. Reactor and catalyst data, and the operating conditions are presented in Table 4.26. The set of model equations fully describing the microchannel operation consist of transport equations for fluid flow and heat flow across the segregating wall (Section 4.2.3), which are subject to the boundary conditions given in Section 4.2.4. The CFD package Comsol™ v3.5a [280], running on a HP xw8400 workstation, equipped with 4×2.00 GHz Xeon™ processors and 4 GB of memory, is used for the simultaneous solution of these equations. The solution domains are discretized into unstructured grids consisting of 4590 (steam reforming of methane) and 6406 (ethane dehydrogenation) quadratic triangular elements. In regions where the rates of reactions are high, the grid is refined so that sharp concentration and temperature gradients can be resolved. PARDISO solver is employed for solution of the linear system of equations with the tolerance set to 1×10^{-6}.

The cascade reactor design procedure is explained in Section 4.3.1 where the one-dimensional pseudohomogeneous reactor model (Eqs. (4.79)-(4.81)) is used for predicting the reactor performance. The resulting set of ordinary differential equations (ODE) are solved on MATLAB^{TM} using a stiff solver. Scale-up of microchannel reactors and heat exchangers are performed following the procedures given in Section 4.2.8.

5.4.1. Combustion-assisted Steam Reforming of Methane in the Microchannel Reactor

Initial modeling is carried out to simulate coupling of combustion and steam reforming of methane in the parallel microchannel configuration, shown in Figure 4.6. The amount of methane fed and the feed compositions are optimized to obtain the desired inlet feed composition for methanol synthesis, which is H_2 : CO : CO_2 = 75 : 24 : 1 per cent by mole at the exit of steam reforming [263]. Methane feeds to the combustion and steam reforming channels are set at $4 \times 10^{-7}\,\mathrm{mol\,s^{-1}}$ and $1.24 \times 10^{-6}\,\mathrm{mol\,s^{-1}}$, respectively. The molar inlet flow of oxygen in air is set at $8 \times 10^{-7}\,\mathrm{mol\,s^{-1}}$, and the amount of steam fed to the steam reforming channel is assigned as $3.1 \times 10^{-6}\,\mathrm{mol\,s^{-1}}$ to come up with an inlet steam-to-carbon ratio of 2.5, which is reported to minimize coke formation over Ni-based catalysts [76]. As demonstrated in the process flow sheet given in Figure 4.2, feed temperatures of the combustion and steam reforming channels are taken as 900 K and 785 K, respectively. The results of the microchannel simulations are presented in Figure 5.12 and in Table 5.4. It can be seen that the temperature in the combustion channel is raised from 900 K to ca. 1290 K as a result of combustion of 88% of methane fed (Figure 5.12 and Table 5.4) over the Pt-based catalyst, which is coated in the first half of the channel (Figure 4.6). The insulation in this zone disables heat transfer into the metallic wall and prevents any reduction in the temperature of the combustion stream. The second half of the combustion channel, on the other hand, involves neither catalyst nor insulation. As a result, no chemical reactions take place due to the absence of homogeneous reactions, and hence heat generated in the catalytic zone is transferred to the steam reforming channel. This leads to a sharp rise in the steam reforming stream temperature from 785 K to 1225 K,

Table 5.4. Comparison of the results of microchannel and cascade systems for combustion-assisted steam reforming of methane.

		Inlet[a]				**Outlet**[b]					**SR**, T_{max} (K)	**Total volume** (m^3)	**Total volume per mole of syngas produced** ($m^3\,mol^{-1}$)
		CH_4 ($mol\,s^{-1}$)	O_2 ($mol\,s^{-1}$)	H_2O ($mol\,s^{-1}$)	T (K)	χ_{HC} (%)	H_2 ($mol\,s^{-1}$)	CO ($mol\,s^{-1}$)	CO_2 ($mol\,s^{-1}$)	T (K)			
Microchannel	**COMB**	4×10^{-7}	8×10^{-7}	—	900	88	—	—	3.52×10^{-7}	1125	1225	17.7×10^{-3}	10.8×10^{-3}
	SR	1.24×10^{-6}	—	3.1×10^{-6}	785	95	3.21×10^{-6}	1.07×10^{-6}	5.6×10^{-10}	1125			
Cascade	**COMB**	0.21	0.42	—	900	80	—	—	0.167	1184	1032	8.2×10^{-3}	4.1×10^{-3}
	SR	0.473	—	1.18	785	91	1.50	0.52	3×10^{-4}	949			

[a] Molar flow rate of N_2 is not shown.

[b] Molar flow rates of N_2, H_2O and unreacted CH_4 are not shown.

accompanied by a ca. 100 K overshoot despite the presence of the reforming reactions running in the second half of the channel coated with Ni-based catalyst (Figure 5.12 and Table 5.4). Such a thermal response may lead to local, temperature-induced problems in catalytic operation, though it will not disturb the nature of the stainless steel. The endothermicity of steam reforming of methane then starts to dominate, and triggers a decreasing trend in temperature to give an exit value of 1125 K. The small dimensions and metallic nature of the segregating wall facilitates rapid heat transfer and allows the temperatures of both streams to equilibrate immediately (Figure 5.12 and Table 5.4).

The high temperatures brought by combustion gave 95% steam reforming conversion of methane and an exit stream composed of $3.21 \times 10^{-6}\,\mathrm{mol\,s^{-1}}$ H_2, $1.07 \times 10^{-6}\,\mathrm{mol\,s^{-1}}$ CO and $5.6 \times 10^{-10}\,\mathrm{mol\,s^{-1}}$ CO_2 with a H_2 : CO ratio of 3.0, which is close to the desired reforming exit composition given above. The small amount of CO_2 reflects the importance of the reverse water-gas shift reaction ($CO_2 + H_2 \rightleftharpoons CO + H_2O, \Delta H^0_{298} = 41.2\,\mathrm{kJ\,mol^{-1}}$) at high temperatures. The analysis of the outlet from the steam reformer shows that conditions desired for the inlet of the methanol synthesis process can be easily achieved, although cooling of the reforming effluent is necessary.

5.4.2. Combustion-assisted Steam Reforming of Methane in the Cascade Reactor

In the cascade system, heat generated in a catalytic combustion bed is transferred to the steam reforming gas stream through a microchannel heat exchanger. The cooled stream is then fed to the next combustion bed to generate heat for steam reforming. The extent of conversion in the combustion beds is limited to less than 20% in order to avoid any uncontrolled temperature rise due to the light-off. The heated reformer stream is then taken to the next catalytic bed in which further reforming conversion takes place adiabatically to give a decreasing trend in temperature. Such heating-cooling cycles lead to saw-tooth temperature profiles along the combustion and reforming arrays which are shown in Figure 5.13. Evolution of the cumulative methane conversion along the steam reforming beds and the product flow rates given in Fig-

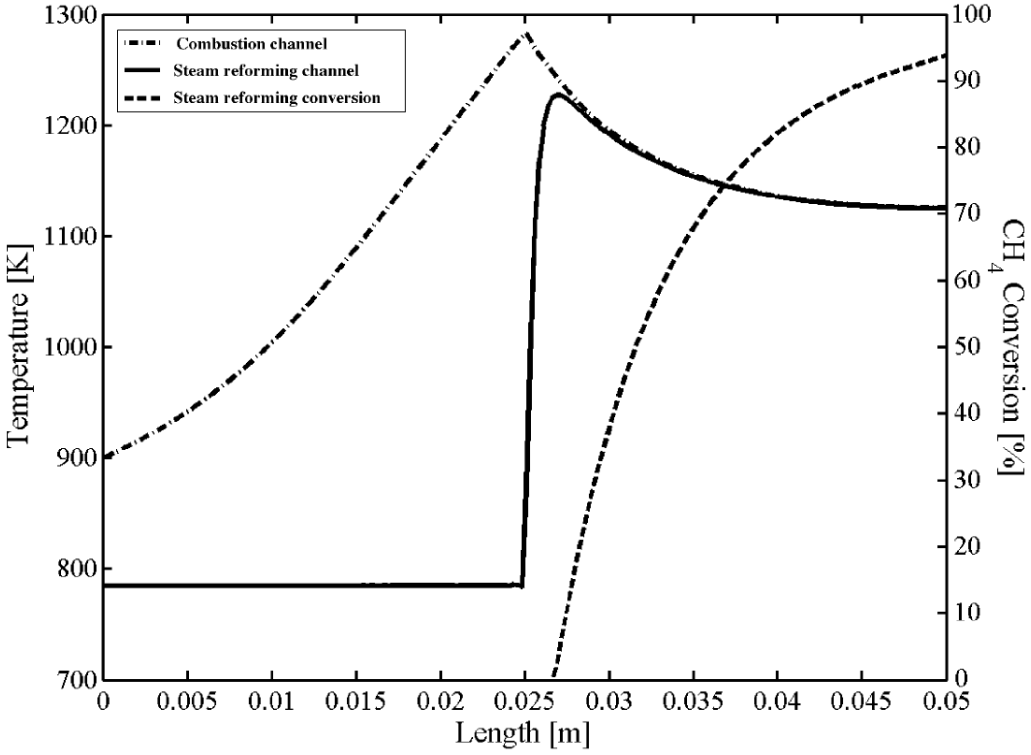

Figure 5.12. Simulation results of coupling of combustion and steam reforming of methane in the microchannel configuration.

ure 5.13 and Table 5.4, respectively. The effluent of the steam reforming beds having a molar H_2 : CO ratio of 2.86 (Table 5.4) shows that the inlet stream composition desired for the methanol synthesis can also be obtained through the cascade system with the advantage of a much better temperature control (Figures 5.12 and 5.13): although the inlet temperatures are the same (Table 5.4), the maximum steam reforming temperatures obtained in the microchannel and in the cascade configurations are 1225 K and 1032 K, respectively. The absence of uncontrolled temperature elevations in the cascade system minimizes the risk of catalyst deactivation due to thermal effects.

The desired conversion/product distribution values and well-controlled temperature are achieved by the use of 10 catalytic beds per gas stream, summing up to a total of 20 catalytic beds. The number of beds is optimal, since using a lower number of beds requires disturbing the methane combustion conversion constraint of 20% per bed to achieve the same effluent temperature and composition, whereas using a higher

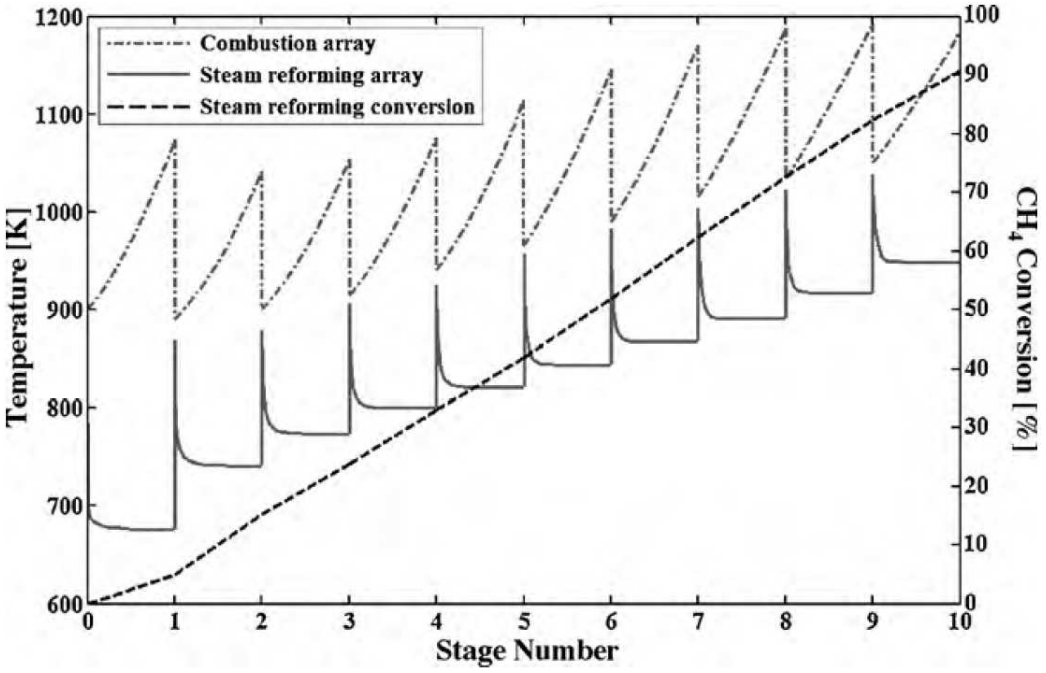

Figure 5.13. Simulation results of combustion-assisted steam reforming of methane in the cascade configuration.

number of beds brings only incremental improvements in conversion. Comparison of the output of the two configurations in Table 5.4 shows that the overall size of the cascade system needed to produce unit amount of syngas is smaller than that of the microchannel arrangement, with the steam reforming conversion slightly higher in the latter due to higher average temperatures. In addition, the ease of replacement of the catalysts in the cascade system, once they deactivate, is a real advantage. This system is also beneficial in the sense that the cooling duty and heat exchanger size needed for cooling the steam reforming exit stream to methanol synthesis conditions is lower than needed in a microchannel system. This is due to the exit temperature of the cascade system, 949 K, which is significantly lower than that of the microchannel configuration, 1125 K (Table 5.4).

5.4.3. Combustion-assisted Ethane Dehydrogenation in the Microchannel Reactor

The two configurations are compared in another reaction system in which heat required to drive ethane dehydrogenation is supplied by methane combustion. Temperature control is much more essential in this case, where excessive coking must be avoided despite the high temperatures involved [264]. Heat from catalytic combustion is provided directly to the dehydrogenation reaction, which is operated ca. 1000 K (Figure 4.3). In order to minimize the risk of coking that may be favored around these temperatures, ethane is mixed with a diluent, N_2, to give a molar feed ratio of $C_2H_6 : N_2 = 4.0$ [264].

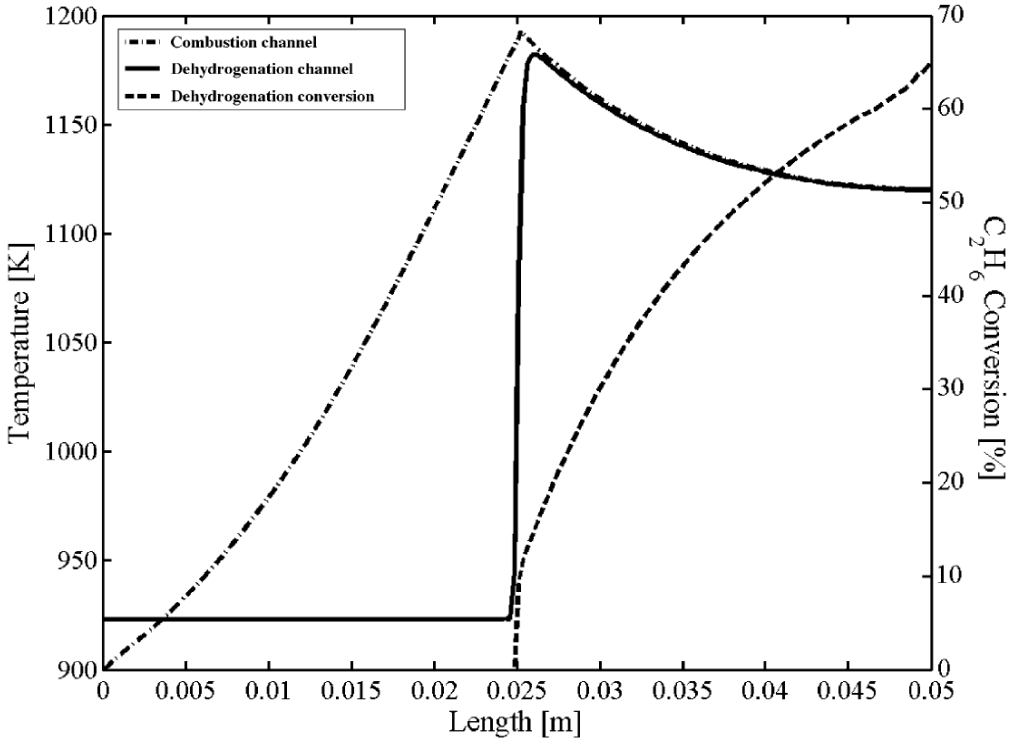

Figure 5.14. Simulation results of coupling of methane combustion and ethane dehydrogenation in the microchannel configuration.

Simulated profiles of temperature and ethane conversion in the microchannels are presented in Figure 5.14 and the related numerical results are given in Table 5.5. The trends of the profiles are in accordance with the assigned microchannel geometry as explained in the case of combustion/steam reforming coupling (Section 5.4.1.

Table 5.5. Comparison of the results of microchannel and cascade systems for combustion-assisted ethane dehydrogenation.

		Inlet				**Outlet**[a]					**ED**, T_{max} (K)	**Total volume** (m^3)	**Total volume per mole of C_2H_4 produced** ($m^3\,mol^{-1}$)
		HC ($mol\,s^{-1}$)	O_2 ($mol\,s^{-1}$)	N_2 ($mol\,s^{-1}$)	T (K)	χ_{HC} (%)	C_2H_4 ($mol\,s^{-1}$)	H_2 ($mol\,s^{-1}$)	N_2 ($mol\,s^{-1}$)	T (K)			
Microchannel	**COMB**	5.2×10^{-7}	1.04×10^{-6}	3.9×10^{-6}	900	94	—	—	3.9×10^{-6}	1120	1180	18.9×10^{-3}	61.8×10^{-3}
	ED	1.16×10^{-6}	—	2.9×10^{-7}	923	65	7.5×10^{-7}	7.5×10^{-7}	2.9×10^{-7}	1120			
Cascade	**COMB**	0.1	0.2	0.752	900	86	—	—	0.752	1245	1121	3×10^{-3}	10.2×10^{-3}
	ED	0.473	—	0.118	923	63.6	0.3	0.3	0.118	1054			

[a] Molar flow rates of CO_2, H_2O and unreacted hydrocarbons (CH_4 and C_2H_6) are not shown.

Temperature rise along the dehydrogenation channel caused by catalytic combustion of 94% of the methane fed follows the expected increase, passing through a maximum of 1180 K as the cooling effect of dehydrogenation becomes apparent (Figure 5.14 and Table 5.5). The lower heat of reaction of dehydrogenation causes a smaller decrease in temperature (ca. 60 K, Figure 5.14) than that associated with steam reforming and gave an exit temperature of 1120 K. The 65% conversion of ethane achieved reflects the dominating effect of thermodynamics of the reaction at the exit conditions, since it is limited by an equilibrium conversion of 72% [264].

5.4.4. Combustion-assisted Ethane Dehydrogenation in the Cascade Reactor

The results of methane combustion/ethane dehydrogenation in the cascade configuration are given in Figure 5.15 and Table 5.5. The familiar saw-tooth temperature pattern is observed both in the combustion cascade and in the dehydrogenation cascade, and the increase in temperature of dehydrogenation occurs only from heat exchange with hot combustion effluents. Temperatures in the combustion beds are controlled by allowing only 20% conversion per bed, in order to avoid light-off. Although the 86% conversion of methane is lower than obtained in the microchannel combustion (94%), efficient heat transfer through the microchannel heat exchangers leads to improved temperature control in the dehydrogenation array with almost no sacrifice from the overall ethane conversion, which is found to be 63.6% (Figure 5.15 and Table 5.5). As expected, the maximum temperature of 1121 K obtained in the dehydrogenation array is lower than 1180 K of the corresponding microchannel array. The optimum number of cascades per gas stream is found to be 10.

Based on the flow rates in a single pair of channels in the microchannel reactor configuration, the total number of microchannels for the steam reforming system is 763000 whereas that for ethane dehydrogenation is 816000. Given the system specifications in Table 4.26, the microchannel reactor volumes for steam reforming and ethane dehydrogenation are $17.7 \times 10^{-3}\,m^3$ and $18.9 \times 10^{-3}\,m^3$, respectively (Tables 5.4 and 5.5).

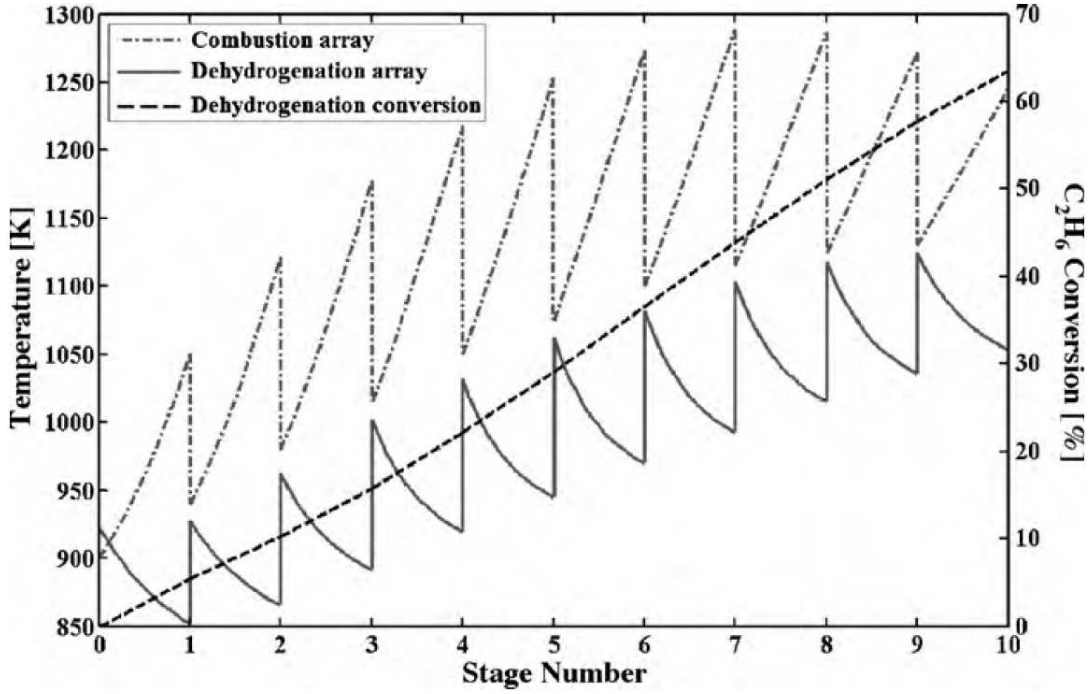

Figure 5.15. Simulation results of coupling of methane combustion and ethane dehydrogenation in the cascade configuration.

The catalyst beds in the cascade configuration are designed for ease of replacement, therefore, they are assumed to be of the same length. The hydraulic diameter and length of each of the 10 combustion beds used in the steam reforming system are 8.25×10^{-2} m and 4.13×10^{-2} m, respectively. The Pt-based catalyst loading is 0.245 kg. The diameter and length of the combustion beds used in ethane dehydrogenation are 6.22×10^{-2} m and 3.11×10^{-2} m, which amount to 0.105 kg of catalyst. Each of the steam reforming reactors has 12.75×10^{-2} m diameter and 4.13×10^{-2} m length, and contains 0.635 kg of Ni-based catalyst. One dehydrogenation reactor is 8.93×10^{-2} m in diameter and 3.11×10^{-2} m in length. The Pd-based catalyst loading is 0.235 kg.

Dimensions of the interconnecting microchannel heat exchangers for the steam reforming and dehydrogenation cascade configurations, based on the highest duty of interstage heat exchange, are 4.83×10^{-3} m (height) $\times$ 3.76×10^{-3} m (width) $\times$ 4.50×10^{-3} m (length) and 3.03×10^{-3} m (height) $\times$ 3.01×10^{-3} m (width) $\times$ 2.00×10^{-3} m (length), respectively. The heat exchangers used in dehydrogenation house a total of

10000 channels while those used in steam reforming have 20000 channels. The 200-μm diameter channels are separated by 100-μm thick stainless steel walls.

Comparison of the results of the two systems given in Table 5.5 shows that, the size of the cascade system, including the heat exchangers, needed to produce unit amount of ethylene is smaller than that of the microchannel system, whereas the conversions of both ethane and methane are higher in the latter configuration. However, the advantage of easy replacement of deactivated catalyst in the cascade system, and better temperature control to minimize the risk of temperature-induced coking, are real benefits.

5.4.5. Summary

The performances of two intensified catalytic reactor configurations, parallel microchannels and cascades, are compared in the contexts of syngas generation for methanol production and of ethylene production by non-oxidative dehydrogenation of ethane using computer-based modeling techniques. Both of the processes involve integration of exothermic (methane combustion) and endothermic (steam reforming of methane or ethane dehydrogenation) reactions, and require careful temperature control. It is shown that either reaction system is capable of meeting the desired conversion/product distribution demands, and possess clear advantages over conventional processing for smaller-scale operations. Feedstock conversions in steam reforming and in dehydrogenation are observed to be slightly higher in the microchannel arrangement. On the other hand, temperature control is found to be much better in the cascade system such that presence of sudden elevations in temperature that increase the risk of thermal degradation of the catalysts are eliminated. The cascade system is also found to be smaller than the microchannel configuration. The ability to remove deactivated catalyst from the reactors easily and the ability to decouple reaction kinetics from heat exchange make the cascade system a promising alternative.

5.5. Steam Reforming of Methane to Syngas in a Catalytic Microchannel Reactor

In this section comparison is drawn between the activities and CO selectivities of Rh, Ru, Pt and Ni based catalysts–under various operating conditions–of methane-to-syngas conversion by steam reforming in a wall-coated microchannel reactor. Each active metal is integrated into porous Al_2O_3 support that is washcoated on FeCrAlY plates. The catalysts are characterized by XRD and SEM/EDX techniques prior to and after reaction tests. Mechanical and chemical stabilities of the Rh- and Ni-based catalysts are tested by 72- and 20-h time-on-stream experiments, respectively. The operating parameters investigated are residence time of reactants, reaction temperature and inlet S : C ratio. The productivities and CO selectivities of the washcoated catalysts are also compared with conventional packed-bed catalysts on a weight hourly space velocity (WHSV) basis in order to emphasize the advantages gained by microchannel operation.

The experimental setup, including the product analysis system, is presented in detail in Section 3.2. Catalyst preparation procedures are outlined in Section 3.3, synthesis of the catalytic microchannel (Figure 3.3) is explained in Section 3.3.2.2, and the range of operating conditions are given in Table 3.5 (Section 3.4.2).

5.5.1. Catalyst Characterization

Characterization of the wall-coated and particulate catalysts and the FeCrAlY plates are carried out by scanning electron microscopy (BSE-SEM), energy dispersive X-ray spectroscopy (EDX) (Philips XL30 ESEM-FEG/EDAX) and X-ray diffraction (XRD) (Rigaku D/MAX-Ultima+) analyses. The effect of heat treatment under atmospheric oxygen on the surface structure of the uncoated plates is shown in Figure 5.16. After heat treatment, a native Al_2O_3 layer is found to cover the surface of the plates due to the diffusion of Al species and their reaction with oxygen, which facilitates adhesion of the coating by increasing the available surface area. Use of heat-treated but uncoated FeCrAlY to support the active metal has been reported in the literature [193, 202, 303].

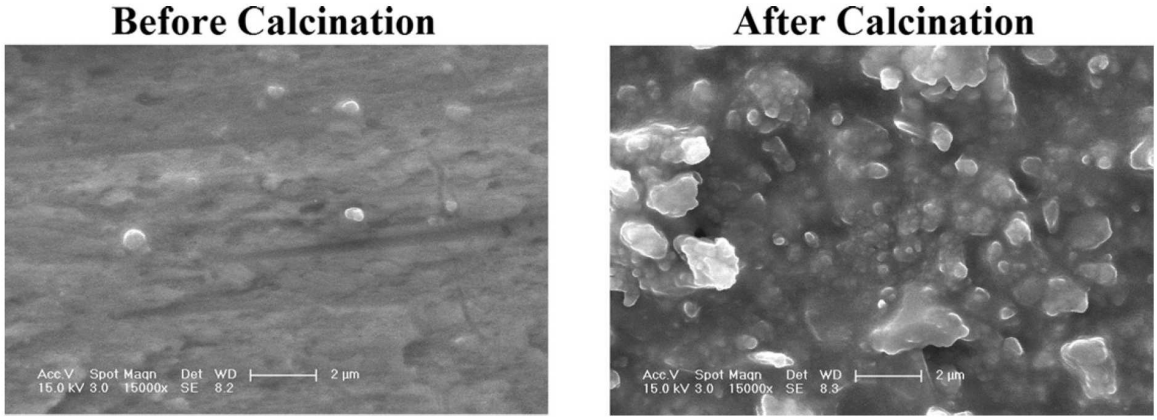

Figure 5.16. SEM micrographs of the uncoated plates before and after treatment at 900°C (500× magnification at 15 kV).

The coatings on the FeCrAlY plates are also analyzed quantitatively by SEM imaging. The coating thickness, scaled through lateral SEM images (Figure 5.17), is around 100 μm regardless of the catalyst type. The total amount of catalyst deposited varies between 11.7 and 19.5 mg because of the differences in density.

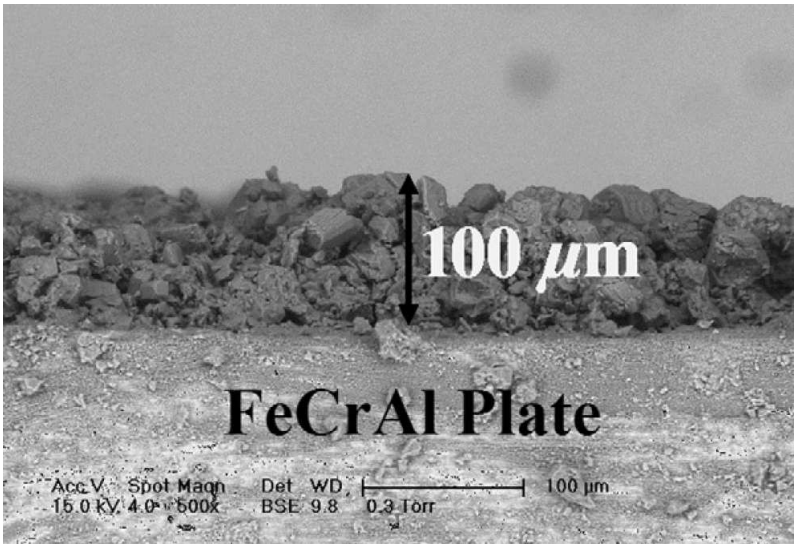

Figure 5.17. Lateral SEM image of a plate coated with Rh/δ-Al_2O_3 catalyst before reduction (500× magnification at 15 kV).

Figure 5.18 shows the XRD patterns of plates coated with Ni/δ-Al_2O_3 catalyst after calcination, reduction and reaction steps. At high calcination temperatures (ca. 900°C), a large portion of Ni impregnated onto Al_2O_3 transforms into the $NiAl_2O_4$

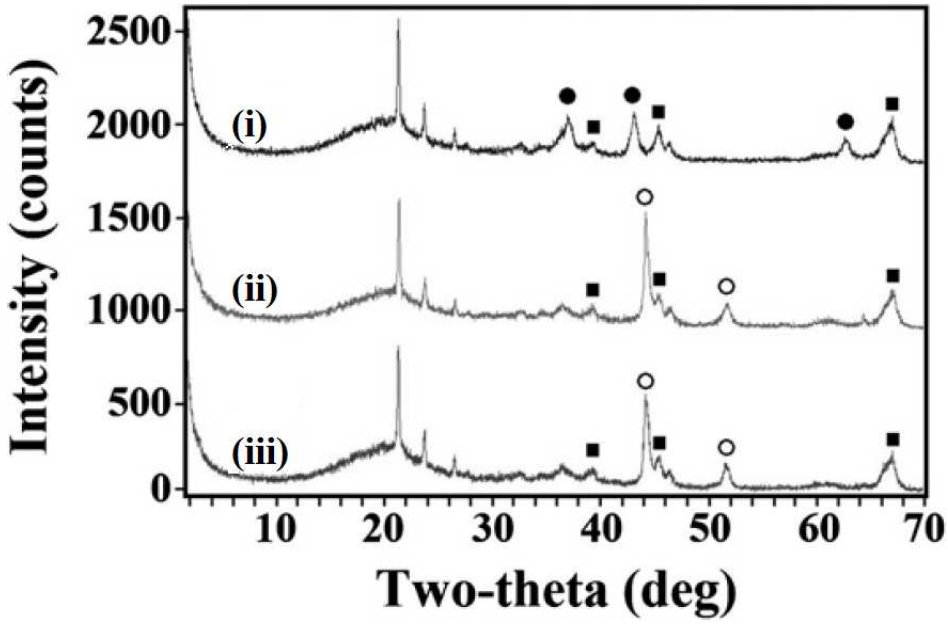

Figure 5.18. XRD patterns for the (i) calcined, (ii) calcined and reduced, and (iii) calcined, reduced and reacted Ni catalysts coated on plates ((■) Al_2O_3, (•) NiO, (○) Ni^0).

spinel phase which is difficult to activate due to its stability [127]. Since calcination in this work is carried out at 600°C, spinel peaks are not detected. The reduction temperature, on the other hand, is set as 800°C because at temperatures below 700°C, Ni/Al_2O_3 catalysts cannot be reduced appreciably, and thus cannot be activated [304]. Upon reduction, metal oxides are reduced to metallic Ni (Figure 5.18). Pretreatment conditions for the noble metal catalysts also require careful consideration. At oxidation temperatures of 600°C and above, rhodium interaction with the alumina support results in loss of reducibility and activity through inactive rhodium aluminate formation [305, 306], and through increasing crystallinity of the alumina [307]. Therefore, Rh/δ-Al_2O_3 is calcined at 500°C. The calcination temperature range for Ru/Al_2O_3 catalysts is usually $450 - 570$°C for the same reasons [308–310]. Pt/Al_2O_3 is also calcined at 500°C following the practice in literature [311].

SEM micrographs of the reduced noble metals on δ-Al_2O_3 for the coated and particulate catalysts are shown in Figure 5.19. Light elements appear dark in contrast whereas heavy elements, specifically the reduced metals appear as bright spots. Rh

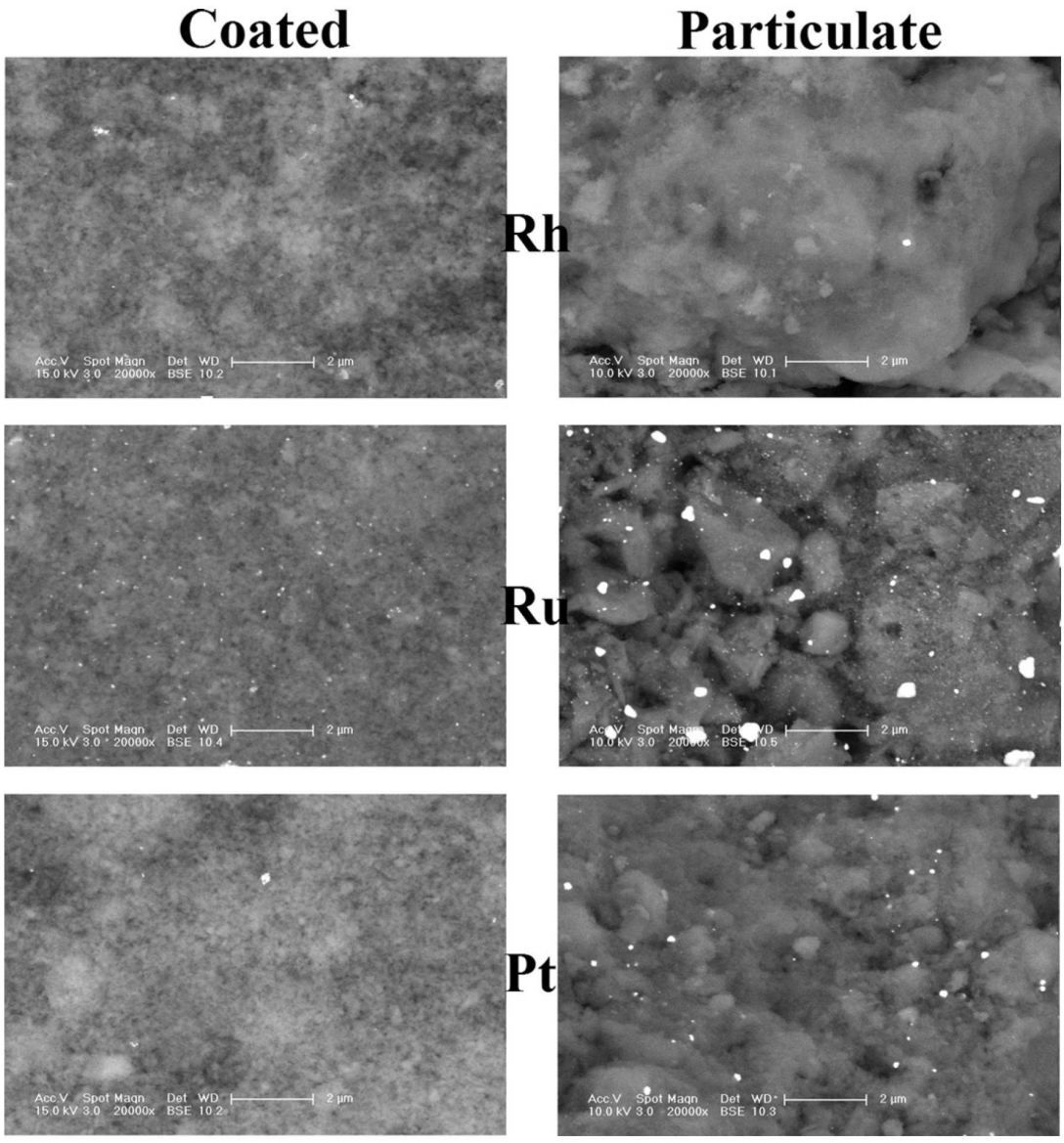

Figure 5.19. Backscattering electron (BSE) SEM micrographs of Rh, Ru and Pt on coated and particulate catalysts at 20000× magnification.

sites are difficult to visualize but their dispersions on both catalysts are similar. Ru sites are dispersed more uniformly on the coating than on the particulate catalyst, i.e., the particle size range is narrower. Dispersion of platinum sites, however, is better on the particulate catalyst.

Table 5.6. SEM/EDX results for the metal contents (by weight) of the catalysts[a].

Metal	**Coated**[b]	**Particulate**[b]	**Target**
Ni	$7.59 < 8.28 < 8.97$	$7.98 < 8.66 < 9.34$	10
Rh	$1.80 < 1.98 < 2.16$	$2.14 < 2.15 < 2.16$	2
Ru	$1.91 < 2.11 < 2.31$	$2.34 < 2.39 < 2.44$	2
Pt	$0.66 < 1.31 < 1.80$	$1.78 < 2.11 < 2.73$	2

[a] Analyses are conducted at 20000× magnification.

[b] Lowest and highest values included as well as the averages.

The percentage metal loading on both the coated and particulate catalysts are determined by the EDX technique. The results, shown in Table 5.6, are obtained on at least three samples out of the same batch, either reduced or reacted. Considering the fact that the penetration depth of the X-rays varies depending on the sample, the coated catalysts are scraped off the plates, and are analyzed in powder form in order to check for uniform distribution of the metals not only in the vicinity of the surface but on the deposited catalyst as a whole. The narrower ranges of percentages indicate that all metals except platinum are deposited uniformly on the samples. Pt content is much closer to the desired value of 2wt.% on particulate alumina. A possible explanation can be that, depending on the drying rate of the impregnated catalysts, majority of the platinum precursor might have been deposited at the deepest ends of the pores [312], thus cannot be detected by the EDX method.

A complete set of microchannel runs, comprised of the parametric variations of residence time, temperature and the S : C ratio, is conducted for each metal using at least two different plates coated with the same catalyst out of the same batch. Spent catalyst on every plate tested is post-characterized under SEM for potential

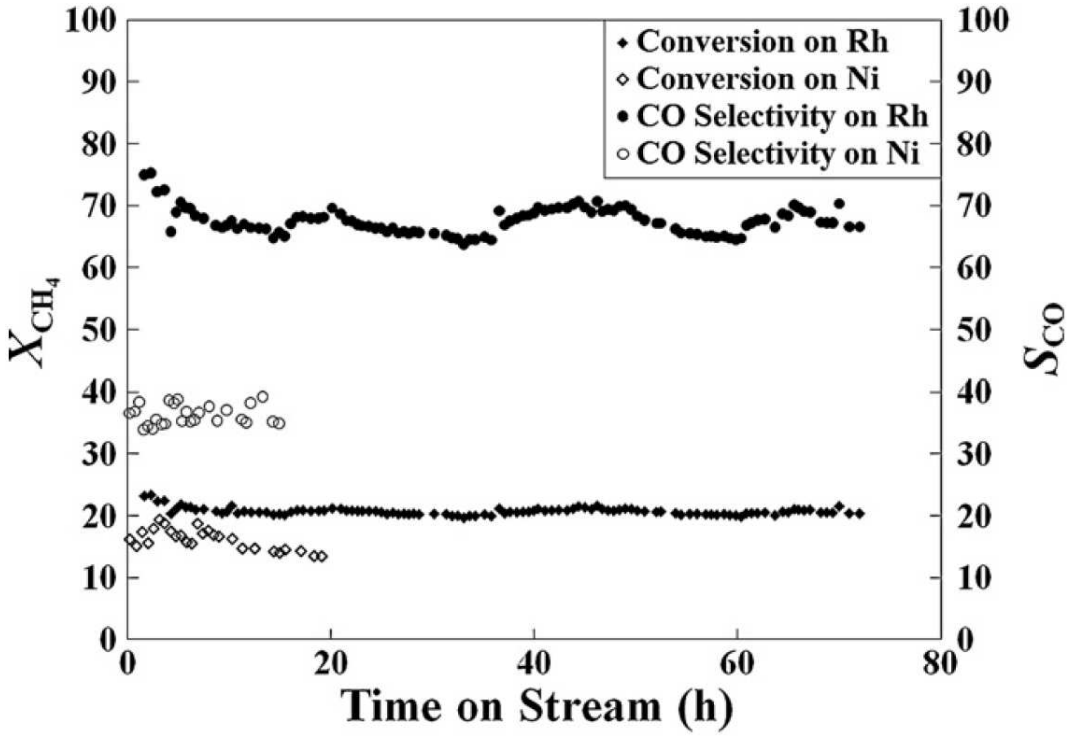

Figure 5.20. Time-on-stream methane conversion and CO selectivity on Rh/δ-Al_2O_3 and Ni/δ-Al_2O_3 in the microchannel reactor configuration. Operating conditions: $T = 750°C, \tau = 12.86\,\text{ms}, \text{S} : \text{C} = 0.5$ (Rh) , $\text{S} : \text{C} = 3.0$ (Ni).

coke formation. No coke deposit is detected even on Ni, which experiences rigorous conditions of high residence time and a S : C ratio as low as 1.5. The stabilities–in terms of maintaining the activity and selectivity–of Rh- and Ni-based catalysts are nevertheless assessed by time-on-stream experiments. Figure 5.20 shows the course of methane conversion and CO selectivity on Rh/δ-Al_2O_3 for 72 h, and on Ni/δ-Al_2O_3 for 20 h. Both experiments are performed at 750°C and at a residence time of 12.86 ms while the S : C ratios are 0.5 and 3.0 for Rh and Ni, respectively. Conversion on Rh is found to be stable at ca. 21% for the period of analysis whereas Ni conversion begins to decline after 19 h on stream, which then falls to 13.5% at the time of termination of the analysis. CO selectivity remains stable on both Rh and Ni respectively at ca. 68% and 35%. Figure 5.21a,b show the SEM micrographs of spent Rh- and Ni-based catalysts on the plates used in the time-on-stream runs. Carbonaceous deposits are not detected over either catalyst. The deactivation of the Ni catalyst can be attributed to reduction of its surface area since coking is not an issue. The loss of either Rh-

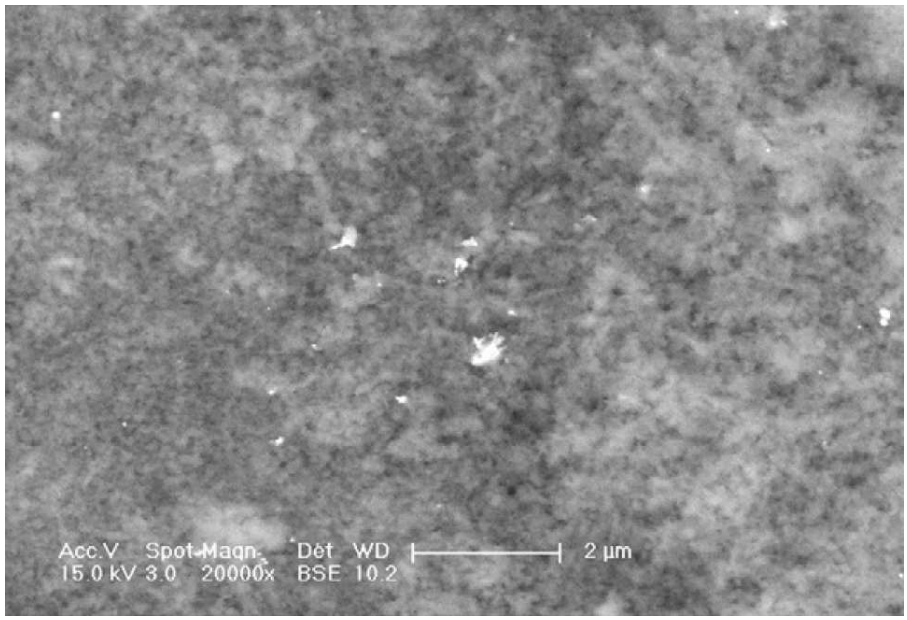

(a)

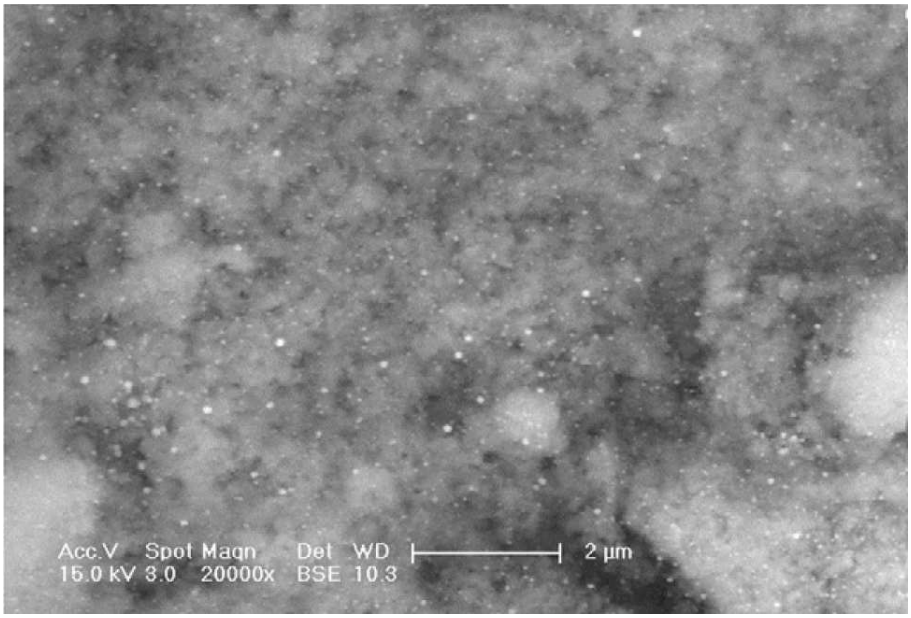

(b)

Figure 5.21. Backscattering electron (BSE) SEM micrographs of spent (a) Rh/δ-Al_2O_3 after 72 h, and (b) Ni/δ-Al_2O_3 after 20 h on stream. Magnification is 20000×.

or Ni-based catalyst is less than 2% by weight. These results clearly show that the catalyst coatings are mechanically stable even at the highest flow rate of 210 Nml min^{-1} that correspond to the smallest residence time of 12.86 ms.

5.5.2. SRM in the Microchannel Reactor

The studies of steam reforming of methane in the microchannel reactor are conducted by changing one parameter at a time while keeping all others constant. To observe if either the temperature or the S : C ratio is in combined effect with the residence time, pertinent runs are made both at the highest and lowest residence times. Since Rh is demonstrated to be highly stable (Section 5.5.1, Figure 5.20), its operating condition range is extended to $T = 800°C$ and to S : C = 0.5. Equilibrium composition for each case is calculated using HSC Chemistry software [313] via the Gibbs free energy minimization method, which includes possible formation of solid carbon. The experimental conditions given in Table 3.5 (Section 3.4.2) guarantees conversions below the equilibrium values for better comparison of catalyst activity and selectivity toward products in different cases.

5.5.2.1. Effect of Residence Time. Methane conversions at different residence times, calculated using Equation 3.1, and confirmed by Equation 3.2, are highest on Rh, and lowest on Ru, with Ni yielding higher conversions than Pt except at very low residence times (Figure 5.22a). Since the Ni loading is different from other metal loadings, and the weight of catalysts deposited varies with metal type, the catalysts are compared on the basis of their productivities (defined as the amount of methane converted per weight of catalyst per time, and expressed in $mol_{CH_4}\, kg_{cat}^{-1}\, s^{-1}$). The results given in Table 5.7 show that Rh performs by far as the most productive catalyst throughout the range of residence times investigated. The productivities of Ru, Pt and Ni are close to each other at $\tau > 40$ ms; however, at smaller residence times Ru and Pt outperform Ni. After $\tau \approx 50$ ms, the consumption rates, especially on Rh, show little change. Higher conversions are obtained with increase in residence time (Figure 5.22a) whereas the consumption rates decline due to the lower flow rate of reactants (Table 5.7). Since

Table 5.7. Rates of methane consumption ($\mathrm{mol_{CH_4}\,kg_{cat}^{-1}\,s^{-1}}$) on different metals in the microchannel reactor in the range of residence times investigated ($T = 750°\mathrm{C}, \mathrm{S:C} = 3.0$).

$\boldsymbol{\tau}$ (ms)	**Ni**	**Rh**	**Ru**	**Pt**
12.86	0.288	0.592	0.435	0.371
19.29	0.230	0.372	0.330	0.270
38.57	0.167	0.238	0.170	0.164
51.43	0.156	0.196	0.144	0.134
77.14	0.126	0.192	0.120	0.107

no noticeable pressure drop is observed in the range of flow rates studied, further decreasing the residence time (or increasing the total flow rate) is viable.

Variations of CO selectivities with residence time are given in Figure 5.22b. It can be observed that CO selectivities go through a maximum, $(S_{\mathrm{CO}})_{\mathrm{max}}$, between 45 and 50 ms, which is most significant and closest to the equilibrium value for S_{CO} on Rh. As τ increases so do the rate of steam reforming reaction, and the product ($\mathrm{CO+H_2}$) concentration. Since the water-gas shift (WGS: $\mathrm{CO + H_2O \rightleftharpoons CO_2 + H_2}$, $\Delta H^0_{298} = -41.2\,\mathrm{kJ\,mol^{-1}}$) reaction requires longer residence times to become significant, S_{CO} keeps on increasing in the $12.86 < \tau <\sim 45$ ms range. However, at the residence time corresponding to the maximum S_{CO}, WGS equilibrium becomes dominant, thus converts more of CO to $\mathrm{CO_2}$, and leads to lesser selectivities for residence times greater than ~ 45 ms.

5.5.2.2. Effect of Temperature. Effect of temperature on methane conversions and CO selectivities over different catalysts together with equilibrium values are shown in Figure 5.23. Conversion increases with temperature, and is always highest on Rh. At $\tau = 12.86$ ms, below 650°C conversion is less sensitive to temperature regardless of the catalyst type. While between 600°C and 700°C conversion decreases in the order Rh > Ru > Ni > Pt ≈ 0 (below 700°C Pt gives no detectable results), the trend begins to change (except for Rh) at 700°C, and the order becomes Rh > Pt > Ni > Ru at 750°C (Figure 5.23a). At the highest residence time investigated, i.e., $\tau = 77.14$ ms,

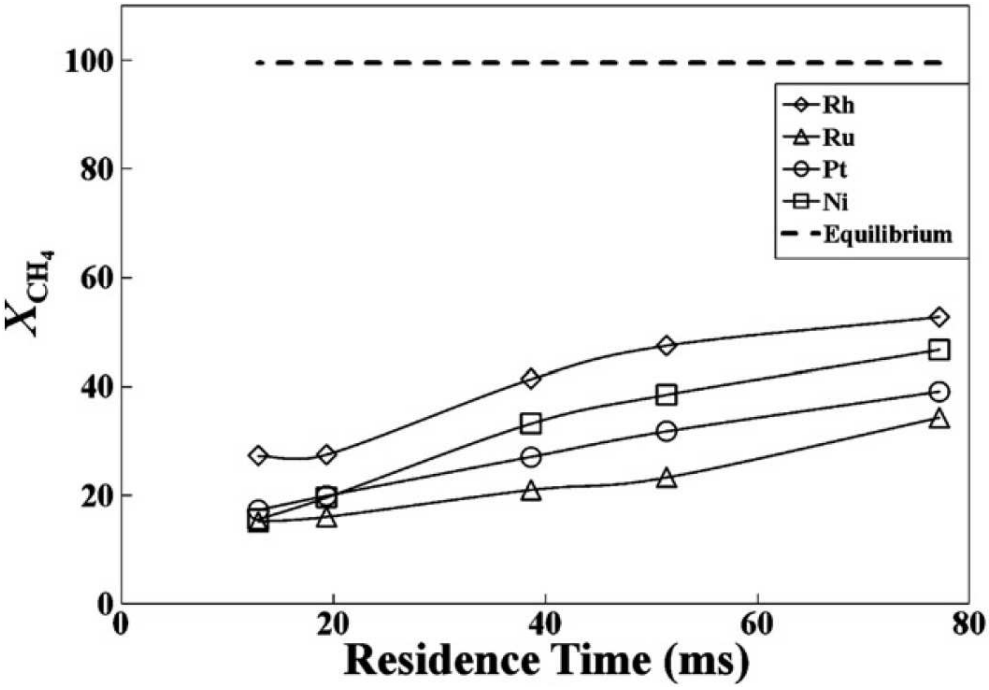

(a)

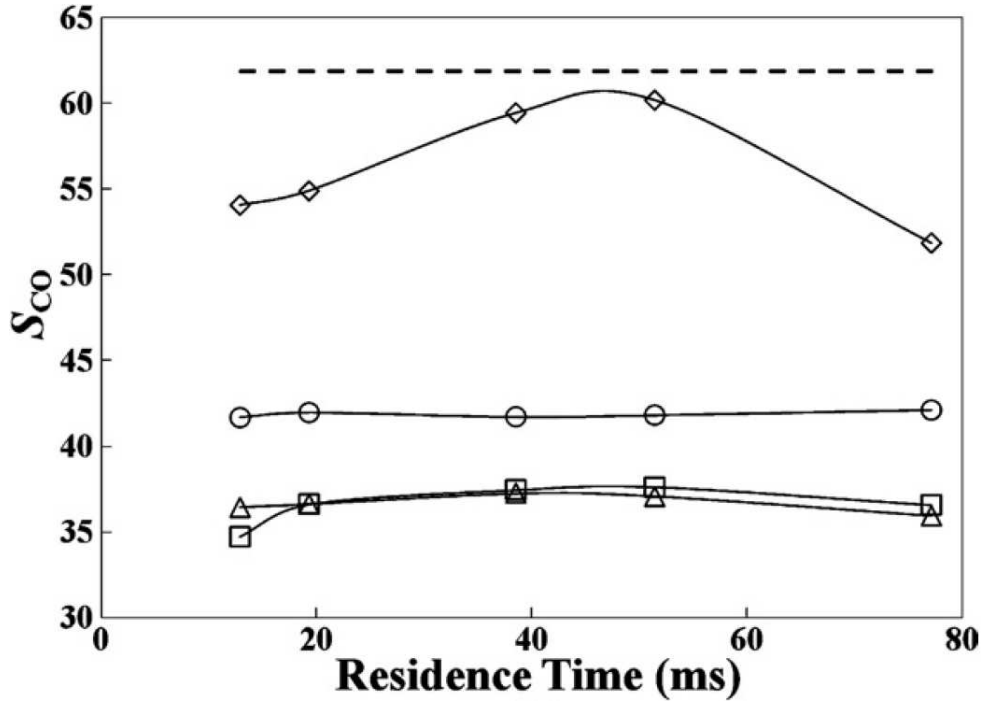

(b)

Figure 5.22. Variations of (a) conversions of methane, and (b) CO selectivities with residence time in the microchannel reactor ($T = 750$°C, S : C = 3.0). The legend is common to both.

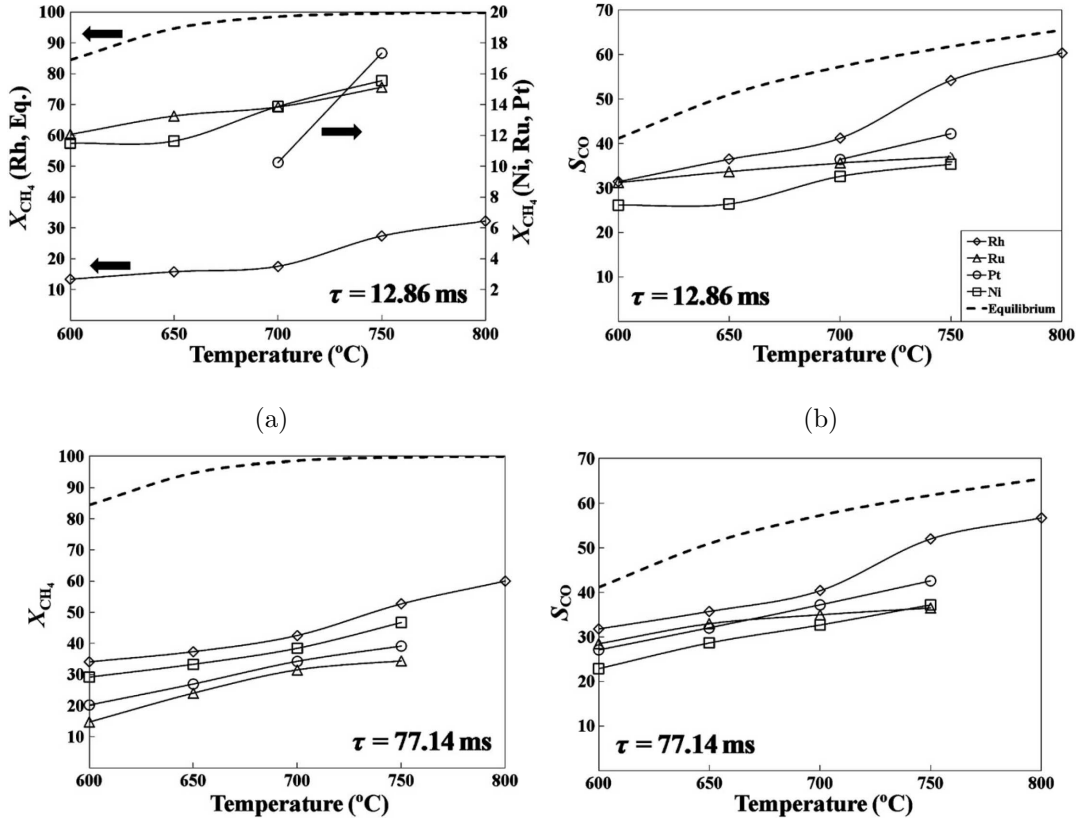

Figure 5.23. Variations of (a), (c) conversions of methane, and (b), (d) CO selectivities with temperature in the microchannel reactor (S : C = 3.0). The residence times are (a), (b) $\tau = 12.86$ ms, and (c), (d) $\tau = 77.14$ ms. The legend is common to all. Left and right arrows designate the left and right ordinates, respectively.

the order of catalysts in terms of the conversion is Rh > Ni > Pt > Ru, which remains unchanged in the $600 - 750$°C range (Figure 5.23c).

Effect of temperature on CO selectivities obtained over different catalysts at residence times of $\tau = 12.86$ ms and 77.14 ms are given in Figure 5.23b,d, respectively. At both the highest and lowest residence times, and in the temperature range studied-especially $T > 700$°C, Rh performs as the most CO-selective among the catalysts, followed immediately by Pt. The continual increase in S_{CO} with temperature is the result of the exothermic WGS reaction running in reverse due to the temperature rise.

Effect of the residence time on S_{CO} is most pronounced at 800°C for Rh, which, in going from $\tau = 12.86$ ms (Figure 5.23b) to 77.14 ms (Figure 5.23d), leads to a 6% fall in selectivity.

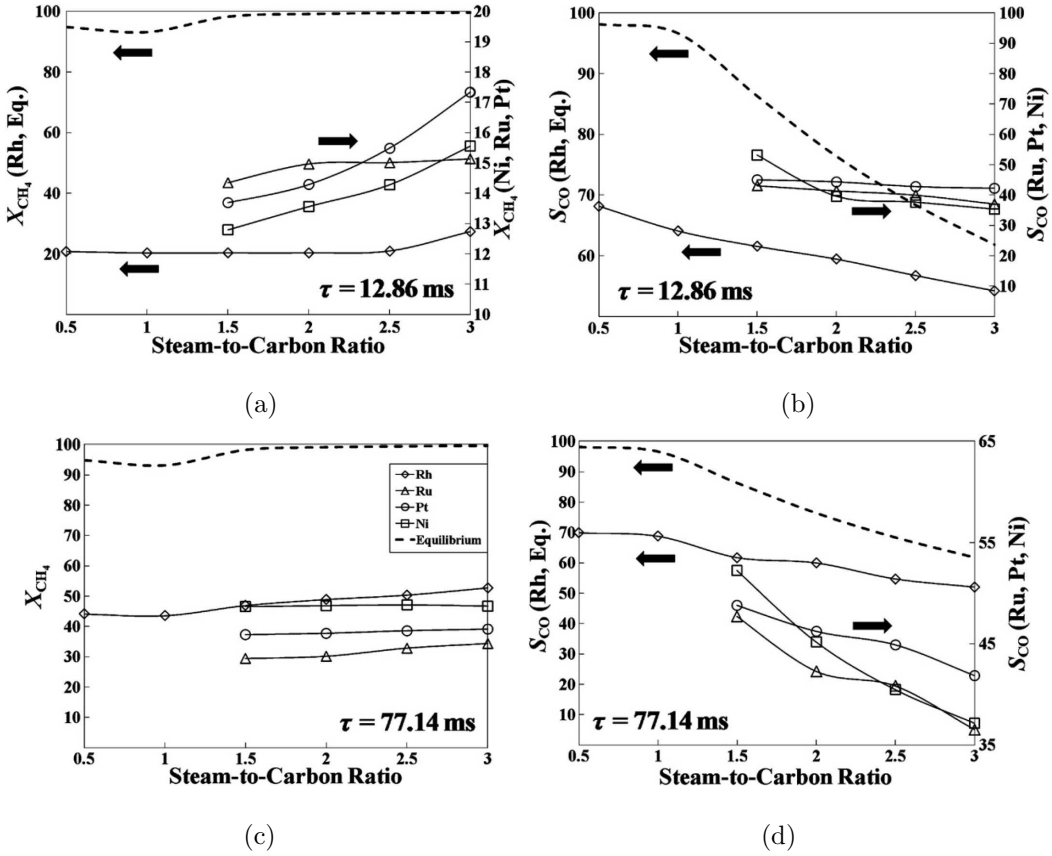

Figure 5.24. Variations of (a), (c) conversions of methane, and (b), (d) CO selectivities with steam-to-carbon ratio in the microchannel reactor ($T = 750$°C). The residence times are (a), (b) $\tau = 12.86$ ms, and (c), (d) $\tau = 77.14$ ms. The legend is common to all. Left and right arrows designate the left and right ordinates, respectively.

5.5.2.3. Effect of Steam-to-Carbon Ratio. Figure 5.24 shows the variations of methane conversions and CO selectivities on different catalysts at two residence times. Rh gives the highest conversions and selectivities at all S : C ratios regardless of the residence time. While there is continuous but minimal increase in conversion and accompanying decrease in selectivity as S : C increases, the only considerable change in conversion at $\tau = 12.86$ ms is when going from S : C = 2.5 to 3.0 (Figure 5.24a). At $\tau = 77.14$ ms conversion is relatively independent of the S : C ratio (Figure 5.24c). S_{CO} changes

with S : C at the two residence times are nearly identical over Rh whereas over other catalysts its dependence is profound at $\tau = 77.14$ ms (Figure 5.24b,d). Based on the results obtained with residence time (Section 5.5.2.1) and temperature (Section 5.5.2.2) variations, further increase in CO selectivity is possible through decrease in τ and increase in the temperature.

It is worth noting that equilibrium conversion is higher at S : C = 0.5 than it is at S : C = 1.0 The probable reason is that methane cracking is also taking place at S : C = 0.5 and 1.0, and at an even faster rate at the lower one. Thus, the amount of solid carbon formed is included in the conversions calculated by the Gibbs free energy minimization method. However, the actual conversion calculation involves a carbon balance (Equation 3.1) that is based on detected gaseous species, CO and CO_2. Therefore, even if there is carbon (coke) formation–which is not the case over Rh as verified by SEM analyses–it does not affect the conversions reported.

While the cost of rhodium precursor may be considered as a drawback in case of commercialization of the microchannel catalyst preparation method outlined herein, the Rh-based catalyst's demonstrated stability and resistance to coke formation at extremely low S : C ratios increase the economic feasibility since the energy requirements due to steam generation and delivery diminish, and the catalyst life is prolonged.

5.5.3. SRM in the Microchannel versus Packed-bed Configurations

Results of the comparison between the microchannel and the packed-bed configurations for productivity and CO selectivity at identical WHSVs (Table 3.6, Section 3.4.2) are shown in Figure 5.25a,b. Due to enhanced heat transfer, the microchannel configuration outperforms the packed bed both in productivity and selectivity with the exception of Pt. Better heat transfer dampens the gradients within the catalyst coating, thus leading to uniform temperature distribution that is inherently higher than that of its counterpart. This phenomenon results not only in increased reforming rates but also increase in CO selectivities since the rate of the reverse WGS reaction, favored at elevated temperatures, is higher.

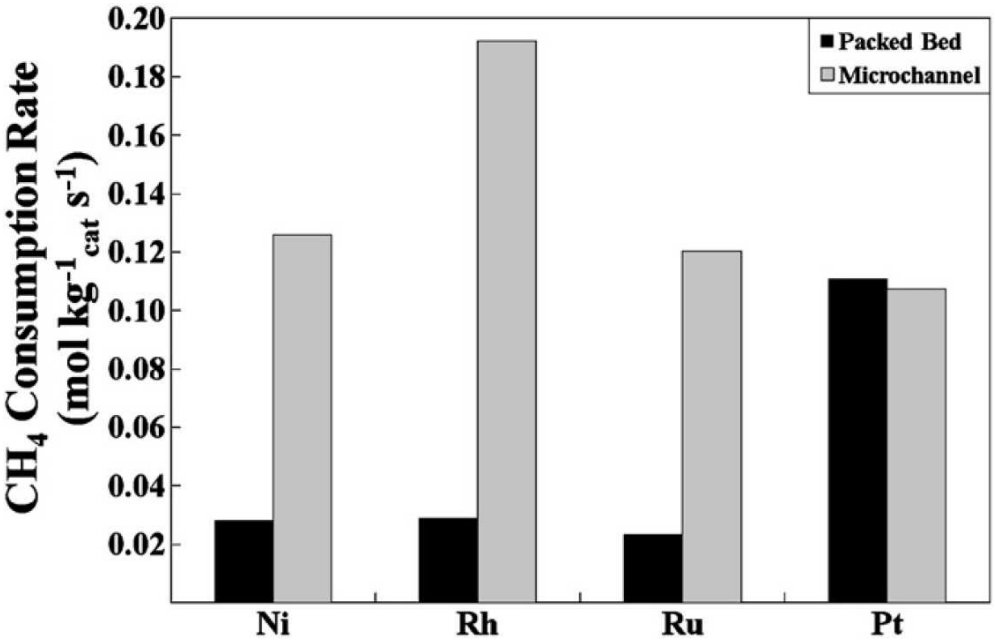

(a)

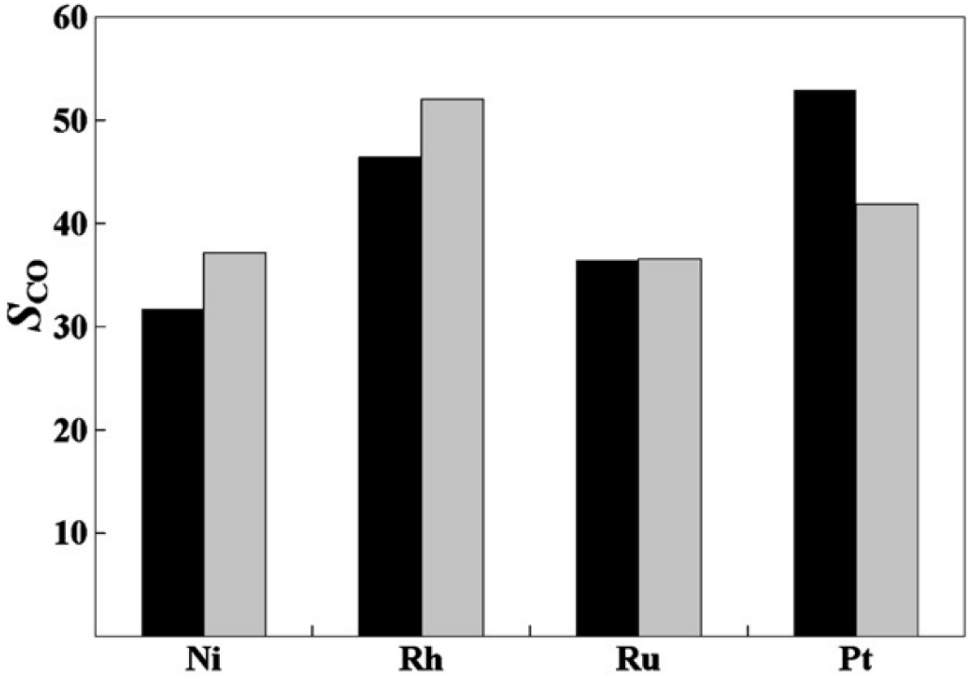

(b)

Figure 5.25. Comparison of (a) methane consumption rates, and (b) CO selectivities in the microchannel and packed-bed reactor configurations. See Table 3.6 for the operating conditions.

As shown graphically in Figure 5.19 and numerically in Table 5.6, the amount and uniformity of dispersion of Pt on the coated catalyst are less than those on the particulate one. These tend to nullify the above-detailed advantages brought by utilizing a wall-coated microchannel reactor. The difference between the performances of the packed bed and the microchannel in case of using Pt is yet minor compared with at least four-fold productivity increase in case of using Ni, Rh or Ru (Figure 5.25a) in the microchannel. This implies that if Pt wall-coated catalyst is improved in such a way that the loading be increased with better dispersion (e.g. by precipitation of the precursor), it will still be advantageous over the particulate catalyst.

5.5.4. Summary

A parametric study of steam reforming of methane (SRM)–involving variations in residence time, reaction temperature and S : C ratio–is conducted in a wall-coated microchannel reactor using noble metal- and nickel-based catalysts, namely, 2wt% Rh, 2wt% Ru, 2wt% Pt- and 10wt% Ni/δ-Al_2O_3. Rh exhibits superior performance compared with other metals on the basis of productivity and CO selectivity in all the cases. Methane conversion on all catalysts increases with residence time, and CO selectivity is maximized at intermediate values of this parameter, most notably on Rh. Both conversion and selectivity increase with temperature since SRM is endothermic, and the reverse water-gas shift (WGS) is favored at high temperatures. There is continuous, yet minimal increase in conversion with the S : C ratio while the selectivity decreases because more steam drives the WGS reaction toward the products. None of the catalysts suffer from coke formation, even at S : C ratios as low as 1.5. Rh, in addition to outperforming other metals, shows excellent stability in activity and selectivity, and resistance to coking for prolonged times on stream. When compared with conventional packed beds on the basis of identical weight hourly space velocities (WHSV), the microchannel reactor presents four- to six-fold increase in productivity and higher CO selectivity as a result of enhanced heat transport rates. The only exception to this outcome is Pt, whose insufficient integration into the coated catalyst has to be improved.

5.6. Testing and Simulation of Syngas Production in a Microchannel Reactor by Autothermal Reforming of Methane

In this section, methane ATR for syngas production is studied in a spatially integrated rectangular microchannel reactor comprised of Pt- and Rh-based catalysts that are coated on opposite walls of the channel. The effects of operating parameters on methane conversion and CO selectivity are analyzed. The parameters considered are the reactants' residence time ($12.86 - 25.72$ ms), reaction temperature ($500 - 650$°C), steam-to-carbon ($0 - 3.0$) and molar oxygen-to-carbon ($0.47 - 0.63$) ratios at the inlet (Section 3.7). Three-dimensional simulation of the described operation is also carried out based on CFD techniques for predicting and analyzing the experimental results. Heat and mass transfer characteristics of the system are also evaluated.

The experimental techniques employed are introduced in Section 3.4.3. Catalyst preparation procedures are outlined in Section 3.3, and synthesis of the catalytic microchannel (Figure 3.4) is explained in Section 3.3.2.2. The 3D model geometry used for the simulation of the system is given in Figure 4.7 in Section 4.2.2. Reaction kinetics of methane combustion (Equation 4.11) over Pt/δ-Al_2O_3 and steam reforming of methane (Equation 4.8) over a Rh-based catalyst are given in Tables 4.12 and 4.23, respectively. Physical properties of the reactive mixture are tabulated in Table 4.25. Reactor and catalyst data, and the operating conditions are summarized in Table 4.26. Momentum and species mass equations describing fluid flow in the microchannel (Section 4.2.3), subject to the boundary conditions given in Section 4.2.4, together with the constitutive equations for the physical properties, fluxes and reaction rates, are solved using the ANSYS Fluent 14.0 CFD software [295] that applies the finite volume method (Section 4.4.4). The 3D Cartesian grid consisting of 8.75×10^5 hexahedral cells is constructed using the preprocessing software GAMBIT 2.4.6. The length (L), width (W) and height (H) (see Figure 3.4) of the microchannel flow domain is respectively discretized into 501, 51 and 36 equally-spaced nodes. The zone corresponding to the combustion catalyst has four times the number of grid elements as does the reforming zone, and twice that the bulk flow zone has, because steep concentration gradients are expected to occur due to the very fast combustion reaction.

The pressure-velocity coupling is done by the pressure-based solver that uses the SIMPLE algorithm (Figure 4.16, Section 4.4.4.2), and the gradients are calculated by the least squares cell-based scheme. The PRESTO! discretization scheme (Section 4.4.4.2) is applied for the pressure while the second-order upwind scheme (Section 4.4.4.1) is applied for the momentum and species conservation equations [295]. Combustion kinetics and concentration-dependent viscosity and diffusivities are implemented in the code and evaluated in each associated cell by means of user-defined functions (UDF), which access the species mass fractions in that cell during each iteration. Velocity inlet ($U^{\text{in}} = 1.59\,\text{m}\,\text{s}^{-1}$ for $\tau = 12.86\,\text{ms}$) and pressure outlet boundary conditions are imposed at the reactor inlet and outlet, respectively. At the catalyst-gas interfaces, continuity of the velocity and the species mass fluxes are required. All other boundaries in the model are treated as impermeable walls with the no-slip condition and zero species flux.

5.6.1. Parametric Study of Methane ATR

Experimental and CFD-based analysis of methane ATR in the microchannel reactor is conducted by changing one parameter in each run while keeping all others constant. Equilibrium methane conversion and CO selectivity are also calculated for each case using HSC Chemistry [313] via the Gibbs free energy minimization method. In all cases conversion below the equilibrium value is guaranteed by the choice of operating conditions given in Table 4.26 for facile comparison of the parameter effects.

5.6.1.1. Effect of Residence Time. Figure 5.26 shows the experimental and simulated values of methane conversion and CO selectivity in the residence time range ($\tau = 12.86 - 25.72\,\text{ms}$) studied. Experimental conversion is very well predicted by the model at all residence times despite the numerous assumptions made (Section 4.2.3.1), among which the independent occurrence of oxidation and reforming over Pt and Rh may actually be an oversimplification of the real process. Doubling the residence time leads to a $\sim 10\%$ increase in methane conversion ($46.6 \rightarrow 51.4\%$). The continuous increase in methane consumption with residence time is due to the increased steam reforming rate.

Since oxygen is depleted in all the runs in the parameter range, methane consumed during oxidation is known by the stoichiometry of reaction (Equation 4.11), which makes it a straightforward task to calculate the amount of methane consumed during steam reforming, hence the reforming rate, which exhibits a $\sim 21\%$ increase with the doubling of the residence time.

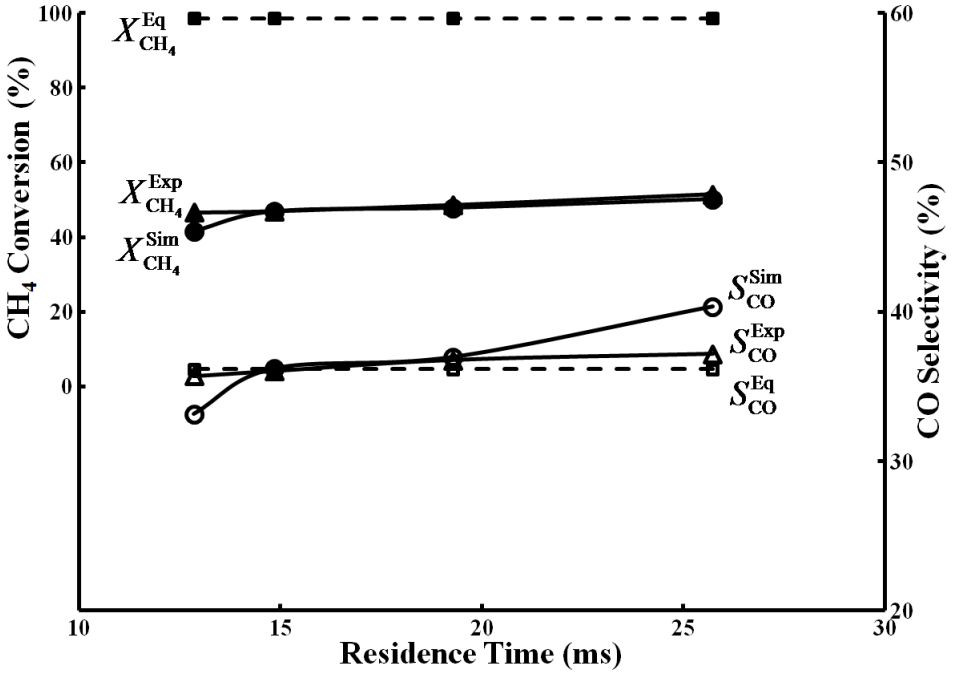

Figure 5.26. Variation of experimental and simulated methane conversion and CO selectivity with residence time in the microchannel reactor ($T = 650°\text{C}, \text{S} : \text{C} = 3.0, \text{O}_2 : \text{C} = 0.47$).

Both the experimental and simulation results are close to the equilibrium CO selectivity values. At residence times above 19 ms, however, actual selectivities higher by $1.6 - 2.8\%$ than the equilibrium selectivities are observed (Figure 5.26). The reason is that reforming is taking place away from equilibrium, and the product selectivity is governed mostly by reaction kinetics [141,314]. The increase in experimental selectivity, though as small as 4% it is, is attributed to the increase in the reforming rate. Since the water-gas shift (WGS) reaction requires longer residence times to become significant, production rate of CO by SR is higher than its consumption rate by WGS in the range considered. The $\text{H}_2 : \text{CO}$ ratio at the reactor outlet is in the range of $2.68 - 3.43$.

The relative independence of conversion and selectivity from the residence time can be justified by the surface coverage results from the simulations. Figure 5.27 shows the variations of CO, H and C coverages, and of the fraction of vacant Rh sites with residence time. While the fraction of the vacant sites, Rh(s), and H(s) decrease slightly with increasing residence time, CO(s) remains essentially the same ($\theta_{CO} \approx 0.85$). It is worth noting that the possibility of carbon deposition on the surface sites rises as the residence time is doubled.

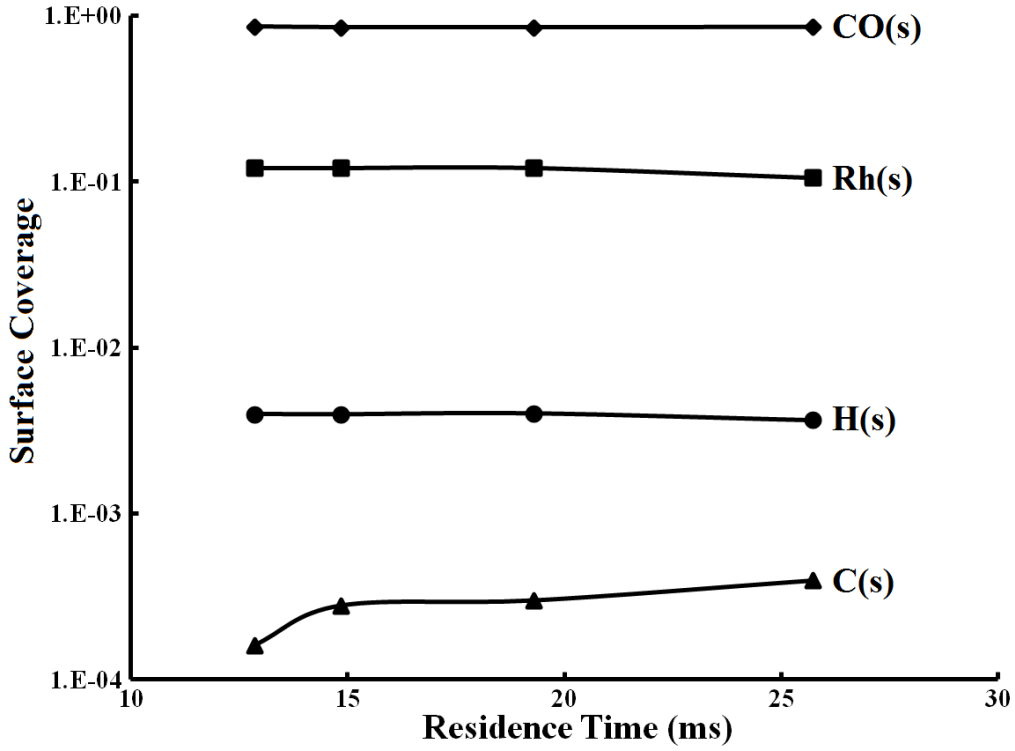

Figure 5.27. Surface coverages of CO, H and C as functions of the residence time ($T = 650°C, S : C = 3.0, O_2 : C = 0.47$).

5.6.1.2. Effect of Temperature. Experimental and simulated methane conversion and CO selectivity values are in good agreement in the temperature range of $600 - 650°C$ with an average error of 9.6% (Figure 5.28). Experimental conversion increases by 27% in going from 550 to 650°C while it almost quadruples in the range $500 - 650°C$. Operation at 500°C poses the only exception to full oxidation conversion among the parametric runs (ca. 50% instead of 100%). As the reaction temperature falls below 570°C, experimental CO selectivity begins to exceed the equilibrium selectivity. In

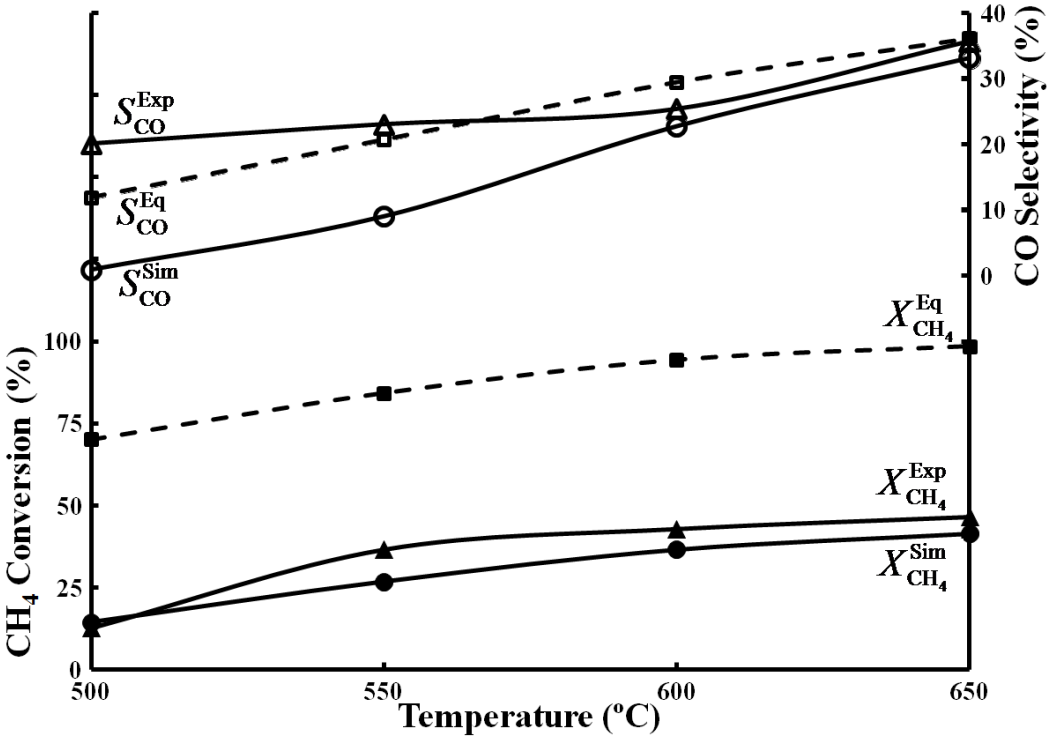

Figure 5.28. Variation of experimental and simulated methane conversion and CO selectivity with reaction temperature ($\tau = 12.86\,\text{ms}$, S : C = 3.0, O_2 : C = 0.47).

equilibrium-limited reaction systems like steam reforming of hydrocarbons, the temperature determines whether the system is thermodynamically or kinetically controlled. Thermodynamic equilibrium is favored at elevated temperatures whereas the kinetic regime is under control at lower temperatures [141, 314]. For the system under consideration the range of lower temperatures is found to be $500 - 570°\text{C}$ where the product selectivity is controlled by reaction kinetics.

Plots of surface coverages over Rh (Figure 5.29) show that at 500°C nearly all the surface sites ($\theta_O \approx 0.97$) are occupied with oxygen atoms since the temperature is too low for adsorption of CH_4 and desorption of CO and H_2 molecules, if there are any that have formed during reforming. C(s) coverage increases by about six orders of magnitude in the range $500 - 570°\text{C}$ as the reforming activity increases and makes a peak, which means that the Rh-based catalyst is most prone to coking in this range of reaction temperatures.

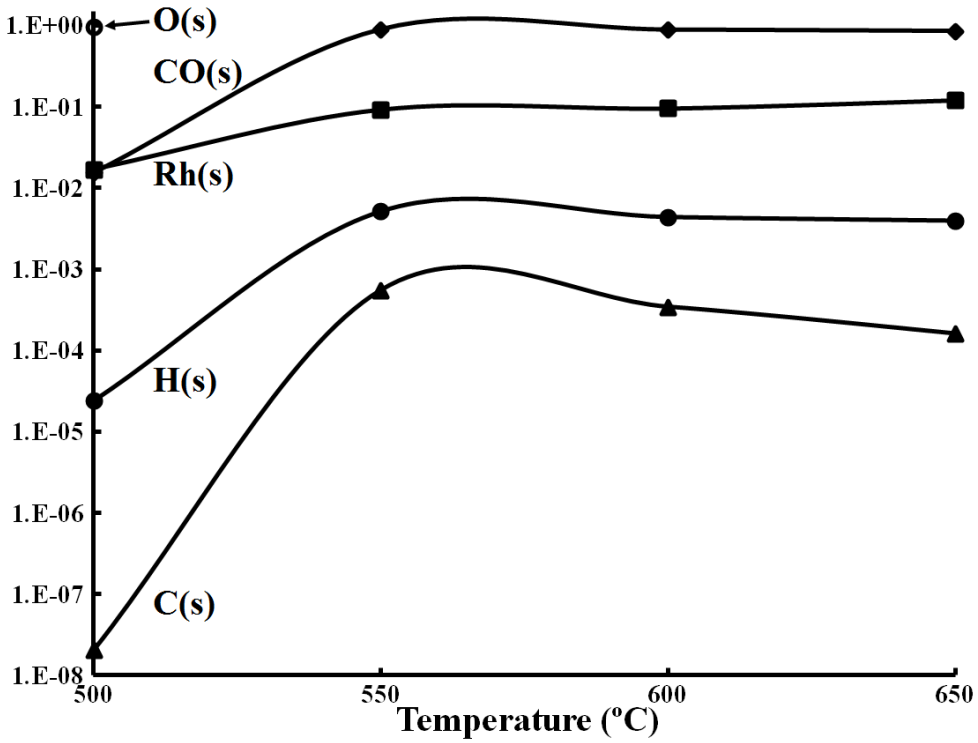

Figure 5.29. Surface coverages of CO, H and C as functions of the reaction temperature ($\tau = 12.86\,\text{ms}$, S : C = 3.0, O_2 : C = 0.47).

5.6.1.3. Effect of Steam-to-Carbon Ratio. Figure 5.30 shows that the dependence of CO selectivity on the steam-to-carbon ratio is weak. Conversion (not shown) increases by merely 10% (41.5 → 46.6%) as the ratio goes from 0 to 3.0. CO selectivity that is also predicted well by the model shows a slight decrease (∼ 8%) with the increase in S : C. The H_2 : CO ratio is most susceptible to changes in S : C whose variation determines the direction (forward or reverse) of the water-gas shift equilibrium. Addition of extra steam should shift the WGS equilibrium to the direction of CO_2 formation ($CO + H_2O \rightleftharpoons CO_2 + H_2$, $\Delta H^0_{298} = -41.2\,\text{kJ mol}^{-1}$). However, at 650°C, a considerably high temperature for the WGS, the reaction is running in reverse that increases the CO concentration in the mixture. The presence of CO_2 produced already by oxidation also shifts the equilibrium to the left. As a result, H_2 : CO ratios as low as 0.93 can be obtained. Referring to Figure 5.30, H_2 : CO = 2.0 is attainable with S : C ≈ 1.30. This finding, in conjunction with the results obtained in the relatively low reaction temperature range, has the strong implication that methane ATR, car-

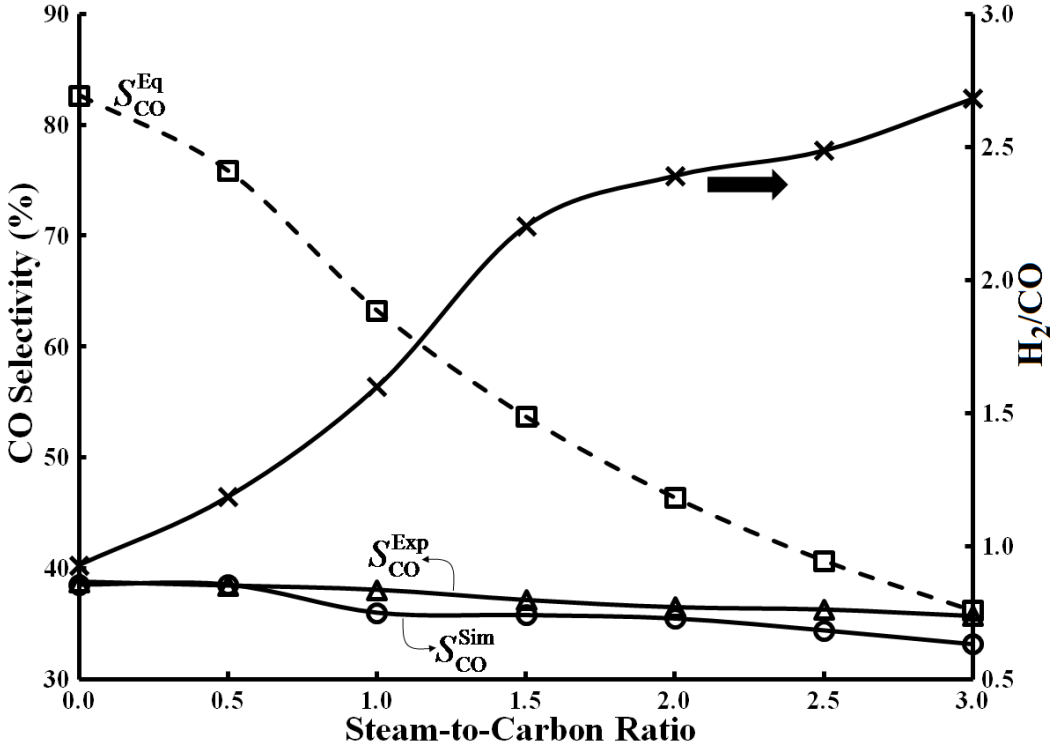

Figure 5.30. Variation of experimental and simulated CO selectivity with the steam-to-carbon ratio at the inlet ($\tau = 12.86$ ms, $T = 650$°C, $O_2 : C = 0.47$).

ried out in microchannel reactors integrated with active and stable catalysts, offers the promising option of producing syngas in a range of desired compositions with minimal operational costs and disruptions that are inevitable when working at elevated temperatures, and when coking is a potential problem.

5.6.1.4. Effect of Oxygen-to-Carbon Ratio. The increase in conversion when the O_2 : C ratio is increased from 0.47 to 0.63 is mainly the result of more methane converted during oxidation (Figure 5.31). The increase in the parameter (O_2 : C) values has its slight effect on reforming and water-gas shift through CO_2, more of which is produced by oxidation. As another remark, CO selectivity decreases with the O_2 : C ratio (Figure 5.31) since the production rate of CO_2 surpasses that of CO. Recalling that when the O_2 : C ratio is equal to 0.47, the threshold temperature is 570°C for transition from the kinetic to the thermodynamic regime (Figure 5.28), which means that at higher temperatures the actual selectivity should be less than the equilibrium selectivity

unless the partial oxidation and steam reforming reaction mechanisms are altered by some other parameter. However, at 650°C, the temperature at which the O_2 : C parameter is investigated, the actual selectivity is still measured to be higher in nearly the whole range of O_2 : C ratios $(0.47 - 0.63)$, possibly due to the alteration of the reaction paths by increased O_2 percentage [314].

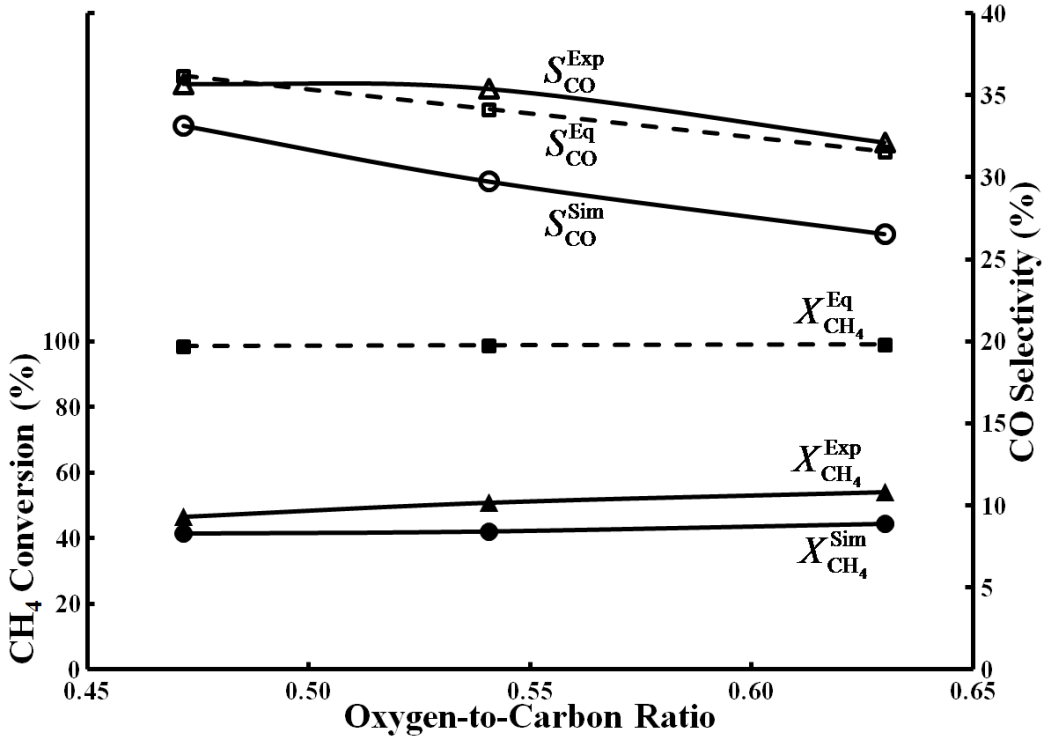

Figure 5.31. Variation of experimental and simulated CO selectivity with the oxygen-to-carbon ratio at the inlet ($\tau = 12.86\,\text{ms}$, $T = 650°\text{C}$, S : C = 3.0).

5.6.2. Evaluation of Mass and Heat Transfer Characteristics

One of the key aspects of microchannel operation is the minimization of both external and internal mass and heat transfer limitations. In the present section, this is tested using several criteria based on observed rate of methane consumption.

5.6.2.1. Mass Transfer at the Gas-Solid Interfaces. Criterion for the absence of external mass transfer limitations is given in Equations 5.2 and 5.3 [315]:

$$\Psi^{\mathrm{OX}}_{\mathrm{MT,ext}} = \frac{\Re^{\mathrm{v}}_{\mathrm{CH_4,OX}} L_s}{k^{\mathrm{OX}}_{\mathrm{g}} c^{\mathrm{in}}_{\mathrm{CH_4}}} < 0.05 \tag{5.2}$$

$$\Psi^{\mathrm{SR}}_{\mathrm{MT,ext}} = \frac{\Re^{\mathrm{s}}_{\mathrm{CH_4,SR}} L_s}{k^{\mathrm{SR}}_{\mathrm{g}} c^{\mathrm{in}}_{\mathrm{CH_4}}} < 0.05 \tag{5.3}$$

where L_s [m] is the characteristic dimension that is equal to the volume of the washcoat (either Pt or Rh) divided by its geometric surface area. The right-hand side of each inequality, which is 0.15 in the original paper of Mears [315], is modified by Görke *et al.* [87] for microchannel catalysts to be 0.05. Calculation of experimental rates of methane consumption during oxidation and steam reforming is straightforward since the O_2 : C ratios are given, and oxygen is depleted in all parametric runs except the one carried out at 500°C. Since the catalyst structuring resembles that of a parallel-plate arrangement, with the assumption of a fully-developed velocity profile, the asymptotic Sherwood number, $Sh_\infty = k_g d_H / D_{\mathrm{CH_4},m}$, equals 7.54072 [316], from which the mass transfer coefficients are found to be $k^{\mathrm{OX}}_{\mathrm{g}} = k^{\mathrm{SR}}_{\mathrm{g}} = 0.975\,\mathrm{m\,s^{-1}}$ with d_H equal to $1.263 \times 10^{-3}\,\mathrm{m}$ and $D_{\mathrm{CH_4},m} = 1.633 \times 10^{-4}\,\mathrm{m^2\,s^{-1}}$ at 650°C. At the base-case operating conditions (see Table 3.7) the overall rates of methane consumption are 4289 and $4182\,\mathrm{mol\,m^{-3}\,s^{-1}}$ respectively for oxidation and reforming. Methane concentration at the inlet, $c^{\mathrm{in}}_{\mathrm{CH_4}}$, is $1.886\,\mathrm{mol\,m^{-3}}$ and $L_s = 5 \times 10^{-5}\,\mathrm{m}$. With the values of 2.33×10^{-2} and 2.27×10^{-2} for Pt and Rh catalysts, the inequalities are then satisfied, meaning the mass transfer resistances are negligible at 650°C. These calculations are performed for all the parameter ranges, and, in all cases, the interfacial mass transfer resistance is found to be negligible.

5.6.2.2. Mass Transfer in the Washcoats. The criterion of Weisz-Prater adapted for washcoated microchannels is [87]

$$\Psi^{\mathrm{OX}}_{\mathrm{MT,int}} = \frac{\Re^{\mathrm{v}}_{\mathrm{CH_4,OX}} L_s^2}{D_{\mathrm{eff,CH_4},m} c^{\mathrm{in}}_{\mathrm{CH_4}}} < 0.1 \tag{5.4}$$

$$\Psi^{\mathrm{SR}}_{\mathrm{MT,int}} = \frac{\Re^{\mathrm{s}}_{\mathrm{CH_4,SR}} L_s^2}{D_{\mathrm{eff,CH_4},m} c^{\mathrm{in}}_{\mathrm{CH_4}}} < 0.1 \tag{5.5}$$

Effective diffusivity of CH_4 in the Pt and Rh catalysts at 650°C is calculated to be $1.268 \times 10^{-4}\,\mathrm{m^2\,s^{-1}}$. Then $\Psi^{\mathrm{OX}}_{\mathrm{MT,int}} = \Psi^{\mathrm{SR}}_{\mathrm{MT,int}} \approx 1.4 \times 10^{-3}$, which means that mass transfer limitations do not exist within the washcoats. The same deduction can be made for all other cases.

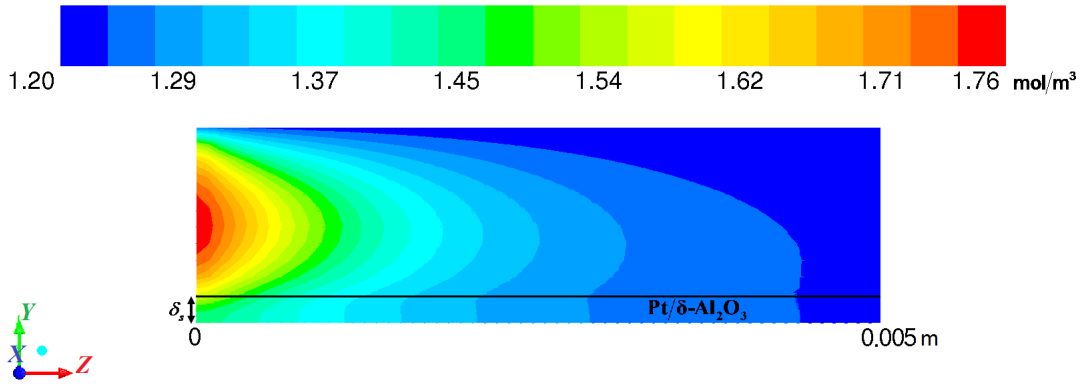

Figure 5.32. 2D plot of methane concentration in the Pt/δ-Al_2O_3 catalyst between $z = 0$ and $z = 5 \times 10^{-3}$ m (no gradients in the x-direction).

With the visual aid of the simulation results a better assessment of the situation is possible. Figure 5.32 shows the surface plot of methane concentration in the Pt catalyst along the first quarter of the length of the microchannel. Even though the transverse (i.e., in the y-direction) concentration gradients in the catalyst layer are notable at the channel upstream (i.e., first one-fourth portion of the channel length), they tend to smooth out beyond this point and eventually nullify.

5.6.2.3. Heat Transfer at the Gas-Solid Interfaces. Absence or presence of resistance to heat transfer at the gas-solid interfaces can be checked using the criterion proposed by Anderson [317] with a slight modification [87] for washcoated catalysts:

$$\Psi^{\mathrm{OX}}_{\mathrm{HT,ext}} = \frac{(-\Delta H_{\mathrm{OX}})\,\Re^{\mathrm{v}}_{\mathrm{CH_4,OX}} L_s}{\alpha_g T}\left(\frac{E_{A,\mathrm{OX}}}{RT}\right) < 0.05 \tag{5.6}$$

$$\Psi^{\mathrm{SR}}_{\mathrm{HT,ext}} = \frac{(-\Delta H_{\mathrm{SR}})\,\Re^{\mathrm{s}}_{\mathrm{CH_4,SR}} L_s}{\alpha_g T}\left(\frac{E_{A,\mathrm{SR}}}{RT}\right) < 0.05 \tag{5.7}$$

α_g is calculated from

$$\alpha_g = \frac{\mathrm{Nu}_\infty k_f}{d_H} \tag{5.8}$$

k_f is evaluated at 650°C using the inlet composition. Then the left-hand sides of the inequalities respectively become 1.6×10^{-1} and 2.7×10^{-1} for the Pt and Rh catalysts, which suggest that heat transfer limitations are present at the interfaces. In all other cases external resistance to heat transfer exists as well. The resistance can be overcome by using catalytic washcoats with thickness less than $15\,\mu$m, which ensures resistance-free heat transfer across the gas-solid boundary. Another possible solution is to decrease the channel height, hence the hydraulic diameter, which enhances the heat transfer coefficient.

5.6.2.4. Heat Transfer in the Washcoats. The criterion of Anderson [317] adapted for microreactors [87] can again be applied:

$$\Psi^{\mathrm{OX}}_{\mathrm{HT,int}} = \frac{(-\Delta H_{\mathrm{OX}})\,\Re^{\mathrm{v}}_{\mathrm{CH_4,OX}} L_s^2}{\lambda^s_{\mathrm{eff}} T}\left(\frac{E_{A,\mathrm{OX}}}{RT}\right) < 0.1 \tag{5.9}$$

$$\Psi^{\mathrm{SR}}_{\mathrm{HT,int}} = \frac{(-\Delta H_{\mathrm{SR}})\,\Re^{\mathrm{s}}_{\mathrm{CH_4,SR}} L_s^2}{\lambda^s_{\mathrm{eff}} T}\left(\frac{E_{A,\mathrm{SR}}}{RT}\right) < 0.1 \tag{5.10}$$

k^s_{eff} assumes a value of $0.5\,\text{W}\,\text{m}^{-1}\,\text{K}^{-1}$, which is typical of porous oxide materials [87]. For oxidation and reforming, the left-hand sides of the inequalities become 3.4×10^{-3} and 5.8×10^{-3} at 650°C, indicating that nearly isothermal behavior is established within the washcoats that show small resistance to internal heat transfer. The criterion for resistance-free heat transfer inside the washcoats is met in all other cases as well.

5.6.3. Summary

Experimental and modeling analysis of methane ATR that involves the parametric variations of the residence time, reaction temperature, and inlet steam-to-carbon and oxygen-to-carbon ratios is carried out in a wall-coated microchannel reactor. The microchannel is configured such that Pt- (facilitating combustion) and Rh-based (facilitating steam reforming) catalysts are coated on opposite walls. The model, incorporating a surface reaction mechanism for steam reforming over Rh and detailed description of the flow field and species transport, predicts the experimental results such as methane conversion and CO selectivity with 8.4% error on average. The maximum conversion increase upon change of a single parameter is 27%, which is obtained by raising the temperature from 550 to 650°C. While 21% increase in conversion of methane in steam reforming alone is observed with the doubling of the residence time, oxygen-to-carbon ratio is seen to have virtually no effect on conversion. CO selectivity is influenced most markedly by variations in temperature which, upon incrementing, boosts the reforming activity. With all the other parameters kept constant at their base-case values, for residence times greater than 19 ms, temperatures less than 570°C and oxygen-to-carbon ratios greater than 0.47, actual (experimental) CO selectivity consistently exceeds the equilibrium CO selectivity, which is attributed to the transition to the kinetic regime, and also to the possible modification of the reaction mechanisms. H_2 : CO ratio, on the other hand, is very susceptible to changes in the steam-to-carbon ratio, which can be manipulated in a wide range for adjusting the desired syngas composition. The system is diagnosed with external heat transfer limitations that may be overcome completely by decreasing the channel height and the thickness of the catalytic washcoats. The analysis results suggest that the designed and tested microchannel reactor, spatially

integrated with active and stable catalysts suitable for conversion of specific hydrocarbons, is capable of delivering syngas at desired compositions with minimal operational costs and disruptions. The reactor model, whose fidelity is checked by experimental data, is proven to serve as an essential design and analysis tool.

6. CONCLUSIONS AND RECOMMENDATIONS

6.1. Conclusions

The major objectives of this research were (i) to construct, develop and classify computational fluid dynamics (CFD) based models that represent the physical models of compact catalytic reaction systems, including parallel microchannel reactors and reactor/heat exchanger cascades, and to present these models in a form applicable to any general catalytic reaction system, (ii) to simulate, using the models, the compact catalytic systems within the context of hydrocarbon and alcohol conversion for hydrogen production for fuel cells and for feedstock production, (iii) to study the reactor geometries and operating conditions on the basis of productivity, selectivity, size and operability considerations, (iv) to design, construct and test an experimental rig for methane-to-syngas conversion in accordance with the guidelines provided by quantitative analysis. The objectives are duly met, as indicated by the following major conclusions:

- Spatially segregated, parallel microchannel reactors were modeled using CFD techniques for analyzing combustion-assisted endothermic reactions, namely, ethane dehydrogenation and steam reforming of hydrocarbons and alcohols. These coupled reaction/heat exchange systems were parametrically investigated by varying the channel side lengths, the thickness and material of construction of the segregating walls, and the channel textures.
- In the couplings of combustion and steam reforming of propane, methanol and ethanol, incremental reduction in channel side length resulted in higher fuel conversions and hydrogen yields due to improved heat transfer coefficients between the fluids and the wall, driven by enhanced mixing. Further reduction adversely affected conversions since the residence times declined drastically.
- The size of a microchannel reactor designed for combustion/steam reforming coupling of methanol, which was capable of delivering enough hydrogen to run a 2-kW PEM fuel cell, was estimated to be $1.2 \times 10^{-3}\,\mathrm{m}^3$.

- In the coupling of combustion of methane and steam reforming of *iso*-octane, fuel conversion and hydrogen yield increase with increasing wall thickness and thermal conductivity due to pronounced axial heat conduction in the wall.
- Use of micro-baffles, which act as static micro-mixers, leads to considerable improvements in conversions and hydrogen yields through the enhancement of heat transfer coefficients.
- Decoupled reaction/heat exchange systems, comprised of cascades of packed-bed reactors and microchannel heat exchangers, were compared with parallel microchannel reactors on the basis of performance and size. Integration of combustion of methane and steam reforming of *n*-heptane resulted in fuel conversions higher than 85%, with the microchannel reactor having a smaller size than the cascade reactor. The fuel processor for producing fuel-cell-grade hydrogen with the cascade reactor at the reforming step turned out to be more efficient in terms of productivity per unit fuel.
- Cascade reactors used for combustion/steam reforming integration of methane and combustion/dehydrogenation integration of methane and ethane were found to be smaller than the microchannel reactors, and they also provided much better temperature control through elimination of hot spots that lead to thermal degradation of the catalysts. Facile replacement of deactivated catalysts from the cascade reactors and decoupling of reaction kinetics from heat exchange were discussed to be key aspects.
- Steam reforming of methane for syngas production was carried out in a microchannel reactor over Ni- and noble metal-based catalysts. The catalysts and the reaction system were designed and prepared by in-house laboratory know-how and technology.
- Methane conversion increased with residence time, temperature and steam-to-carbon ratio.
- The microchannel reactor surpassed the packed-bed reactor in terms of productivity and carbon monoxide selectivity due to improved heat transfer.
- Rh exhibited superior performance compared with Ni, Ru and Pt on the basis of productivity and selectivity, and yielded near-equilibrium selectivity at interme-

diate residence times in the studied range.

- None of the catalysts based on Rh, Ru, Pt and Ni suffer from coke formation even at steam-to-carbon ratios as low as 1.5, possibly due to reduced residence times.
- Rh catalyst maintained its reforming activity and carbon monoxide selectivity for at least 72 h at a steam-to-carbon ratio of 0.5. Its stability and resistance to coke formation increase the economic feasibility due to reduced energy requirements and prolonged catalyst life.
- Conversion and selectivity results of experimental and CFD analyses of autothermal reforming of methane in the spatially integrated microchannel reactor were in good agreement within 8.4% error, meaning the reactor model can be used as a reliable design and analysis tool.
- Certain operating conditions lead to experimental carbon monoxide selectivities greater than the equilibrium selectivity due to the transition to the kinetic regime, and also to the possible modification of the reaction mechanisms.
- The steam-to-carbon ratio, a key parameter available for manipulation in the studied system, was shown to affect the composition of the product syngas notably.
- Autothermal reforming of methane, carried out in a microchannel reactor integrated with active and stable catalysts, at lower temperatures compared with industrial practice, and at low steam-to-carbon ratios, stood out as a promising option of producing syngas in a range of desired compositions with minimal operational costs and disruptions.
- Pressure drop along the microchannel reactors was insignificant.

6.2. Recommendations

The following improvements and complements to the presented work are recommended for future research that is expected to require higher precision, larger scales and throughputs, and greater complexity (e.g. nonisothermal experimental runs, three-phase reactions):

- The modeling studies can be extended so as to comprise the complete simulation of microchannel reactors including the inlet and outlet manifolds to the channels. Uniformity of flow into and inside the channels can be tested; non-uniformities resulting in process inefficiencies, for example, due to insufficient mixing, can be identified.
- Referring to the previous item and the general numbering-up strategy, theoretical knowledge gained by accurate simulations can be used for the manufacture of reactor sheets consisting of multiple channels of various shapes and integration of these sheets in order to increase the throughput. Such a setup that facilitates coupling of exothermic and endothermic reactions also makes it possible to run the system without the continuous need for external heating by the furnace, and to probe temperature variations along the length of the reactor.
- Catalyst characterization can include techniques such as nitrogen adsorption for BET surface area measurements of porous catalysts, and hydrogen chemisorption for determining metal dispersion over the catalyst supports.

APPENDIX A: CALIBRATION OF THE MASS FLOW CONTROLLERS

Calibration curves of the Bronkhorst F-201CV series mass flow controllers used in the experiments (Section 3) are given below.

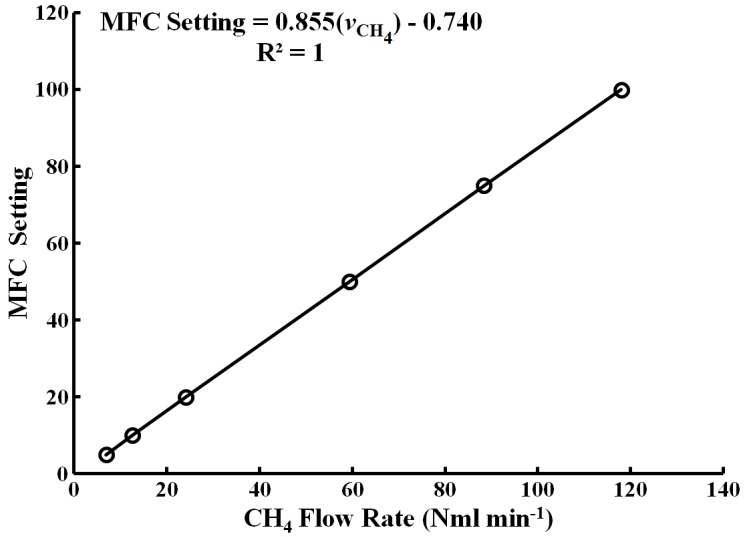

Figure A.1. Calibration curve of the methane mass flow controller.

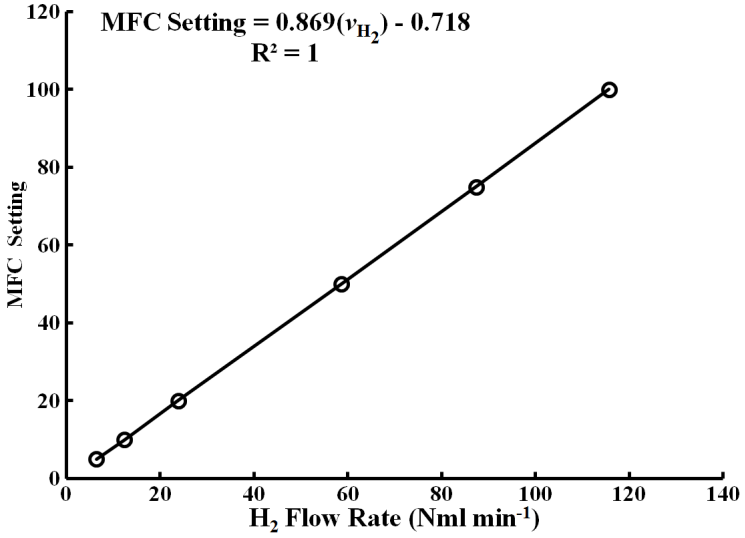

Figure A.2. Calibration curve of the hydrogen mass flow controller.

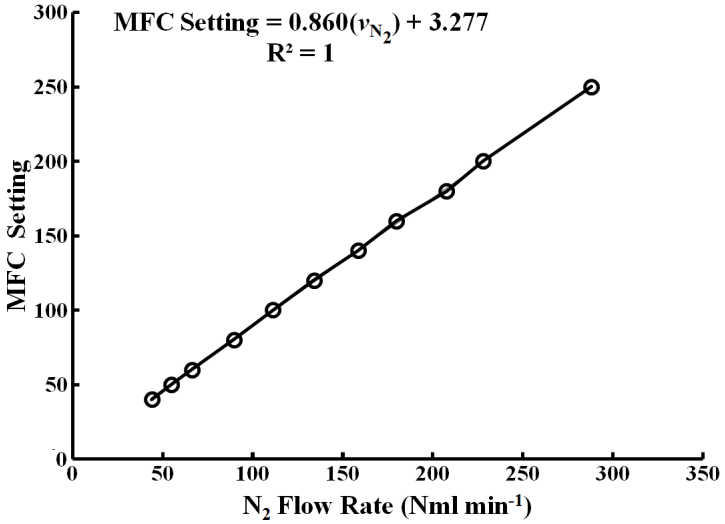

Figure A.3. Calibration curve of the nitrogen mass flow controller.

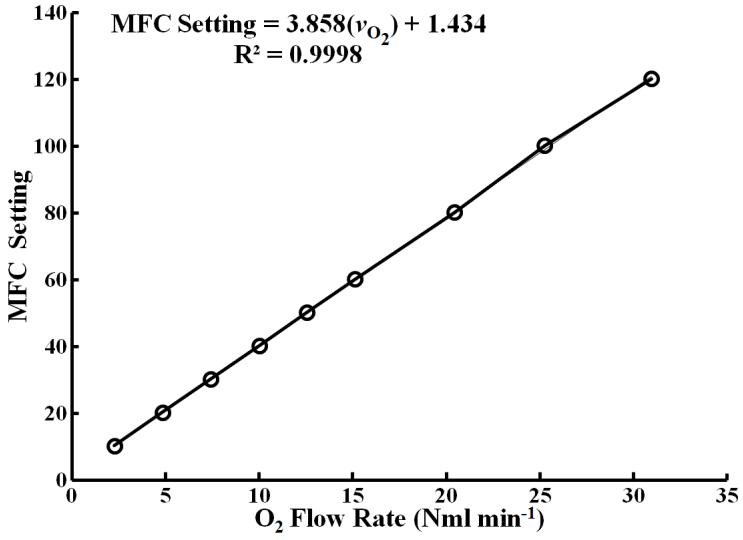

Figure A.4. Calibration curve of the dry air mass flow controller for oxygen.

APPENDIX B: CALIBRATION OF THE GAS CHROMATOGRAPH

Calibration curves of the GC-2014 gas chromatograph used in the experiments (Section 3) are given below.

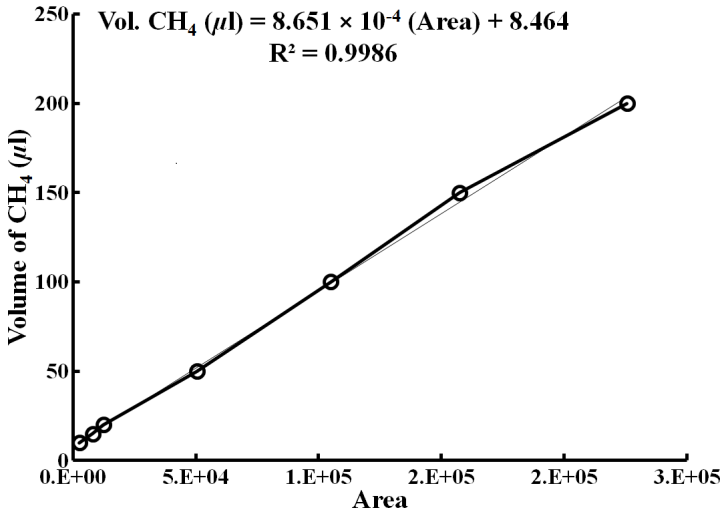

Figure B.1. GC calibration curve for methane.

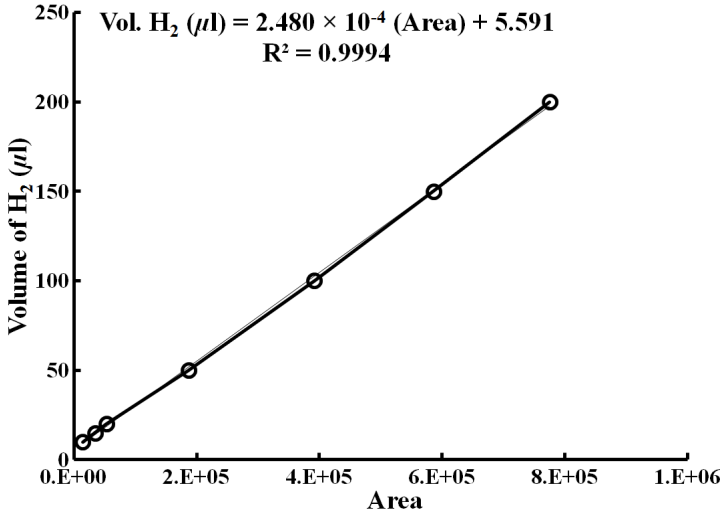

Figure B.2. GC calibration curve for hydrogen.

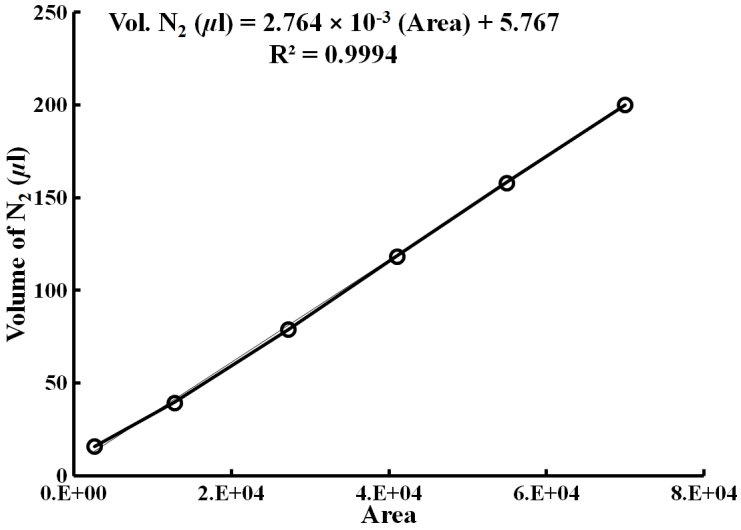

Figure B.3. GC calibration curve for nitrogen.

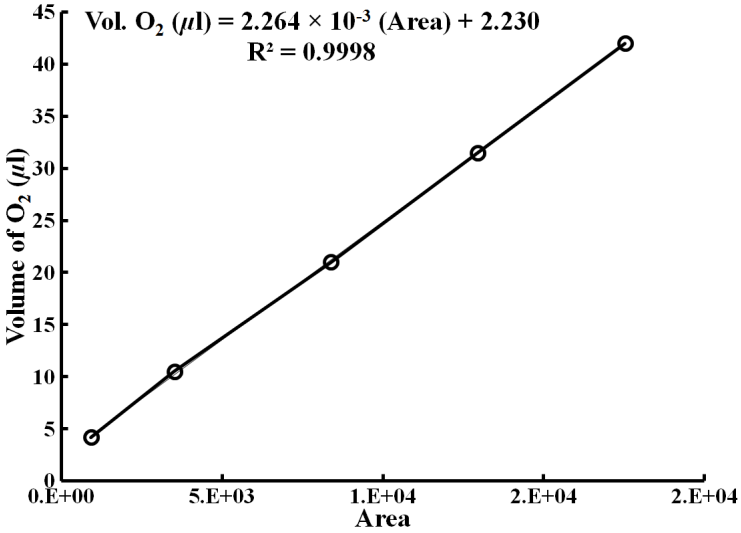

Figure B.4. GC calibration curve for oxygen.

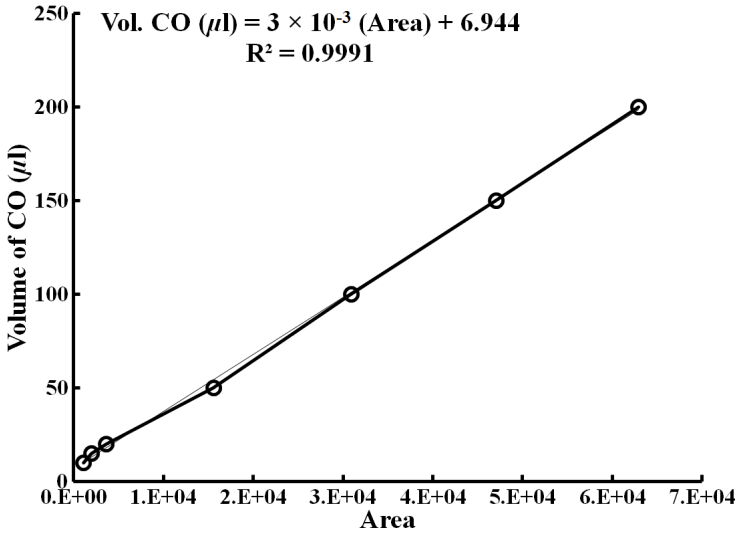

Figure B.5. GC calibration curve for carbon monoxide.

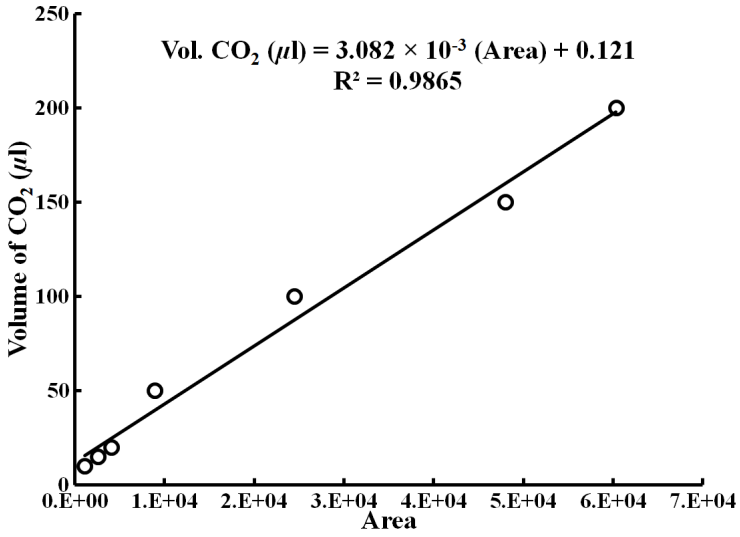

Figure B.6. GC calibration curve for carbon dioxide.

APPENDIX C: SHAPE FUNCTIONS

C.1. One-dimensional quadratic elements

A better approximation for the variation of ϕ is possible with the use of parabolic arcs over each element (Figure 4.12). The function $\phi(x)$ will be quadratic in x within each element, and is of the form

$$\phi(x) = \alpha_1 + \alpha_2 x + \alpha_3 x^2 \tag{C.1}$$

There are now three parameters to be determined and hence the value of ϕ is needed at one more point in addition to two end points of an element. If the midpoint in addition to the end values is chosen, the following equations for ϕ can be written:

$$\begin{aligned} \phi_i &= \alpha_1 \\ \phi_j &= \alpha_1 + \alpha_2 \frac{l}{2} + \alpha_3 \left(\frac{l}{2}\right)^2 \\ \phi_k &= \alpha_1 + \alpha_2 l + \alpha_3 l^2 \end{aligned} \tag{C.2}$$

from which the following values for the three constants α_1, α_2 and α_3 are obtained:

$$\begin{aligned} \alpha_1 &= \phi_i \\ \alpha_2 &= \frac{1}{l}(-3\phi_i + 4\phi_j - \phi_k) \\ \alpha_3 &= \frac{2}{l^2}(\phi_i - 2\phi_j + \phi_k) \end{aligned} \tag{C.3}$$

Substitution of these into Eq. (C.1) gives, after some manipulation,

$$\phi = N_i \phi_i + N_j \phi_j + N_k \phi_k \tag{C.4}$$

with the shape functions equal to

$$\begin{aligned} N_i &= \left[1 - \frac{3x}{l} + \frac{2x^2}{l^2}\right] \\ N_j &= \left[4\frac{4}{l} - 4\frac{x^2}{l^2}\right] \\ N_k &= \left[2\frac{x^2}{l^2} - \frac{x}{l}\right] \end{aligned} \tag{C.5}$$

The first derivative of ϕ can now be written as

$$\frac{d\phi}{dx} = \frac{d\phi_i}{dx}\phi_i + \frac{d\phi_j}{dx}\phi_j + \frac{d\phi_k}{dx}\phi_k \tag{C.6}$$

or

$$\frac{d\phi}{dx} = \left[\frac{4x}{l^2} - \frac{3}{l}\right]\phi_i + \left[\frac{4}{l} - \frac{8}{l^2}\right]\phi_j + \left[\frac{4x}{l^2} - \frac{1}{l}\right]\phi_k \tag{C.7}$$

In matrix form, this is written as

$$g = [\mathbf{B}]\,[\boldsymbol{\phi}] \tag{C.8}$$

The matrix $[\mathbf{B}]$ is given as

$$[\mathbf{B}] = \left[\left(\frac{4x}{l^2} - \frac{3}{l}\right) + \left(\frac{4}{l} - \frac{8}{l^2}\right) + \left(\frac{4x}{l^2} - \frac{1}{l}\right)\right] \tag{C.9}$$

According to Eq. (C.5), $N_i = 1$ at i and 0 at j and k, $N_j = 1$ at j and 0 at i and k, and $N_k = 1$ at k and 0 at i and j. Within an element the summation over the shape functions is equal to unity:

$$\sum_{i=1}^{3} N_i = 1 \tag{C.10}$$

Even though the derivatives of the quadratic element are functions of the independent variable x, they will not be continuous at the inter-element nodes. The type of interpolation used here is known as *Lagrangian*, and it only guarantees the continuity of the function across the inter-element boundaries. These types of elements are known as C^0 *elements*, in which the superscript indicates that only the derivatives of zero order are continuous, that is, the function.

The C^0 shape functions can be determined by using Lagrangian polynomial formulae. The one-dimensional $(n-1)$th order Lagrange interpolation polynomial is the ratio of two products. For an element with n nodes, $(n-1)$ order polynomial, the interpolation function is

$$N_k^e(x) = \prod_{i=1,k\neq i}^{n} \frac{x - x_i}{x_k - x_i} \tag{C.11}$$

C.2. Two-dimensional linear triangular elements

In almost all of the cases that focus on modeling fluid flow and transport phenomena in confined and sometimes irregular geometries, one-dimensional approximations are not sufficient, which makes it necessary to employ multi-dimensional approximations. A triangle is the simplest geometric shape that can be used to approximate irregular surfaces, and it currently finds widespread use in finite element calculations.

The two-dimensional linear triangular element, also known as a *simplex element* (Figure C.1), is represented by [291]

$$\phi x, y = \alpha_1 + \alpha_2 x + \alpha_3 y \tag{C.12}$$

where the polynomial is linear in x and y, and contains three coefficients.

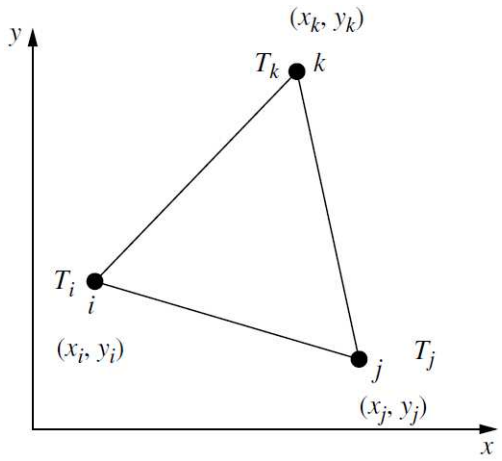

Figure C.1. A linear triangular element [291].

The values of α_1, α_2 and α_3 are determined from

$$\begin{aligned} \phi_i &= \alpha_1 + \alpha_2 x_i + \alpha_3 y_i \\ \phi_j &= \alpha_1 + \alpha_2 x_j + \alpha_3 y_j \\ \phi_k &= \alpha_1 + \alpha_2 x_k + \alpha_3 y_k \end{aligned} \tag{C.13}$$

to be

$$\begin{aligned} \alpha_1 &= \frac{1}{2A}\left[\left(x_j y_k - x_k y_j\right)\phi_i + \left(x_k y_i - x_i y_k\right)\phi_j + \left(x_i y_j - x_j y_i\right)\phi_k\right] \\ \alpha_2 &= \frac{1}{2A}\left[\left(y_j - y_k\right)\phi_i + \left(y_k - y_i\right)\phi_j + \left(y_i - y_j\right)\phi_k\right] \\ \alpha_3 &= \frac{1}{2A}\left[\left(x_k - x_j\right)\phi_i + \left(x_i - x_k\right)\phi_j + \left(x_j - x_i\right)\phi_k\right] \end{aligned} \tag{C.14}$$

where A is the area of the triangle given by

$$2A = \det\begin{bmatrix} 1 & x_i & y_i \\ 1 & x_j & y_j \\ 1 & x_k & y_k \end{bmatrix} = \left(x_i y_j - x_j y_i\right) + \left(x_k y_i - x_i y_k\right) + \left(x_j y_k - x_k y_j\right) \tag{C.15}$$

Substitution of α_1, α_2 and α_3 into Eq. (C.13) gives

$$\phi = N_i\phi_i + N_j\phi_j + N_k\phi_k = \begin{bmatrix} N_i & N_j & N_k \end{bmatrix} \begin{Bmatrix} \phi_i \\ \phi_j \\ \phi_k \end{Bmatrix} \tag{C.16}$$

where

$$\begin{aligned} N_i &= \frac{1}{2A}\left(a_i + b_i x + c_i y\right) \\ N_j &= \frac{1}{2A}\left(a_j + b_j x + c_j y\right) \\ N_k &= \frac{1}{2A}\left(a_k + b_k x + c_k y\right) \end{aligned} \tag{C.17}$$

and

$$\begin{aligned} a_i &= x_j y_k - x_k y_j; \quad b_i = y_j - y_k; \quad c_i = x_k - x_j \\ a_j &= x_k y_i - x_i y_k; \quad b_j = y_k - y_i; \quad c_j = x_i - x_k \\ a_k &= x_i y_j - x_j y_i; \quad b_k = y_i - y_j; \quad c_k = x_j - x_i \end{aligned} \tag{C.18}$$

If N_i is evaluated at node i, where the coordinates are (x_i, y_i),

$$\left(N_i\right)_i = \frac{1}{2A}\left[\left(x_j y_k - x_k y_j\right) + \left(y_j - y_k\right) x_i + \left(x_k - x_j\right) y_i\right] = \frac{2A}{2A} = 1 \tag{C.19}$$

Similarly, $\left(N_j\right)_i = \left(N_k\right)_i = 0$, so it is evident that the shape functions have a value of unity at the designated vertex and zero at all other vertices. It is possible to show that

$$N_i + N_j + N_k = 1 \tag{C.20}$$

The gradients of ϕ are given by

$$\begin{aligned}\frac{\partial \phi}{\partial x} &= \frac{\partial N_i}{\partial x}\phi_i + \frac{\partial N_j}{\partial x}\phi_j + \frac{\partial N_j}{\partial x}\phi_k = \frac{b_i}{2A}\phi_i + \frac{b_j}{2A}\phi_j + \frac{b_k}{2A}\phi_k \\ \frac{\partial \phi}{\partial y} &= \frac{\partial N_i}{\partial y}\phi_i + \frac{\partial N_j}{\partial y}\phi_j + \frac{\partial N_j}{\partial y}\phi_k = \frac{c_i}{2A}\phi_i + \frac{c_j}{2A}\phi_j + \frac{c_k}{2A}\phi_k \end{aligned} \tag{C.21}$$

or

$$\{\mathbf{g}\} = \left\{ \begin{array}{c} \partial\phi/\partial x \\ \partial\phi/\partial y \end{array} \right\} = \frac{1}{2A} \left[\begin{array}{ccc} b_i & b_j & b_k \\ c_i & c_j & c_k \end{array} \right] \left\{ \begin{array}{c} \phi_i \\ \phi_j \\ \phi_k \end{array} \right\} = [\mathbf{B}]\{\boldsymbol{\phi}\} \tag{C.22}$$

APPENDIX D: LIST OF PUBLICATIONS OF MUSTAFA KARAKAYA

D.1. Refereed International Journals

- Karakaya, M. and A. K. Avci, "Testing and Simulation of Syngas Production in a Microchannel Reactor by Autothermal Reforming of Methane", submitted to *Chemical Engineering Journal*.
- Hosukoglu, I., M. Karakaya and A. K. Avci, "Modeling and Simulation of Hydrocracking of Fischer-Tropsch Hydrocarbons", accepted for publication in *Industrial & Engineering Chemistry Research*.
- Karakaya, M., S. Keskin and A. K. Avci, "Parametric Study of Methane Steam Reforming to Syngas in a Catalytic Microchannel Reactor", *Applied Catalysis: A*, Vol. 411 – 412, pp. 114 – 122, 2012.
- Karakaya, M. and A. K. Avci, "Microchannel Reactor Modeling for Combustion Driven Reforming of *iso*-Octane", *International Journal of Hydrogen Energy*, Vol. 36, pp. 6569 – 6577, 2011.
- Avci, A. K., M. Karakaya and D. L. Trimm, "Microreactor Catalytic Combustion for Chemicals Processing", *Catalysis Today*, Vol. 155, pp. 66 – 74, 2010.
- Karakaya, M. and A. K. Avci, "Comparison of Compact Reformer Configurations for On-board Fuel Processing", *International Journal of Hydrogen Energy*, Vol. 35, pp. 2305 – 2316, 2010.
- Karakaya, M. and A. K. Avci, "Simulation of On-board Fuel Conversion in Catalytic Microchannel Reactor-Heat Exchanger Systems", *Topics in Catalysis*, Vol. 52, pp. 2112 – 2116, 2009.
- Aktas, S., M. Karakaya and A. K. Avci, "Thermodynamic Analysis of Steam Assisted Conversions of Bio-oil Components to Synthesis Gas", *International Journal of Hydrogen Energy*, Vol. 34, pp. 1752 – 1759, 2009.
- Karakaya, M., A. K. Avci, A. E. Aksoylu and Z. I. Onsan, "Steady State and Dynamic Modeling of Indirect Partial Oxidation of Methane in a Wall-coated

Microchannel", *Catalysis Today*, Vol. 139, pp. 312 – 321, 2009.

- Örücü, E., M. Karakaya, A. K. Avci, Z. I. Onsan, "Investigation of Ethanol Conversion for Hydrogen Fuel Cells Using Computer Simulations", *Journal of Chemical Technology & Biotechnology*, Vol. 80, pp. 1103 – 1110, 2005.

D.2. International Conferences & Meetings

- Karakaya, M. and A. K. Avci, "Simulation and Testing of Syngas Production in a Heat-exchange Integrated Microchannel Reactor", ISCRE 22 - 22nd International Symposium on Chemical Reaction Engineering, 2−5 September 2012, Maastricht, the Netherlands (Accepted for oral presentation).
- Karakaya, M., E. Simsek, A. K. Avci and Z. I. Onsan, "Oxidative Steam Reforming of Methane in Microchannel Reactors", ISCRE 22 - 22nd International Symposium on Chemical Reaction Engineering, 2−5 September 2012, Maastricht, the Netherlands (Accepted for oral presentation).
- Karakaya, M., E. Simsek, Z. I. Onsan and A. K. Avci, "Microchannel Catalyst Configurations for Oxidative Steam Reforming of Methane to Syngas", 15th International Congress on Catalysis, 1 – 6 July 2012, Munich, Germany (Accepted for poster presentation).
- Karakaya, M. and A. K. Avci, "Investigation of Syngas Production by Oxidative Steam Reforming of Methane in a Microchannel Reactor", IMRET 12 - 12th International Conference on Microreaction Technology, 20 – 22 February 2012, Lyon, France.
- Karakaya, M. and A. K. Avci, "Experimental Investigation of Syngas Production by Methane Steam Reforming in a Microchannel Reactor", EFCATS Summer School, 20 – 23 June 2011, Kerkrade, the Netherlands.
- Karakaya, M. and A. K. Avci, "Synthesis Gas Production by Methane Steam Reforming in a Catalytic Microchannel Reactor", CAMURE-8 & ISMR-7 (Catalysis in Multiphase Reactors and International Symposium on Multifunctional Reactors), 22 – 25 May 2011, Naantali, Finland.
- Kircin, R. M., M. Karakaya, A. K. Avci, A. E. Aksoylu, Z. I. Onsan, "Modeling

of a Catalytic Plate Reactor Producing Hydrogen for Fuel Processor Systems", CHEMREACTOR-19 - 19th International Conference on Chemical Reactors, 5−9 September 2010, Vienna, Austria.

- Karakaya, M. and A. K. Avci, "Comparison of Two Compact Reactor Systems for Hydrogen Production", IMRET 11 - 11th International Conference on Microreaction Technology, 8 − 10 March 2010, Kyoto, Japan.
- Karakaya, M. and A. K. Avci, "Microchannel Reactor Modeling and Design for Catalytic Hydrocarbon Steam Reforming", AIChE 2009 Annual Meeting, 8 − 13 November 2009, Nashville, TN, USA.
- Karakaya, M. and A. K. Avci, "Simulation of On-board Fuel Conversion in Catalytic Microchannel Reactor-Heat Exchanger Systems", CAPoC 8 - 8th International Congress on Catalysis and Automotive Pollution Control, 15 − 17 April 2009, Brussels, Belgium.
- Talay, G., M. Karakaya and A. K. Avci, "Design and Optimization of Micro Reactor-Heat Exchanger Cascade Configurations for Autothermal Conversion of *iso*- Octane to Hydrogen", AIChE 2008 Annual Meeting, 16−21 November 2008, Philadelphia, PA, USA.

REFERENCES

1. Stankiewicz, A. and J. A. Moulijn, "Process Intensification", *Industrial & Engineering Chemistry Research*, Vol. 41, No. 8, pp. 1920–1924, 2002.

2. van Gerven, T. and A. Stankiewicz, "Structure, Energy, Synergy, Times–The Fundamentals of Process Intensification", *Industrial & Engineering Chemistry Research*, Vol. 48, No. 5, pp. 2465–2474, 2009.

3. Stankiewicz, A. I. and J. A. Moulijn, "Process Intensification: Transforming Chemical Engineering", *Chemical Engineering Progress*, Vol. 96, No. 1, pp. 22–34, 2000.

4. Stankiewicz, A. I. and A. A. H. Drinkenburg, "Process Intensification: History, Philosophy, Principles", In: A. I. Stankiewicz and J. A. Moulijn (Eds.), *Re-engineering the chemical processing plant: Process Intensification*, pp. 1–32, Marcel Dekker, New York, 2004.

5. Kockmann, N., "Process Engineering Methods and Microsystem Technology", In: O. Brand, G. K. Fedder, C. Hierold, J. G. Korvink and O. Tabata (Eds.), *Micro Process Engineering*, Advanced Micro & Nanosystems, Vol. 5, pp. 1–46, Wiley-VCH, Weinheim, 2006.

6. Schenk, R., V. Hessel, C. Hofmann, J. Kiss, H. Löwe and A. Ziogas, "Numbering-up of Micro Devices: A First Liquid-Flow Splitting Unit", *Chemical Engineering Journal*, Vol. 101, No. 1-3, pp. 421–429, 2004.

7. Kiwi-Minsker, L. and A. Renken, "Microstructured Reactors for Catalytic Reactions", *Catalysis Today*, Vol. 110, No. 1-2, pp. 2–14, 2005.

8. Kolb, G. and V. Hessel, "Micro-structured Reactors for Gas Phase Reactions", *Chemical Engineering Journal*, Vol. 98, No. 1-2, pp. 1–38, 2004.

9. Horny, C., L. Kiwi-Minsker and A. Renken, "Micro-structured String-Reactor for Autothermal Production of Hydrogen", *Chemical Engineering Journal*, Vol. 101, No. 1-3, pp. 3–9, 2004.

10. Reuse, P., A. Renken, K. Haas-Santo, O. Görke and K. Schubert, "Hydrogen Production for Fuel Cell Application in an Autothermal Micro-channel Reactor", *Chemical Engineering Journal*, Vol. 101, No. 1-3, pp. 133–141, 2004.

11. Tonkovich, A. Y., S. Perry, Y. Wang, D. Qiu, T. LaPlante and W. A. Rogers, "Microchannel Process Technology for Compact Methane Steam Reforming", *Chemical Engineering Science*, Vol. 59, No. 22-23, pp. 4819–4824, 2004.

12. Petrachi, G. A., G. Negro, S. Specchia, G. Saracco, P. L. Maffettone and V. Specchia, "Combining Catalytic Combustion and Steam Reforming in a Novel Multifunctional Reactor for On-board Hydrogen Production from Middle Distillates", *Industrial & Engineering Chemistry Research*, Vol. 44, No. 25, pp. 9422–9430, 2005.

13. Ryi, S. K., J. S. Park, S. H. Choi and S. H. Kim, "Novel Micro Fuel Processor for PEMFCs with Heat Generation by Catalytic Combustion", *Chemical Engineering Journal*, Vol. 113, No. 1, pp. 47–53, 2005.

14. Deshmukh, S. R. and D. G. Vlachos, "CFD Simulations of Coupled, Countercurrent Combustor/Reformer Microdevices for Hydrogen Production", *Industrial & Engineering Chemistry Research*, Vol. 44, No. 14, pp. 4982–4992, 2005.

15. Deshmukh, S. R. and D. G. Vlachos, "Effect of Flow Configuration on the Operation of Coupled Combustor/Reformer Microdevices for Hydrogen Production", *Chemical Engineering Science*, Vol. 60, No. 21, pp. 5718–5728, 2005.

16. Ryi, S. K., J. S. Park, S. H. Choi and S. H. Kim, "Fast Start-up of Microchannel Fuel Processor Integrated with an Igniter for Hydrogen Combustion", *Journal of Power Sources*, Vol. 161, No. 2, pp. 1234–1240, 2006.

17. Kirillov, V. A., S. I. Fadeev, N. A. Kuzin and A. B. Shigarov, "Modeling of a Heat-Coupled Catalytic Reactor with Co-current Oxidation and Conversion Flows", *Chemical Engineering Journal*, Vol. 134, No. 1-3, pp. 131–137, 2007.

18. Horny, C., L. Kiwi-Minsker and A. Renken, "Compact String Reactor for Autothermal Hydrogen Production", *Catalysis Today*, Vol. 120, No. 1, pp. 45–53, 2007.

19. Stefanidis, G. D. and D. G. Vlachos, "Millisecond Methane Steam Reforming via Process and Catalyst Intensification", *Chemical Engineering & Technology*, Vol. 31, No. 8, pp. 1201–1209, 2008.

20. Stefanidis, G. D. and D. G. Vlachos, "High vs. Low Temperature Reforming for Hydrogen Production via Microtechnology", *Chemical Engineering Science*, Vol. 64, No. 23, pp. 4856–4865, 2009.

21. Stefanidis, G. D., D. G. Vlachos, N. S. Kaisare and M. Maestri, "Methane Steam Reforming at Microscales: Operation Strategies for Variable Power Output at Millisecond Contact Times", *AIChE Journal*, Vol. 55, No. 1, pp. 180–191, 2009.

22. Arzamendi, G., P. M. Diéguez, M. Montes, J. A. Odriozola, E. F. Sousa-Aguiar and L. M. Gandía, "Methane Steam Reforming in a Microchannel Reactor for GTL Intensification: A Computational Fluid Dynamics Simulation Study", *Chemical Engineering Journal*, Vol. 154, No. 1-3, pp. 168–173, 2009.

23. Kundu, A., J. H. Jang, H. R. Lee, S. Kim, J. H. Gil, C. R. Jung and Y. S. Oh, "MEMS-based Micro-fuel Processor for Application in a Cell Phone", *Journal of Power Sources*, Vol. 162, No. 1, pp. 572–578, 2006.

24. Seris, E. L. C., G. Abramowitz, A. M. Johnston and B. S. Haynes, "Demonstration Plant for Distributed Production of Hydrogen from Steam Reforming of Methane", *Chemical Engineering Research and Design*, Vol. 83, No. 6, pp. 619–625, 2005.

25. Seris, E. L. C., G. Abramowitz, A. M. Johnston and B. S. Haynes, "Scaleable, Microstructured Plant for Steam Reforming of Methane", *Chemical Engineering Journal*, Vol. 135, No. S1, pp. S9–S16, 2008.

26. Tsuzuki, N., Y. Kato and T. Ishiduka, "High Performance Printed Circuit Heat Exchanger", *Applied Thermal Engineering*, Vol. 27, No. 10, pp. 1702–1707, 2007.

27. Kim, D. E., M. H. Kim, J. E. Cha and S. O. Kim, "Numerical Investigation on Thermal-Hydraulic Performance of New Printed Circuit Heat Exchanger Model", *Nuclear Engineering and Design*, Vol. 238, No. 12, pp. 3269–3276, 2008.

28. Kim, J. H., S. Baek, S. Jeong and J. Jung, "Hydraulic Performance of a Microchannel PCHE", *Applied Thermal Engineering*, Vol. 30, No. 14-15, pp. 2157–2162, 2010.

29. Sadykov, V., V. Sobyanin, N. Mezentseva, G. Alikina, Z. Vostrikov, Y. Fedorova, V. Pelipenko, V. Usoltsev, S. Tikhov, A. Salanov, L. Bobrova, S. Beloshapkin, J. R. H. Ross, O. Smorygo, V. Ulyanitskii and V. Rudnev, "Transformation of CH_4 and Liquid Fuels into Syngas on Monolithic catalysts", *Fuel*, Vol. 89, No. 6, pp. 1230–1240, 2010.

30. Wiles, C. and P. Watts, "Recent Advances in Micro Reaction Technology", *Chemical Communications*, Vol. 47, pp. 6512–6535, 2011.

31. Kandlikar, S. G. and W. J. Grande, "Evolution of Microchannel Flow Passages−Thermohydraulic Performance and Fabrication Technology", *Heat Transfer Engineering*, Vol. 24, No. 1, pp. 3–17, 2003.

32. Mehendale, S. S., A. M. Jacobi and R. K. Shah, "Fluid Flow and Heat Transfer at Micro- and Meso-scales with Applications to Heat Exchanger Design", *Applied Mechanics Review*, Vol. 53, No. 7, pp. 175–193, 2000.

33. Herwig, H., "Momentum and Heat Transfer in Microsized Devices", In: O. Brand,

G. K. Fedder, C. Hierold, J. G. Korvink and O. Tabata (Eds.), *Micro Process Engineering*, Advanced Micro & Nanosystems, Vol. 5, pp. 47–70, Wiley-VCH, Weinheim, 2006.

34. Guo, Z. Y. and Z. X. Li, "Size Effect on Microscale Single-Phase Flow and Heat Transfer", *International Journal of Heat and Mass Transfer*, Vol. 46, No. 1, pp. 149–159, 2003.

35. Tiselj, I., G. Hetsroni, B. Mavko, A. Mosyak, E. Pogrebnyak and Z. Segal, "Effect of Axial Conduction on the Heat Transfer in Micro-channels", *International Journal of Heat and Mass Transfer*, Vol. 47, No. 12-13, pp. 2551–2565, 2004.

36. Hetsroni, G., A. Mosyak, E. Pogrebnyak and L. P. Yarin, "Heat Transfer in Micro-channels: Comparison of Experiments with Theory and Numerical Results", *International Journal of Heat and Mass Transfer*, Vol. 48, No. 25-26, pp. 5580–5601, 2005.

37. Palo, D. R., V. S. Stenkamp, R. A. Dagle and G. N. Jovanovic, "Industrial Applications of Microchannel Process Technology in the United States", In: O. Brand, G. K. Fedder, C. Hierold, J. G. Korvink and O. Tabata (Eds.), *Micro Process Engineering*, Advanced Micro & Nanosystems, Vol. 5, pp. 387–414, Wiley-VCH, Weinheim, 2006.

38. Ehrfeld, W., V. Hessel and H. Löwe, *Microreactors: New Technology for Modern Chemistry*, Wiley-VCH, Mainz, 2000.

39. Alm, B., R. Knitter and J. Haußelt, "Development of a Ceramic Micro Heat Exchanger: Design, Construction, and Testing", *Chemical Engineering & Technology*, Vol. 28, No. 12, pp. 1554–1560, 2005.

40. Brandner, J. J., H. Moritz and W. Pfleging, "Microfabrication in Metals and Polymers", In: O. Brand, G. K. Fedder, C. Hierold, J. G. Korvink and O. Tabata (Eds.), *Micro Process Engineering*, Advanced Micro & Nanosystems, Vol. 5, pp.

267–319, Wiley-VCH, Weinheim, 2006.

41. Jaeger, R. C., *Introduction to Microelectronic Fabrication*, 2nd edition, Prentice Hall, New Jersey, 2002.

42. Pluess, C. and B. K. Paul, "Application of Controlled Thermal Expansion in Microlamination for the Economical Production of Bulk Microchannel Systems", *Chemical Engineering Communications*, Vol. 194, pp. 1259–1270, 2007.

43. Hesselgreaves, J. E., *Compact Heat Exchangers: Selection, Design and Operation*, Elsevier, UK, 2001.

44. Pua, L. M. and S. O. Rumbold, "Industrial Microchannel Devices−Where Are We Today?", In: *Proceedings of the 1st International Conference on Microchannels and Minichannels*, pp. 773–780, American Society of Mechanical Engineers, New York, 2003.

45. Peng, X. F. and G. P. Peterson, "Convective Heat Transfer and Flow Friction for Water Flow in Microchannel Structures", *International Journal of Heat and Mass Transfer*, Vol. 39, No. 12, pp. 2599–2608, 1996.

46. Ravigururajan, T. S. and M. K. Drost, "Single-Phase Flow Thermal Performance Characteristics of a Parallel Microchannel Heat Exchanger", *Journal of Enhanced Heat Transfer*, Vol. 6, No. 5, pp. 383–393, 1999.

47. Celata, G. P., M. Cumo, M. Guglielmi and G. Zummo, "Experimental Investigation of Hydraulic and Single-Phase Heat Transfer in 0.130 mm Capillary Tube", *Microscale Thermophysical Engineering*, Vol. 6, pp. 85–97, 2002.

48. Mala, G. M. and D. Li, "Flow Characteristics of Water in Microtubes", *International Journal of Heat and Fluid Flow*, Vol. 20, No. 2, pp. 142–148, 1999.

49. Lee, P. S., S. V. Garimella and D. Liu, "Investigation of Heat Transfer in Rectan-

gular Microchannels", *International Journal of Heat and Mass Transfer*, Vol. 48, No. 9, pp. 1688–1704, 2005.

50. Judy, J., D. Maynes and B. W. Webb, "Characterization of Frictional Pressure Drop for Liquid Flows through Microchannels", *International Journal of Heat and Mass Transfer*, Vol. 45, No. 17, pp. 3477–3489, 2002.

51. Fan, Y. and L. Luo, "Recent Applications of Advances in Microchannel Heat Exchangers and Multi-Scale Design Optimization", *Heat Transfer Engineering*, Vol. 29, No. 5, pp. 461–474, 2008.

52. Kockmann, N., "Transport Processes and Exchange Equipment", In: O. Brand, G. K. Fedder, C. Hierold, J. G. Korvink and O. Tabata (Eds.), *Micro Process Engineering*, Advanced Micro & Nanosystems, Vol. 5, pp. 71–113, Wiley-VCH, Weinheim, 2006.

53. Bayer, T. and M. Kinzl, "Industrial Applications in Europe", In: O. Brand, G. K. Fedder, C. Hierold, J. G. Korvink and O. Tabata (Eds.), *Micro Process Engineering*, Advanced Micro & Nanosystems, Vol. 5, pp. 415–438, Wiley-VCH, Weinheim, 2006.

54. Quadir, G. A., A. Mydin and K. N. Seetharamu, "Analysis of Microchannel Heat Exchangers Using FEM", *International Journal of Numerical Methods for Heat & Fluid Flow*, Vol. 11, No. 1, pp. 59–75, 2000.

55. Lee, H. W., Y. J. Teng, I. A. Azid and K. N. Seetharamu, "Neuro-genetic Optimization of Micro Compact Heat Exchanger", *International Journal of Numerical Methods for Heat & Fluid Flow*, Vol. 17, No. 1, pp. 20–33, 2007.

56. Luo, L., Y. Fan and D. Tondeur, "Heat Exchanger: From Micro- to Multi-Scale Design Optimization", *International Journal of Energy Research*, Vol. 31, No. 13, pp. 1266–1274, 2007.

57. Foli, K., T. Okabe, M. Olhofer, Y. Jin and B. Sendhoff, "Optimization of Micro Heat Exchanger: CFD, Analytical Approach and Multi-objective Evolutionary Algorithms", *International Journal of Heat and Mass Transfer*, Vol. 49, No. 5-6, pp. 1090–1099, 2006.

58. Tonomura, O., S. Tanaka, M. Noda, M. Kano, S. Hasebe and I. Hashimoto, "CFD-based Optimal Design of Manifold in Plate-fin Microdevices", *Chemical Engineering Journal*, Vol. 101, No. 1-3, pp. 397–402, 2004.

59. Husain, A. and K. Y. Kim, "Optimization of a Microchannel Heat Sink with Temperature Dependent Fluid Properties", *Applied Thermal Engineering*, Vol. 28, No. 8-9, pp. 1101–1107, 2008.

60. Ahmed, S. and M. Krumpelt, "Hydrogen from Hydrocarbon Fuels for Fuel Cells", *International Journal of Hydrogen Energy*, Vol. 26, No. 4, pp. 291–301, 2001.

61. Avci, A. K., *Computational and Experimental Investigation of Catalytic Hydrocarbon Fuel Processing for Autothermal Hydrogen Production*, Ph.D. Thesis, Boğaziçi University, 2003.

62. Onsan, Z. I. and A. K. Avci, "Reactor Design for Fuel Processing", In: D. Shekhawat, J. J. Spivey and D. A. Berry (Eds.), *Fuel Cells: Technologies for Fuel Processing*, pp. 451–516, Elsevier, Amsterdam, 2011.

63. Joensen, F. and J. Rostrup-Nielsen, "Conversion of Hydrocarbons and Alcohols for Fuel Cells", *Journal of Power Sources*, Vol. 105, No. 2, pp. 195–201, 2002.

64. Hickman, D. A. and L. D. Schmidt, "Synthesis Gas Formation by Direct Oxidation of Methane over Pt Monoliths", *Journal of Catalysis*, Vol. 138, No. 3-4, pp. 267–282, 1992.

65. Witt, P. M. and L. D. Schmidt, "Effect of Flow Rate on the Partial Oxidation of Methane and Ethane", *Journal of Catalysis*, Vol. 163, No. 2, pp. 465–475, 1996.

66. Basile, A., S. Fasson, G. Vitulli and E. Drioli, "An Experimental Study of the Partial Oxidation of Methane in a Membrane Reactor", In: A. Parmaliana, D. Sanfilippo, F. Frusteri, A. Vaccari and F. Arena (Eds.), *Natural Gas Conversion V*, Studies in Surface Science and Catalysis, Vol. 119, pp. 453–458, Elsevier, Amsterdam, 1998.

67. Trimm, D. L. and Z. I. Onsan, "Onboard Fuel Conversion for Hydrogen-Fuel-Cell-Driven Vehicles", *Catalysis Reviews: Science and Engineering*, Vol. 43, No. 1-2, pp. 31–84, 2001.

68. Avci, A. K., Z. I. Onsan and D. L. Trimm, "On-board Fuel Conversion for Hydrogen Fuel Cells: Comparison of Different Fuels by Computer Simulations", *Applied Catalysis A: General*, Vol. 216, No. 1-2, pp. 243–256, 2001.

69. Trimm, D. L., "Catalysts for the Control of Coking during Steam Reforming", *Catalysis Today*, Vol. 49, No. 1-3, pp. 3–10, 1999.

70. Avci, A. K., D. L. Trimm and Z. I. Onsan, "Simulation of Alternative Catalyst Bed Configurations in Autothermal Hydrogen Production", *Studies in Surface Science and Catalysis*, Vol. 130, pp. 2753–2758, 2000.

71. Freni, S., G. Calogero and S. Cavallaro, "Hydrogen Production from Methane through Catalytic Partial Oxidation Reactions", *Journal of Power Sources*, Vol. 87, No. 1-2, pp. 28–38, 2000.

72. Aasberg-Petersen, K., J. H. Bak Hansen, T. S. Christensen, I. Dybkjaer, S. Seier Christensen, C. Stub Nielsen, S. E. L. Winter Madsen and J. R. Rostrup-Nielsen, "Technologies for Large-Scale Gas Conversion", *Applied Catalysis A: General*, Vol. 221, No. 1-2, pp. 379–387, 2001.

73. Jamal, Y. and M. L. Wyszynski, "On-board Hydrogen Generation of Hydrogen-Rich Gaseous Fuels—A Review", *International Journal of Hydrogen Energy*, Vol. 19, No. 7, pp. 557–572, 1994.

74. Brown, L. F., "A Comparative Study of Fuels for On-board Hydrogen Production for Fuel-Cell-Powered Automobiles", *International Journal of Hydrogen Energy*, Vol. 26, No. 4, pp. 381–397, 2001.

75. Thomas, C. E., B. D. James, F. D. Lomax Jr. and I. F. Kuhn Jr., "Fuel Options for the Fuel Cell Vehicle: Hydrogen, Methanol or Gasoline?", *International Journal of Hydrogen Energy*, Vol. 25, No. 6, pp. 551–567, 2000.

76. Rostrup-Nielsen, J. R., "Catalytic Steam Reforming", In: J. R. Anderson and M. Boudart (Eds.), *Catalysis, Science & Technology*, Vol. 5, pp. 1–117, Springer-Verlag, Berlin, 1984.

77. Urban, P. M., A. Funke, J. T. Müller, M. Himmen and A. Docter, "Catalytic Processes in Solid Polymer Electrolyte Fuel Cell Systems", *Applied Catalysis A: General*, Vol. 221, No. 1-2, pp. 459–470, 2001.

78. Springmann, S., M. Bohnet, A. Docter, A. Lamm and G. Eigenberger, "Cold Start Simulations of a Gasoline Based Fuel Processor for Mobile Fuel Cell Applications", *Journal of Power Sources*, Vol. 128, No. 1, pp. 13–24, 2004.

79. Mariño, F., M. Boveri, G. Baronetti and M. Laborde, "Hydrogen Production from Steam Reforming of Bioethanol Using Cu/Ni/K/γ-Al_2O_3 Catalysts. Effect of Ni", *International Journal of Hydrogen Energy*, Vol. 26, No. 7, pp. 665–668, 2001.

80. Fatsikostas, A. N. and X. E. Verykios, "Reaction Network of Steam Reforming of Ethanol over Ni-based Catalysts", *Journal of Catalysis*, Vol. 225, No. 2, pp. 439–452, 2004.

81. Akande, A., A. Aboudheir, R. Idem and A. Dalai, "Kinetic Modeling of Hydrogen Production by the Catalytic Reforming of Crude Ethanol over a Co-precipitated Ni-Al_2O_3 Catalyst in a Packed Bed Tubular Reactor", *International Journal of Hydrogen Energy*, Vol. 31, No. 12, pp. 1707–1715, 2006.

82. Vaidya, P. D. and A. E. Rodrigues, "Kinetics of Steam Reforming of Ethanol over a Ru/Al_2O_3 Catalyst", *Industrial & Engineering Chemistry Research*, Vol. 45, No. 19, pp. 6614–6618, 2006.

83. Sahoo, D. R., S. Vajpai, S. Patel and K. K. Pant, "Kinetic Modeling of Steam Reforming of Ethanol for the Production of Hydrogen over Co/Al_2O_3 Catalyst", *Chemical Engineering Journal*, Vol. 125, No. 3, pp. 139–147, 2007.

84. Akpan, E., A. Akande, A. Aboudheir, H. Ibrahim and R. Idem, "Experimental, Kinetic and 2-D reactor Modeling for Simulation of the Production of Hydrogen by the Catalytic Reforming of Concentrated Crude Ethanol (CRCCE) over a Ni-based Commercial Catalyst in a Packed-bed Tubular Reactor", *Chemical Engineering Science*, Vol. 62, No. 12, pp. 3112–3126, 2007.

85. Soyal-Baltacioglu, F., A. E. Aksoylu and Z. I. Onsan, "Steam Reforming of Ethanol over Pt-Ni Catalysts", *Catalysis Today*, Vol. 138, No. 3-4, pp. 183–186, 2008.

86. Mas, V., M. L. Bergamini, G. Baronetti, N. Amadeo and M. Laborde, "A Kinetic Study of Ethanol Steam Reforming Using a Nickel Based Catalyst", *Topics in Catalysis*, Vol. 51, No. 1-4, pp. 39–48, 2008.

87. Görke, O., P. Pfeifer and K. Schubert, "Kinetic Study of Ethanol Reforming in a Microreactor", *Applied Catalysis A: General*, Vol. 360, No. 2, pp. 232–241, 2009.

88. Ciambelli, P., V. Palma and A. Ruggiero, "Low Temperature Catalytic Steam Reforming of Ethanol. 2. Preliminary Kinetic Investigation of Pt/CeO_2 Catalysts", *Applied Catalysis B: Environmental*, Vol. 96, No. 1-2, pp. 190–197, 2010.

89. Lu, P. J., T. S. Chen and J. M. Chern, "Reaction Network and Kinetic Analysis of Ethanol Steam Reforming over a Ru/Al_2O_3 Catalyst", *Catalysis Today*, Vol. 174, No. 1, pp. 17–24, 2011.

90. Peela, N. R. and D. Kunzru, "Steam Reforming of Ethanol in a Microchannel Reactor: Kinetic Study and Reactor Simulation", *Industrial & Engineering Chemistry Research*, Vol. 50, No. 23, pp. 12881–12894, 2011.

91. Llera, I., V. Mas, M. L. Bergamini, M. Laborde and N. Amadeo, "Bio-ethanol Steam Reforming on Ni Based Catalyst. Kinetic Study", *Chemical Engineering Science*, Vol. 71, pp. 356–366, 2012.

92. Garcia, E. and M. Laborde, "Hydrogen Production by the Steam Reforming of Ethanol: Thermodynamic Analysis", *International Journal of Hydrogen Energy*, Vol. 16, No. 5, pp. 307–312, 1991.

93. Ioannides, T., "Thermodynamic Analysis of Ethanol Processors for Fuel Cell Applications", *Journal of Power Sources*, Vol. 92, No. 1-2, pp. 17–25, 2001.

94. Örücü, E., M. Karakaya, A. K. Avci and Z. I. Onsan, "Investigation of Ethanol Conversion for Hydrogen Fuel Cells Using Computer Simulations", *Journal of Chemical Technology & Biotechnology*, Vol. 80, No. 10, pp. 1103–1110, 2005.

95. Armor, J. N., "The Multiple Roles for Catalysis in the Production of H_2", *Applied Catalysis A: General*, Vol. 176, No. 2, pp. 159–176, 1999.

96. Dicks, A. L., "Hydrogen Generation from Natural Gas for the Fuel Cell Systems of Tomorrow", *Journal of Power Sources*, Vol. 61, No. 1-2, pp. 113–124, 1996.

97. Amadeo, N. E. and M. A. Laborde, "Hydrogen Production from the Low-Temperature Water-Gas Shift Reaction: Kinetics and Simulation of the Industrial Reactor", *International Journal of Hydrogen Energy*, Vol. 20, No. 12, pp. 949–956, 1995.

98. Özkara, S. and A. E. Aksoylu, "Selective Low Temperature Carbon Monoxide Oxidation in H_2-rich Gas Streams over Activated Carbon Supported Catalysts", *Applied Catalysis A: General*, Vol. 251, No. 1, pp. 75–83, 2003.

99. İnce, T., G. Uysal, A. N. Akın and R. Yıldırım, "Selective Low-Temperature CO Oxidation over Pt-Co-Ce/Al_2O_3 in Hydrogen-rich Streams", *Applied Catalysis A: General*, Vol. 292, pp. 171–176, 2005.

100. Utaka, T. K., K. Sekizawa and K. Eguchi, "CO Removal by Oxygen-assisted Water Gas Shift Reaction over Supported Cu Catalysts", *Applied Catalysis A: General*, Vol. 194-195, pp. 21–26, 2000.

101. Dalla Beta, R. A. and T. Rostrup-Nielsen, "Application of Catalytic Combustion to a 1.5 MW Industrial Gas Turbine", *Catalysis Today*, Vol. 47, No. 1-4, pp. 369–375, 1999.

102. Finnerty, C., G. A. Tompsett, K. Kendall and R. M. Ormerod, "SOFC System with Integrated Catalytic Fuel Processing", *Journal of Power Sources*, Vol. 86, No. 1-2, pp. 459–463, 2000.

103. Seo, Y. S., S. K. Kang, M. H. Han and Y. S. Baek, "Development of a Catalytic Burner with Pd/NiO Catalysts", *Catalysis Today*, Vol. 47, No. 1-4, pp. 421–427, 1999.

104. Trimm, D. L., "Catalytic Combustion", *Applied Catalysis A: General*, Vol. 7, No. 3, pp. 249–282, 1983.

105. Jiang, C., *Studies of the Production of Hydrogen from Methanol Steam Reforming at Low Temperatures*, Ph.D. Thesis, University of New South Wales, 1992.

106. Jiang, C., D. L. Trimm and M. S. Wainwright, "New Technology for Hydrogen Production by the Catalytic Oxidation and Steam Reforming of Methanol at Low Temperatures", *Chemical Engineering & Technology*, Vol. 18, No. 1, pp. 1–6, 1995.

107. Ma, L., D. L. Trimm and C. Jiang, "The Design and Testing of an Autothermal Reactor for the Conversion of Light Hydrocarbons to Hydrogen I. The Kinetics of the Catalytic Oxidation of Light Hydrocarbons", *Applied Catalysis A: General*,

Vol. 138, No. 2, pp. 275–283, 1996.

108. Aryafar, M. and F. Zaera, "Kinetic Study of the Catalytic Oxidation of Alkanes over Nickel, Palladium and Platinum Foils", *Catalysis Letters*, Vol. 48, No. 3-4, pp. 173–183, 1997.

109. Burch, R., D. J. Crittle and M. J. Hayes, "C−H Bond Activation in Hydrocarbon Oxidation on Heterogeneous Catalysts", *Catalysis Today*, Vol. 47, No. 1, pp. 229–234, 1999.

110. Ciaparu, D. and L. Pfefferle, "Methane Combustion Activity of Supported Palladium Catalysts After Partial Reduction", *Applied Catalysis A: General*, Vol. 218, No. 1-2, pp. 369–375, 2001.

111. Lee, J. H., D. L. Trimm and N. W. Cant, "The Catalytic Combustion of Methane and Hydrogen Sulphide", *Catalysis Today*, Vol. 47, No. 1-4, pp. 353–357, 1999.

112. Trimm, D. L. and C. W. Lam, "The Combustion of Methane on Platinum-alumina Fibre Catalysts", *Chemical Engineering Science*, Vol. 35, No. 6, pp. 1405–1413, 1980.

113. Veser, G. and L. D. Schmidt, "Ignition and Extinction in the Catalytic Oxidation of Hydrocarbons over Platinum", *AIChE Journal*, Vol. 42, No. 4, pp. 1077–1087, 1996.

114. Hicks, R. F., H. Qi, M. L. Young and R. G. Lee, "Effect of Catalyst Structure on Methane Oxidation over Palladium on Alumina", *Journal of Catalysis*, Vol. 122, No. 2, pp. 295–306, 1990.

115. Otto, K., J. M. Andino and C. L. Parks, "The Influence of Platinum Concentration and Particle Size on the Kinetics of Propane Oxidation over Pt/γ-alumina", *Journal of Catalysis*, Vol. 131, No. 1, pp. 243–251, 1991.

116. Ma, L., *Hydrogen Production from Steam Reforming of Light Hydrocarbons in an Autothermic System*, Ph.D. Thesis, University of New South Wales, 1995.

117. Bui, P. A., D. G. Vlachos and P. R. Westmoreland, "Catalytic Ignition of Methane/Oxygen Mixtures over Platinum Surfaces: Comparison of Detailed Simulations and Experiments", *Surface Science*, Vol. 385, No. 2-3, pp. 1029–1034, 1997.

118. Veser, G., M. Ziauddin and L. D. Schmidt, "Ignition in Alkane Oxidation on Noble-metal Catalysts", *Catalysis Today*, Vol. 47, No. 1-4, pp. 219–228, 1999.

119. Ma, L. and D. L. Trimm, "Alternative Catalyst Bed Configurations for the Autothermic Conversion of Methane to Hydrogen", *Applied Catalysis A: General*, Vol. 138, No. 2, pp. 265–273, 1996.

120. Opoku-Gyamfi, K. and A. A. Adesina, "Kinetic Studies of CH_4 Oxidation over Pt-NiOδ-Al_2O_3 in a Fluidised Bed Reactor", *Applied Catalysis A: General*, Vol. 180, No. 1, pp. 113–122, 1999.

121. Rostrup-Nielsen, J. R. and I. Alstrup, "Innovation and Science in the Process Industry. Steam Reforming and Hydrogenolysis", *Catalysis Today*, Vol. 53, No. 3, pp. 311–316, 1999.

122. Kvamsdal, H. M., H. F. Svendsen, T. Hertzberg and O. Olsvik, "Dynamic Simulation and Optimization of a Catalytic Steam Reformer", *Chemical Engineering Science*, Vol. 54, No. 13, pp. 2697–2706, 1999.

123. Rostrup-Nielsen, J. R., J. Sehested and J. K. Nørskov, "Hydrogen and Synthesis Gas by Steam- and CO_2 reforming", *Advances in Catalysis*, Vol. 47, pp. 65–139, 2002.

124. Rostrup-Nielsen, J. R. and J. H. Bak Hansen, "CO_2-reforming of Methane over Transition Metals", *Journal of Catalysis*, Vol. 144, No. 1, pp. 38–49, 1993.

125. Borowiecki, T., A. Golebiowski and B. Stasinska, "Effects of Small MoO_3 Additions on the Properties of Nickel Catalysts for the Steam Reforming of Hydrocarbons", *Applied Catalysis A: General*, Vol. 153, No. 1-2, pp. 141–156, 1997.

126. Horiuchi, T., K. Sakuma, T. Fukui, Y. Kubo, T. Osaki and T. Mori, "Supression of Carbon Deposition in the CO_2-reforming of CH_4 by Adding Basic Metal Oxides to a Ni/Al_2O_3 Catalyst", *Applied Catalysis A: General*, Vol. 144, No. 1-2, pp. 111–120, 1996.

127. Jeong, J. H., J. W. Lee, D. J. Seo, Y. Seo, W. L. Yoon, D. K. Lee and D. H. Kim, "Ru-doped Ni Catalysts Effective for the Steam Reforming of Methane without the Pre-reduction Treatment with H_2", *Applied Catalysis A: General*, Vol. 302, No. 2, pp. 151–156, 2006.

128. Li, D., T. Shishido, Y. Oumi, T. Sano and K. Takehira, "Self-Activation and Self-Regenerative Activity of Trace Rh-doped Ni/Mg(Al)O Catalysts in Steam Reforming of Methane", *Applied Catalysis A: General*, Vol. 332, No. 1, pp. 98–109, 2007.

129. Li, D., K. Nishida, Y. Zhan, T. Shishido, Y. Oumi, T. Sano and K. Takehira, "Superior Catalytic Behavior of Trace Pt-doped Ni/Mg(Al)O in Methane Reforming under Daily Start-up and Shut-down Operation", *Applied Catalysis A: General*, Vol. 350, No. 2, pp. 225–236, 2008.

130. Yamazaki, O., K. Tomishige and K. Fujimoto, "Development of Highly Stable Nickel Catalyst for Methane-Steam Reaction under Low Steam to Carbon Ratio", *Applied Catalysis A: General*, Vol. 136, No. 1, pp. 49–56, 1996.

131. Bradford, M. C. J. and M. A. Vannice, "Catalytic Reforming of Methane with Carbon Dioxide over Nickel Catalysts. II. Reaction Kinetics", *Applied Catalysis A: General*, Vol. 142, No. 1, pp. 97–122, 1996.

132. Takano, A., T. Tagawa and S. Goto, "Carbon Dioxide Reforming of Methane on

Supported Nickel Catalysts", *Journal of Chemical Engineering of Japan*, Vol. 27, No. 6, pp. 727–731, 1994.

133. Elnashaie, S. S. E. H., A. M. Adris, A. S. Al-Ubaid and M. A. Soliman, "On the Non-Monotonic Behaviour of Methane Steam Reforming Kinetics", *Chemical Engineering Science*, Vol. 45, No. 2, pp. 491–501, 1990.

134. Xu, J. and G. F. Froment, "Methane Steam Reforming, Methanation and Water Gas Shift. I. Intrinsic Kinetics", *AIChE Journal*, Vol. 35, No. 1, pp. 88–96, 1989.

135. Xu, J. and G. F. Froment, "Methane Steam Reforming, Methanation and Water Gas Shift. II. Diffusional Limitations and Reactor Simulation", *AIChE Journal*, Vol. 35, No. 1, pp. 97–103, 1989.

136. Numaguchi, T. and K. Kikuchi, "Intrinsic Kinetics and Design Simulation in a Complex Reaction Network: Steam-Methane Reforming", *Chemical Engineering Science*, Vol. 43, No. 8, pp. 2295–2301, 1988.

137. de Smet, C. R. H., M. H. J. M. de Croon, R. J. Berger, G. B. Marin and J. C. Schouten, "Design of Adiabatic Fixed-Bed Reactors for the Partial Oxidation of Methane to Synthesis Gas. Application to Production of Methanol and Hydrogen-for-fuel-cells", *Chemical Engineering Science*, Vol. 56, No. 16, pp. 4849–4861, 2001.

138. Pena, M. A., J. P. Gomez and J. L. G. Fierro, "New Catalytic Routes for Syngas and Hydrogen Production", *Applied Catalysis A: General*, Vol. 144, No. 1-2, pp. 7–57, 1996.

139. Bharadwaj, S. S. and L. D. Schmidt, "Catalytic Partial Oxidation of Natural Gas to Syngas", *Fuel Processing Technology*, Vol. 42, No. 2-3, pp. 109–127, 1995.

140. Spath, P. L. and D. C. Dayton, *Technical and Economic Assessment of Synthesis Gas to Fuels and Chemicals with Emphasis on the Potential for Biomass-derived*

Syngas, Tech. Rep. NREL/TP-510-34929, National Renewable Energy Laboratory, 2003.

141. Dissanayake, D., M. P. Rosynek, K. C. C. Kharas and J. H. Lunsford, "Partial Oxidation of Methane to Carbon Monoxide and Hydrogen over a Ni/Al_2O_3 Catalyst", *Journal of Catalysis*, Vol. 132, No. 1, pp. 117–127, 1991.

142. Mukainakano, Y., B. Li, S. Kado, T. Miyazawa, K. Okumura, T. Miyao, S. Naito, K. Kunimori and K. Tomishige, "Surface Modification of Ni Catalysts with Trace Pd and Rh for Oxidative Steam Reforming of Methane", *Applied Catalysis A: General*, Vol. 318, pp. 252–264, 2007.

143. Tomishige, K., "Oxidative Steam Reforming of Methane over Ni Catalysts Modified with Noble Metals", *Journal of the Japan Petroleum Institute*, Vol. 50, No. 6, pp. 287–298, 2007.

144. Tomishige, K., S. Kanazawa, K. Suzuki, M. Asadullah, M. Sato, K. Ikushima and K. Kunimori, "Effective Heat Supply from Combustion to Reforming in Methane Reforming with CO_2 and O_2: Comparison between Ni and Pt Catalysts", *Applied Catalysis A: General*, Vol. 233, No. 1, pp. 35–44, 2002.

145. Li, B., K. Maruyama, M. Nurunnabi, K. Kunimori and K. Tomishige, "Temperature Profiles of Alumina-supported Noble Metal Catalysts in Autothermal Reforming of Methane", *Applied Catalysis A: General*, Vol. 275, No. 1-2, pp. 157–172, 2004.

146. Karakaya, M. and A. K. Avci, "Parametric Study of Methane Steam Reforming to Syngas in a Catalytic Microchannel Reactor", *Applied Catalysis A: General*, Vol. 411-412, pp. 114–122, 2012.

147. Li, B., S. Kado, Y. Mukainakano, M. Nurunnabi, T. Miyao, S. Naito, K. Kunimori and K. Tomishige, "Temperature Profile of Catalyst Bed during Oxidative Steam Reforming of Methane over Pt-Ni Bimetallic Catalysts", *Applied Catalysis A:*

General, Vol. 304, pp. 62–71, 2006.

148. Li, B., S. Kado, Y. Mukainakano, T. Miyazawa, T. Miyao, S. Naito, K. Okumura, K. Kunimori and K. Tomishige, "Surface Modification of Ni Catalysts with Trace Pt for Oxidative Steam Reforming of Methane", *Journal of Catalysis*, Vol. 245, No. 1, pp. 144–155, 2007.

149. Li, D., Y. Nakagawa and K. Tomishige, "Methane Reforming to Synthesis Gas over Ni Catalysts Modified with Noble Metals", *Applied Catalysis A: General*, Vol. 408, No. 1-2, pp. 1–24, 2011.

150. Mukainakano, Y., K. Yoshida, K. Okumura, K. Kunimori and K. Tomishige, "Catalytic Performance and Characterization of Pt-Ni Bimetallic Catalysts for Oxidative Steam Reforming of Methane", *Chemical Engineering Science*, Vol. 63, No. 20, pp. 4891–4901, 2008.

151. Nurunnabi, M., Y. Mukainakano, S. Kado, T. Miyazawa, K. Okumura, T. Miyao, S. Naito, K. Suzuki, K. Fujimoto, K. Kunimori and K. Tomishige, "Oxidative Steam Reforming of Methane under Atmospheric and Pressurized Conditions over Pd/NiO-MgO Solid Solution Catalysts", *Applied Catalysis A: General*, Vol. 308, pp. 1–12, 2006.

152. Parizotto, N. V., D. Zanchet, K. O. Rocha, C. M. P. Marques and J. M. C. Bueno, "The Effects of Pt Promotion on the Oxi-reduction Properties of Alumina Supported Nickel Catalysts for Oxidative Steam-reforming of Methane: Temperature-resolved XAFS Analysis", *Applied Catalysis A: General*, Vol. 366, No. 1, pp. 122–129, 2009.

153. Yoshida, K., K. Okumura, T. Miyao, S. Naito, S. Ito, K. Kunimori and K. Tomishige, "Oxidative Steam Reforming of Methane over Ni/α-Al_2O_3 Modified with Trace Pd", *Applied Catalysis A: General*, Vol. 351, No. 2, pp. 217–225, 2008.

154. Yoshida, K., N. Begum, S. Ito and K. Tomishige, "Oxidative Steam Reforming of Methane over Ni/α-Al_2O_3 Modified with Trace Noble Metals", *Applied Catalysis A: General*, Vol. 358, No. 2, pp. 186–192, 2009.

155. Hickman, D. A. and L. D. Schmidt, "Production of Syngas by Direct Catalytic Partial Oxidation of Methane", *Science*, Vol. 259, pp. 343–346, 1993.

156. Boucouvalas, Y., Z. L. Zhang and X. E. Verykios, "Partial Oxidation of Methane to Synthesis Gas via the Direct Reaction Scheme over Ru/TiO_2 Catalyst", *Catalysis Letters*, Vol. 40, No. 3-4, pp. 189–195, 1996.

157. Jin, R., Y. Chen, W. Li, W. Cui, Y. Ji, C. Yu and Y. Jiang, "Mechanism for Catalytic Partial Oxidation of Methane to Syngas over a Ni/Al_2O_3 Catalyst", *Applied Catalysis A: General*, Vol. 201, No. 1, pp. 71–80, 2000.

158. Avci, A. K., D. L. Trimm and Z. I. Onsan, "Heterogeneous Reactor Modeling for Simulation of Catalytic Oxidation and Steam Reforming of Methane", *Chemical Engineering Science*, Vol. 56, No. 2, pp. 641–649, 2001.

159. Avci, A. K., D. L. Trimm and Z. I. Onsan, "Quantitative Investigation of Catalytic Natural Gas Conversion for Hydrogen Fuel Cell Applications", *Chemical Engineering Journal*, Vol. 90, No. 1-2, pp. 77–87, 2002.

160. Bartholomew, C. H., "Mechanisms of Catalyst Deactivation", *Applied Catalysis A: General*, Vol. 212, No. 1-2, pp. 17–60, 2001.

161. Rostrup-Nielsen, J. R., "Industrial Relevance of Coking", *Catalysis Today*, Vol. 37, No. 3, pp. 225–232, 1997.

162. Rostrup-Nielsen, J. R., "New Aspects of Syngas Production and Use", *Catalysis Today*, Vol. 63, No. 2, pp. 159–164, 2000.

163. Thevenin, P. O., A. G. Ersson, H. M. J. Kusar, P. G. Menon and S. G. Jaras,

"Deactivation of High Temperature Combustion Catalysts", *Applied Catalysis A: General*, Vol. 212, No. 1-2, pp. 189–197, 2001.

164. Trimm, D. L., *Design of Industrial Catalysts*, Elsevier, Amsterdam, 1980.

165. Arai, H. and M. Machida, "Thermal Stabilization of Catalyst Supports and Their Application to High-Temperature Catalytic Combustion", *Applied Catalysis A: General*, Vol. 138, No. 2, pp. 161–176, 1996.

166. van der Laan, G. and A. A. C. M. Beenackers, "Kinetics and Selectivity of the Fischer–Tropsch Synthesis: A Literature Review", *Catalysis Reviews: Science and Engineering*, Vol. 41, No. 3-4, pp. 255–318, 1999.

167. Schulz, H., "Short History and Present Trends of Fischer-Tropsch Synthesis", *Applied Catalysis A: General*, Vol. 186, No. 1-2, pp. 3–12, 1999.

168. Schulz, H. and M. Claeys, "Kinetic Modelling of Fischer-Tropsch Product Distributions", *Applied Catalysis A: General*, Vol. 186, No. 1-2, pp. 91–107, 1999.

169. Yang, J., Y. Liu, J. Chang, Y. N. Wang, L. Bai, Y. Y. Xu, H. W. Xiang, Y. W. Li and B. Zhong, "Detailed Kinetics of Fischer-Tropsch Synthesis on an Industrial Fe-Mn Catalyst", *Industrial & Engineering Chemistry Research*, Vol. 42, No. 21, pp. 5066–5090, 2003.

170. Steynberg, A. P., "Introduction to Fischer-Tropsch Technology", In: A. P. Steynberg and M. Dry (Eds.), *Fischer-Tropsch Technology*, Studies in Surface Science and Catalysis, Vol. 152, pp. 1–63, Elsevier, UK, 2004.

171. Lox, E. S. and G. F. Froment, "Kinetics of the Fischer-Tropsch Reaction on a Precipitated Promoted Iron Catalyst. 1. Experimental Procedure and Results", *Industrial & Engineering Chemistry Research*, Vol. 32, No. 1, pp. 61–70, 1993.

172. van der Laan, G. and A. A. C. M. Beenackers, "Hydrocarbon Selectivity Model

for the Gas-Solid Fischer-Tropsch Synthesis on Precipitated Iron Catalysts", *Industrial & Engineering Chemistry Research*, Vol. 38, No. 4, pp. 1277–1290, 1999.

173. Wang, Y. N., W. P. Ma, Y. J. Lu, J. Yang, Y. Y. Xu, H. W. Xiang, Y. W. Li, Y. L. Zhao and B. J. Zhang, "Kinetics Modelling of Fischer-Tropsch Synthesis over an Industrial Fe-Cu-K Catalyst", *Fuel*, Vol. 82, No. 2, pp. 195–213, 2003.

174. Dry, M. E., "Fischer-Tropsch Reactions and the Environment", *Applied Catalysis A: General*, Vol. 189, No. 2, pp. 185–190, 1999.

175. Fox III, J. M., "The Different Catalytic Routes for Methane Valorization: An Assessment of Processes for Liquid Fuels", *Catalysis Reviews: Science and Engineering*, Vol. 35, No. 2, pp. 169–212, 1993.

176. Gregor, J. H., "Fischer-Tropsch Products as Liquid Fuels or Chemicals: An Economic Evaluation", *Catalysis Letters*, Vol. 7, No. 1-4, pp. 317–332, 1990.

177. Dry, M. E., "The Fischer-Tropsch Process: 1950−2000", *Catalysis Today*, Vol. 71, No. 3-4, pp. 227–241, 2002.

178. Dancuart, L. P., R. de Haan and A. de Klerk, "Processing of Primary Fischer-Tropsch Products", In: A. P. Steynberg and M. Dry (Eds.), *Fischer-Tropsch Technology*, Studies in Surface Science and Catalysis, Vol. 152, pp. 482–532, Elsevier, UK, 2004.

179. Dry, M. E. and A. P. Steynberg, "Commercial FT Process Applications", In: A. P. Steynberg and M. E. Dry (Eds.), *Fischer-Tropsch Technology*, Studies in Surface Science and Catalysis, Vol. 152, pp. 406–481, Elsevier, UK, 2004.

180. Lu, Y. and T. Lee, "Influence of the Feed Gas Composition on the Fischer-Tropsch Synthesis in Commercial Operations", *Journal of Natural Gas Chemistry*, Vol. 16, No. 4, pp. 329–341, 2007.

181. Donnelly, T. J. and C. N. Satterfield, "Product Distributions of the Fischer-Tropsch Synthesis on Precipitated Iron Catalysts", *Applied Catalysis A: General*, Vol. 52, No. 1, pp. 93–114, 1989.

182. Ji, Y., H. W. Xiang, J. L. Yang, Y. Y. Xu, Y. W. Li and B. Zhong, "Effect of Reaction Conditions on the Product Distribution during Fischer-Tropsch Synthesis over an Industrial Fe-Mn Catalyst", *Applied Catalysis A: General*, Vol. 214, No. 1, pp. 77–86, 2001.

183. Wang, Y., B. R. Johnson, J. Cao, Y. Chin, R. T. Rozmiarek, Y. Gao and A. L. Tonkovich, "Engineered Catalysts for Microchannel Reactor Applications", In: Y. Wang and J. D. Holladay (Eds.), *Microreactor Technology and Process Intensification*, ACS Symposium Series, Vol. 914, pp. 102–118, American Chemical Society, Washington, D.C., 2005.

184. Enger, B. C., J. Walmsley, E. Bjørgum, R. Lødeng, P. Pfeifer, K. Schubert, A. Holmen and H. J. Venvik, "Performance and SEM Characterization of Rh Impregnated Microchannel Reactors in the Catalytic Partial Oxidation of Methane and Propane", *Chemical Engineering Journal*, Vol. 144, No. 3, pp. 489–501, 2008.

185. Ryu, J., K. Lee, H. La, H. Kim, J. Yang and H. Jung, "Ni Catalyst Wash-coated on Metal Monolith with Enhanced Heat-transfer Capability for Steam Reforming", *Journal of Power Sources*, Vol. 171, No. 2, pp. 499–505, 2007.

186. Wang, Y., Y. H. Chin, R. T. Rozmiarek, B. R. Johnson, Y. Gao, J. Watson, A. Y. L. Tonkovich and D. P. Vander Wiel, "Highly Active and Stable Rh/MgO-Al_2O_3 Catalysts for Methane Steam Reforming", *Catalysis Today*, Vol. 98, No. 4, pp. 575–581, 2004.

187. Tonkovich, A. L. Y., B. Yang, S. T. Perry, S. P. Fitzgerald and Y. Wang, "From Seconds to Milliseconds to Microseconds through Tailored Microchannel Reactor Design of a Steam Methane Reformer", *Catalysis Today*, Vol. 120, No. 1, pp. 21–29, 2007.

188. Izquierdo, U., V. L. Barrio, J. F. Cambra, J. Requies, M. B. Güemez, P. L. Arias, G. Kolb, R. Zapf, A. M. Gutiérrez and J. R. Arraibi, "Hydrogen Production from Methane and Natural Gas Steam Reforming in Conventional and Microreactor Reaction Systems", *International Journal of Hydrogen Energy*, Vol. 37, No. 8, pp. 7026–7033, 2012.

189. Wichert, M., Y. Men, M. O'Connell, D. Tiemann, R. Zapf, G. Kolb, S. Butschek, R. Frank and A. Schiegl, "Self-sustained Operation and Durability Testing of a 300 W-class Micro-structured LPG Fuel Processor", *International Journal of Hydrogen Energy*, Vol. 36, No. 5, pp. 3496–3504, 2011.

190. Thormann, J., P. Pfeifer, K. Schubert and U. Kunz, "Reforming of Diesel Fuel in a Micro Reactor for APU Systems", *Chemical Engineering Journal*, Vol. 135, No. S1, pp. S74–S81, 2008.

191. Gawade, P. V., D. Patel, G. G. Lipscomb and M. A. Abraham, "Kinetics and Modeling of the Flexible Fuel Reformer: *n*-Hexadecane Steam Reforming and Combustion", *Industrial & Engineering Chemistry Research*, Vol. 49, No. 15, pp. 6931–6940, 2010.

192. Grote, M., M. Maximini, Z. Yang, P. Engelhardt, H. Köhne, K. Lucka and M. Brenner, "Experimental and Computational Investigations of a Compact Steam Reformer for Fuel Oil and Diesel Fuel", *Journal of Power Sources*, Vol. 196, No. 21, pp. 9027–9035, 2011.

193. Aartun, I., B. Silberova, H. Venvik, P. Pfeifer, O. Görke, K. Schubert and A. Holmen, "Hydrogen Production from Propane in Rh-Impregnated Metallic Microchannel Reactors and Alumina Foams", *Catalysis Today*, Vol. 105, No. 3-4, pp. 469–478, 2005.

194. Fichtner, M., J. Mayer, D. Wolf and K. Schubert, "Microstructured Rhodium Catalysts for the Partial Oxidation of Methane to Syngas under Pressure", *Industrial & Engineering Chemistry Research*, Vol. 40, No. 16, pp. 3475–3483, 2001.

195. Younes-Metzler, O., J. Svagin, S. Jensen, C. H. Christensen, O. Hansen and U. Quaade, "Microfabricated High-Temperature Reactor for Catalytic Partial Oxidation of Methane", *Applied Catalysis A: General*, Vol. 284, No. 1-2, pp. 5–10, 2005.

196. Makarshin, L. L., D. V. Andreev, A. G. Gribovskyi and V. N. Parmon, "Catalytic Partial Oxidation of Methane in Microchannel Reactors with Co-current and Countercurrent Reagent Flows: An Experimental Comparison", *Chemical Engineering Journal*, Vol. 178, pp. 276–281, 2011.

197. Bae, J. M., S. Ahmed, R. Kumar and E. Doss, "Microchannel Development for Autothermal Reforming of Hydrocarbon Fuels", *Journal of Power Sources*, Vol. 139, No. 1-2, pp. 91–95, 2005.

198. Chen, G., S. Li and Q. Yuan, "Pd-Zn/Cu-Zn-Al Catalysts Prepared for Methanol Oxidation Reforming in Microchannel Reactors", *Catalysis Today*, Vol. 120, No. 1, pp. 63–70, 2007.

199. Peela, N. R. and D. Kunzru, "Oxidative Steam Reforming of Ethanol over Rh Based Catalysts in a Micro-channel Reactor", *International Journal of Hydrogen Energy*, Vol. 36, No. 5, pp. 3384–3396, 2011.

200. Johnson, B. R., N. L. Canfield, D. N. Tran, R. A. Dagle, X. S. Li, J. D. Holladay and Y. Wang, "Engineered SMR Catalysts Based on Hydrothermally Stable, Porous, Ceramic Supports for Microchannel Reactors", *Catalysis Today*, Vol. 120, No. 1, pp. 54–62, 2007.

201. Zhai, X., S. Ding, Z. Liu, Y. Jin and Y. Cheng, "Catalytic Performance of Ni Catalysts for Steam Reforming of Methane at High Space Velocity", *International Journal of Hydrogen Energy*, Vol. 36, No. 1, pp. 482–489, 2011.

202. Aartun, I., H. Venvik, A. Holmen, P. Pfeifer, O. Görke and K. Schubert, "Temperature Profiles and Residence Time Effects during Catalytic Partial Oxidation

and Oxidative Steam Reforming of Propane in Metallic Microchannel Reactors", *Catalysis Today*, Vol. 110, No. 1-2, pp. 98–107, 2005.

203. Pennemann, H., V. Hessel, G. Kolb, H. Löwe and R. Zapf, "Partial Oxidation of Propane Using Micro Structured Reactors", *Chemical Engineering Journal*, Vol. 135, No. S1, pp. S66–S73, 2008.

204. Park, G. G., S. D. Yim, Y. G. Yoon, C. S. Kim, D. J. Seo and K. Eguchi, "Hydrogen Production with Integrated Microchannel Fuel Processor Using Methanol for Portable Fuel Cell Systems", *Catalysis Today*, Vol. 110, No. 1-2, pp. 108–113, 2005.

205. Men, Y., G. Kolb, R. Zapf, D. Tiemann, M. Wichert, V. Hessel and H. Löwe, "A Complete Miniaturized Microstructured Methanol Fuel Processor/Fuel Cell System for Low Power Applications", *International Journal of Hydrogen Energy*, Vol. 33, No. 4, pp. 1374–1382, 2008.

206. Xinhai, Y., S. Tung, W. Zhendong and H. Huajiang, "Investigation on Methanol Steam Reforming in a Microchannel Reactor by Experiments and Mathematical Model Analysis", *International Journal of Green Energy*, Vol. 5, pp. 281–296, 2008.

207. Cao, C., Y. Wang and R. T. Rozmiarek, "Heterogeneous Reactor Model for Steam Reforming of Methane in a Microchannel Reactor with Microstructured Catalysts", *Catalysis Today*, Vol. 110, No. 1-2, pp. 92–97, 2005.

208. Stutz, M. J., N. Hotz and D. Poulikakos, "Optimization of Methane Reforming in a Microreactor−Effects of Catalyst Loading and Geometry", *Chemical Engineering Science*, Vol. 61, No. 12, pp. 4027–4040, 2006.

209. Stutz, M. J. and D. Poulikakos, "Optimum Washcoat Thickness of a Monolith Reactor for Syngas Production by Partial Oxidation of Methane", *Chemical Engineering Science*, Vol. 63, No. 7, pp. 1761–1770, 2008.

210. Thormann, J., L. Maier, P. Pfeifer, U. Kunz, O. Deutschmann and K. Schubert, "Steam Reforming of Hexadecane over a Rh/CeO_2 Catalyst in Microchannels: Experimental and Numerical Investigation", *International Journal of Hydrogen Energy*, Vol. 34, No. 12, pp. 5108–5120, 2009.

211. Gonzo, E. E., "Hydrogen from Methanol-Steam Reforming. Isothermal and Adiabatic Monolith Reactors' Simulation", *International Journal of Hydrogen Energy*, Vol. 33, No. 13, pp. 3511–3516, 2008.

212. Chen, F., M. Chang, C. Kuo, C. Hsueh and W. Yan, "Analysis of a Plate-Type Microreformer for Methanol Steam Reforming Reaction", *Energy & Fuels*, Vol. 23, No. 10, pp. 5092–5098, 2009.

213. Hsueh, C., H. Chu and W. Yan, "Numerical Study on Micro-reformer Performance and Local Transport Phenomena of the Plate Methanol Steam Micro-reformer", *Journal of Power Sources*, Vol. 187, No. 2, pp. 535–543, 2009.

214. Hsueh, C., H. Chu, W. Yan, C. Chen and M. Chang, "Numerical Study of Heat and Mass Transfer in the Plate Methanol Steam Micro-reformer Channels", *Applied Thermal Engineering*, Vol. 30, No. 11-12, pp. 1426–1437, 2010.

215. Jang, J., Y. Huang and C. Cheng, "The Effects of Geometric and Operating Conditions on the Hydrogen Production Performance of a Micro-methanol Steam Reformer", *Chemical Engineering Science*, Vol. 65, No. 20, pp. 5495–5506, 2010.

216. Chein, R., Y. Chen and J. N. Chung, "Thermal Resistance Effect on Methanol-Steam Reforming Performance in Micro-scale Reformers", *International Journal of Hydrogen Energy*, Vol. 37, No. 1, pp. 250–262, 2012.

217. Chein, R., Y. Chen and J. N. Chung, "Axial Heat Conduction and Heat Supply Effects on Methanol-Steam Reforming Performance in Micro-scale Reformers", *International Journal of Heat and Mass Transfer*, Vol. 55, No. 11-12, pp. 3029–3042, 2012.

218. Hao, Y., X. Du, L. Yang, Y. Shen and Y. Yang, "Numerical Simulation of Configuration and Catalyst-layer Effects on Micro-channel Steam Reforming of Methanol", *International Journal of Hydrogen Energy*, Vol. 36, No. 24, pp. 15611–15621, 2011.

219. Ni, M., D. Y. C. Leung and M. K. H. Leung, "A Review on Reforming Bio-ethanol for Hydrogen Production", *International Journal of Hydrogen Energy*, Vol. 32, No. 15, pp. 3238–3247, 2007.

220. Rass-Hansen, J., R. Johansson, M. Møller and C. H. Christensen, "Steam Reforming of Technical Bioethanol for Hydrogen Production", *International Journal of Hydrogen Energy*, Vol. 33, No. 17, pp. 4547–4554, 2008.

221. Uriz, I., G. Arzamendi, E. López, J. Llorca and L. M. Gandía, "Computational Fluid Dynamics Simulation of Ethanol Steam Reforming in Catalytic Wall Microchannels", *Chemical Engineering Journal*, Vol. 167, No. 2-3, pp. 603–609, 2011.

222. Chin, Y., J. Hu, C. Cao, Y. Gao and Y. Wang, "Preparation of a Novel Structured Catalyst Based on Aligned Carbon Nanotube Arrays for a Microchannel Fischer-Tropsch Synthesis Reactor", *Catalysis Today*, Vol. 110, No. 1-2, pp. 47–52, 2005.

223. Guillou, L., P. Balloy, P. Supiot and V. Le Courtois, "Preparation of a Multilayered Composite Catalyst for Fischer-Tropsch Synthesis in a Micro-chamber Reactor", *Applied Catalysis A: General*, Vol. 324, pp. 42–51, 2007.

224. Guillou, L., S. Paul and V. Le Courtois, "Investigation of H_2 Staging Effects on CO Conversion and Product Distribution for Fischer-Tropsch Synthesis in a Structured Microchannel Reactor", *Chemical Engineering Journal*, Vol. 136, No. 1, pp. 66–76, 2008.

225. Zhao, S., V. S. Nagineni, N. V. Seetala and D. Kuila, "Microreactors for Syngas Conversion to Higher Alkanes: Effect of Ruthenium on Silica-supported Iron-cobalt Nanocatalysts", *Industrial & Engineering Chemistry Research*, Vol. 47,

No. 5, pp. 1684–1688, 2008.

226. Knochen, J., R. Güttel, C. Knobloch and T. Turek, "Fischer-Tropsch Synthesis in Milli-structured Fixed-bed Reactors: Experimental Study and Scale-up Considerations", *Chemical Engineering and Processing*, Vol. 49, No. 9, pp. 958–964, 2010.

227. Myrstad, R., S. Eri, P. Pfeifer, E. Rytter and A. Holmen, "Fischer-Tropsch synthesis in a Microstructured Reactor", *Catalysis Today*, Vol. 147, No. S, pp. S301–S304, 2009.

228. Almeida, L. C., F. J. Echave, O. Sanz, M. A. Centeno, G. Arzamendi, L. M. Gandía, E. F. Sousa-Aguiar, J. A. Odriozola and M. Montes, "Fischer-Tropsch Synthesis in Microchannels", *Chemical Engineering Journal*, Vol. 167, No. 2-3, pp. 536–544, 2011.

229. Cao, C., D. R. Palo, A. L. Y. Tonkovich and Y. Wang, "Catalyst Screening and Kinetic Studies Using Microchannel Reactors", *Catalysis Today*, Vol. 125, No. 1-2, pp. 29–33, 2007.

230. Yu, L., R. Nassar, J. Fang, D. Kuila and K. Varahramyan, "Investigation of a Novel Microreactor for Enhancing Mixing and Conversion", *Chemical Engineering Communications*, Vol. 195, pp. 745–757, 2008.

231. Arzamendi, G., P. M. Diéguez, M. Montes, J. A. Odriozola, E. F. Sousa-Aguiar and L. M. Gandía, "Computational Fluid Dynamics Study of Heat Transfer in a Microchannel Reactor for Low-temperature Fischer–Tropsch Synthesis", *Chemical Engineering Journal*, Vol. 160, No. 3, pp. 915–922, 2010.

232. Derevich, I. V., V. S. Ermolaev and V. Z. Mordkovich, "Modeling of Hydrodynamics in Microchannel Reactor for Fischer-Tropsch Synthesis", *International Journal of Heat and Mass Transfer*, Vol. 55, No. 5-6, pp. 1695–1708, 2012.

233. Frauhammer, J., G. Eigenberger, L. Hippel and D. Arnatz, "A New Reactor Concept for Endothermic High-Temperature Reactions", *Chemical Engineering Science*, Vol. 54, No. 15-16, pp. 3661–3670, 1999.

234. Polman, E. A., J. M. der Kinderen and F. M. A. Thuis, "Novel Compact Steam Reformer for Fuel Cells with Heat Generation by Catalytic Combustion Augmented by Induction Heating", *Catalysis Today*, Vol. 47, No. 1, pp. 347–351, 1999.

235. Zanfir, M. and A. Gavriilidis, "Modeling of a Catalytic Plate Reactor for Dehydrogenation-Combustion Coupling", *Chemical Engineering Science*, Vol. 56, No. 8, pp. 2671–2683, 2001.

236. Kolios, G., J. Frauhammer and G. Eigenberger, "Efficient Reactor Concepts for Coupling of Endothermic and Exothermic Reactions", *Chemical Engineering Science*, Vol. 57, No. 9, pp. 1505–1510, 2002.

237. Arana, L. R., S. B. Schaevitz, A. J. Franz, K. F. Jensen and M. A. Schmidt, "A Microfabricated Suspended-Tube Chemical Reactor for Thermally Efficient Fuel Processing", *Journal of Microelectromechanical Systems*, Vol. 12, No. 5, pp. 600–612, 2003.

238. Cao, C., Y. Wang, J. Holladay, E. O. Jones and D. R. Palo, "Design of Micro-Scale Fuel Processors Assisted by Numerical Modeling", *AIChE Journal*, Vol. 51, No. 3, pp. 982–988, 2005.

239. Arzamendi, G., P. M. Diéguez, M. Montes, M. A. Centeno, J. A. Odriozola and L. M. Gandía, "Integration of Methanol Steam Reforming and Combustion in a Microchannel Reactor for H_2 Production: A CFD simulation study", *Catalysis Today*, Vol. 143, No. 1-2, pp. 25–31, 2009.

240. Arzamendi, G., I. Uriz, P. M. Diéguez, L. M. Gandía, M. Montes, M. A. Centeno and J. A. Odriozola, "A CFD Study on the Effect of the Characteristic Dimension

of Catalytic Wall Microreactors", *AIChE Journal*, 2011.

241. Zhai, X., S. Ding, Y. Cheng, Y. Jin and Y. Cheng, "CFD Simulation with Detailed Chemistry of Steam Reforming of Methane for Hydrogen Production in an Integrated Micro-reactor", *International Journal of Hydrogen Energy*, Vol. 35, No. 11, pp. 5383–5392, 2010.

242. Hsueh, C., H. Chu, W. Yan, G. Leu and J. Tsai, "Three-dimensional Analysis of a Plate Methanol Steam Micro-reformer and a Methanol Catalytic Combustor with Different Flow Channel Designs", *International Journal of Hydrogen Energy*, Vol. 36, No. 21, pp. 13575–13586, 2011.

243. Kolb, G., J. Schürer, D. Tiemann, M. Wichert, R. Zapf, V. Hessel and H. Löwe, "Fuel Processing in Integrated Micro-structured Heat-exchanger Reactors", *Journal of Power Sources*, Vol. 171, No. 1, pp. 198–204, 2007.

244. Froment, G. F. and K. B. Bischoff, *Chemical Reactor Analysis and Design*, Wiley, New York, 1990.

245. Jaisathaporn, P. and W. L. Luyben, "Dynamic Comparison of Alternative Tubular Reactor Systems", *Industrial & Engineering Chemistry Research*, Vol. 43, No. 4, pp. 1003–1029, 2004.

246. Akın, A. N., *Development of Coprecipitated Cobalt-Alumina Catalysts for the Production of C_1–C_4 Hydrocarbons by Carbon Monoxide Hydrogenation*, Ph.D. Thesis, Boğaziçi University, 1996.

247. Doesburg, E. B. M., K. P. de Jong and J. H. C. van Hooff, "Preparation of Catalyst Supports, Zeolites and Mesoporous Materials", In: R. A. van Santen, P. W. N. M. van Leeuwen and B. A. Averill (Eds.), *Catalysis: An Integrated Approach*, pp. 433–456, Elsevier, Amsterdam, 1999.

248. Avci, A. K., D. L. Trimm, A. E. Aksoylu and Z. I. Onsan, "Hydrogen Production

by Steam Reforming of n-butane over supported Ni and Pt-Ni Catalysts", *Applied Catalysis A: General*, Vol. 258, No. 2, pp. 235–240, 2004.

249. Varesano, A., I. Guaglio, G. Saracco and P. L. Maffettone, "Dynamics of a Methanol Reformer for Automotive Applications", *Industrial & Engineering Chemistry Research*, Vol. 44, No. 4, pp. 759–768, 2005.

250. Ismagilov, I. Z., E. M. Michurin, O. B. Sukhova, L. T. Tsykoza, E. V. Matus, M. A. Kerzhentsev, Z. R. Ismagilov, A. N. Zagoruiko, E. V. Rebrov, M. H. J. M. de Croon and J. C. Schouten, "Oxidation of Organic Compounds in a Microstructured Catalytic Reactor", *Chemical Engineering Journal*, Vol. 135, No. S1, pp. S57–S65, 2008.

251. Lee, J. K., J. B. Ko and D. H. Kim, "Methanol Steam Reforming over $Cu/ZnO/Al_2O_3$ Catalyst: Kinetics and Effectiveness Factor", *Applied Catalysis A: General*, Vol. 278, No. 1, pp. 25–35, 2005.

252. Tottrup, P. B., "Evaluation of Intrinsic Steam Reforming Kinetic-Parameters from Rate Measurements on Full Particle Size", *Applied Catalysis A: General*, Vol. 4, No. 4, pp. 377–389, 1982.

253. Semelsberger, T. A., L. F. Brown, R. L. Borup and M. A. Inbody, "Equilibrium Products from Autothermal Processes for Generating Hydrogen-rich Fuel-cell Feeds", *International Journal of Hydrogen Energy*, Vol. 29, No. 10, pp. 1047–1064, 2004.

254. Tingelöf, T., L. Hedström, N. Holmström, P. Alvfors and G. Lindbergh, "The Influence of CO_2, CO and Air Bleed on the Current Distribution of a Polymer Electrolyte Fuel Cell", *International Journal of Hydrogen Energy*, Vol. 33, No. 8, pp. 2064–2072, 2008.

255. Hla, S. S., D. Park, G. J. Duffy, J. H. Edwards, D. G. Roberts, A. Ilyushechkin, L. D. Morpeth and T. Nguyen, "Kinetics of High-temperature Water-gas Shift Re-

action over Two Iron-based Commercial Catalysts Using Simulated Coal-derived SyngasesMor", *Chemical Engineering Journal*, Vol. 146, No. 1, pp. 148–154, 2009.

256. Choi, Y. and H. G. Stenger, "Water Gas Shift Reaction Kinetics and Reactor Modeling for Fuel Cell Grade Hydrogen", *Journal of Power Sources*, Vol. 124, No. 2, pp. 432–439, 2003.

257. Golunski, S., "HotSpot™ Fuel Processor: Advancing the Case for Fuel Cell Powered Cars", *Platinum Metals Review*, Vol. 42, No. 1, pp. 2–7, 1998.

258. Song, C. S., "Fuel Processing for Low-temperature and High-temperature Fuel Cells–Challenges, and Opportunities for Sustainable Development in the 21st Century", *Catalysis Today*, Vol. 77, No. 1-2, pp. 17–49, 2002.

259. Sedmak, G., S. Hočevar and J. Levec, "Kinetics of Selective CO Oxidation in Excess of H_2 over the Nanostructured $Cu_{0.1}Ce_{0.9}O_{2-y}$ Catalyst", *Journal of Catalysis*, Vol. 213, No. 2, pp. 135–150, 2003.

260. Tan, O., E. Masalaci, Z. I. Onsan and A. K. Avci, "Design of a Methane Processing System Producing High-Purity Hydrogen", *International Journal of Hydrogen Energy*, Vol. 33, No. 20, pp. 5516–5526, 2008.

261. Praharso, A. A. Adesina, D. L. Trimm and N. W. Cant, "Kinetic Study of *iso*-octane Steam Reforming over a Nickel-based Catalyst", *Chemical Engineering Journal*, Vol. 99, No. 2, pp. 131–136, 2004.

262. Shi, L. M., D. J. Bayless and M. A. Prudich, "A Model of Steam Reforming of *iso*-octane: The Effect of Thermal Boundary Conditions on Hydrogen Production and Reactor Temperature", *International Journal of Hydrogen Energy*, Vol. 33, No. 17, pp. 4577–4585, 2008.

263. Bridger, G. W. and M. S. Spencer, "Methanol Synthesis", In: M. V. Twigg (Ed.), *Catalyst Handbook*, pp. 441–468, Wolfe, London, 1989.

264. Kearby, R. K., "Catalytic Dehydrogenation", In: P. H. Emmett (Ed.), *Catalysis*, Vol. III, pp. 453–491, Reinhold, New York, 1955.

265. Zanfir, M. and A. Gavriilidis, "Catalytic Combustion Assisted Methane Steam Reforming in a Catalytic Plate Reactor", *Chemical Engineering Science*, Vol. 58, No. 17, pp. 3947–3960, 2003.

266. Zanfir, M. and A. Gavriilidis, "Influence of Flow Arrangement in Catalytic Plate Reactors for Methane Steam Reforming", *Chemical Engineering Research and Design*, Vol. 82, No. 2, pp. 252–258, 2004.

267. Veser, G. and J. Frauhammer, "Modelling Steady State and Ignition during Catalytic Methane Oxidation in a Monolith Reactor", *Chemical Engineering Science*, Vol. 55, No. 12, pp. 2271–2286, 2000.

268. Kleinstreuer, C. and J. Koo, "Computational Analysis of Wall Roughness Effects for Liquid Flow in the Micro-conduits", *Journal of Fluids Engineering–Transactions of the ASME*, Vol. 126, No. 1, pp. 1–9, 2004.

269. Durlofsky, L. and J. F. Brady, "Analysis of the Brinkman Equation as a Model for Flow in Porous Media", *Physics of Fluids*, Vol. 30, No. 11, pp. 3329–3340, 1987.

270. Givler, R. C., "A Determination of the Effective Viscosity for the Brinkman-Forchheimer Flow Model", *Journal of Fluid Mechanics*, Vol. 258, pp. 355–370, 1994.

271. Donald, A. N. and A. Bejan, *Convection in Porous Media*, 3rd edition, Springer, New York, 2006.

272. Schädel, B. T., M. Duisberg and O. Deutschmann, "Steam Reforming of Methane, Ethane, Propane, Butane, and Natural Gas over a Rhodium-based Catalyst", *Catalysis Today*, Vol. 142, No. 1-2, pp. 42–51, 2009.

273. Gobina, E., K. Hou and R. Hughes, "Ethane Dehydrogenation in a Catalytic Membrane Reactor Coupled with a Reactive Sweep Gas", *Chemical Engineering Science*, Vol. 50, No. 14, pp. 2311–2319, 1995.

274. Kee, R. J., M. E. Coltrin and P. Glarborg, *Chemically Reacting Flow: Theory and Practice*, John Wiley & Sons, New Jersey, 2003.

275. Wilke, C., "A Viscosity Equation for Gas Mixtures", *Journal of Chemical Physics*, Vol. 18, No. 4, pp. 517–519, 1950.

276. Poling, B. E., J. M. Prausnitz and J. P. O'Connell, *The Properties of Gases and Liquids*, 5th edition, McGraw-Hill, New York, 2001.

277. Bird, R. B., W. E. Stewart and E. N. Lightfoot, *Transport Phenomena*, 2nd edition, John Wiley & Sons, New York, 2002.

278. Fuller, E. N., P. D. Schettler and J. C. Giddings, "New Method for Prediction of Binary Gas Phase Diffusion Coefficients", *Industrial & Engineering Chemistry*, Vol. 58, No. 5, pp. 18–27, 1966.

279. Perry, R. H. and D. W. Green, *Perry's Chemical Engineers' Handbook*, 7th edition, McGraw-Hill, New York, 1997.

280. COMSOL Multiphysics User's Guide, version 3.4, COMSOL AB, Stockholm, Sweden, 2007.

281. Kaviany, M., *Principles of Heat Transfer in Porous Media*, Springer-Verlag, Berlin, 1995.

282. Beeckman, J. W., "Measurement of the Effective Diffusion-Coefficient of Nitrogen Monoxide through Porous Monolith-type Ceramic Catalysts", *Industrial & Engineering Chemistry Research*, Vol. 30, No. 2, pp. 428–430, 1991.

283. Sinnott, R. K., *Design*, 3rd edition, Coulson & Richardson's Chemical Engineer-

ing, Vol. 6, Butterworth-Heinemann, London, 2003.

284. Ergun, S., "Fluid Flow through Packed Columns", *Chemical Engineering Progress*, Vol. 48, No. 2, pp. 89–94, 1952.

285. Hayes, R. E., S. T. Kolaczkowskib, P. K. C. Li and S. Awdry, "Evaluating the Effective Diffusivity of Methane in the Washcoat of a Honeycomb Monolith", *Applied Catalysis B: Environmental*, Vol. 25, No. 2-3, pp. 93–104, 2000.

286. Karatzas, X., J. Dawody, A. Grant, E. E. Svensson and L. J. Pettersson, "Zone-coated Rh-based Monolithic Catalyst for Autothermal Reforming of Diesel", *Applied Catalysis B: Environmental*, Vol. 101, No. 3-4, pp. 226–238, 2011.

287. Nakamura, I., Y. Kobayashi, H. Hamada and T. Fujitani, "Adsorption Behavior and Reaction Properties of NO and CO on Rh(1 1 1)", *Surface Science*, Vol. 600, No. 16, pp. 3235–3242, 2006.

288. Brandner, J. J., E. Anurjew, L. Bohn, E. Hansjosten, T. Henning, U. Schygulla, A. Wenka and K. Schubert, "Concepts and Realization of Microstructure Heat Exchangers for Enhanced Heat Transfer", *Experimental Thermal and Fluid Science*, Vol. 30, No. 8, pp. 801–809, 2006.

289. Versteeg, H. K. and W. Malalasekera, *An Introduction to Computational Fluid Dynamics: The Finite Volume Method*, 2nd edition, Pearson Education Limited, New York, 2007.

290. Peirǿ, J. and S. Sherwin, "Finite Difference, Finite Element and Finite Volume Methods for Partial Differential Equations", In: S. Yip (Ed.), *Handbook of Materials Modeling*, pp. 2415–2446, Springer, Berlin, 2005.

291. Lewis, R. W., P. Nithiarasu and K. N. Seetharamu, *Fundamentals of the Finite Element Method for Heat and Fluid Flow*, Wiley, New York, 2004.

292. Davis, T. A. and I. S. Duff, "A Combined Unifrontal/Multifrontal Method for Unsymmetric Sparse Matrices", *ACM Transactions on Mathematical Software*, Vol. 25, No. 1, pp. 1–19, 1997.

293. Davis, T. A. and I. S. Duff, "An Unsymmetric-pattern Multifrontal Method for Sparse LU Factorization", *SIAM Journal on Matrix Analysis and Applications*, Vol. 18, No. 1, pp. 140–158, 1997.

294. Schenk, O. and K. Gärtner, "Solving Unsymmetric Sparse Systems of Linear Equations with PARDISO", *Future Generation Computer Systems*, Vol. 20, No. 3, pp. 475–487, 2004.

295. ANSYS FLUENT 14.0 User's Guide, ANSYS Inc., Canonsburg, PA, 2011.

296. Patankar, S. V. and D. B. Spalding, "A Calculation Procedure for Heat, Mass and Momentum Transfer in Three-dimensional Parabolic Flows", *International Journal of Heat and Mass Transfer*, Vol. 15, No. 10, pp. 1787–1806, 1972.

297. Patankar, S. V., *Numerical Heat Transfer and Fluid Flow*, Hemisphere, New York, 1980.

298. Vandoormaal, J. P. and G. D. Raithby, "Enhancements of the SIMPLE Method for Predicting Incompressible Flows", *Numerical Heat Transfer*, Vol. 7, pp. 147–163, 1984.

299. Hardt, S., W. Ehrfeld, V. Hessel and K. M. van den Bussche, "Strategies for Size Reduction of Microreactors by Heat Transfer", *Chemical Engineering Communications*, Vol. 190, pp. 540–559, 2003.

300. Zalc, J. M. and D. G. Löffler, "Fuel Processing for PEM Fuel Cells: Transport and Kinetic Issues of System Design", *Journal of Power Sources*, Vol. 111, No. 1, pp. 58–64, 2002.

301. Maranzana, G., I. Perry and M. D., "Mini- and Micro-Channels: Influence of Axial Conduction in the Walls", *International Journal of Heat and Mass Transfer*, Vol. 47, No. 17-18, pp. 3993–4004, 2004.

302. Kolb, G., *Fuel Processing for Fuel Cells*, Wiley-VCH, Weinheim, 2008.

303. Aartun, I., T. Gjervan, H. Venvik, O. Görke, P. Pfeifer, M. Fathi, A. Holmen and K. Schubert, "Catalytic Conversion of Propane to Hydrogen in Microstructured Reactors", *Chemical Engineering Journal*, Vol. 101, No. 1-3, pp. 93–99, 2004.

304. Matsumura, Y. and T. Nakamori, "Steam Reforming of Methane over Nickel Catalysts at Low Reaction Temperature", *Applied Catalysis A: General*, Vol. 258, No. 1, pp. 107–114, 2004.

305. Gandhi, H. S., G. W. Graham and R. W. McCabe, "Automotive Exhaust Catalysis", *Journal of Catalysis*, Vol. 216, No. 1-2, pp. 433–442, 2003.

306. Skoglundh, M. and E. Fridell, "Strategies for Enhancing Low-temperature Activity", *Topics in Catalysis*, Vol. 28, No. 1-4, pp. 79–87, 2004.

307. Fiedorow, R. M. J. and S. E. Wanke, "Effect of γ-Alumina Crystallinity on the State of Rhodium During High-temperature Treatments in Oxygen and Hydrogen", *Applied Catalysis B: Environmental*, Vol. 14, No. 3, pp. 249–259, 1997.

308. Guerrero-Ruiz, A., P. Ferreira-Aparicio, M. B. Bachiller-Baeza and I. Rodríguez-Ramos, "Isotopic Tracing Experiments in Syngas Production from Methane on Ru/Al_2O_3 and Ru/SiO_2", *Catalysis Today*, Vol. 46, No. 2, pp. 99–105, 1998.

309. Lanza, R., S. G. Jaras and P. Canu, "Partial Oxidation of Methane over Supported Ruthenium Catalysts", *Applied Catalysis A: General*, Vol. 325, No. 1, pp. 57–67, 2007.

310. Rabe, S., M. Nachtegaal and F. Vogel, "Catalytic Partial Oxidation of Methane

to Synthesis Gas over a Ruthenium Catalyst: The Role of the Oxidation State", *Physical Chemistry Chemical Physics*, Vol. 9, No. 12, pp. 1461–1468, 2007.

311. Souza, M. M. V. M. and M. Schmal, "Autothermal Reforming of Methane over $Pt/ZrO_2/Al_2O_3$ Catalysts", *Applied Catalysis A: General*, Vol. 281, No. 1-2, pp. 19–24, 2005.

312. Bartholomew, C. H. and R. J. Farrauto, *Fundamentals of Industrial Catalytic Processes*, 2nd edition, John Wiley & Sons, New Jersey, 2006.

313. HSC Chemistry User's Guide, Outotec, Pori, Finland, 2006.

314. Choudhary, V. R., A. M. Rajput and B. Prabhakar, "Nonequilibrium Oxidative Conversion of Methane to CO and H_2 with High Selectivity and Productivity over Ni/Al_2O_3 at Low Temperatures", *Journal of Catalysis*, Vol. 139, No. 1, pp. 326–328, 1993.

315. Mears, D. E., "Tests for Transport Limitations in Experimental Catalytic Reactors", *Industrial and Engineering Chemistry Process Design and Development*, Vol. 10, No. 4, pp. 541–547, 1971.

316. Bhattacharya, M., M. P. Harold and V. Balakotaiah, "Mass-Transfer Coefficients in Washcoated Monoliths", *AIChE Journal*, Vol. 50, No. 11, pp. 2939–2955, 2004.

317. Anderson, J. B., "A Criterion for Isothermal Behaviour of a Catalyst Pellet", *Chemical Engineering Science*, Vol. 18, No. 2, pp. 147–148, 1963.